



**HAL**  
open science

# Towards new efficient nanostructured hybrid materials for ECL applications

Serena Carrara

► **To cite this version:**

Serena Carrara. Towards new efficient nanostructured hybrid materials for ECL applications. Other. Université de Strasbourg, 2017. English. NNT : 2017STRAF016 . tel-01663033

**HAL Id: tel-01663033**

**<https://theses.hal.science/tel-01663033v1>**

Submitted on 13 Dec 2017

**HAL** is a multi-disciplinary open access archive for the deposit and dissemination of scientific research documents, whether they are published or not. The documents may come from teaching and research institutions in France or abroad, or from public or private research centers.

L'archive ouverte pluridisciplinaire **HAL**, est destinée au dépôt et à la diffusion de documents scientifiques de niveau recherche, publiés ou non, émanant des établissements d'enseignement et de recherche français ou étrangers, des laboratoires publics ou privés.

**ÉCOLE DOCTORALE DES SCIENCES CHIMIQUES**  
**Institut de Science et d'Ingénierie Supramoléculaires**

**THÈSE** présentée par :

**Serena CARRARA**

soutenue le : 11 Avril 2017

pour obtenir le grade de : **Docteur de l'université de Strasbourg**

Discipline/ Spécialité : Chimie

**Towards new efficient nanostructured  
hybrid materials for ECL applications**

**THÈSE dirigée par :**

**M<sup>me</sup> DE COLA Luisa**

Professeur, Université de Strasbourg

**RAPPORTEURS :**

**M<sup>me</sup> CERONI Paola**

Professeur, Università degli Studi di Bologna (Italie)

**M. SOJIC Neso**

Professeur, Université de Bordeaux

---

**AUTRE MEMBRE DU JURY :**

**M. BONNEFONT Antoine**

Maître de Conférences, Université de Strasbourg



*"Where should I go?" -Alice. "That depends on where you want to end up." -The Cheshire Cat.*

*Lewis Carroll*





# Table of Contents

<b>Résumé de These .....</b>	<b>4</b>
<b>Chapter 1: Introduction .....</b>	<b>17</b>
1.1 Historical overview .....	18
1.2 Luminescence: how to generate an excited state .....	18
1.2.1 Ion annihilation ECL .....	20
1.2.2 Co-reactant ECL .....	23
1.2.2.1A model ECL system: Ru(bpy) <sub>3</sub> <sup>2+</sup> /TPrA system.....	23
1.3 ECL luminophores .....	26
1.3.1 Transition metal complexes .....	26
1.3.1.1Ruthenium(II) complexes .....	26
1.3.1.2Iridium(III) complexes.....	29
1.3.1.3Platinum(II) complexes .....	34
1.3.2 Nanomaterials .....	35
1.4 ECL Co-reactants.....	37
1.5 ECL Analytical applications .....	38
1.5.1 Application in CE, HPLC and FIA systems .....	39
1.5.2 ECL Assays for diagnostics .....	40
1.6 Aim of the thesis .....	40
1.7 References.....	42
<b>Chapter 2: Aggregation-Induced ECL of Platinum(II) Complexes.....</b>	<b>49</b>
2.1 Introduction.....	50
2.1.1 Electronic configuration of square-planar Pt(II) complexes .....	50
2.1.2 Supramolecular architectures of square-planar Pt(II) complexes.....	52
2.2 Results and discussion .....	53
2.3 Photophysical properties .....	54
2.4 Electrochemistry and AIECL behavior.....	59
2.4.1 Pt-Amide.....	59
2.4.2 Pt-PEG .....	65
2.4.3 Pt-2PEG .....	67
2.5 Conclusion .....	71
2.6 Experimental section.....	71
2.7 References.....	76
<b>Chapter 3: Solid-state ECL Films based on Iridium(III) Complexes..</b>	<b>81</b>
3.1 Introduction.....	82
3.2 Synthesis of Ir(pphen) <sub>2</sub> (mVbpy).....	84
3.3 Absorption and emission spectroscopy.....	84

3.4	Reductive electropolymerization of Ir(pphen) <sub>2</sub> (mVbpy).....	86
3.5	ECL properties of Ir(pphen) <sub>2</sub> (mVbpy) and poly-Ir.....	91
3.6	Conclusion .....	92
3.7	Experimental section.....	93
3.8	References.....	95

**Chapter 4: Amine-Rich Nitrogen-doped Carbon NanoDots (NCNDs):  
Revealing and Tailoring Co-reactant Properties ..... 99**

4.1	Introduction.....	100
4.2	Synthesis and characterization of primary and tertiary NCNDs.....	102
4.3	Electrochemical properties .....	105
4.4	Effect of (m)NCNDs on the ECL of Ru(bpy) <sub>3</sub> <sup>2+</sup> .....	108
4.5	Epinephrine sensing .....	111
4.6	Conclusion .....	113
4.7	Experimental section.....	114
4.8	References.....	117

**Chapter 5: Transition Metal Complexes-Nanoparticle Hybrid  
Nanostructures for ECL Applications ..... 121**

5.1	Introduction.....	122
5.2	Ruthenium(II) and Iridium(III) complexes – NCNDs nanostructured materials.....	124
5.2.1	Grafting of metal complexes onto NCNDs .....	124
5.2.2	Characterization .....	125
5.2.3	Photophysical properties.....	127
5.2.4	Electrochemistry .....	131
5.2.4.1	Ru-NCNDs .....	131
5.2.4.1	Ir-NCNDs .....	133
5.2.5	Electrochemiluminescence .....	135
5.2.6	Nanohybrids as self-enhancing and multi-label for ECL platforms .....	138
5.2.6.1	Self-enhancing ECL platform.....	138
5.2.6.2	Multi-label ECL platform.....	139
5.3	Conclusion .....	140
5.4	Experimental section.....	142
5.5	References.....	147

**Chapter 6: Electrochemical Impedance Spectroscopy and  
Electrochemiluminescence for the detection of Troponin I ..... 151**

6.1	Introduction.....	152
6.1.1	Cardiac biomarkers:Troponin I, the gold standard .....	152
6.1.2	Electrochemical Impedance Spectroscopy (EIS) as sensing technique .....	153

6.1.3	ECL biosensors and immunoassays.....	157
6.1.4	Aim of the work.....	158
6.2	Electrochemical sensor based on labeled antibodies with Ir(III) complexes (MAb-Ir) .....	159
6.2.1	Labeling of MAb with Iridium(III) complexes .....	159
6.2.1.1	Photophysical characterization .....	159
6.2.2	Immunoassay configuration.....	161
6.2.3	Electrochemistry .....	161
6.2.4	Confocal microscopy .....	162
6.3	Troponin I sensing .....	166
6.3.1	EIS measurements .....	166
6.3.2	Electrochemiluminescence .....	169
6.4	Conclusion .....	172
6.5	Experimental section.....	173
6.6	References.....	176
<b>Chapter 7: Experimental Techniques .....</b>		<b>181</b>
7.1	Absorption spectroscopy.....	182
7.2	Fluorescence spectroscopy .....	183
7.3	Luminescence quantum yield .....	185
7.4	Lifetime measurements.....	187
7.5	Scanning electron microscopy (SEM) .....	189
7.6	Fluorescence microscopy.....	190
7.7	Transmission Electron Microscopy (TEM) .....	192
7.8	Electrochemistry .....	193
7.9	References.....	194
<b>Summary of the Thesis .....</b>		<b>197</b>
<b>Acknowledgements .....</b>		<b>211</b>
<b>Curriculum Vitae .....</b>		<b>215</b>



# Résumé de Thèse

La sensibilité et la fiabilité sont des conditions fondamentales pour les capteurs biologiques et médicaux. De nombreuses techniques analytiques, ainsi que des méthodes de détection sont basées sur l'utilisation de la fluorescence en raison de la sensibilité et de la technologie relativement peu coûteuse.

La **Chimio-Luminescence Electro-générée** (ECL) est un phénomène qui connaît un grand succès dans les applications utilisant des biocapteurs. L'ECL est le procédé par lequel les espèces générées au niveau des électrodes, avec l'aide d'un agent réducteur ou oxydant, subissent des réactions de haute énergie de transfert d'électrons pour former des états excités qui émettent de la lumière.<sup>1</sup> Étant donné que l'intensité lumineuse est en général proportionnelle à la concentration des espèces d'émission, l'ECL, en tant qu'outil analytique puissant, a trouvé une très large application dans le diagnostic.<sup>2,3</sup>

Elle offre une détection très sensible, jusqu'à des concentrations en dessous du picomolaire avec une gamme dynamique extrêmement large (plus de six ordres de grandeur). Étant donné qu'aucune source de lumière n'est nécessaire, le système est simple et il peut être facilement combiné avec d'autres technologies telles que la technologie microfluidique et l'électrophorèse capillaire.<sup>2</sup> Tous les essais requièrent la présence d'un luminophore. Ce dernier attestera de la présence de l'analyte, dans le cas des immuno-essais, et est couplé à une espèce redox, un co-réactif.

Le marqueur le plus courant pour des études en ECL est un dérivé de ruthenium(II) tris(2,2'-bipyridyl) ( $\text{Ru}(\text{bpy})_3^{2+}$ ) en raison de son émission lumineuse, de son excellente stabilité, de ses propriétés redox idéales, et de la possibilité d'utiliser une variété de co-réactifs en combinaison avec une tension positive ou négative appliquée à l'électrode. Récemment, toutefois, la nécessité d'un marqueur plus sensible et la recherche d'émetteurs multicolores pour les essais communément appelés « multiplex », a conduit à l'étude de différents complexes métalliques, tels que les complexes d'Iridium (III)<sup>4-6</sup> ou des dendrimères et petits polymères qui possèdent plus d'un marqueur.<sup>7</sup>

En ce qui concerne le co-réactif, la Tri-(n)-propylamine (TPrA) est la molécule la plus utilisée, fournissant le signal ECL optimal lorsqu'elle est utilisée en combinaison avec  $\text{Ru}(\text{bpy})_3^{2+}$ .<sup>8</sup> Même dans ce cas, il est souhaitable de remplacer la TPrA, qui est toxique,

corrosive, volatile et doit être utilisée à des concentrations élevées (habituellement jusqu'à 100 mM) pour obtenir une bonne sensibilité.<sup>9</sup>

Cette thèse de doctorat vise à **développer de nouveaux matériaux hybrides pour les applications ECL**. En particulier, l'étude commence avec les propriétés ECL des nouvelles formes agrégées de complexes métalliques, basés sur le platine (II) et l'iridium (III), et une nouvelle classe de co-réactifs à base de "nanopoints" ("nanodots") de carbone fonctionnalisés par les groupements de type amino, pour aboutir au développement de nouveaux matériaux hybrides nés de la combinaison de nanoparticules et de complexes métalliques. Enfin, une approche pour la réalisation de plateformes d'immunodosage dans un but de détection de biomarqueurs cardiaques sera présentée.

Dans le premier chapitre de cette thèse, les principes généraux de l'ECL sont présentés. En général, les voies d'excitation ECL sont étroitement liées à leurs voies d'excitation photoluminescentes correspondantes.<sup>10</sup>

L'état excité d'une molécule peut être produit par la réaction de radicaux générés à partir cette même molécule (émetteur), dans le mécanisme dit d'**annihilation** d'ions, ou à partir de deux précurseurs différents (émetteur et co-réactif), via le **co-réactif** ECL (Figure 1).<sup>1,11</sup> Ceci représente la colonne vertébrale du travail expérimental présenté dans les autres chapitres. Comme l'utilisation du co-réactif ECL présente plus d'applications, les luminophores ECL et co-réactifs les plus utilisés sont également présentés avec un aperçu critique dans les récentes utilisations des nanomatériaux dans ce domaine. Dans la dernière partie de ce chapitre, les principales applications de l'ECL sont brièvement décrites.

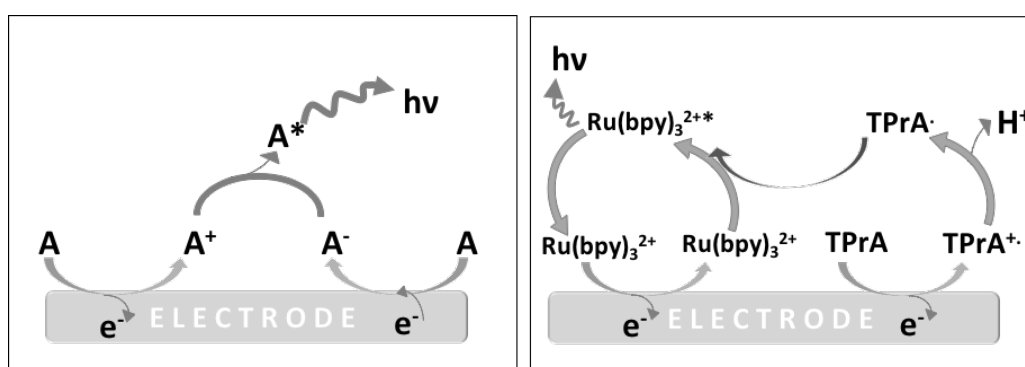


**Figure 1.** Diagramme schématique décrivant les réactions de transfert d'électrons responsables de l'émission pendant l'annihilation ECL (à gauche) et co-réactif ECL (à droite).

Le deuxième chapitre est consacré à l'étude d'une nouvelle classe de complexes métalliques pour des applications en ECL, basée sur l'auto-assemblage supramoléculaire de complexes de Pt (II), à géométrie plane carrée. Ces complexes sont capables de former différents assemblages supramoléculaires en fonction de la concentration, du solvant et de la température.<sup>12,13</sup>

En raison de leur configuration électronique  $d^8$ , les complexes de platine (II) ont une géométrie carrée plane, leur permettant de s'auto-assembler par des interactions non covalentes telles que le  $\pi$ - $\pi$  stacking (entre les ligands) ou les interactions métal -métal (par recouvrement des orbitales  $5d_{z^2}$ ).<sup>14,15</sup> Dans ce dernier cas, de nouvelles transitions électroniques peuvent survenir, par exemple, par photo-excitation, par la formation de nouvelles orbitales moléculaires. Comme cela est représenté sur la figure 2, les transitions électroniques entre l'HOMO localisée sur les métaux et la LUMO impliquant que les ligands peuvent se produire. Ces transitions sont donc des transferts de charge métal-métal à ligand (MMLCT) (figure 2). Les nouveaux états excités correspondants sont, en raison de la présence de l'atome lourd, de type triplet par nature et peuvent ainsi conduire à des changements spectaculaires dans les propriétés de luminescence des agrégats formés par rapport au monomère.

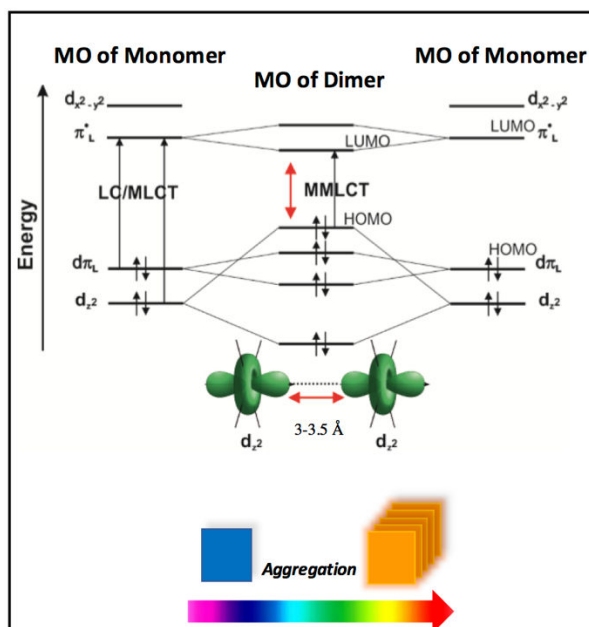


**Figure 2.** Diagramme simplifié d'orbitales moléculaires montrant l'effet des interactions et du recouvrement orbitaire (haut). Représentation schématique de l'agrégation des complexes de Pt(II) (bas).



Malgré le grand intérêt dans les propriétés photophysiques des complexes de Pt (II) luminescents et leurs assemblages, il n'y a que peu de publications concernant leurs propriétés ECL.<sup>16-18</sup> Inspiré par le phénomène dit d'émission induite par agrégation (AIE), typique pour de tels auto-assemblages,<sup>13,19,20</sup> nous avons classifié l'émission ECL de ces agrégats comme ECL induite par agrégation (AIECL), ce phénomène ne présentant à ce jour aucune publication.

Les complexes de platine étudiés, nommés ici par leur fonctionnalisation chimique **Pt-Amide**, **Pt-PEG** et **Pt-2PEG** (Figure 3a-bc), présentent une capacité très intéressante d'émettre une phosphorescence orange via ECL lors de l'agrégation (Figure 3d), ce qui est dû à la établissement d'interactions métallophiles Pt...Pt par des stimuli électriques ou mécaniques, ou par agrégation spontanée. Notamment, **Pt-2PEG** présente une émission orange intense en ECL qui donne un rendement quantique plus élevé par rapport au complexe couramment utilisée Ru (bpy)<sub>3</sub><sup>2+</sup>, comme le montre la Figure 4a-b. Puisque le complexe de platine à son état de monomère présente une photoluminescence bleue dans des solvants appropriés,<sup>12,13</sup> l'émission orange est le résultat d'une agrégation dans une solution aqueuse déclenchée par des exigences énergétiques.

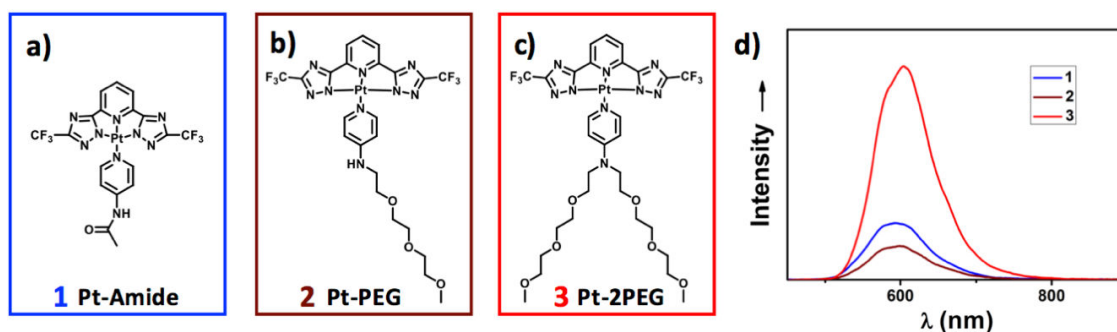


**Figure 3.** a) structure de **Pt-Amide**; b) structure de **Pt-PEG**; c) structure de **Pt-2PEG**; d) émissions de ECL du système Pt(II) complexe / C<sub>2</sub>O<sub>4</sub><sup>2-</sup> obtenues pendant un balayage potentiel continu entre +1.65 V et 0.5 V après dépôt goutte à goutte d'une solution de 1 (trace bleue), 2 (trace marron), 3 (trace rouge) dans de l'acétone (méthanol pour le 3) sur l'électrode imprimée de carbone.

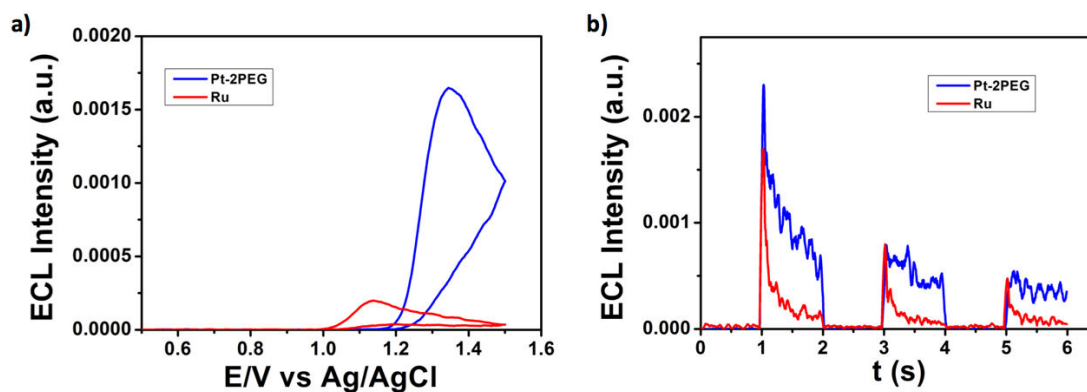


**Figure 4.** a) ECL pendant un balayage potentiel de solution aqueuse  $10^{-5}$  M de  $\text{Ru}(\text{bpy})_3^{2+}$  (trace rouge) et **Pt-2PEG** (trace bleue) en utilisant  $\text{LiClO}_4$  0.1 M en tant qu'électrolyte de support, par addition de 10 mM de  $\text{Na}_2\text{C}_2\text{O}_4$ . Vitesse de balayage : 0.05 V/s. Carbone vitreux (GC) comme électrode de travail, Ag/AgCl comme électrode de référence et fil de Pt comme contre-électrode; B) Intensités ECL en temps de  $\text{Ru}(\text{bpy})_3^{2+}$  (trace rouge) et **Pt-2PEG** (trace bleue) dans une solution 0.1 M d'eau  $\text{LiClO}_4$  en utilisant 10 mM de  $\text{Na}_2\text{C}_2\text{O}_4$  comme co-réactif. GC comme électrode de travail, Ag/AgCl comme électrode de référence et Pt comme électrode de contre-électrode. Pulse à +1.4 V.

Grâce à sa double nature hydrophile/ hydrophobe, nous supposons que le complexe tente de minimiser les interactions entre le ligand chélaté hydrophobe et l'environnement aqueux, formant ainsi une structure micellaire avec les chaînes PEG dirigées extérieurement vers l'eau. Une telle agrégation se forme à travers des interactions métallobiphiles, donnant lieu à une nouvelle transition appelée MMLCT (metal-metal to ligand charge transfer), responsable du déplacement bathochromique de l'émission.

Dans la recherche de nouveaux complexes pouvant être utilisés à ce profit, le chapitre trois traite de complexes d'Ir (III) pour la fabrication de **plateformes ECL à l'état solide**. [Ir (pphent) 2 (dMebpy)] (pphent = phenyl-phénanthridine; dMebpy = 4,4'-vinyl methyl bipyridine) contiennent un ligand qui peut polymériser en raison du groupe vinyl attaché à la bipyridine. Les procédures d'électrodéposition ainsi que les propriétés photophysiques, électrochimiques et ECL sont présentées (figure 5). Elles montrent une forte émission pendant différents cycles voltammétriques, bien que d'autres améliorations soient encore en cours pour rendre le film électrodéposé stable au cours des cycles.

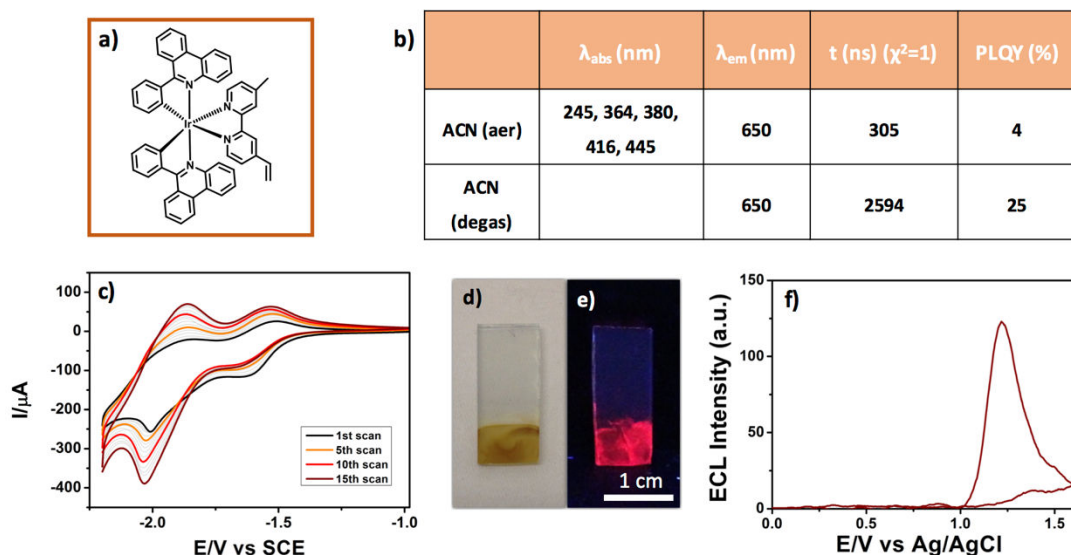


**Figure 5.** **a)** structure de  $[Ir(pphnt)_2(dMebpy)]$ ; **b)** propriétés photophysiques du complexe dans l'acétonitrile (solution aérée et dégazée); **c)** électropolymérisation du complexe dans une solution d'acétonitrile TBAPF<sub>6</sub> 0.1 M sur électrode FTO. Vitesse de balayage 0.1 V/s ; **d-e)** couche électropolymérisée du complexe sur FTO (à gauche) et sous irradiation UV-vis (à droite) ; **f)** ECL pendant un balayage potentiel de poly-Ir couche sur FTO pendant un balayage de potentiel entre +1.6 V et 0 V, après addition de 10 mM de TPrA comme co-réactif. Vitesse de balayage 0.05 V/s.

Dans le quatrième chapitre, les propriétés co-réactives des « nanodots » de carbone contenant un nombre important d'azotes (groupements amines et noyaux hétéroaromatiques, NCND) ont été révélées et adaptées. Comme nous l'avons mentionné dans l'introduction, le grand défi consiste à remplacer la TPrA par un composé moins volatile et non toxique, tout en présentant une efficacité similaire. Les NCNDs présentés montrent des groupes amino abondants sur leur surface.

Puisque ces groupes sont l'unité co-réactive la plus efficace et la plus utilisée en combinaison avec  $Ru(bpy)_3^{2+}$ , ce projet met l'accent sur l'étude des NCNDs portant des groupements alkylamines primaires et tertiaires en surface comme co-réactif pour  $Ru(bpy)_3^{2+}$  génération ECL (figure 6).

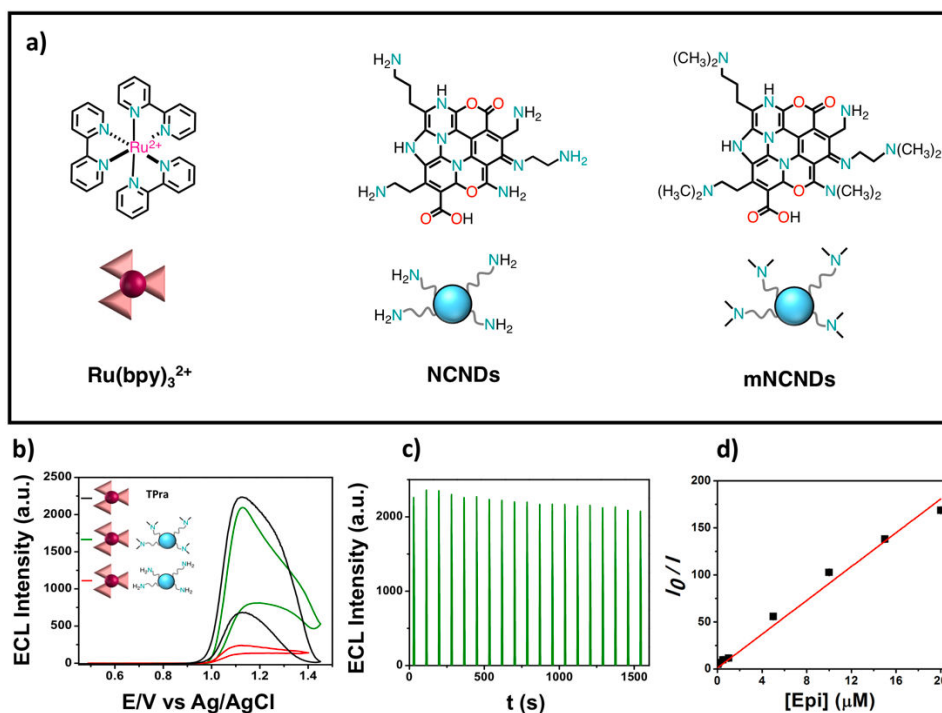


**Figure 6.** **a)** tris (2,2'-bipyridine) ruthénium (II) ( $\text{Ru}(\text{bpy})_3^{2+}$ ) à gauche, NCNDs au milieu et NCNDs méthylés (mNCNDs) à droite; **b)** comparaison entre l'émission de  $\text{Ru}(\text{bpy})_3^{2+}$  augmentée par 0.1 mg/mL de NCND (traces noires), 0.1 mg/mL de mNCND (traces rouges) et 20 mM de TPrA (traits en pointillés bleus); potentiel rapporté Ag/AgCl (KCl sat.) à température ambiante. Fil de platine comme contre-électrode; **c)** Réponses ECL du système  $\text{Ru}(\text{bpy})_3^{2+}$ /mNCNDs obtenu lors d'un balayage potentiel continu entre + 1.1 V et -0.9 V (20 cycles sous vitesse de balayage 0.05 V/s). Potentiel rapporté Ag/AgCl (KCl sat.) à température ambiante. Fil de platine comme contre-électrode; **d)** ajustement linéaire de  $I_0/I$  par rapport à la concentration d'épinéphrine (EP) lorsque des mNCND sont utilisés comme co-réactif dans la concentration de 0,1 mg/mL. Les barres d'erreur sont de la même taille que le symbole carré.

Leur synthèse facile et peu coûteuse, une bonne solubilité dans l'eau et la biocompatibilité, font de nos NCNDs une alternative conviviale prometteuse à la TPrA toxique. Nous démontrons que, des amines primaires aux amines tertiaires, leur capacité à générer l'état excité émissif de  $\text{Ru}(\text{bpy})_3^{2+}$  s'améliore. En particulier, les émissions de  $\text{Ru}(\text{bpy})_3^{2+}$  augmentent de 10 fois avec les NCNDs tertiaires (mNCNDs) par rapport aux NCNDs, ce qui montre que le TPrA toxique peut être remplacé jusqu'à une concentration de 20 mM (Figure 6b). Fait intéressant, la réponse ECL constante (à moins de 10%) a été obtenue pendant plus de 20 cycles, en utilisant mNCNDs comme co-réactif (Figure 6c).

De surcroît, dans le but d'évaluer l'utilisation possible de ce nouveau système ECL NCNDs/Ru(bpy)<sub>3</sub><sup>2+</sup> comme plateforme de biocapteur, la détection de la L-épinéphrine, neurotransmetteur important étudié pour le diagnostic de troubles neurologiques, est discutée. En utilisant les mNCNDs, la limite de détection (LOD) et la quantification (LOQ) ont diminué d'un facteur 10 par rapport aux NCNDs, respectivement 30 nM et 110 nM (ratio signal / bruit = 3). Ce résultat est dix fois plus élevé que celui rapporté pour différents CNDs<sup>21,22</sup> et il atteint la même limite que celle obtenue avec d'autres types de techniques (figure 6d).<sup>23-27</sup>

Le cinquième chapitre est construit sur le domaine de la recherche active des systèmes ECL fonctionnalisés avec des nanomatériaux. Des variétés de nanomatériaux, et en particulier des nanoparticules, comme des nanoparticules (NPs) d'or ou de silicium, ont été étudiées dans le cadre d'un système hybride ECL avec des complexes de métaux de transition comme émetteurs.<sup>28-31</sup> Cependant, le système ECL hybride à base de nanodots de carbone n'a pas encore été exploré.

En effet, dans le contexte de l'utilisation de nanoparticules visant à obtenir l'amélioration du signal ECL, qui représente la ligne de recherche la plus intéressante pour le développement de la technique ECL, nous étudions l'utilisation des nanodots de carbone comme support pour les étiquettes ECL. En effet, nos NCNDs présentent des avantages exceptionnels par rapport aux autres nanoparticules courantes. Leur surface facilement fonctionnalisable sans la nécessité de traitements supplémentaires après la synthèse et leur petite taille, conjointement avec toutes les caractéristiques attrayantes mentionnées ci-dessus, font des NCNDs un support particulièrement intéressant pour les espèces actives d'ECL.

Nous présentons des **nanohybrides à base de NCNDs** portant plusieurs complexes de ruthénium ou d'iridium comme des marqueurs ECL (figure 7a). Une étude approfondie montre leurs propriétés rédox et photophysiques (Figure 7b-c) afin d'évaluer l'effet des NCNDs sur les unités actives de l'ECL. La principale préoccupation concernant les systèmes hybrides à base de nanomatériaux est associée à la proximité des centres d'oxydoréduction à la surface de l'électrode, à leur aptitude à diffuser et à l'apparition de phénomènes d'extinction de luminescence, affectant leurs propriétés optiques et électrochimiques.

Les nouveaux systèmes présentés se révèlent être une plateforme d'auto-amplification ECL, qui est un modèle de réaction ECL prometteur avec une efficacité lumineuse améliorée (figure 7d). De plus, l'immobilisation de ces hybrides sur la surface de l'électrode prouve l'intensification de l'intensité du signal due à la présence d'un grand nombre d'unités génératrices de signal sur chaque NCND (Figure 7e).

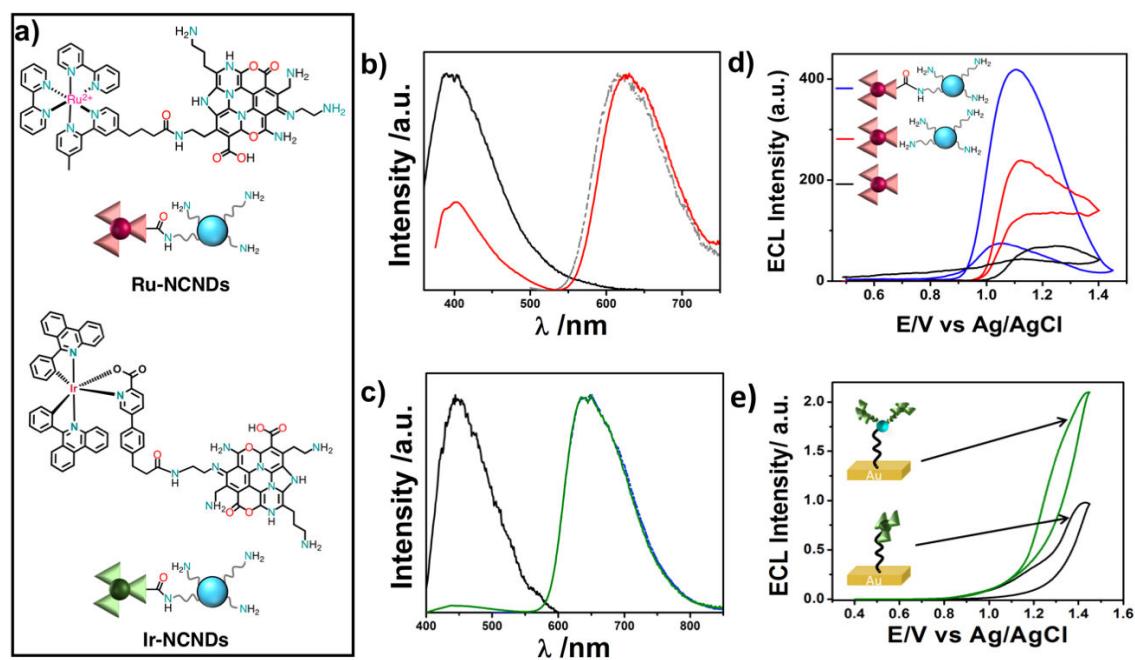


**Figure 7.** *a)* le nanoconjugué  $Ru(bpy)_3^{2+}$ -NCNDs lié de manière covalente au-dessus, et le nanoconjugué Ir-COOH-NCNDs lié par covalence en-dessous; *b)* Spectres d'émission normalisés de Ru-NCNDs (trace rouge),  $Ru(bpy)_3^{2+}$  (trace grise) et NCNDs (trace noire) dans la solution Procell® (exc = 340 nm); *c)* Spectres d'émission normalisés des Ir-NCND (trace verte), Ir-COOH (trace bleue) et NCNDs (trace noire) dans la solution Procell® (exc = 380 nm); *d)* Intensité de l'ECL pendant un balayage potentiel de la solution  $10^{-4}$  M de PBS de  $Ru(bpy)_3^{2+}$  (trace noire), après addition de 0.1 mg / ml de NCNDs (trace rouge) et de Ru-NCNDs (trace bleue) avec une concentration  $10^{-4}$  M de complexe. Vitesse de balayage 0.05 V/s; *e)* Intensités ECL enregistrées lors d'un CV dans PBS / Triton X 100 / TPrA 10 mM d'Ir-NCNDs (trace verte) et Ir-COOH (tracs noire) après immobilisation sur des électrodes d'or. Vitesse de balayage: 0,05 V/s.

Dans le sixième chapitre, une nouvelle approche de détection basée sur la spectroscopie d'impédance électrochimique (EIS) et l'ECL pour la détection de la troponine I (cTnI) est présentée. L'objectif de ce travail est d'utiliser un complexe d'Ir (III),  $[Ir(pphen)_2(Cepic)]$  pour réaliser un **dispositif de biocapteur en ECL** pour la détection de cTnI avec des propriétés améliorées. L'innovation dans ce projet consiste à utiliser une technique qui, par

rapport à celles utilisées pour la détection des biomarqueurs cardiaques, est plus sensible, avec un complexe métallique plus émissif qui peut remplacer le  $\text{Ru}(\text{bpy})_3^{2+}$ , en permettant une détection de très faibles quantités de l'antigène dans des échantillons de sang avec une méthode peu onéreuse, rapide et sans risques pour l'environnement.

Les anticorps marqués avec le complexe Ir (III) (Ir-MAb) ont été étudiés par spectroscopie et microscopie confocale. La configuration d'immunodosage est représentée dans la figure 8a, et pour chaque concentration, des méthodes électrochimiques cTnI ainsi que des micrographes confocales peuvent être utiles pour calculer la couverture de surface de l'électrode (figure 8d-e). L'EIS est utilisée comme technique analytique dans la gamme de concentration 1  $\mu\text{g}/\text{mL}$ -1  $\text{ng}/\text{mL}$  de cTnI. Des changements dans les spectres EIS peuvent montrer l'évolution de la résistance et de la capacité de l'interface, fournissant ainsi un aperçu de l'effet de la modification de surface (figure 8b-c).

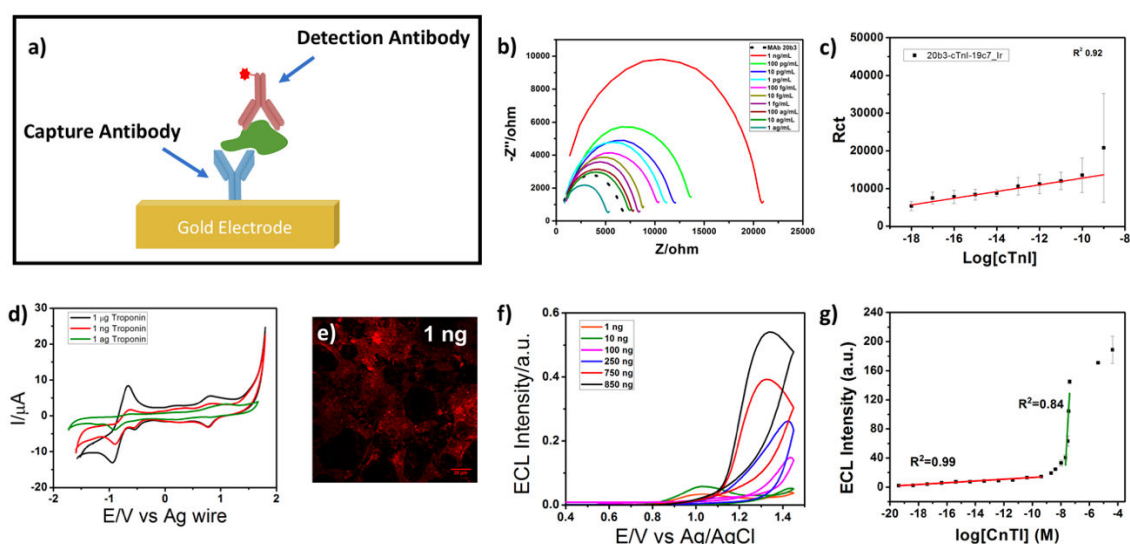


**Figure 8.** *a)* schéma représentatif pour la fabrication d'un immunodosage pour la détection de cTnI; *b)* diagrammes de Nyquist de l'immunodosage avec la concentration de cTnI, variant systématiquement de 1  $\mu\text{g}/\text{mL}$  à 1  $\text{ng}/\text{mL}$  dans 1 mM de DPBS ( $N=3$ ). La fourchette de fréquences est comprise entre 0.01 et 100000 Hz, l'amplitude en courant alternatif est de 25 mV et le potentiel de courant continu était réglé sur circuit ouvert; *c)* régression linéaire de R; *d)* voltammétrie cyclique de l'immunodosage à différentes concentrations de cTnI: trace verte : 1  $\mu\text{g}/\text{mL}$ , trace rouge : 1  $\text{ng}/\text{mL}$  et trace noire : 1  $\mu\text{g}/\text{mL}$  *e)* images confocales de l'immunodosage avec des concentrations de 1  $\text{ng}/\text{mL}$  d'anticorps. Echelle : 20  $\mu\text{m}$ ; *f)* intensité de l'ECL en fonction de la concentration de cTnI (concentration élevée 1 ng - 850 ng); *g)* zone d'intensité ECL en fonction de  $\log [cTnI]$  (concentration à pleine échelle) et régression linéaire des deux zones de concentration. Les barres d'erreur sont comparables ou inférieures à la taille des symboles.



En appliquant cette technique, la limite de détection a donné 10 ag/mL (voir figure 8c), qui a été en outre améliorée en utilisant l'ECL. Grâce à cette technique, le LOD a été calculé à 0,42 ag/mL, ce qui correspond à  $1.76 \times 10^{-20}$  M (ratio signal/bruit = 4), donnant ainsi le résultat le plus bas jusqu'à maintenant rapporté pour les biocapteurs basés sur l'ECL (voir figure 8f-g).<sup>32-35</sup> Cet excellent résultat provient de l'amélioration du marqueur employé, plus facilement détectable que le  $\text{Ru}(\text{bpy})_3^{2+}$  classique, en termes d'efficacité. De plus, la gamme étudiée par l'ECL est 1 ng/mL- 1 mg/mL de cTnI. La figure 8g montre la dépendance de l'intensité ECL en fonction de  $\log [\text{CnTI}]$  sur toute la gamme. A partir de cette courbe,  $K_D$  (constante de dissociation) peut être obtenue et elle est d'environ  $10^{-8}$  M, plutôt en accord avec celle en solution calculée pour le même anticorps ( $10^{-9}$  M)<sup>36</sup> et montrant la grande affinité de cet anticorps pour CnTI.

En conclusion, nous avons étudié avec succès de nouveaux systèmes efficaces allant des complexes métalliques aux nanoparticules pour des applications ECL. Nous avons exploré les propriétés électrochimiluminescentes de nouveaux complexes de Pt (II) et d'Ir (III) comme alternative au marqueur  $\text{Ru}(\text{bpy})_3^{2+}$  existant. La combinaison d'étiquettes et de NCNDs portant des groupes primaires ou tertiaires à la surface comme espèces co-réactives alternatives à la TPrA, toxique, a abouti à une stratégie intéressante pour éliminer la TPrA. En particulier, les NCNDs dans un système lié par liaison covalente avec  $\text{Ru}(\text{bpy})_3^{2+}$  (Ru-NCNDs) sont non seulement un support innocent pour les espèces actives d'ECL, mais agissent également comme co-réactif dans le procédé ECL, se révélant être une plateforme auto-améliorante en ECL. Enfin, un véritable immuno-essai pour la détection des marqueurs cardiaques a été mis au point avec une sensibilité et une stabilité accrues, ce qui est d'une importance fondamentale pour les applications de détection biologique et biomédicale. La même technologie peut alors être appliquée à une variété d'autres analytes, ouvrant ainsi le site à d'autres dosages.

## References

- (1) Bard, A. J. *Electrogenerated Chemiluminescence*; Marcel Dekker, Inc.: New York., **2004**.
- (2) Miao, W. *Chem. Rev.* **2008**, *108* (7), 2506.



- (3) Hu, L.; Xu, G. *Chem. Soc. Rev.* **2010**, 39 (8), 3275.
- (4) Swanick, K. N.; Ladouceur, S.; Zysman-Colman, E.; Ding, Z. *Chem. Commun.* **2012**, 48, 3179.
- (5) Barbante, G. J.; Doeven, E. H.; Francis, P. S.; Stringer, B. D.; Hogan, C. F.; Kheradmand, P. R.; Wilson, D. J. D.; Barnard, P. J. *Dalt. Trans.* **2015**, 44 (18), 8564.
- (6) Fernandez-Hernandez, J. M.; Longhi, E.; Cysewski, R.; Polo, F.; Josel, H.-P.; De Cola, L. *Anal. Chem.* **2016**, 88 (8), 4174.
- (7) Staffilani, M.; Höss, E.; Giesen, U.; Schneider, E.; Hartl, F.; Josel, H. P.; De Cola, L. *Inorg. Chem.* **2003**, 42 (24), 7789.
- (8) Miao, W.; Choi, J.-P.; Bard, A. J. *J. Am. Chem. Soc.* **2002**, 124 (48), 14478.
- (9) Liu, X.; Shi, L.; Niu, W.; Li, H.; Xu, G. *Angew. Chem. - Int. Ed.* **2007**, 46 (3), 421.
- (10) Santhanam, K.; Bard, A. *J. Am. Chem. ...* **1965**, 2243, 139.
- (11) Richter, M. M. *Chem. Rev.* **2004**, 104 (6), 3003.
- (12) Sinn, S.; Biedermann, F.; Vishe, M.; Aliprandi, A. *ChemPhysChem* **2016**, 17, 1829.
- (13) Aliprandi, A.; Mauro, M.; Cola, L. *De. Nat. Chem.* **2016**, 8 (January), 10.
- (14) Miskowski, V. M.; Houlding, V. H. *Inorg. Chem.* **1989**, 28 (8), 1529.
- (15) Lu, W.; Chan, M. C. W.; Zhu, N.; Che, C. M.; Li, C.; Hui, Z. *J. Am. Chem. Soc.* **2004**, 126 (24), 7639.
- (16) Chen, Z.; Wong, K. M.; Kwok, E. C.; Zhu, N.; Zu, Y.; Yam, V. W. *Inorg. Chem.* **2011**, 50, 2125.
- (17) Li, C.; Wang, S.; Huang, Y.; Zheng, B.; Tian, Z.; Wen, Y.; Li, F. *Dalt. Trans.* **2013**, 42, 4059.
- (18) Reid, E. F.; Cook, V. C.; Wilson, D. J. D.; Hogan, C. F. *Chem. A Eur. J.* **2013**, 19, 15907.
- (19) Mauro, M.; Aliprandi, A.; Cebrián, C.; Wang, D.; Kübel, C.; De Cola, L. *Chem. Commun.* **2014**, 50 (55), 7269.
- (20) Aliprandi, A.; Genovese, D.; Mauro, M.; De Cola, L. *Chem. Lett.* **2015**, 44 (9), 1152.
- (21) Long, Y.-M.; Bao, L.; Zhao, J.-Y.; Zhang, Z.-L.; Pang, D.-W. *Anal. Chem.* **2014**, 86 (15), 7224.
- (22) Xu, Z.; Yu, J.; Liu, G. *Sensors Actuators B Chem.* **2013**, 181, 209.
- (23) Kang, J.; Yin, X. B.; Yang, X.; Wang, E. *Electrophoresis* **2005**, 26 (9), 1732.

- (24) Guo, Y.; Yang, J.; Wu, X.; Du, A. *J. Fluoresc.* **2005**, *15* (2), 131.
- (25) Babaei, A.; Mirzakhani, S.; Khalilzadeh, B. *J. Braz. Chem. Soc.* **2009**, *20* (10), 1862.
- (26) Guo, Z. H.; Dong, S. J. *Electroanalysis* **2005**, *17* (7), 607.
- (27) Li, F. *Talanta* **2003**, *59* (3), 627.
- (28) Yu, Y.; Zhou, M.; Cui, H. *J. Mater. Chem.* **2011**, *21* (34), 12622.
- (29) Zanarini, S.; Rampazzo, E.; Bonacchi, S.; Juris, R.; Marcaccio, M.; Montalti, M.; Paolucci, F.; Prodi, L. *J. Am. Chem. Soc.* **2009**, *131* (40), 14208.
- (30) Valenti, G.; Rampazzo, E.; Bonacchi, S.; Khajvand, T.; Juris, R.; Montalti, M.; Marcaccio, M.; Paolucci, F.; Prodi, L. *Chem. Commun.* **2012**, *48*, 4187.
- (31) Ding, Z.; Quinn, B. M.; Haram, S. K.; Pell, L. E.; Korgel, B. A.; Bard, A. J. *Science* (80-. ). **2002**, *296* (5571), 1293.
- (32) Zhou, Y.; Zhuo, Y.; Liao, N.; Chai, Y.; Yuan, R. *Talanta* **2014**, *129*, 219.
- (33) Qi, H.; Qiu, X.; Xie, D.; Ling, C.; Gao, Q.; Zhang, C. *Anal. Chem.* **2013**, *85*, 3886.
- (34) Shen, W.; Tian, D.; Cui, H.; Yang, D.; Bian, Z. *Biosens. Bioelectron.* **2011**, *27* (1), 18.
- (35) Li, F.; Yu, Y.; Cui, H.; Yang, D.; Bian, Z. *Analyst* **2013**, *138* (6), 1844.
- (36) Conroy, P. J.; Okennedy, R. J.; Hearty, S. *Protein Eng. Des. Sel.* **2012**, *25* (6), 295.



# Chapter 1

## Introduction

*Electrogenerated ChemiLuminescence is the emission of light from the relaxation of excited states produced by reacting intermediates generated at the surface of an electrode.<sup>1-4</sup>*

### Abstract

This chapter introduces the general principles of electrogenerated chemiluminescence (also called electrochemiluminescence – in short, ECL). After a brief historical overview, the current state of the art in ECL will be detailed, with special attention to two main techniques, namely the **ion annihilation** and the **co-reactants** approaches, which constitute the backbone of the experimental work presented in later chapters. The most frequently used **luminophores** and **co-reactants** will also be described and the recent advances in the use of **nanomaterials** will be critically assayed. In the last part of this chapter, the principal applications of ECL are briefly described, focusing mostly on **diagnostics**.

## 1.1 HISTORICAL OVERVIEW

The first reports of luminescence arising from electrochemical reactions date back to the 1920s<sup>5,6</sup> and were developed into fully-fledged ECL studies starting in 1960s. Aromatic hydrocarbons were the first molecules to be studied in this regard under alternating potentials,<sup>7,8</sup> to develop early models on electron transfers in ECL. A milestone experimental observation followed in 1972, studying the emission of Tris(2,2'-bipyridyl)dichlororuthenium(II) by cycling the potential on a platinum electrode: the energy at which this complex emits after electrochemical stimulus is exactly the same as the maximum observed upon photoexcitation.<sup>9</sup> This means that it is possible to generate the same excited state by an electrical initiation. A breakthrough towards the practical application of ECL was the use of co-reactants, first proposed in 1977. This approach stemmed from the observation of characteristic emissions during the simultaneous oxidation of oxalate and a fluorophore, the latter being either an hydrocarbon (like rubrene or 9,10-diphenylanthracene) or a metal complex (such as bipyridyl chelates of bivalent ruthenium and osmium).<sup>10</sup> Ten years later, aliphatic amines, especially tri-n-propylamine, were established as the standard ECL co-reactants thanks to their efficiency and low cost.<sup>11,12</sup> ECL-based bioassays started to be marketed in the early 1990s and found widespread use thanks to their high sensitivity and good selectivity. To date, ECL systems are commercialised, e.g., by Roche Diagnostics Corp. and by MesoScale Diagnostic for a variety of assays, with a particular emphasis on immunoassay for the detection of many important biological molecules and macromolecules.<sup>2,3,13</sup>

## 1.2 LUMINESCENCE: HOW TO GENERATE AN EXCITED STATE?

Luminescence is the process occurring when a molecule releases a radiation through relaxation from an excited state to the ground state. The process involves the transition of an electron from an orbital to one with lower energy and the energy difference  $\Delta E$  is released as a photon with wavelength  $\lambda = h/\Delta E$ , where  $h$  is the Plank's constant. Various energy states available to a molecule can be presented by an energy level diagram, called Jablonsky diagram, as reported in Figure 1.1.

Upon a proper excitation stimulus, a molecule can be quickly ( $10^{-15}$  s) promoted from ground state (singlet  $S_0$ ) to an excited electronic state. Due to spin selection rules, the excited state has the same spin multiplicity as the initial state. The electron cloud can

quickly rearrange upon external perturbation, whereas the heavier nuclei can be considered stationary (Born–Oppenheimer approximation) and the electronic transition vertical (Frank-Condon principle). After the absorption of a photon, the population undergoes a fast (typically with  $10^{-14} - 10^{-11}$  s) vibrational relaxation to the lowest vibrational state followed by internal conversion (IC) to the lowest singlet state ( $S_1$ ). Due to the time scale, the most relevant photophysical and photochemical processes occur from lowest excited singlet state (Kasha's rule).

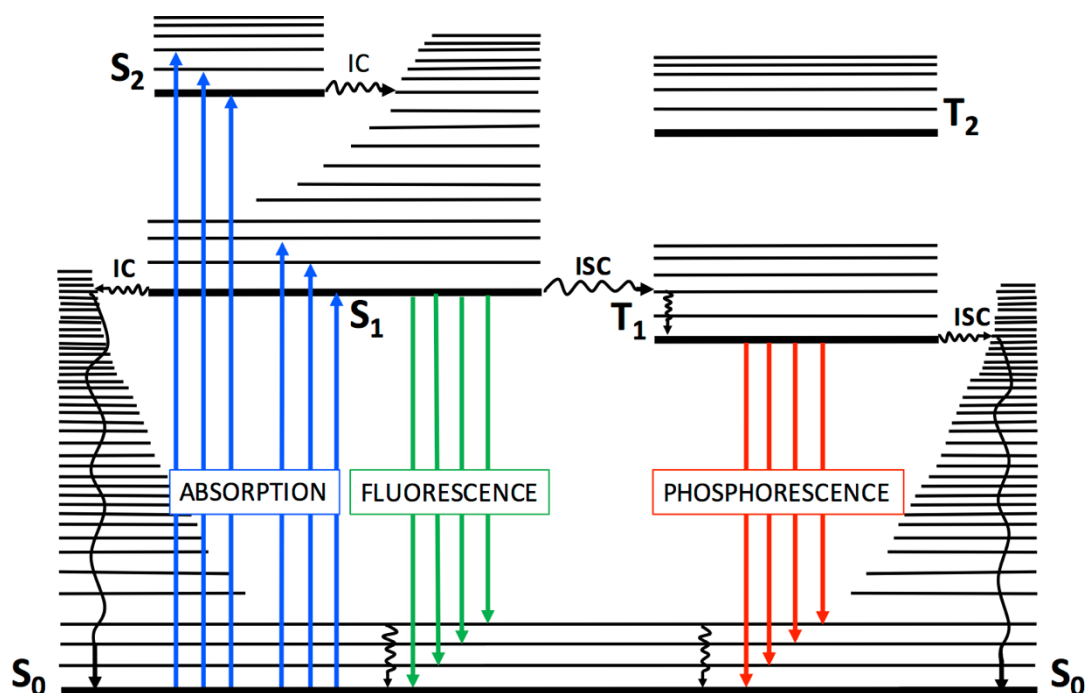


**Figure 1.1.** Perrin–Jablonski diagram. The vibrational manifold associated with electronic states is also depicted. Straight lines indicate radiative processes, whereas wavy lines denote non-radiative transitions.<sup>14</sup>

Depending on the molecular rigidity radiative and non-radiative deactivation can take place. The radiative one between lowest excited state and ground state is called fluorescence if it occurs with conservation of electronic spin ( $10^{-7} - 10^{-9}$  s). Generally, the emitted light possesses lower energy compared to the absorbed light (Stokes shift) due to the loss of heat and reorganisation energy. Intersystem crossing (ISC) between singlet and triplet state (T) can also occur. Due to its spin-forbidden nature it is insignificant and characterised by long lifetimes ( $10^{-6}$ - 1 s). Despite that, spin orbit coupling (SOC) can overcome the selection rule as the flip of the electronic spin is coupled to a change of orbital angular momentum (El-Sayed's rules). Heavy atoms favour ISC, for instance, by collision (external heavy atom effect). The effect is much more pronounced if they are part of the

molecule and involved in the electronic transitions, like for organo-metallic systems based on transition metals such as Cu, Ru, Os, Re, Ir, Pt and Au.

The **generation of an excited state** can be obtained in different ways, therefore according to them different types of luminescence can be classified. Examples can be found in photoluminescence, in which the stimulus is a light external source, and chemiluminescence, process in which the excited state is generated from an electron-transfer reaction between two reacting species. Also, it is worth mentioning the electroluminescence, originated upon applying an electric field and the triboluminescence, achievable by mechanical stress of the material.

In ECL, the excited state responsible for the emission of the photon, is generated from the reaction of intermediates generated electrochemically. Indeed, ECL shares features with both chemiluminescence and electroluminescence, since light emission is ultimately initiated and controlled by application of a potential at an electrode.

In a basic ECL experiment, a potential scan from anodic to cathodic part is performed to a solution of Tris(2,2'-bipyridyl)dichlororuthenium(II). A red luminescence develops at the working electrode at the oxidation and reduction potentials of the complex. The same red emission can be obtained when in solution is added an amine. Upon anodic scan, it is possible to collect light right in front of the electrode surface.

The two cases outlined represent the two main approaches used in the development of ECL applications, dubbed the ion annihilation and the co-reactant approaches, that will be described in detail in the next two paragraphs.

### 1.2.1 Ion annihilation

Historically, the ion annihilation approach to the generation of excited states was the first one explored due to the relative simplicity of the system involved. Its mechanism is outlined in Figure 1.2a and equations 1.1-1.4.

One single species, A, is both reduced and oxidised (to  $A^{\bullet+}$  and  $A^{\bullet-}$ , respectively) at an electrode, by alternate pulsing of the electrode potential, according to equations (1.1) and (1.2).<sup>2,3</sup> These species react in the Nernst diffusion layer over the electrode according to (1.3), to yield an excited state  $A^*$  along with a molecule in its ground state A, as shown in Figure 1.2b.

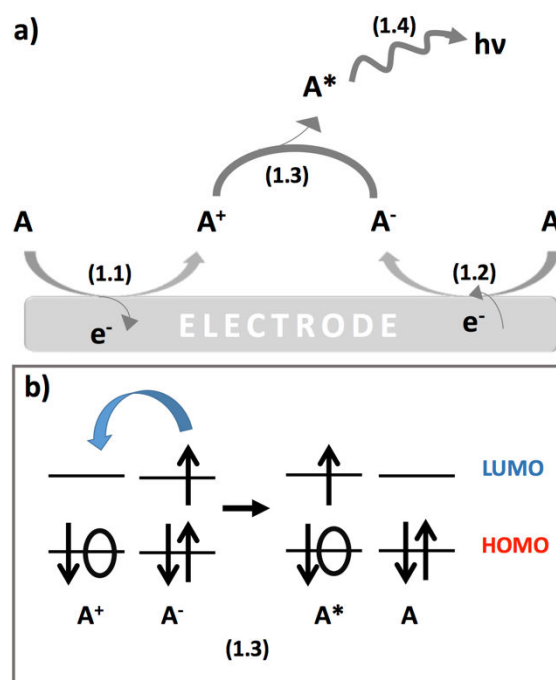
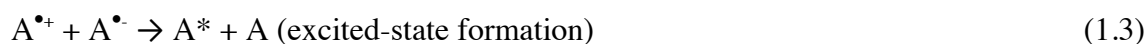


**Figure 1.2.** a) Schematic diagram describing the electron transfer reactions responsible for emission during annihilation ECL; b) Schematic energetic diagram describing the eq 1.3 responsible of the excited-state formation (ion annihilation step).



The annihilation step (eq 1.3) may also occur in “mixed systems”, where the radical cation and radical anion are from different molecules. The system possesses an energy directly connected to the redox potentials for the reactions 1.1 and 1.2. This energy is an enthalpy of annihilation and it can be calculated by eq 1.5:<sup>3</sup>

$$-\Delta H_{ann} = \Delta G + T\Delta S = E_p \left( \frac{A}{A^{\bullet+}} \right) - E_p \left( \frac{A}{A^{\bullet-}} \right) - 0.16 \quad (1.5)$$

Where  $-\Delta H_{ann}$  (in eV) is the enthalpy for ion annihilation,  $E_p$  is the peak potential for electrochemical oxidation or reduction. The value 0.16 is the entropy approximation term ( $T\Delta S$ ) estimated to be  $\sim 0.1$  eV with an addition of 0.059 eV resulting from the difference between two reversible peak potentials of the redox reaction. Depending on the energy available in the annihilation reaction, the produced  $A^*$  can be either in the lowest excited



singlet state  $^1A^*$  or in the triplet state  $^3A^*$ . When it generates  $^1A^*$ , the system is called *energy-sufficient system* and the reaction follows the (S)-route (eq 1.6):



If  $-\Delta H_{\text{ann}}$  is smaller than the energy of singlet excited state but larger than the energy of triplet excited state, a triplet excited state  $^3A^*$  is formed (eq 1.7).  $^3A^*$  can be transformed to  $^1A^*$  by triplet-triplet annihilation (TTA) (eq 1.8). This system is called *energy-deficient system* and the reaction is said to follow the (T)-route:



In order to have a successful ion annihilation ECL, both radical anion and cation need to be generated at the electrode surface, and within a potential range that is accessible in the employed solvent. Once the radical ions are formed, they must be sufficiently long-lived to diffuse, encounter each other, and undergo electron transfer. These electrochemical properties can be evaluated by cyclic voltammetry. Photoluminescence efficiencies and high photoluminescence lifetime is required which often can be evaluated from the fluorescent experiment. Finally, sufficient energy in the reaction of annihilation is required to form one of the excited states mentioned above. This energy is equal to:

$$E = h\nu = hc/\lambda \quad (1.9)$$

Where  $h$  is the Plank constant ( $6.626 \times 10^{-34}$  J·s),  $\nu$  is frequency (Hz),  $c$  is speed of light ( $2.99 \times 10^8$  m/s) and  $\lambda$  is wavelength of emission (m). As the energy for visible range emission (~400-700 nm) covers from 3.1 to 1.8 eV (eq 1.9) the potential window of an electrochemical system should be wide enough (from ~3.3 to 2 V). Thus, ion annihilation ECL is mainly performed in rigorously purified and deoxygenated non-aqueous media, because the available potential range in water is too narrow to generate the required energetic precursors. For this intent, acetonitrile, dimethyl-sulfoxide or methylene-chloride are the most employed, with tetra-n-butylammonium perchlorate or tetraethylammonium perchlorate as supporting electrolyte. Water and oxygen are harmful to these experiments because they can quench ECL. Thus, cells and electrodes have to be constructed to allow transfer of solvent and degassing on high-vacuum line or in inert atmosphere (glove-boxes).<sup>2</sup>

## 1.2.2 Co-reactant ECL

Of more interest for practical applications, the use of co-reactants was considered a real turning in the history of ECL. Compared with ion annihilation ECL which requires strict conditions, co-reactant ECL is more comfortable for work not only in aqueous media and in the air but also in physiological conditions (pH  $\sim$  7.4). That is why the most of the applications of ECL are based on co-reactant ECL. Co-reactant ECL involves the simultaneous oxidation or reduction of the luminophore species, the emitter, with a helping reagent, the co-reactant, in a single potential step or scan. After oxidation or reduction, co-reactants form radicals as intermediates then decompose producing a powerful reducing or oxidising species. These unstable species react with the oxidised or reduced luminophore to produce the excited state that emits light. Depending on the case, if the luminophore is first oxidised at the electrode surface and then reduced by strongly reducing intermediate, the corresponding ECL is called *oxidative-reduction* ECL. On the other way around, if a cathodic potential is applied and the reduced luminophore is oxidised by a strongly oxidizing intermediate, the corresponding ECL is called *reductive-oxidation* ECL. Considering one potential step generation, co-reactant ECL shows several advantages over annihilation ECL. First, there is no need for wide potential window so other solvents with a narrow potential window and aqueous solution can be also used. Further, there is no need of rigorously purified and deoxygenated solvents because oxygen and water quenching is less efficient. Thus, reaction can be carried out in air. Finally, the use of co-reactant makes ECL possible even for some fluorophores that have only a reversible electrochemical oxidation or reduction while annihilation ECL in general requires both of them.

### 1.2.2.1 A model ECL system: $\text{Ru}(\text{bpy})_3^{2+}/\text{TPrA}$ system

$\text{Ru}(\text{bpy})_3^{2+}$  or its derivats with tripropylamine (TPrA) as co-reactant exhibits the highest ECL efficiency and represent the most common luminophore/co-reactant couple which forms the basis of commercial immunoassays and DNA analyses,<sup>3,13</sup> and it can be considered as an ECL standard. In 1990 Leland<sup>12</sup> first reported the use of TPrA with  $\text{Ru}(\text{bpy})_3^{2+}$  to produce highly intense ECL. The experiment was carried out on a gold electrode in a buffer solution of TPrA and  $\text{Ru}(\text{bpy})_3^{2+}$ .

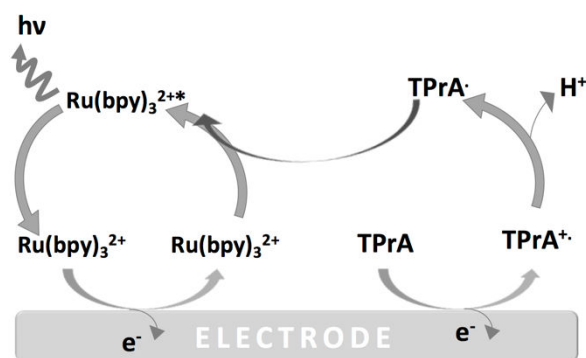


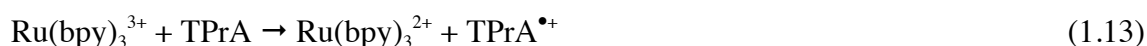
*Figure 1.3.* Schematic diagram describing the electron transfer reactions responsible for emission during a co-reactant ECL reaction involving  $\text{Ru}(\text{bpy})_3^{2+}$  and TPrA.

They proposed a mechanism represented by the following reactions (see Figure 1.3 for general mechanism):<sup>12,15,16</sup>

Acid-base equilibrium:



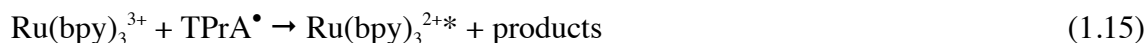
Oxidation step:



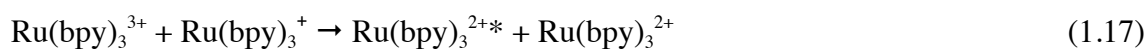
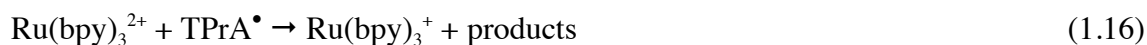
Deprotonation:



Excited state formation 1:



Excited state formation 2:



Light emission:



During the anodic scan, both  $\text{Ru}(\text{bpy})_3^{2+}$  and TPrA are oxidised (eqs 1.11-1.13). The oxidation of TPrA shows a broad wave due to preceding acid-base equilibrium (eq 1.10) ( $\text{pK}_a$  of  $\sim 10.4$ ).<sup>16</sup> TPrA can be oxidised both by directly oxidation on the electrode surface (eq 1.12) and via catalytic homogeneous oxidation by  $\text{Ru}(\text{bpy})_3^{3+}$  (eq 1.13). The relative contribution of the two routes depends on a variety of factors, such as the relative concentrations of  $\text{Ru}(\text{bpy})_3^{2+}$  and TPrA.<sup>15</sup> When the  $\text{Ru}(\text{bpy})_3^{2+}$  concentration is higher than the co-reactant, the oxidation of this last one mainly proceeds via the catalytic pathway. Instead, direct oxidation plays an important role in the ECL process, particularly in dilute  $\text{Ru}(\text{bpy})_3^{2+}$  solutions (less than approximately micromolar) and concentrated TPrA.<sup>15</sup>

The oxidation of TPrA gives a short-lived intermediate radical cation which undergo fast deprotonation forming strong reducing free radical (eq 1.14) which can reduce  $\text{Ru}(\text{bpy})_3^{3+}$  to form the excited state  $\text{Ru}(\text{bpy})_3^{2+*}$  (eq 1.15), that finally emits light (eq 1.18). When the concentration of TPrA is high and the concentration of  $\text{Ru}(\text{bpy})_3^{2+}$  is low, the ECL profile shows two peaks.<sup>15,17,18</sup> The second peak appears at the potential which correspond to the oxidation of  $\text{Ru}(\text{bpy})_3^{2+}$  but the first one appears earlier before its oxidation. With the mechanism that involves direct oxidation of  $\text{Ru}(\text{bpy})_3^{2+}$  this result cannot be explained. Miao and Bard reported the possibility to produce the ruthenium excited state without the direct oxidation of  $\text{Ru}(\text{bpy})_3^{2+}$ , in a mechanism that involves reactive radical cation of TPrA, according to the following reactions:<sup>17</sup>



This mechanism explains how the ECL emission shows a pre-peak at less positive potential than the oxidation of ruthenium centers. Moreover, the emission and the formation of the pre-peak show a strong dependence on the electrode material. The oxidation is more efficient onto glassy carbon electrode than on gold or platinum where it is blocked by formation of surface oxides.<sup>15</sup> The electrode hydrophobicity has also an effect on direct TPrA oxidation and ECL intensity. It was found that addition of some non-ionic surfactants such as Triton X-100 significantly increases ECL intensity on Pt and Au electrodes.<sup>19-21</sup>

To summarise, the excited state of  $\text{Ru}(\text{bpy})_3^{2+}$  may be produced via three different routes:

- 1)  $\text{Ru}(\text{bpy})_3^{3+}$  reduction by TPrA;
- 2)  $\text{Ru}(\text{bpy})_3^{3+}$  and  $\text{Ru}(\text{bpy})_3^+$  annihilation reaction;

3) Ru(bpy)<sub>3</sub><sup>+</sup> oxidation by TPrA<sup>•+</sup> radical cation.

The ECL intensity of the first and second waves are proportional to the concentration of both Ru(bpy)<sub>3</sub><sup>2+</sup> and TPrA in a very large dynamic range,<sup>12,15-17</sup> with detection limits of 0.5 pM for Ru(bpy)<sub>3</sub><sup>2+</sup>,<sup>22</sup> and 10 nM for TPrA.<sup>23</sup>

### 1.3 ECL LUMINOPHORES

Most recent studies mainly utilised inorganic systems such as metal complexes, organic systems and nanomaterials as ECL luminophores.

#### 1.3.1 Transition metal complexes

Transition metal complexes with high photoluminescence quantum yields (PLQYs) are usually expected to exhibit intense ECL. For example, Ru(bpy)<sub>3</sub><sup>2+</sup> with an ECL efficiency of  $\Phi_{\text{ECL}}=0.05$  produces an emitting charge-transfer triplet with an efficiency that approaches unity and is comparable with photoluminescence data of  $\Phi_{\text{PL}}\sim 0.05$ .<sup>24</sup>

##### 1.3.1.1 Ruthenium(II) complexes

The first report of ECL from a luminescent metal complex was made in 1972 by Tokel and Bard.<sup>9</sup> This study explored the annihilation ECL of Ru(bpy)<sub>3</sub><sup>2+</sup>. The number of electrochemiluminescent ruthenium complexes was expanded in subsequent reports.<sup>25</sup>

Ru(bpy)<sub>3</sub><sup>2+</sup> is the first inorganic complex ECL luminophore and is the most successful luminophore with very broad applications. The great chemical, electrochemical and ECL properties of ruthenium complexes lead to an extensive study of new ruthenium complex ECL systems to improve color tunability, light-emitting efficiency and applicability.

Ru<sup>2+</sup> is a d<sup>6</sup> system with electron configuration [Kr]4d<sup>6</sup>. In Ru(bpy)<sub>3</sub><sup>2+</sup>, the metal is surrounded by three bidentate polypyridine ligands that are usually colorless molecules possessing  $\sigma$ -donor orbitals localised on the nitrogen atoms and  $\pi$ -donor and  $\pi^*$ -acceptor orbitals more or less delocalised on aromatic rings.<sup>26</sup>

Most of the ruthenium complexes have a maximum wavelength between 600 and 650 nm. It is very hard to tune the color of ruthenium complexes due to the limited ligand-field splitting energies of central metal ions.

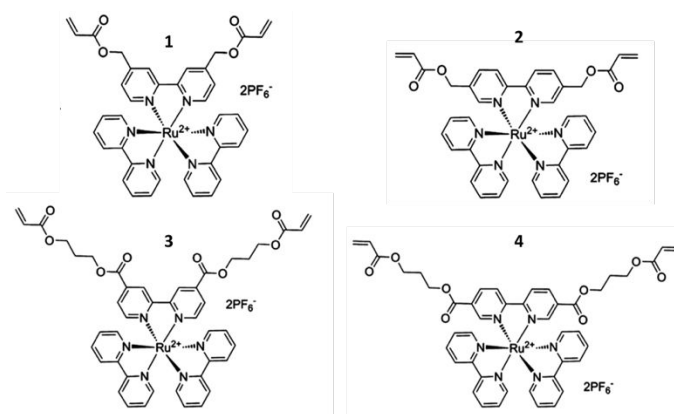


**Figure 1.4.** Acrylate-containing  $Ru(bpy)_3^{2+}$ -based coordination complexes reported in reference (27).

A new series of acrylate-containing  $Ru(bpy)_3^{2+}$  complexes (Figure 1.4) with photoluminescence emission maxima ranging from 640 to 700 nm have been reported.<sup>27</sup> The ECL emission of these compounds are in the range of 688 to 722 nm. It is the lowest-energy emission reported so far in light-emitting electrochemical cells (LECs) based on tris-chelated ruthenium complexes.

Other important goals are to find new luminophores with higher ECL efficiencies and to synthesise functional moieties of the emitter suitable for labeling biomolecules. To increase the sensitivity of the system which is especially important for ECL sensing application, multimetallic ruthenium complexes have been reported.<sup>28–30</sup> This strategy has the advantage of providing multiple redox centers, thereby increasing the number of charge recombination events (Figure 1.5). Fundamental requirements for this improvement are (i) accessibility of the ruthenium centers to the electrode surface and to active TPrA species and (ii) electronic equivalence of the chromophores to avoid intramolecular energy transfer from the excited chromophores to a lowest-lying unoccupied molecular orbital (LUMO) of an acceptor moiety. Different dendritic complexes have been synthesised  $[Ru2-Dend]^{4+}$ ,  $[Ru4-Dend]^{8+}$  and  $[Ru8-Dend]^{16+}$  (Figure 1.5), and bound to a modified progesterone molecule for ECL-based progesterone immunoassays.<sup>28</sup>

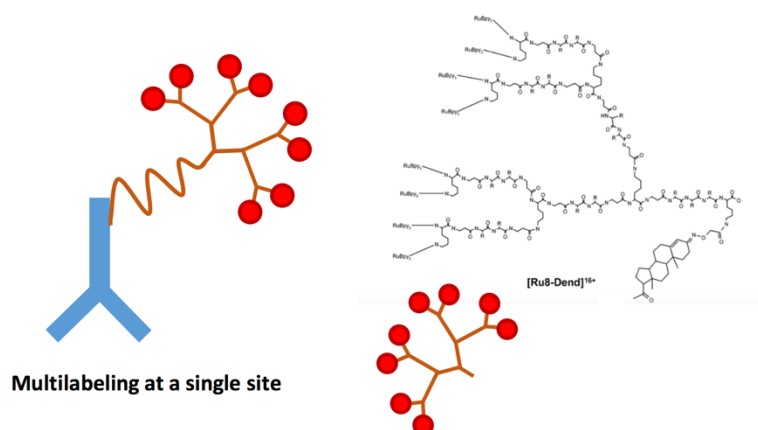


**Figure 1.5.** Example of multilabeling a biomolecule at a single site with a dendritic structure bearing multiple signal-generating units. Dendrimer  $[Ru_8\text{-Dend}](PF_6)_{16}$  reported in reference (28).

It was found that the ECL signal is proportional to the number of ruthenium units. Multimetallic system with several ruthenium centers, however, could undergo nonspecific bonding to antibodies, increasing the background ECL intensity and lowering the sensitivity of immunoassay.

Many attempts have been made in designing or modifying the ligands of Ruthenium complexes to improve molecular recognition ability.  $Ru(bpy)_2(dppz)^{2+}$  ( $dppz = \text{dipyrido}[3, 2\text{-}a:2', 3'\text{-}c]$  phenazine) has been found to intercalate into DNA with high affinity ( $K_a = \sim 10^6 \text{ M}^{-1}$ ) due to its extended aromatic structure.<sup>31</sup> It is a popular “light switch” molecule because it shows no photoluminescence in aqueous solutions, but displays intense photoluminescence in the presence of DNA. Its ECL properties have recently been investigated as well.<sup>32</sup>  $Ru(bpy)_2(dppz)^{2+}$  ECL increased  $\sim 1000$  times in the presence of DNA (Figure 1.6).  $Ru(bpy)_2(dppz)^{2+}$  shows no photoluminescence in aqueous solution, because its triplet metal-to-ligand charge transfer (MLCT) excited state is effectively quenched by hydrogen bonding between water and the phenazine nitrogen of the ligand. When it binds to DNA, the interaction between the ligand and the base pairs of duplex nucleic acid protects the phenazine nitrogen from water, leading to intense emission.

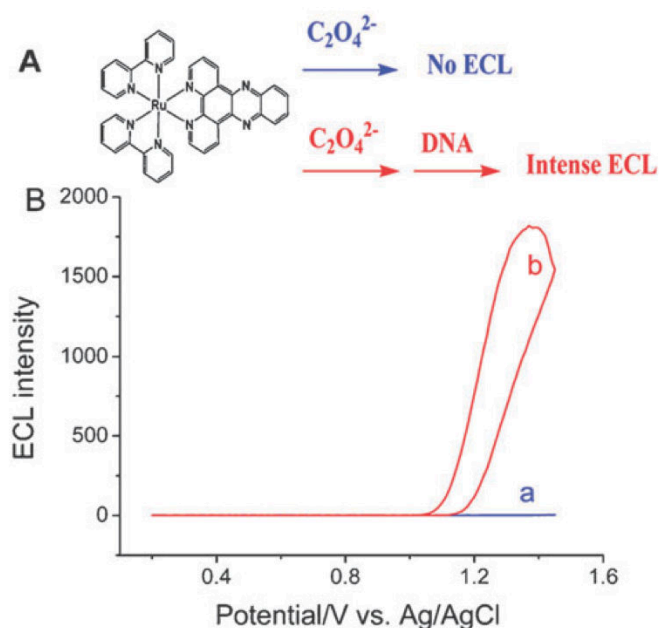


**Figure 1.6.** a) Scheme of ECL switch based on  $[Ru(bpy)_2dppz]^{2+}$  and DNA; b) ECL intensities in 5mM pH 5.5 oxalate solution containing 0.1 mM  $[Ru(bpy)_2dppz]^{2+}$  (curve a) and 0.1 mM  $[Ru(bpy)_2dppz]^{2+}$  + 0.16 mM DNA (curve b). Readapted from reference (32).

The remarkable increase in ECL intensity in the presence of DNA not only allows easier investigation of DNA interaction, but also provides a sensitive method for the determination of analytes that compete for intercalation into double-stranded DNA segments.

To conclude, it is noteworthy that since the initial work by Bard in 1972,<sup>9</sup> there have been over 3700 papers published concerning the ECL of ruthenium complexes, a considerable share of the field representing at least 70% of all ECL papers.

### 1.3.1.2 Iridium(III) complexes

Iridium complexes are a good and promising alternative to ruthenium with high quantum efficiencies for color tuning due to higher ligand-field splitting energies of the trivalent iridium ion. Over 90% of known luminescent iridium(III) complexes have been reported since 2000<sup>33</sup> and an important driver was their use as emitter in emergent light emitting devices. Among the first studies on  $Ir(ppy)_3$ ,<sup>34-37</sup> Kapturkiewicz realised that by careful selection of ligands to fine tune the energy levels of the complex, it was possible, in principle, to obtain an ECL system that was 100% efficient.<sup>37-39</sup> An important breakthrough was made by Kim *et al* who reported superior ECL intensities for the bis-cyclometallated



complexes  $\text{Ir}(\text{ppy})_2(\text{bpy})^+$  and  $\text{Ir}(\text{ppy})_2(\text{phen})^+$  as well as a series of phenylquinoline-based iridium complexes (Figure 1.7).<sup>40,41</sup>

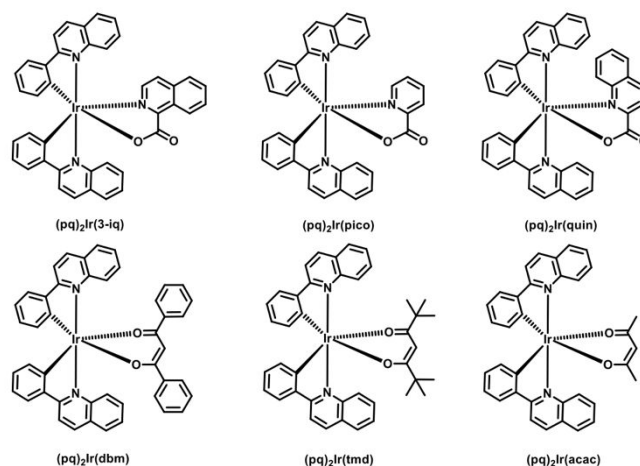


**Figure 1.7.** Structure of bis (2-phenylquinoline) iridium(III) (LX) complexes. LX in  $(\text{pq})_2\text{Ir}(\text{LX})$  corresponds to (3-*iq*), 3-isoquinaldate anion; (*pico*), picolinate anion; (*quin*), quinaldate anion; (*dbm*), dibenzoylmethane anion; (*tmd*), 2,2',6,6'-tetramethylhepta-3,5-dione anion; and (*acac*), acetylacetonate anion. Readapted from reference (41).

Those complexes exhibit high intense ECL efficiency in three measured ways: annihilation, TPrA co-reactant and  $\text{S}_2\text{O}_8^{2-}$  co-reactant methods. As a result,  $\text{Ir}(\text{pq})_2(\text{acac})$  displays ECL efficiency 77-fold higher than  $\text{Ru}(\text{bpy})_3^{2+}$  standard in TPrA method, but only 3-fold higher than standard in annihilation method. That is due to the unstable anion species of  $\text{Ir}(\text{pq})_2(\text{acac})$  which shows irreversible reduction process. The annihilation method requires combination of two oxidative and reductive species, and the unstable cation (or anion) can reduce the ECL efficiency. In contrast,  $\text{Ir}(\text{pq})_2(\text{pico})$  complex shows reversible redox process, resulting high efficient ECL in all three methods.

Schmittel's group published a study on the study of azacrown appended iridium complexes, as shown in figure 1.8, for the ECL detection of metal cations.<sup>42</sup> The iridium based sensors displayed large intensity changes on binding, outperforming the analogous ruthenium systems for the detection of certain metal cations, in particular  $\text{Ba}^{2+}$  and  $\text{Ag}^+$ . The iridium complex displayed a red shift in emission upon cation binding, as shown in figure 1.8. This was due to the metal cation binding event stabilising the ancillary ligand-based LUMO of the iridium complex, leaving the HOMO energy relatively untouched.

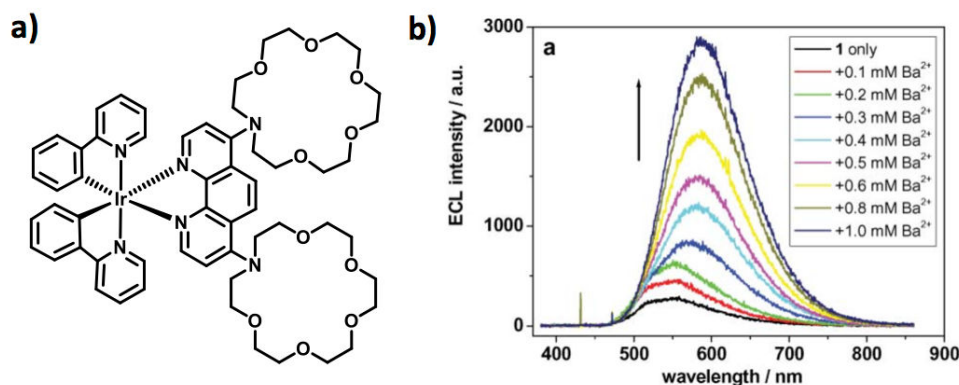


**Figure 1.8.** a) Azacrown appended iridium complex for ECL detection of metal cations and b) typical ECL response. Adapted from reference (42).

The most important prospective area of application for electrochemiluminescent iridium complexes is as biological labelling reagents, where the complex is used, following bioconjugations, to detect associations of proteins (e.g., immunoassays) or DNA (e.g., DNA hybridisation assays). Notwithstanding the success of ECL-based bioassays based on ruthenium polypyridyl systems, new emitters too are needed with higher ECL efficiencies, to deliver higher sensitivity, and a greater variety of emission colours, to enable multiplexed analysis. In literature, some few reports show interesting and promising approaches for assays and sensing applications.<sup>43,44</sup> For instance, Schmittel's group have reported a series of "lab-on-a-molecule" type sensors that exploit a multi-channel mode of operation.<sup>45-48</sup> The first example was a two-channel approach (see figure 1.9): the precursor dimer  $\text{Ir}(\text{pq})_2\text{Cl}_2$ , which is almost completely non-emissive, was cleaved upon the addition of cyanide anions to produce  $\text{Ir}(\text{pq})_2(\text{CN})_2^-$ . Though not electrochemiluminescent, due to oxidation of the cyano groups at relatively low potentials, intense PL emission is observed at 579 nm on optical excitation. In the ECL channel for this system, acetate anions produced a significant increase in the ECL emission in the presence of the dimer. The authors postulated that a Kolbe type reaction occurred to form a methyl radical from electrochemical oxidation of the acetate anion. This radical produced the new luminophores upon reaction with the oxidised dimer. Notably, since cyanide ions had no effect in the ECL, the two channels did not interfere with one another.<sup>45</sup>

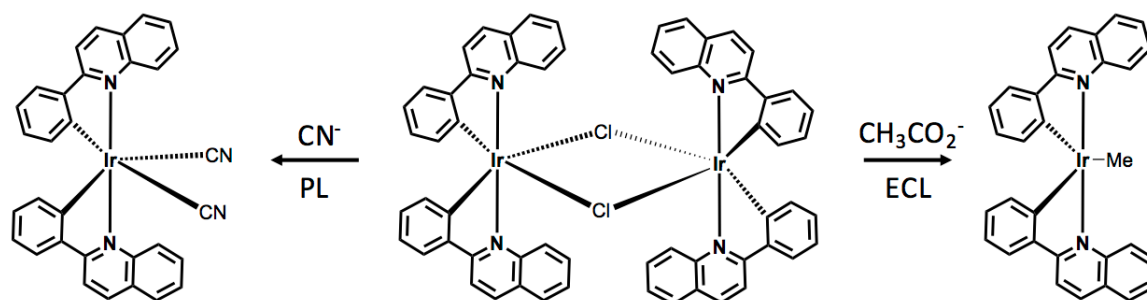


**Figure 1.9.** Iridium dimer  $[\text{Ir}(\text{pq})_2\text{Cl}_2]$  used in a dual channel “lab-on-a-molecule” sensor exploiting both PL and ECL modes of sensing. Reproduced from reference (45).

It should be noted that the vast majority of studies relating to the photophysical and/or electrochemical properties of iridium complexes have been carried out with the luminophore dissolved in organic media. However, most of the applications envisaged for these compounds in the area of sensing and biosensing demand a degree of aqueous solubility that has been difficult to obtain for iridium-based luminophores. The method for enhancing aqueous solubility generally rely upon modifying the ligand architecture by introducing polar groups. Unfortunately, both PLQY and the electrochemical reversibility are typical somewhat adversely affected by the change of the solvent.<sup>49</sup> For example, Zanarini *et al.*<sup>50</sup> reported intense ECL for  $\text{Ir}(\text{ppy})_2(\text{pytl-Me})^+$  and similar complexes in PBS with DBAE as co-reactant. Unfavourable electrochemical characteristics for the oxidation process in this medium resulted in rapid electrode passivation, necessitating continual electrochemical cleaning of the surface. The addition of polar substituents such as sulfonate groups<sup>49,51</sup> on the ancillary ligand has also been shown to improve water solubility and enable aqueous ECL of iridium complexes. However, many iridium complexes display high efficient ECL only in nonaqueous solutions. In order to use iridium complexes in biological assays, water solubility is necessary to consider. So far, only few examples in aqueous media or aqueous/organic media have been reported,<sup>43,50,52,53</sup> and the conditions described for the measurements are very different from those applied in commercial immunoassays analysis.<sup>46</sup> Recently, Fernandez-Hernandez *et al.* reported a family of red neutral bis-cyclometalated iridium complexes used as label under immunoassay conditions.<sup>54</sup> Among them, the complex based on phenylphenanthridine (pphent) as the C^N ligand, exhibits such great performance that it can be chosen as substitute of the commercially available Ru-based label in diagnostics (Figure 1.10).

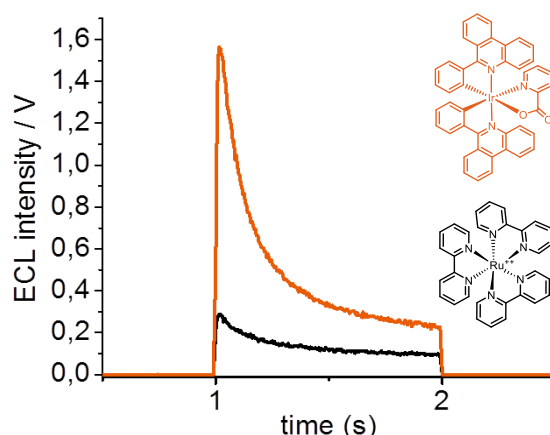


**Figure 1.10.** ECL response during time of  $[\text{Ir}(\text{pphnt})(\text{pic})]$  and  $\text{Ru}(\text{bpy})_3^{2+}$  under 1s potentiostatic impulse at + 1.4 V vs Ag/AgCl, reported in reference (54).

As already said, Iridium complexes have become attractive because of the easy color tunability. Recently, Paolucci *et al.* reported near IR ECL emitters based on cyclometalated iridium complexes.<sup>55</sup> ECL emissions were recorded in acetonitrile with maxima in the range of 700-720. The species showed a strong increase in ECL intensity upon employing benzoyl peroxide (BPO) as a co-reactant with respect to the annihilation. Such evidence, even though the efficiencies drop comparing to the standard  $\text{Ru}(\text{bpy})_3^{2+}$ , make them promising candidates for development of iridium-based labels in diagnostics where near-IR emission is advantageous.

Nowadays, a great challenge is the synthesis of blue-emitting complexes. Efficient blue-shifted ECL emission can be accomplished by stabilizing the highest occupied molecular orbital (HOMO) with electron-withdrawing substituents on the cyclometalated ligands, while only moderately stabilizing (or destabilizing) the LUMO via introducing electron-donating substituents on the neutral ancillary ligands, which will enlarge the HOMO-LUMO gap ensuring favorable thermodynamics and kinetics for ECL reaction.

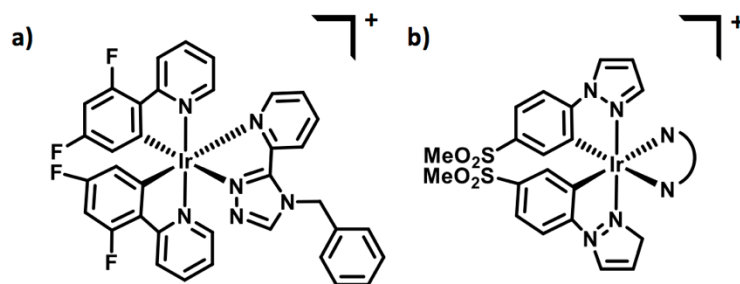


**Figure 1.11.** **a)**  $\text{Ir}(\text{df-ppy})_2(\text{ptb})^+$  complex. Reprinted from reference (52); **b)** class of complexes  $\text{Ir}(\text{msppz})_2(\text{N}^{\wedge}\text{N})^+$ . Readapted from reference (56).

Very recently, a number of blue-emitting iridium(III) complexes was explored.<sup>52</sup> Among these,  $\text{Ir}(\text{df-ppy})_2(\text{ptb})^+$  (Figure 1.11a) was the most potent complex showing a considerable hypsochromic shift (ca. 60 nm) and over 16-fold greater co-reactant ECL intensities than the similar  $\text{Ir}(\text{ppy})_3$  complex. To obtain green-emitting ECL complexes, a methylsulfone electron-withdrawing substituent was introduced into the cyclometalated phenylpyrazole ligand to stabilise the HOMO (Figure 1.11b).<sup>56</sup>

In addition, the emission colors of ECL systems can also be tuned by changing the co-reactant molecule,<sup>57</sup> pH of the solution,<sup>58</sup> frequency of the applied current<sup>59</sup> or energy transfer processes.<sup>60</sup> Recently, a new strategy for color tunable ECL was developed by adjusting potential to tune the color of the ECL emission from a binary mixture of a red light-emitting luminophore  $\text{Ru}(\text{bpy})_2(\text{L})^{2+}$  and a green light-emitting luminophore  $\text{Ir}(\text{df-ppy})_2(\text{BPS})^-$ .<sup>61</sup> This approach opens new avenues for multianalyte ECL detection and also for the characterisation of the photophysical properties and energy transfer mechanisms of luminescent metal complexes. Moreover, the ability to tune the emission ratio of multiple electrochemiluminophores with distinct spectral distributions creates new possibilities for colour selection in light-emitting devices.

### 1.3.1.3 Platinum(II) complexes

Platinum (II) complexes are not well known for their ECL properties. Few reports in literature show that this kind of complexes do not improve the performances of ruthenium polypyridil systems,<sup>62–65</sup> making them not appealing like the iridium (III) complexes.

The use of square-planar platinum (II) complexes for ECL was investigated using different pathways. Platinum (II) schiff base complexes were studied via ion annihilation mechanism

and using TPrA as co-reactant.<sup>63</sup> Even though the ECL intensities do not exceed that of  $\text{Ru}(\text{bpy})_3^{2+}$ , the ability to tune the colour of emission from yellow to near-infrared remains unsurpassed in ECL systems.

Chen and co-workers reported the first example of ECL generation using  $\text{S}_2\text{O}_8^{2-}$  as co-reactant of an alkynylplatinum (II) terpyridil complex.<sup>65</sup> The system can generate an intense orange emission at more positive potentials when compared to that of  $\text{Ru}(\text{bpy})_3^{2+}$ , making it more suitable for specific biological activities in water.

### 1.3.2 Nanomaterials

Since the ECL phenomenon of silicon nanocrystals was first reported in 2002,<sup>66</sup> a series of miscellaneous nanomaterials with various compositions, sizes and shapes, such as nanoparticles and nanotubes prepared from metals, semiconductor, carbon or polymeric species have also been used as ECL emitters in the recent years.<sup>60,67-78</sup>

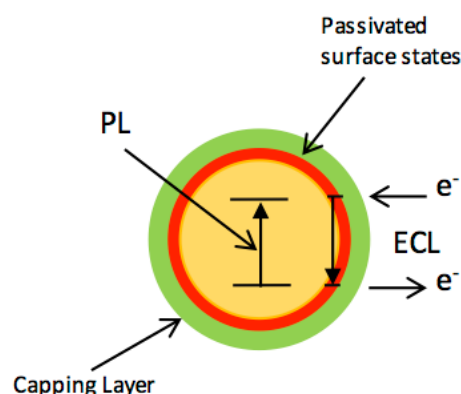


**Figure 1.12.** Schematic representation of PL and ECL in semiconductor NPs. Readapted from reference (79).

Among them, semiconductor quantum dots (QDs) are particularly attractive and various ECL investigations have been reported.<sup>79-81</sup> A common feature of ECL behaviour obtained from QDs is their red-shifted ECL maxima compare to their photoluminescence, suggesting that the emitting states are different.<sup>3</sup> This was explained by the fact that photoluminescence responses appears from electron transfer mainly from the interior of particles while ECL occurs at the surface where the surface chemistry has greater influence (Figure 1.12).<sup>82</sup> However, apart from some examples, low solubility and low stability of the oxidised and reduced species usually limit their applications. ECL of water soluble CdTe QDs has been recently reported.

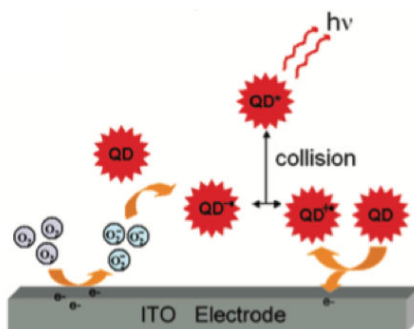


**Figure 1.13.** Anodic ECL mechanism of QDs. Reprinted from reference (83).

Stable and intense ECL was obtained from mercaptopropionic acid-capped CdTe QDs at about 1.2 V vs. Ag/AgCl in phosphate buffer (pH 9.3). The ECL emission involved the generation of superoxide ions at the ITO electrode surface, which then injected an electron into CdTe QDs to form a CdTe anion species. Then, the collisions between the CdTe anion species and the oxidation products led to the formation of species in an excited state that emitted light at around 580nm (figure 1.13).<sup>83</sup>

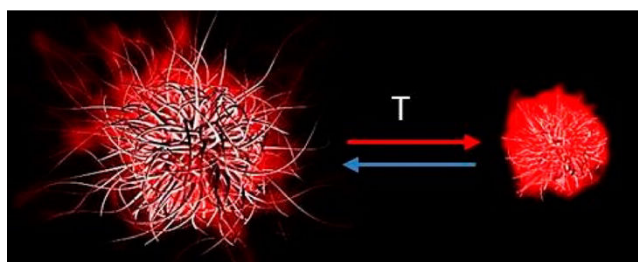


**Figure 1.13.** Schematic representation of the thermoresponsive ECL microgels in the swollen (left) and collapsed (right) states. Reprinted from reference (72).<sup>72</sup>

Despite that many nanomaterials-based luminophores have been developed, they generally have certain disadvantages, such as uneven size distribution, easy influence by the structure, and great changes of luminescent properties after interaction with other substances. The combination of traditional light-emitting reagents with nanoparticles is a very promising way to develop new efficient luminophores.<sup>84</sup>

Nanomaterials hold great promise as ECL labels carriers and great efforts have been made to produce a strong ECL signal, improving the sensitivity through the use of multiple ECL labels loaded on metal nanoparticles,<sup>85</sup> carbon nanotubes,<sup>86</sup> microsized polystyrene microspheres<sup>87</sup> and silica nanoparticles.<sup>18,55,60,69,88–94</sup> In particular this last group was largely used to encapsulate metal complexes not soluble in aqueous media. However, most studies

report on the use of nanomaterials with size between 100 and 7 nm for the development of hybrid systems with typically low diffusion coefficients.<sup>18</sup> Obtaining an observable ECL signal from such NPs is not a trivial task, in fact, the redox centres (chromophores) must be in very close contact with the electrode surface, they must be able to diffuse to it, or there must be another component that carries electrochemical energy from the electrode surface to the redox centres (co-reactants).

Stimuli-responsive hydrogel nanoparticles (or microgels) are a kind of particularly fascinating nanomaterials, because their properties can be modulated by an external stimulus. The combination of ECL-active metal complexes with stimuli-responsive microgels to design novel nanomaterials is attractive, because the ECL signal of the chromophores can be caused not only by the electrode potential but also by an external stimulus. Recently, the ECL of thermoresponsive redox microgels, synthesised by incorporation of the ruthenium complex derivative into the thermo-responsive monomer with a cross-linker agent, was investigated by Sojic's group (Figure 1.14).<sup>72</sup> Interestingly, ECL intensities change reversibly by reversibly changing temperatures, and an amplification of the ECL intensity up to 2 orders of magnitude in 100 nm thermoresponsive microgels is achieved. This behaviour is related to the microgel shrinking, which decreases the average distance between adjacent redox sites. The decrease of this distance favours both charge diffusion by electron-hopping in the microgels and also the ECL ion annihilation mechanism, giving as result the ECL enhancement.

#### 1.4 ECL CO-REACTANTS

A co-reactant is a species that, upon electrochemical oxidation or reduction, immediately undergoes chemical decomposition to form a strong reducing or oxidizing intermediate that can react with an oxidised or reduced ECL luminophore to generate excited states.<sup>1</sup> The development of the so-called co-reactant approach was a crucial point for the implementation of ECL as analytical technique since it permits to exploit the technique in environmentally-benign and user-friendly aqueous solutions. Common co-reactants for oxidative reduction ECL are oxalate and tertiary amines. Upon oxidation, the oxalate ion loses  $\text{CO}_2$ , producing  $\text{CO}_2^{\bullet-}$ ,<sup>10,95,96</sup> a strongly reducing agent, whereas tertiary amines deprotonate to yield strongly reducing radical species.<sup>12</sup> A typical example of co-reactants used for reductive oxidation ECL is peroxydisulfate, which, upon reduction, forms  $\text{SO}_4^{\bullet-}$ ,



a strong oxidant.<sup>97,98</sup> Due to its excellent ECL response,  $\text{Ru}(\text{bpy})_3^{2+}$ /TPrA system is the ECL pair that is the most used in different analytical and commercial applications.<sup>2,3</sup> TPrA has several disadvantages, being toxic, corrosive, volatile and scarcely soluble. Moreover it needs to be used in high concentrations (usually up to 100 mM) to obtain good sensitivity resulting, eventually, in interference with the target biochemical analytes.<sup>99</sup> However, only a few co-reactants are more effective than TPrA, such as 2-(dibutylamino)ethanol (DBAE)<sup>100</sup> and N-butyl-diethanolamine (BDAE).<sup>101</sup> Recently, N-(3-amino-propyl)diethanolamine (APDEA) has been explored as a potential co-reactant for enhancing  $\text{Ru}(\text{bpy})_3^{2+}$  ECL.<sup>102</sup> It is much more effective than tripropylamine at gold and platinum electrodes although it has one primary amine group besides a tertiary amine group. The ECL intensities of the  $\text{Ru}(\text{bpy})_3^{2+}$ /APDEA system are approximately 10 and 36 times stronger than that of  $\text{Ru}(\text{bpy})_3^{2+}$ /TPrA system and about 1.6 and 1.14 times stronger than that of  $\text{Ru}(\text{bpy})_3^{2+}$ /BDAE system at Au and Pt electrodes, respectively. It is 2.42 times stronger than that of  $\text{Ru}(\text{bpy})_3^{2+}$ /BDAE at glassy carbon electrodes.<sup>102</sup> A special importance in the group of amine co-reactants has  $\beta$ -nicotinamide adenine dinucleotide reduced salt (NADH).<sup>23</sup> Namely, it was found that NADH oxidises to  $\text{NADH}^+$  which deprotonates forming highly reducing species  $\text{NAD}^\bullet$ . On the other hand,  $\beta$ -nicotinamide adenine dinucleotide ( $\text{NAD}^+$ ) has aromatic structure and do not undergo electrochemiluminescent reaction. For this reason, ECL is used for detection of NADH, especially in enzymatic systems where NADH is produced from  $\text{NAD}^+$ .<sup>71,103</sup>

## 1.5 ECL ANALYTICAL APPLICATIONS

Analytical applications of ECL appeared in the literature sporadically throughout the 1970s and only really took hold in the 1980s. Over the next two decades, ECL developed rapidly and has emerged as a very powerful technique.<sup>1</sup> Analytical applications are based on the fact that ECL intensity is proportional to the concentration of the ECL luminophore or the concentration of co-reactant. If ECL experiments are carried out in the presence of high and constant concentrations of co-reactant, ECL intensity will linearly depend on the concentration of ECL emitter in a wide dynamic range. Alternatively, if the experiments are running in the presence of constant emitter concentration, ECL signal will show dependence on co-reactant concentration.

### 1.5.1. Application in CE, HPLC and FIA systems

ECL can be easily integrated in analytical systems such as capillary electrophoresis (CE), high performance liquid chromatography (HPLC) and flow injection analysis (FIA). The analytes or its derivatives should behave like an ECL co-reactant which often means to have secondary or tertiary amine groups with an  $\alpha$ -carbon hydrogen so that efficient ECL can be produced in the presence of  $\text{Ru}(\text{bpy})_3^{2+}$ . Because tertiary amines can produce sensitive ECL responses, a lot of efforts have been made to introduce such groups to initially less or non-ECL sensitive analytes such as amino acids and fatty acids.<sup>104,105</sup> Amino acids such as proline, valine and leucine can be successfully detected in CE-ECL system with detection limit in the  $\mu\text{M}$  -  $\text{nM}$  concentration range.<sup>105</sup> The group of E. Wang employed CE- ECL for different applications. For example, CE-ECL was applied for investigation of drug- protein binding.<sup>106</sup> Three basic drugs, pridinol, procyclidine and trihexyphenidyl, were successfully separated by capillary zone electrophoresis with end-column  $\text{Ru}(\text{bpy})_3^{2+}$  ECL detection. Thermodynamic and kinetic studies have been also realised using CE-ECL system. A number of advantages are offered by CE-ECL with respect to other commonly used separation-detection methods including UV-vis or fluorescent detection. ECL-based detection methods offer very powerful resolving ability, good selectivity, high sensitivity and easy sample preparation as there is no need of sample pre-treatment.<sup>107</sup> HPLC may be also coupled with ECL. When combined with chromatography,  $\text{Ru}(\text{bpy})_3^{2+}$  can be added to the system in different ways. Besides pre- and post- column methods,<sup>108,109</sup> the immobilisation of  $\text{Ru}(\text{bpy})_3^{2+}$  on a solid electrode surface can provide several advantages, such as reducing the consumption of expensive reagent, simplifying experimental design, and creating a regenerable detector based on  $\text{Ru}(\text{bpy})_3^{2+}$  recycled on the electrode surface during the ECL reaction. For example, a simple method based on reverse-phase HPLC with  $\text{Ru}(\text{bpy})_3^{2+}$  modified single Pt wire ECL detector for the determination of metoclopramide, itopride and sulpiride was developed.<sup>110</sup> The method allowed for the simultaneous detection of these antiemetic drugs in human serum and offered short analysis times. Under optimal conditions, the resulting analytical performances were good. This system is a two-electrode system, there is no post-column reagent addition, so it is very simple with good stability, lower baseline and background noise levels.

### 1.5.2. ECL Assays for diagnostics

One of the most important applications of ECL is its use in diagnostic assays.<sup>4,111,112</sup> ECL assays are usually either solution phase or solid phase. Solid phase is used for biomolecules which have very poor or no co-reactant ability, which are linked with the ECL labels and they are immobilised onto a solid substrate (like screen printed electrode, microsized polystyrene beads or magnetic beads etc.). The ECL signal is proportional to the concentration of the analyte in the presence of added ECL co-reactant. Conventional antigen-antibody reactions have also been combined with ECL generation with the help of streptavidin coated magnetic particles.<sup>113</sup> The sample is combined with a reagent containing the biotinylated capture antibody and a ruthenium labelled secondary antibody. During incubation, the antibodies capture the target molecules, the microparticles are then added and during a second incubation period the biotinylated antibody attaches to the streptavidin coated particles. The samples are then drawn into the ECL measuring cell along with a buffer containing TPrA. A magnet located under the electrode captures the microparticles at the electrode surface and all unbound reagent is washed from the cell. The magnet is then removed and a potential is applied to the electrode, initiating ECL. The technology has since been purchased by Roche Diagnostics which markets the electrogenerated chemiluminescence immunoassay.

## 1.6 AIM OF THE THESIS

This doctoral dissertation aims to develop new hybrid materials for ECL applications. Particular attention is paid to the ECL properties of metal complexes, based on Platinum(II) and Iridium(III), and a new class of co-reactant based on Amino-Rich Carbon Nanodots, to end up in the development of new hybrid materials coming from the combination of nanoparticles and metal complexes. This will open up an avenue for the development of new analytical techniques.

Chapter 2 is dedicated to an unexplored and emerging class of metal complexes for ECL, square-planar platinum(II) complexes. Despite the large study on the rich photophysical properties, really few reports on ECL properties exist. Herein, electrochemistry and ECL of different Pt(II) complexes are examined both in solution and upon immobilisation onto the electrode surface. In particular, it will be enlightened the ability of such complexes to

give ECL emission upon aggregation, giving rise to a phenomenon called *Aggregation-Induced ECL (AIECL)*.

In Chapter 3, the synthesis of a cyclometalated iridium(III) complex bearing an ancillary ligand able to electropolymerise is presented with its photophysical and electrochemical properties. A simple way based on electropolymerisation to fabricate ECL solid state emitters is presented in its proof of concept. In particular, the ability of electropolymerizing onto an electrode surface gives as result the formation of an emitting polymeric solid layer that shows stability during different voltammetric cycles and high ECL emission.

Chapter 4 focuses on the co-reactant properties of Amino-Rich Nitrogen-doped Carbon NanoDots (NCNDs). It was investigated for the first time the possibility to use carbon nanodots with primary and tertiary amino functional groups, which are already known to be the best and the most used group as co-reactant for promoting  $\text{Ru}(\text{bpy})_3^{2+}$  ECL generation. The system was evaluated for bioanalytical applications, reporting a simple methodology to detect Epinephrine (EP), the important neurotransmitter studied for diagnosis of neurological disorders, such as the Parkinson's disease.

Chapter 5 describes the ECL of hybrid materials composed by metal complexes and nanoparticles. Nanoparticles contain large surface area that can be modified by different functional groups in order to graft molecules like metal complexes. NCNDs were coupled with ruthenium(II) and iridium(III) metal complexes. ECL measurements were performed in immunoassay media in order to test them for possible applications in the field. The novel systems were evaluated for self-enhanced ECL, which is a promising ECL reaction pattern with enhanced luminous efficiency. Additionally, we investigated the immobilisation of these hybrids on the electrode surface for signal intensity enhancement due to the presence of a plurality of signal-generating units on each NCNDs.

In Chapter 6 a sensing approach based on Electrochemical Impedance Spectroscopy (EIS) and ECL for the detection of Troponin I (cTnI) is presented. The work aims to the use of a high-ECL emissive iridium(III) complex to realise an ECL biosensing device for cTnI detection with enhanced properties. The innovation in this project consists in using a technique that, compared to the ones used for cardiac biomarkers detection, is higher sensitive by using a brighter iridium(III) metal complex, that can substitute the typical

Ru(bpy)<sub>3</sub><sup>2+</sup>, permitting a detection of lower quantities of antigen in blood samples with a not expensive, fast and not harmful to the environment method.

## 1.7 REFERENCES

- (1) Bard, A. J. *Electrogenerated Chemiluminescence*; Marcel Dekker, Inc.: New York., **2004**.
- (2) Richter, M. M. *Chem. Rev.* **2004**, *104* (6), 3003.
- (3) Miao, W. *Chem. Rev.* **2008**, *108* (7), 2506.
- (4) Liu, Z.; Qi, W.; Xu, G. *Chem. Soc. Rev.* **2015**, *44* (10), 3117.
- (5) Harvey, N. J. *Phys. Chem.* **1929**, *33*, 1456.
- (6) Dufford, R. T.; Nightingale, D.; Gaddum, L. W. *J. Am. Chem. Soc.* **1927**, *49*, 1858.
- (7) Visco, R. E.; Chandross, E. A. *J. Am. Chem. Soc.* **1965**, *87*, 139.
- (8) Santhanam, K. S. V.; Bard, A. J. *J. Am. Chem. Soc.* **1965**, *87*, 139.
- (9) Tokel, N. E.; Bard, A. J. *J. Am. Chem. Soc.* **1972**, *94* (8), 2862.
- (10) Chang, M. M.; Saji, T.; Bard, A. J. *J. Am. Chem. Soc.* **1977**, *99*, 5399.
- (11) Noffsinger, J. B.; Danielson, N. D. *Anal. Chem.* **1987**, *59* (6), 865.
- (12) Leland, J. K.; Powell, M. J. *J. Electrochem. Soc.* **1990**, *137*, 3127.
- (13) Forster, R. J.; Bertoncillo, P.; Keyes, T. E. *Annu. Rev. Anal. Chem. (Palo Alto. Calif.)*. **2009**, *2*, 359.
- (14) Lakowicz, J. R. *Principles of Fluorescence Spectroscopy*; **2006**.
- (15) Zu, Y.; Bard, A. J. *Anal. Chem.* **2000**, *72* (14), 3223.
- (16) Kanoufi, F.; Zu, Y.; Bard, A. J. *J. Phys. Chem. B* **2001**, *105*, 210.
- (17) Miao, W.; Choi, J.-P.; Bard, A. J. *J. Am. Chem. Soc.* **2002**, *124* (48), 14478.
- (18) Zanarini, S.; Rampazzo, E.; Ciana, L. Della; Marcaccio, M.; Marzocchi, E.; Montalti, M.; Paolucci, F.; Prodi, L. *J. Am. Chem. Soc.* **2009**, *131* (6), 2260.
- (19) Zu, Y.; Bard, A. J. *Society* **2001**, *73* (16), 3960.
- (20) Bruce, D.; McCall, J.; Richter, M. M. *Analyst* **2002**, *127* (1), 125.
- (21) Factor, B.; Muegge, B.; Workman, S.; Bolton, E.; Bos, J.; Richter, M. M. *Anal. Chem.* **2001**, *73* (19), 4621.
- (22) Arora, A.; de Mello, A. J.; Manz, A. *Anal. Commun.* **1997**, *34* (12), 393.
- (23) Downey, T. M.; Nieman, T. A. *Anal. Chem.* **1992**, *64* (3), 261.

- (24) Luttmer, J. D.; Bard, a J. *J. Phys. Chem.* **1981**, 85 (9), 1155.
- (25) Tokel-Takvoryan, N. E.; Hemingway, R. E.; Bard, A. J. *J. Am. Chem. Soc.* **1973**, 95 (20), 6582.
- (26) Juris, A.; Balzani, V.; Barigelletti, F.; Campagna, S.; Belser, P.; von Zelewsky, A. *Coord. Chem. Rev.* **1988**, 84 (C), 85.
- (27) Puodziukynaite, E.; Oberst, J. L.; Dyer, A. L.; Reynolds, J. R. *J. Am. Chem. Soc.* **2012**, 134 (2), 968.
- (28) Staffilani, M.; Höss, E.; Giesen, U.; Schneider, E.; Hartl, F.; Josel, H. P.; De Cola, L. *Inorg. Chem.* **2003**, 42 (24), 7789.
- (29) Zhou, M.; Roovers, J.; Robertson, G. P.; Grover, C. P. *Anal. Chem.* **2003**, 75 (23), 6708.
- (30) Zhou, M.; Roovers, J. *Macromolecules* **2001**, 34 (2), 244.
- (31) Friedman, A. E.; Chambron, J.-C.; Sauvage, J.-P.; Turro, N. J.; Barton, J. K. *J. Am. Chem. Soc.* **1990**, 112 (1 1), 4960.
- (32) Hu, L.; Bian, Z.; Li, H.; Han, S.; Yuan, Y.; Gao, L.; Xu, G. *Anal. Chem.* **2009**, 81 (23), 9807.
- (33) Flamigni, L.; Barbieri, A.; Sabatini, C.; Ventura, B.; Barigelletti, F. In *Photochemistry and Photophysics of Coordination Compounds II*, Balzani, V.; Campagna, S.; **2007**; pp 143–203.
- (34) Vogler, A.; Kunkely, H. In *High-Energy Processes in Organometallic Chemistry*; **1987**; Vol. 333, pp 155–168.
- (35) Gross, E. M.; Armstrong, N. R.; Wightman, R. M. **2002**, 137.
- (36) Bruce, D.; Richter, M. M. *Anal. Chem.* **2002**, 74 (6), 1340.
- (37) Kapturkiewicz, A.; Angulo, G. *Dalt. Trans.* **2003**, 20, 3907.
- (38) Kapturkiewicz, A.; Chen, T.; Laskar, I. R.; Nowacki, J. *Electrochem. commun.* **2004**, 6 (8), 827.
- (39) Kapturkiewicz, A.; Nowacki, J.; Borowicz, P. *Electrochim. Acta* **2005**, 50, 3395.
- (40) Kim, J. Il; Shin, I.; Kim, H.; Lee, J. *J. Am. Chem. Soc.* **2005**, 127 (Iii), 1614.
- (41) Shin, I.; Kim, J. Il; Kwon, T.; Hong, J.; Lee, J.; Kim, H. *J. Phys. Chem. C* **2007**, 111, 2280.
- (42) Lin, H.; Cinar, M. E.; Schmittel, M. *Dalt. Trans.* **2010**, 39, 5130.
- (43) Li, C.; Lin, J.; Guo, Y.; Zhang, S. *Chem. Commun.* **2011**, 47, 4442.

- (44) Zhou, H.; Yang, Y.; Li, C.; Yu, B.; Zhang, S. *Chem. A Eur. J.* **2014**, *20* (45), 14736.
- (45) Schmittel, M.; Qinghai, S. *Chem. Commun.* **2012**, *48* (21), 2707.
- (46) Shu, Q.; Birlenbach, L.; Schmittel, M. *Inorg. Chem.* **2012**, *51*, 13123.
- (47) Chen, K.; Schmittel, M. *Analyst* **2013**, *138* (22), 6742.
- (48) Chen, K.; Schmittel, M. *Chem. Commun.* **2014**, *50* (43), 5756.
- (49) Kiran, R. V.; Hogan, C. F.; James, B. D.; Wilson, D. J. D. *Eur. J. Inorg. Chem.* **2011**, No. 31, 4816.
- (50) Zanarini, S.; Felici, M.; Valenti, G.; Marcaccio, M.; Prodi, L.; Bonacchi, S.; Contreras-carballada, P.; Williams, R. M.; Feiters, M. C.; Nolte, R. J. M.; Cola, L. De; Paolucci, F. *Chem. A Eur. J.* **2011**, *17*, 4640.
- (51) Kiran, R. V.; Zammit, E. M.; Hogan, C. F.; James, B. D.; Barnett, N. W.; Francis, P. S. *Analyst* **2009**, *134* (7), 1297.
- (52) Barbante, G. J.; Doeven, E. H.; Kerr, E.; Connell, T. U.; Donnelly, P. S.; White, J. M.; Lópes, T.; Laird, S.; Wilson, D. J. D.; Barnard, P. J.; Hogan, C. F.; Francis, P. S. *Chem. A Eur. J.* **2014**, *20*, 3322.
- (53) Tong, B.; Ma, P.; Mei, Q.; Hua, Z. *Inorganica Chim. Acta* **2014**, *421*, 405.
- (54) Fernandez-Hernandez, J. M.; Longhi, E.; Cysewski, R.; Polo, F.; Josel, H.-P.; De Cola, L. *Anal. Chem.* **2016**, *88* (8), 4174.
- (55) Kesarkar, S.; Rampazzo, E.; Valenti, G.; Marcaccio, M.; Bossi, A.; Prodi, L.; Paolucci, F. *ChemElectroChem* **2017**.
- (56) Tordera, D.; Bünzli, A. M.; Pertegus, A.; Junquera-hernández, J. M.; Constable, E. C.; Zampese, J. A.; Housecroft, C. E.; Ortí, E.; Bolink, H. J. *Chem. A Eur. J.* **2013**, *19*, 8597.
- (57) Valenti, G.; Bruno, C.; Rapino, S.; Fiorani, A.; Jackson, E. A.; Scott, L. T.; Paolucci, F.; Marcaccio, M.; Ciamician, C. G.; Uni, V. **2010**, 19467.
- (58) Lin, L.; Wen, Y.; Liang, Y.; Xiao, D. *Anal. Methods* **2013**, *5*, 457.
- (59) Nobeshima, T.; Nakakomi, M.; Nakamura, K.; Kobayashi, N. *Adv. Opt. Mater.* **2013**, *1*, 144.
- (60) Valenti, G.; Rampazzo, E.; Bonacchi, S.; Khajvand, T.; Juris, R.; Montalti, M.; Marcaccio, M.; Paolucci, F.; Prodi, L. *Chem. Commun.* **2012**, *48*, 4187.
- (61) Doeven, E. H.; Zammit, E. M.; Barbante, G. J.; Hogan, C. F.; Barnett, N. W.; Francis, P. S. *Angew. Chem. - Int. Ed.* **2012**, *51*, 1.

- (62) Li, C.; Wang, S.; Huang, Y.; Zheng, B.; Tian, Z.; Wen, Y.; Li, F. *Dalt. Trans.* **2013**, 42 (11), 4059.
- (63) Reid, E. F.; Cook, V. C.; Wilson, D. J. D.; Hogan, C. F. *Chem. A Eur. J.* **2013**, 19, 15907.
- (64) Canty, P.; Väre, L.; Håkansson, M.; Spehar, A. M.; Papkovsky, D.; Ala-Kleme, T.; Kankare, J.; Kulmala, S. *Anal. Chim. Acta* **2002**, 453 (2), 269.
- (65) Chen, Z.; Wong, K. M.; Kwok, E. C.; Zhu, N.; Zu, Y.; Yam, V. W. *Inorg. Chem.* **2011**, 50, 2125.
- (66) Ding, Z.; Quinn, B. M.; Haram, S. K.; Pell, L. E.; Korgel, B. A.; Bard, A. J. *Science*, **2002**, 296 (5571), 1293.
- (67) Zhao, M.; Chen, A.-Y.; Huang, D.; Zhuo, Y.; Chai, Y.-Q.; Yuan, R. *Anal. Chem.* **2016**, 88, 11527.
- (68) Ma, H.; Li, X.; Yan, T.; Li, Y.; Liu, H.; Zhang, Y.; Wu, D.; Du, B. *Sci. Rep.* **2016**, 6 (February), 1.
- (69) Valenti, G.; Rampazzo, E.; Bonacchi, S.; Petrizza, L.; Marcaccio, M.; Montalti, M.; Prodi, L.; Paolucci, F. *J. Am. Chem. Soc.* **2016**, 138 (49), 15935.
- (70) Rusling, J. F.; Bishop, G. W.; Doan, N.; Papadimitrakopoulos, F. *J. Mater. Chem. B. Mater. Biol. Med.* **2014**, 2 (1), 12.
- (71) Milutinovic, M.; Sallard, S.; Manojlovic, D.; Mano, N.; Sojic, N. *Bioelectrochemistry* **2011**, 82 (1), 63.
- (72) Pinaud, F.; Russo, L.; Pinet, S.; Gosse, I.; Sojic, N. *J. Am. Chem. Soc.* **2013**, 135, 5517.
- (73) Chang, Y.-L.; Palacios, R. E.; Fan, F.-R. F.; Bard, A. J.; Barbara, P. F. *J. Am. Chem. Soc.* **2008**, 130 (28), 8906.
- (74) Wu, L.; Wang, J.; Ren, J.; Li, W.; Qu, X. *Chem. Commun. (Camb)*. **2013**, 49 (50), 5675.
- (75) Zhou, C.; Chen, Y.; Shang, P.; Chi, Y. *Analyst* **2016**, 141, 3379.
- (76) Fang, Y.; Song, J.; Li, J.; Wang, Y.; Yang, H.; Sun, J.; Chen, G. *Chem. Commun.* **2011**, 47, 2369.
- (77) Dong, Y.; Chen, C.; Lin, J.; Zhou, N.; Chi, Y.; Chen, G. *Carbon N. Y.* **2013**, 56, 12.
- (78) Chen, Z.; He, X.; Wang, Y.; Wang, K.; Du, Y.; Yan, G. *Biosens. Bioelectron.* **2013**, 41, 519.



- (79) Bertonecello, P.; Stewart, A. J.; Dennany, L. *Anal. Bioanal. Chem.* **2014**, *406*, 5573.
- (80) Amelia, M.; Lincheneau, C.; Credi, A. *Chem. Soc. Rev.* **2012**, *41*, 5728.
- (81) Wu, P.; Hou, X.; Xu, J.; Chen, H. *Chem. Rev.* **2014**, *114*, 11027.
- (82) Myung, N.; Bae, Y.; Bard, A. J. *Nano Lett.* **2003**, *3* (8), 1053.
- (83) Liu, X.; Jiang, H.; Lei, J.; Ju, H. *Anal. Chem.* **2007**, *79* (21), 8055.
- (84) Rampazzo, E.; Bonacchi, S.; Genovese, D.; Juris, R.; Marcaccio, M.; Montalti, M.; Paolucci, F.; Sgarzi, M.; Valenti, G.; Zaccheroni, N.; Prodi, L. *Coord. Chem. Rev.* **2012**, *256* (15–16), 1664.
- (85) Yu, Y.; Zhou, M.; Cui, H. *J. Mater. Chem.* **2011**, *21* (34), 12622.
- (86) Tao, Y.; Lin, Z. J.; Chen, X. M.; Chen, X.; Wang, X. R. *Anal. Chim. Acta* **2007**, *594* (2), 169.
- (87) Miao, W.; Bard, a. J. *Anal. Chem.* **2004**, *76* (18), 5379.
- (88) Zhang, L.; Dong, S. *Electrochem. commun.* **2006**, *8* (10), 1687.
- (89) Zhang, L.; Dong, S. *Anal. Chem.* **2006**, *78* (14), 5119.
- (90) Qian, B. L.; Yang, X. *Adv. Funct. Mater.* **2007**, *17*, 1353.
- (91) Wei, H.; Zhou, L.; Li, J.; Liu, J.; Wang, E. *J. Colloid Interface Sci.* **2008**, *321* (2), 310.
- (92) Zanarini, S.; Rampazzo, E.; Bonacchi, S.; Juris, R.; Marcaccio, M.; Montalti, M.; Paolucci, F.; Prodi, L. *J. Am. Chem. Soc.* **2009**, *131* (40), 14208.
- (93) Yang, X.; Yuan, R.; Chai, Y.; Zhuo, Y.; Mao, L.; Yuan, S. *Biosens. Bioelectron.* **2010**, *25* (7), 1851.
- (94) Wang, Q.; Chen, M.; Zhang, H.; Wen, W.; Zhang, X.; Wang, S. *Sensors Actuators B. Chem.* **2016**, *222*, 264.
- (95) Rubinstein, I.; Bard, A. J. *J. Am. Chem. Soc.* **1981**, *103* (3), 512.
- (96) Ege, D.; Becker, W. G.; Bard, A. J. *Anal. Chem.* **1984**, *56* (13), 2413.
- (97) White, H. S.; Bard, A. J. *J. Am. Chem. Soc.* **1982**, *104* (25), 6891.
- (98) Bolletta, F.; Ciano, M.; Balzani, V. *Inorganica Chim. Acta* **1982**, *62*, 207.
- (99) Xu, J.; Huang, P.; Qin, Y.; Jiang, D.; Chen, H. *Anal. Chem.* **2016**, *88*, 4609.
- (100) Liu, X.; Shi, L.; Niu, W.; Li, H.; Xu, G. *Angew. Chem. - Int. Ed.* **2007**, *46* (3), 421.
- (101) Han, S.; Niu, W.; Li, H.; Hu, L.; Yuan, Y.; Xu, G. *Talanta* **2010**, *81* (1–2), 44.
- (102) Kitte, S. A.; Wang, C.; Li, S.; Zholudov, Y.; Qi, L. *Anal. Bioanal. Chem.* **2016**, No.

- 19, 7059.
- (103) Sentic, M.; Arbault, S.; Goudeau, B.; Manojovic, D.; Kuhn, A.; Bouffier, L.; Sojic, N. *Chem. Commun.* **2014**, 50, 10202.
- (104) Morita, H.; Konishi, M. *Anal. Chem.* **2003**, 75 (4), 940.
- (105) Li, J.; Yan, Q.; Gao, Y.; Ju, H. *Anal. Chem.* **2006**, 78 (8), 2694.
- (106) Zhao, X.; You, T.; Liu, J.; Sun, X.; Yan, J.; Yang, X.; Wang, E. *Electrophoresis* **2004**, 25, 3422.
- (107) Yuan, J.; Li, T.; Yin, X.; Guo, L.; Jiang, X.; Jin, W.; Yang, X.; Wang, E. *Anal. Chem.* **2006**, 78 (9), 2934.
- (108) Pérez-Ruiz, T.; Martínez-Lozano, C.; García, M. D. *J. Chromatogr. A* **2007**, 1169, 151.
- (109) Forbes, G. A.; Nieman, T. A.; Sweedler, J. V. *Anal. Chim. Acta* **1997**, 347, 289.
- (110) Li, Y.; Zhang, Z. *Anal. Methods* **2012**, 4, 4014.
- (111) Hu, L.; Xu, G. *Chem. Soc. Rev.* **2010**, 39 (8), 3275.
- (112) Gross, E. M.; Maddipati, S. S.; Snyder, S. M. *Bioanalysis* **2016**, 8 (19), 2071.
- (113) Hsueh, Y.; Collins, S. D.; Smith, R. L. *Sensors Actuators B. Chem.* **1998**, 49, 1.



# Chapter 2

## **Aggregation-Induced ECL of Platinum(II) Complexes**

### **Abstract**

This chapter describes a series of square-planar Pt(II) complexes which are capable of emitting electrochemiluminescence when they form supramolecular aggregated nanostructures, naming the phenomenon as Aggregation-Induced ECL. The different complexes have been characterised in terms of their photophysical, electrochemical and ECL properties in order to shed light on the mechanism that produces the excited state. Significantly, the emission from this self-assembled system is the first example of ECL of Pt(II) complexes in aqueous solution having higher efficiency than  $\text{Ru}(\text{bpy})_3^{2+}$ . There is great potential for applications of such systems in ECL-based assays.

## 2.1 INTRODUCTION

Supramolecular nanostructures based on organometallic systems constitutes today a research area of great interest due to the possibility of developing new functional materials with more complex properties than the corresponding singular molecular entities. In particular, square-planar platinum(II) and palladium(II)  $d^8$  complexes with protruding filled  $d_{z^2}$  orbitals are versatile building blocks for such nanostructures since they facilitate supramolecular stacking through weak non-covalent metal-metal and/or  $\pi$ - $\pi$  (ligand–ligand) interactions.<sup>1–3</sup>

### 2.1.1 Electronic configuration of square-planar Pt(II) complexes

Luminescent platinum compounds bearing strong field cyclometalating ligands as well as good  $\pi$ -accepting moieties, possess HOMO and LUMO levels with  $d\pi$  and  $\pi^*$  character, respectively. As shown in Figure 2.1, if a metal is coordinated by  $\pi$ -conjugated ligands, the set of s, p and d orbitals of the metal are mixed with symmetry-adapted orbitals from the ligands.

Optical excitation leads to the formation of excited states described, on the basis of their electronic transition configuration that can be classified as Metal Centered (**MC**), involving mainly d-orbitals, occupied non-bonding  $\pi_M$  anti-bonding unoccupied  $\sigma_M^*$  orbitals, Ligand Centered (**LC**) involving mainly occupied bonding orbital  $\pi_L$  and unoccupied anti-bonding  $\pi_L^*$  orbital located on the ligands, and Metal to Ligand Charge Transfer (**MLCT**) involving mainly occupied metal centered bonding orbitals  $\pi_M$  and unoccupied ligand centered anti-bonding orbitals  $\pi_L^*$ .

The LUMO is also mainly centered on the ligands with contributions from the anti-bonding orbitals  $\pi_L^*$ . The relative energy levels of MLCT and LC transitions depend on the energy of the orbitals,  $\pi_L$  and  $d_{z^2}$ , involved in the electronic configuration of the excited state.

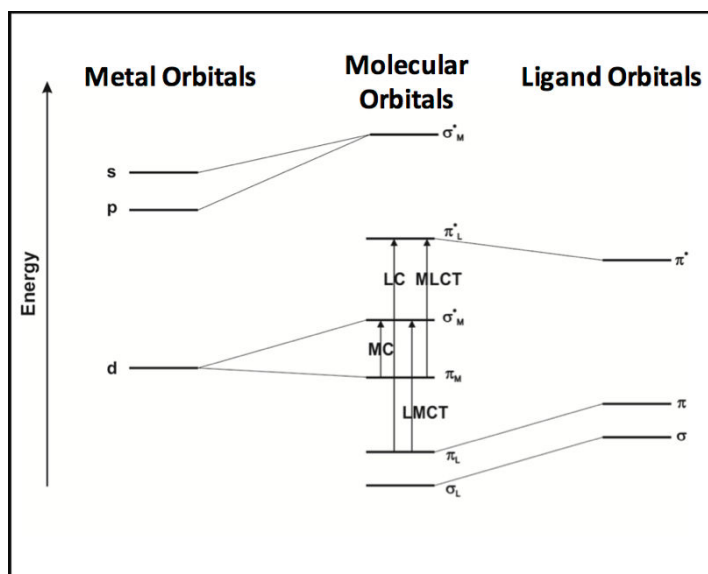


**Figure 2.1.** Simplified MO diagram for a generic transition metal complex and relative spectroscopic excitation transitions.

According to the ligand field theory, for a metal center set in a square planar arrangement of the coordinating ligands, relaxation of degeneracy of the d orbitals leads to a filled  $d_{z^2}$  orbital normal to the plane of the molecule, which does not interact with the ligands coordination sphere.

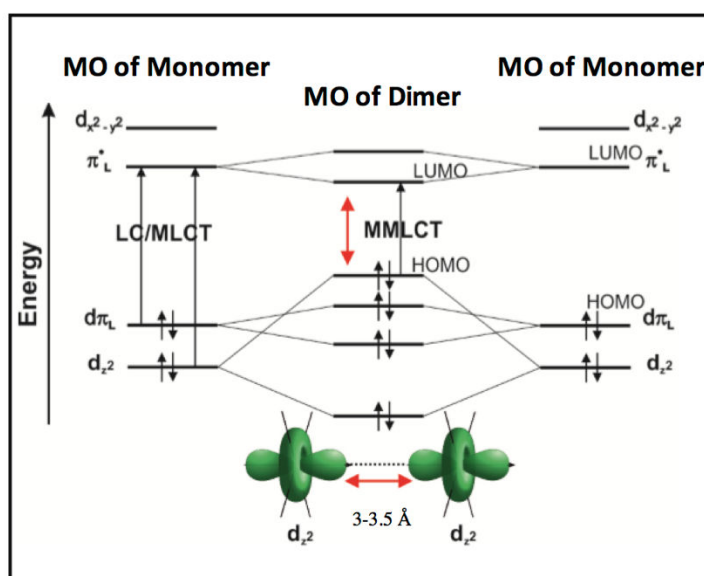


**Figure 2.2.** General scheme showing energy levels of Pt(II) square planar complexes before and after aggregation. In the bottom, cartoon showing interaction between  $d_{z^2}$  orbitals perpendicular to molecular plane.

The  $d_{z^2}$  occupied orbitals are therefore prone to interact with surrounding species such as solvent molecules or neighbouring platinum complexes (Figure 2.2). In the latter case, the ground-state metallophilic interaction splits the energy of the  $d_{z^2}$  into two filled energy

level, one stabilised and one destabilised, that switches the character of the HOMO level from  $d\pi$  to  $\sigma^*$  (i.e.,  $d_{z^2}\cdots d_{z^2}$ ). Owing to the Pt $\cdots$ Pt interaction, new transitions are formed such as metal-metal-to-ligand charge transfer, namely **MMLCT** ( $d\sigma^*-\pi^*$ ), and ligand-to-metal-metal charge-transfer (**LMMCT**). These charge transfer (CT) transitions typically show absorption and luminescence that are substantially bathochromically shifted compared to the parental non-interacting platinum complexes. Moreover, it is important to note that the energy of such CT transitions is strongly dependent on the metal-metal distance, since the electronic interaction occurs only at distances below 3.0 - 3.5 Å.

### 2.1.2 Supramolecular architectures of square planar Pt(II) complexes

The use of self-assembly in chemistry is a very powerful tool for the bottom-up preparation of systems and architectures that can create nano-organised materials with superior properties than the single components or the bulk materials, with controlled spatial disposition and molecular organisation.<sup>4-6</sup> The concept of self-assembly is closely connected with biology and in particular with biological structures such as membranes, proteins, enzymes, and DNA, just to name a few. They have attracted considerable attention as a result of their interesting biological activities, such as antitumor cytotoxicity,<sup>7</sup> DNA intercalation,<sup>8</sup> and protein binding behavior.<sup>9</sup>

In light of the electronic description provided for square planar  $d8$  complexes, supramolecular chemistry has the potential to tune the photophysical properties of such systems, by precisely controlling their interactions with the surrounding environment. Self-assembled functional architectures have indeed been proposed for applications in optoelectronic devices such as organic light emitting diodes (OLEDs),<sup>10,11</sup> field effect transistors (FETs),<sup>12,13</sup> and organic light-emitting FETs (OLEFETs).<sup>14</sup>

Despite the large number of studies on their photophysics, there are few reports of the ECL properties of platinum (II) complexes,<sup>15-21</sup> since the most efficient ECL systems found to date are all based on Ru(II) and Ir(III) species.<sup>22-25</sup> In particular, there are no previous reports relating to the ECL of assemblies/aggregates of this kind.

In this chapter, we focus the attention on the study of a series of square-planar Pt(II) complexes, which show electrochemiluminescence properties through a phenomenon that can be named **Aggregation-Induced ECL (AIECL)** similar to Aggregation-Induced

Emission (AIE),<sup>26</sup> opening up a new class of yet unexplored ECL luminophore (see Figure 2.3).

We will describe the photophysical properties and self-assembly of platinum complexes and we will relate them to the electrochemiluminescent features observed in solid state and in solution. These systems display the very interesting ability to emit ECL light only upon aggregation, which can be triggered either by external stimuli, (e.g. electrical or mechanical), or by spontaneous aggregation.

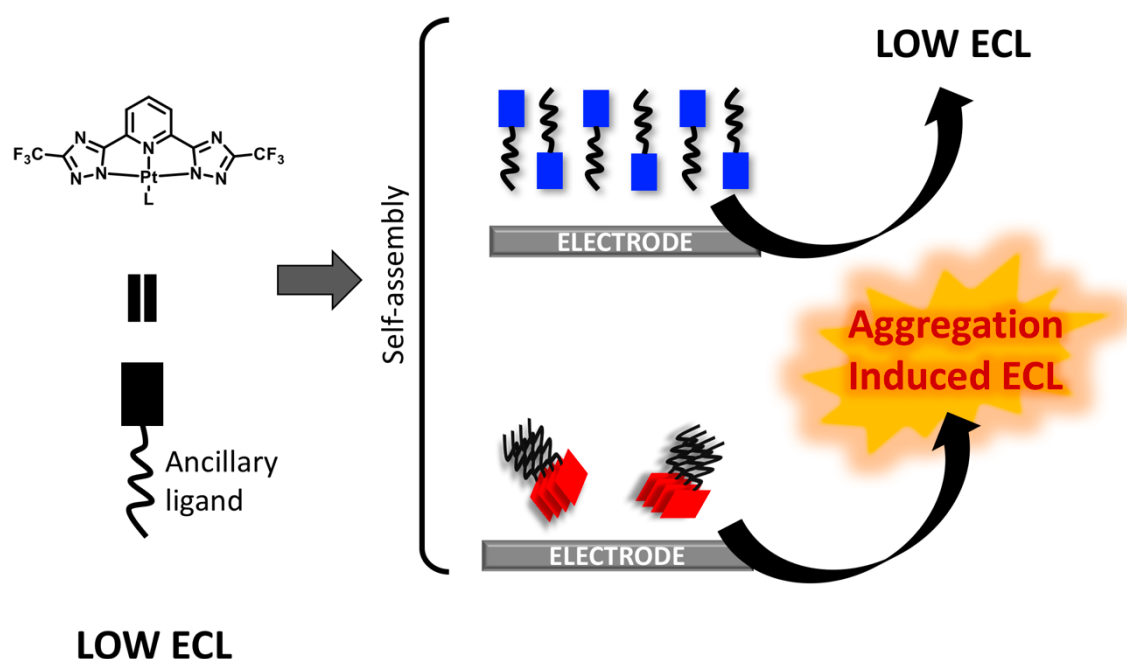


Figure 2.3. Schematic representation of possible self-assembly of Pt (II) complexes that give AIECL.

## 2.2 RESULTS AND DISCUSSION

Pt(II) complexes employed for AIECL investigation are depicted in figure 2.4. They all contain a tridentate ligand bearing two triazoles, the 2,6-bis(3-(trifluoromethyl)-1H-1,2,4-triazol-5-yl)pyridine (**pyC<sub>5</sub>-CF<sub>3</sub>-tzH<sub>2</sub>**), which has previously studied in other platinum (II) complexes due to their interesting photophysical properties.<sup>27</sup> The supramolecular assemblies of **Pt-Amide** and **Pt-PEG** (figure 2.4a-b) have been extensively studied in some publications by our group.<sup>28,29</sup> **Pt-2PEG** was synthesised by a former member of the group in order to obtain a complex soluble in water that forms stable aggregates with an emission typical of MMLCT transition, then bathochromically shifted.



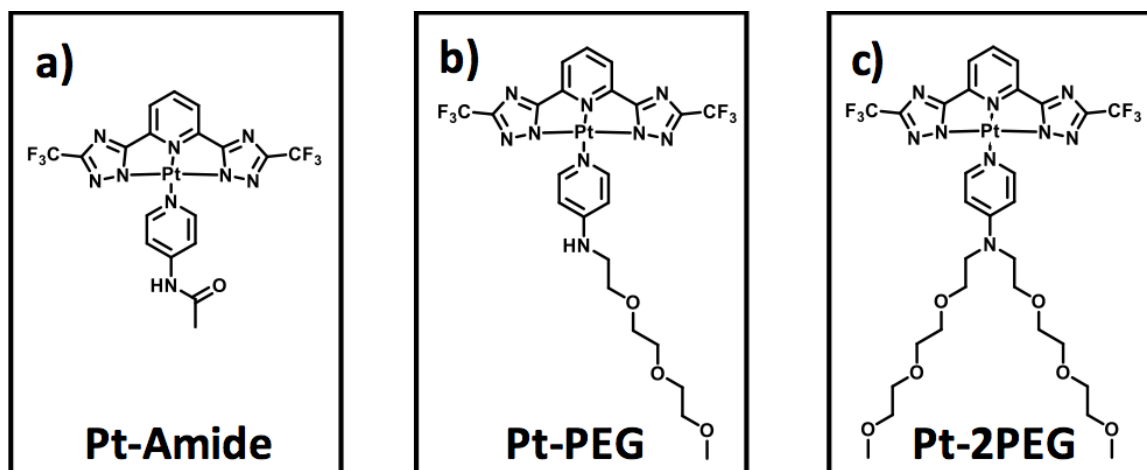


Figure 2.4. a) Pt-Amide, b) Pt-PEG and c) Pt-2PEG structures.

To obtain **Pt-2PEG** two hydrophilic triethylene glycol chains were attached to the 4-amino pyridine moiety. This is useful to increase the amphiphilic character of the molecule and play an important role in the self-assembly (details of the synthesis in section 2.6).

### 2.3 PHOTOPHYSICAL PROPERTIES

In order to explore the self-assembly of the selected complexes, a photophysical study was undertaken in different solvents suitable for each complex and for the formation of different types of aggregates.

**Pt-Amide** photophysical properties were studied in both THF because of good solubility,<sup>28</sup> and in acetone because this solvent is suitable for drop-casting techniques, which in turn allows facile electrode modification (see section 2.4.1). Results are summarised in table 2.1. The compound displays characteristic absorption bands in the UV region (270–350 nm), related to LC transitions, whereas at lower energy (350–430 nm), MLCT transitions are observed (Figure 2.5). It shows structured emission spectra (464–567 nm) assigned to ligand-centered states<sup>10</sup> with relatively short excited-state lifetimes of a few nanoseconds in solution, which are typical for molecularly dissolved monomeric Pt (II) complexes with CF<sub>3</sub>-tzH<sub>2</sub> as the cyclometalating ligand (see Table 2.1). On the other hand, in a 10<sup>-3</sup> M acetone solution, Pt···Pt interactions lead to aggregation of the complex and orange phosphorescence with longer lifetime (see Table 2.1).<sup>30</sup> As shown in Figure 2.5 (red solid trace), spectral features associated with the monomeric form can still be seen at shorter wavelengths under these conditions. When the concentration is fixed at 10<sup>-4</sup> M the spectrum is dominated by monomer emission.

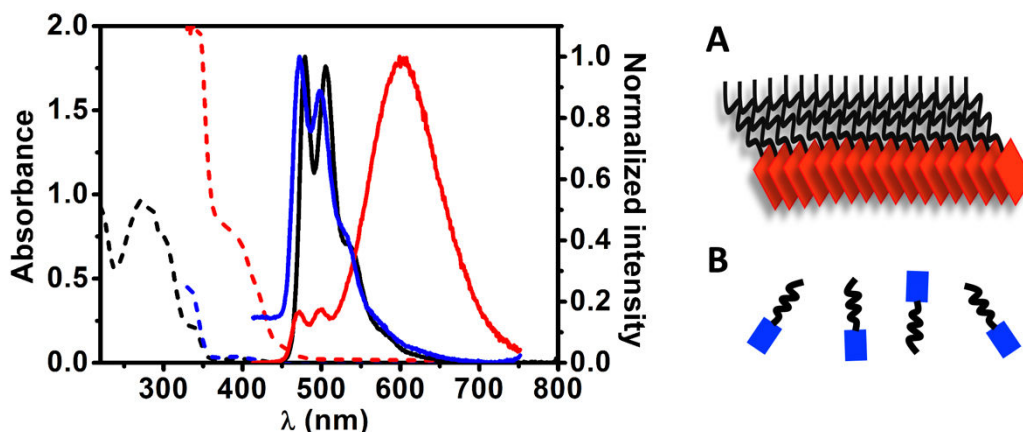


**Figure 2.5.** Electronic absorption (dotted trace) and emission (solid trace) spectra of Pt-Amide in THF ( $c = 10^{-5}$  M, black trace, assembly B), and acetone ( $c = 10^{-4}$  M, blue trace, assembly A,  $c = 10^{-3}$  M, red trace, assembly B).

**Table 2.1.** Photophysical properties of Pt-Amide measured in THF and Acetone. a)  $\lambda_{exc}=300$  nm, b) Average scan  $\lambda_{exc}=280-400$  nm; c)  $\lambda_{exc}=375$  nm; d)  $\lambda_{em}=461$  nm; e)  $\lambda_{exc}=343$  nm; f)  $\lambda_{exc}=400$  nm; g)  $\lambda_{em}=600$  nm.

	THF solution					Acetone solution			
	$\lambda_{abs}$ (nm)	$\lambda_{em}$ (nm) <sup>a</sup>	$\phi$ (%) <sup>b</sup>	$\tau$ (ns) <sup>c,d</sup>		$\lambda_{abs}$ (nm)	$\lambda_{em}$ (nm) <sup>e,f</sup>	$\phi$ (%) <sup>b</sup>	$\tau$ (ns)
$10^{-5}$ M	273, 299(sh), 335, 397	463, 490, 527, 567	<1	2.1	$10^{-3}$ M	346, 380, 396, 450	459, 490, 600	2	4.3 <sup>c,d</sup> 153 <sup>c,g</sup>
					$10^{-4}$ M	330, 396	457, 487, 522, 567	<1	4.3 <sup>c,d</sup> 4 <sup>c,g</sup>

**Pt-PEG** has been extensively studied in a recent work of the group in Nature Chemistry.<sup>29</sup> We report in brief the characterisation done in air-equilibrated 1,4-dioxane and after flash-injection in water (figure 2.6),<sup>29</sup> since the monomer is well solubilised by 1,4-dioxane and it forms kinetically-trapped metastable and thermodynamic aggregates once it is flash-injected in water (figure 2.5 A-B).

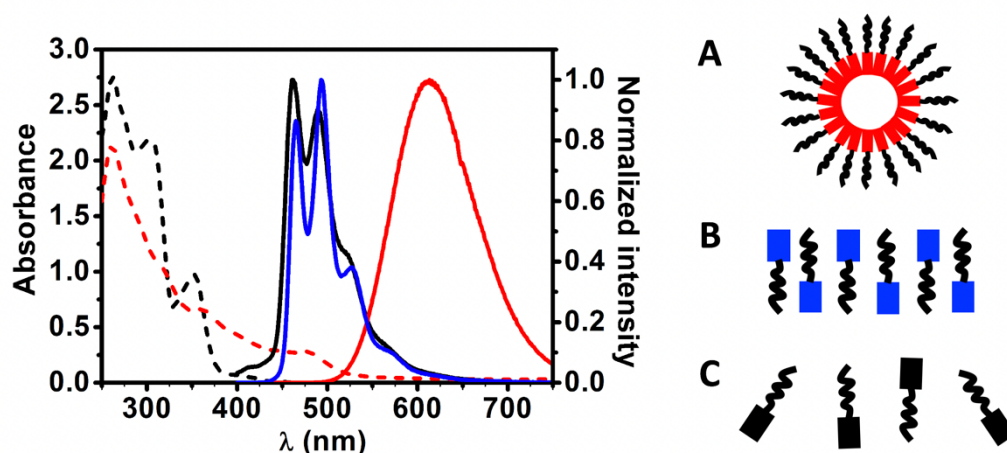


**Figure 2.6.** Electronic absorption (dotted trace) and emission (solid trace) spectra of Pt-PEG in pure 1,4 dioxane ( $c = 10^{-4}$  M, black), after flash-injection into water to form assembly A ( $c = 10^{-4}$  M, 95% water content, red trace) and assembly B (blue trace).

**Table 2.2.** Photophysical properties of Pt-PEG measured in 1,4 dioxane and upon flash-injection ( $H_2O$ : dioxane 95:5, fresh and aged one). a)  $L_{exc}=300$  nm, b) Average scan  $L_{exc}=300-500$  nm; c)  $L_{exc}=405$  nm.

	Pt-PEG			
	$\lambda_{abs}$ (nm)	$\lambda_{em}$ (nm) <sup>a</sup>	$\phi$ (%) <sup>b</sup>	$\tau$ (ns) <sup>c</sup>
<b>0.1-200x10<sup>-5</sup> M 1,4 dioxane</b>	262, 300, 352	461, 489, 521	1	2.6
<b>10<sup>-4</sup> M H<sub>2</sub>O: dioxane 95:5</b>	260, 360, 400-550	613	84	646
<b>10<sup>-4</sup> M H<sub>2</sub>O: dioxane 95:5 after 3 weeks</b>	-	461, 494, 527	20	1080

As shown in Figure 2.6, when **Pt-PEG** is dissolved in air-equilibrated 1,4-dioxane ( $c = 0.1-200 \times 10^{-5}$  M) only a weak blue emission is detected, with a PLQY of about 1% and short excited state lifetime (table 2.2) arising from an excited state with mainly triplet ligand centered ( $^3LC$ ) character. Upon flash-injecting a 1,4-dioxane solution ( $[Pt-PEG] = 2 \times 10^{-3}$  M) into water, that is a solvent in which the complex is not solubilised, we noticed a

bathochromic shift in the emission due to the formation of an emissive species namely assembly A.<sup>29</sup> The final H<sub>2</sub>O:dioxane ratio was 95:5 and the resulting platinum complex concentration was 10<sup>-4</sup> M. Pt··Pt interactions lead to the formation of a new band in the absorption spectrum between 400 and 550 nm, assigned to a transition with <sup>1</sup>MMLCT character. More importantly, such assemblies are characterised by strong orange phosphorescence with longer lifetime (see data table 2.2) despite the air-equilibrated condition, which instead should promote an efficient quenching of the triplet manifold excited state by the dioxygen molecules (Figure 2.6 red trace). Such emission is indeed due to the establishment of a sizeable extent of close Pt··Pt metallophilic interactions between neighbour molecules of Pt-PEG,<sup>10,30-32</sup> due to the fast – i.e., kinetically controlled – formation of the emitting nanoparticles, as reported and demonstrated in the published work<sup>29</sup> by DLS, SEM and confocal microscopy (Figure 2.6 A).

The sample spontaneously interconverted into a thermodynamically stable isoform (assembly B figure 2.6) over three weeks at room temperature.<sup>29</sup> It possesses the same emission energy and profile as the monomeric species (Figure 2.6), but with much higher PLQY and longer lifetime (see table 2.2). The fact that the energy and profile of the emission spectra for the monomer and for C are identical suggests an absence of any Pt··Pt and  $\pi$ - $\pi$  interactions. The higher PLQY is therefore due to an increased rigidity and to the shielding from oxygen quenching accomplished by packing into fiber structures.

Photophysical measurement of complex **Pt-2PEG** were performed in water and in DCM in order to control the assembly, and in addition in Procell, a PBS solution enriched of TPrA (0.1 M) and different surfactants with a confidential specific chemical composition used for ECL purposes. They have been investigated by means of steady-state and time-resolved techniques and the results are reported in Figure 2.7 and Table 2.3.

Complex **Pt-2PEG** is completely soluble in aprotic solvents such as DCM, and it forms an orange-emitting stable colloidal system in aqueous solvent, similar to micellar solutions, characterised by the presence of a foam when shaken. Particularly, we expect it to form micelle-like structures in water due to its two PEG chains that impart it a surfactant-like structure. The hypothesised micellar structure forces platinum complexes to aggregate (figure 2.7 A), giving as result the formation of the typical <sup>1</sup>MMLCT band, which is correlated to a transition at lower energies, red shifted. In DCM, instead, it exists as

monomeric form (figure 2.7 B), showing a blue emission typical of LC transitions. These hypotheses are also supported by the recent published results on Pt-PEG, discussed above.<sup>29</sup>

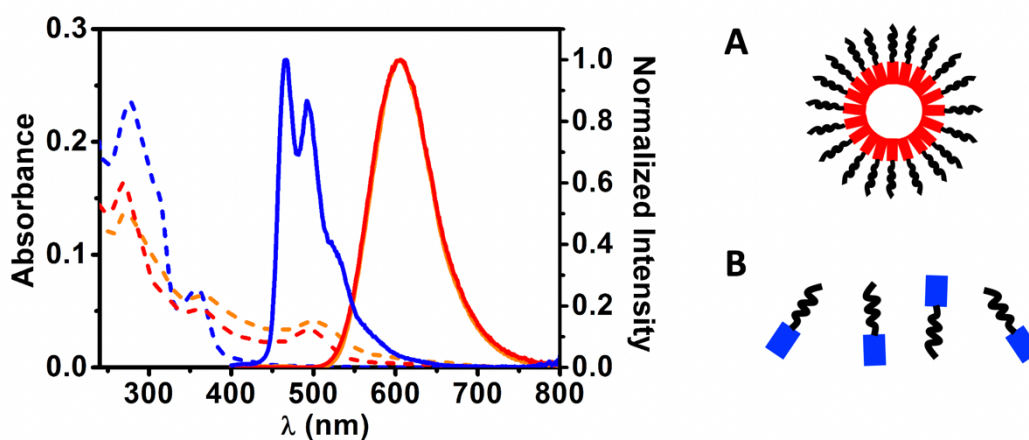


**Figure 2.7.** Electronic absorption (dotted trace) and emission (solid trace) spectra of Pt-2PEG in DCM ( $c = 10^{-5}$  M, blue trace, assembly B), H<sub>2</sub>O and Procell ( $c = 10^{-5}$  M, red and orange traces, assembly A).

**Table 2.3.** Photophysical properties of Pt-2PEG measured in DCM, Water and Procell at room temperature. a)  $\lambda_{exc} = 300$  nm, b) Average scan  $\lambda_{exc} = 300-500$  nm; c)  $\lambda_{exc} = 405$  nm.

	Pt-2PEG			
	$\lambda_{abs}$ (nm)	$\lambda_{em}$ (nm) <sup>a</sup>	$\phi$ (%) <sup>b</sup>	$\tau$ (ns) <sup>c</sup>
<b>10<sup>-5</sup> M DCM</b>	280, 360	464, 492, 525	1	72
<b>10<sup>-5</sup> M H<sub>2</sub>O</b>	280, 370, 400-570	600	72	414
<b>10<sup>-5</sup> M Procell</b>	280, 370, 400-570	600	51	389

In dilute DCM solution ( $10^{-5}$  M) at room temperature (figure 2.7 blue traces), the absorption spectrum of Pt-2PEG displays intense bands in the UV region. These transitions are mainly attributed to the intra-ligand (<sup>1</sup>IL) and metal-perturbed inter-ligand charge transfer (<sup>1</sup>ILCT) states. At lower energies, the complex absorbs until 440 nm. This band is ascribed to the admixture of spin-allowed metal-to-ligand charge transfer (<sup>1</sup>MLCT) and intra-ligand (<sup>1</sup>IL)

transitions corresponding to the HOMO–LUMO excitation process. These assignments are further corroborated by similarity with already reported Pt(II) complexes.<sup>27,33–36</sup>

Upon photoexcitation, a structured blue luminescence signal is observed, peaking at 464, 492 and 525 nm, with a vibronic progression of 1236–1504 cm<sup>-1</sup> attributable to the tridentate intra-ligand vibrational modes. Such low (PLQY = 1%) luminescence is characterised by a very fast radiative decay, that can be attributed to the T<sub>1</sub>-S<sub>0</sub> transition with mainly metal-perturbed <sup>3</sup>LC character.<sup>31</sup>

When the same complex is dissolved in water, the resulting solution shows a strong orange emission under UV irradiation. Pt··Pt interactions lead to the formation of a new band in the absorption spectrum between 400 and 570 nm (figure 2.7 red trace) assigned to a transition with <sup>1</sup>MMLCT character. Such assemblies are characterised by strong orange phosphorescence with longer lifetime (figure 2.7 red trace and table 2.3) similar to the one observed for Pt-PEG aggregates. This emission is due to Pt··Pt metallophilic interactions between neighbour molecules of Pt-2PEG.<sup>10,30–32,37–39</sup>

In Procell a similar behaviour is observed, with an emission centered at 600 nm coming from the excited state <sup>1</sup>MMLCT (figure 2.7 orange traces and table 2.3), even though the PLQY decreases notably from 72 % (water) to 51 %. This can be rationalised considering the presence of surfactants in Procell, which may intercalate between two platinum complexes weakening (or even breaking) the Pt··Pt interactions.

## 2.4 ELECTROCHEMISTRY AND AIECL BEHAVIOUR

### 2.4.1 Pt-Amide

The investigation of electrochemical properties of Pt-Amide started with the characterisation of the compound in acetonitrile at 1.0 and 0.1 mM. The resulting CVs are shown in figure 2.8a. It shows irreversibility in oxidation and reduction, except for the reduction peak related to the ligand at -1.92V vs SCE that exhibits quasi-reversible behaviour. Comparison of the two different concentrations shows that the peak at +1.1 V vs SCE disappears when the solution is diluted. This peak could be related to the presence in solution of aggregates of Pt-Amide, therefore it is visible only in the more concentrated solution. The peak at +1.29 V is instead associated to the oxidation of the monomeric Pt<sup>2+</sup>

to  $\text{Pt}^{4+}$ . Despite that, we would expect the HOMO of the aggregate to be more significantly destabilised, therefore with an oxidation at lower potentials.

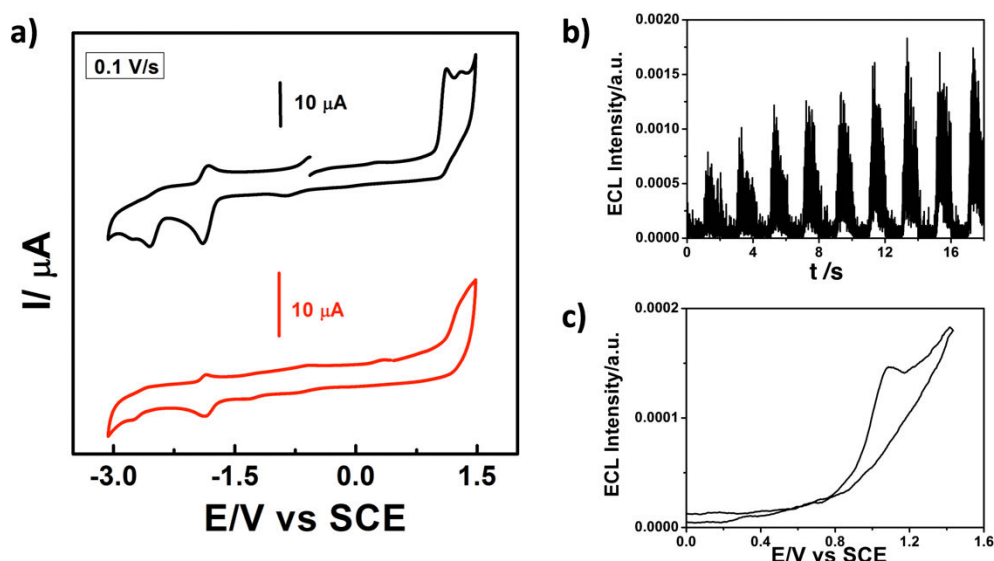


**Figure 2.8.** a) Cyclic voltammograms of 1 mM (black trace) and 0.1 mM (red trace) Pt-Amide in 0.1 M TBAPF<sub>6</sub> CH<sub>3</sub>CN solution at GC electrode. Scan rate 0.1 V s<sup>-1</sup>. SCE as reference electrode and Pt wire as counter electrode; b) ECL emission of 1mM Pt-Amide in 0.1 M TBAPF<sub>6</sub> CH<sub>3</sub>CN solution generated by ion annihilation at GC electrode with pulsing (1 s) between 2<sup>nd</sup> oxidation and 1<sup>st</sup> reduction peak potentials of the complex; c) ECL emission of 1 mM Pt-Amide recorded during a cyclic voltammetry at scan rate 0.05 V s<sup>-1</sup> in 0.1 M TBAPF<sub>6</sub> CH<sub>3</sub>CN solution with 1mM TPrA as co-reactant.

Ion annihilation ECL experiments were first attempted. Pulsing in CH<sub>3</sub>CN solution between the oxidation potential and either the first or second reduction potential resulted in little emission. ECL was also attempted using tripropylamine as co-reactant. As shown in figure 2.8b-c, this did not show an encouraging result either, with only very low intensity emission produced. ECL spectra could not be recorded via either the annihilation or co-reactant pathway due to the low emission intensities. This is perhaps not surprising given the low photoluminescence quantum yield (which sets the upper limit for the ECL efficiency); combined with the relative instability of the oxidised and reduced forms of the complex. Moreover, though the ECL reactions are energy sufficient in both cases, they may be only marginally so, as the blue-emitting excited state is relatively difficult to populate.

ECL was found to be notably more intense upon immobilisation of the complex onto screen-printed electrode (SPE) surface using as co-reactant TPrA in low concentration (1-10 mM). Two ways were tested for the immobilisation of the complex: physical transfer (solid particles contacted with the surface) and drop casting from acetone solution. In both cases, the emission peaks at +1.6 V vs Ag/AgCl, quite after the oxidation potential of both

co-reactant and Pt-Amide, suggesting that an additional energy is necessary to the system to give ECL emission. In the drop casting test, the complex dried on the surface of the SPE, yielding aggregates that displayed orange photoluminescence (figure 2.5, assembly A).

It is clear from Figure 2.9b (red traces) that the ECL spectrum of Pt-Amide/TPrA system is almost identical with its PL one, indicating that the excited state obtained on photoexcitation is also generated in the ECL experiment.

When TPrA is employed as co-reactant, its strong reducing power in the radical form TPrA<sup>•</sup> ( $E_{\text{TPrA}^{\bullet}} = -1.7 \text{ V}$ ) allows to give electron transfer on the LUMO of the aggregated form for the generation of the excited state that emits the 600 nm light.

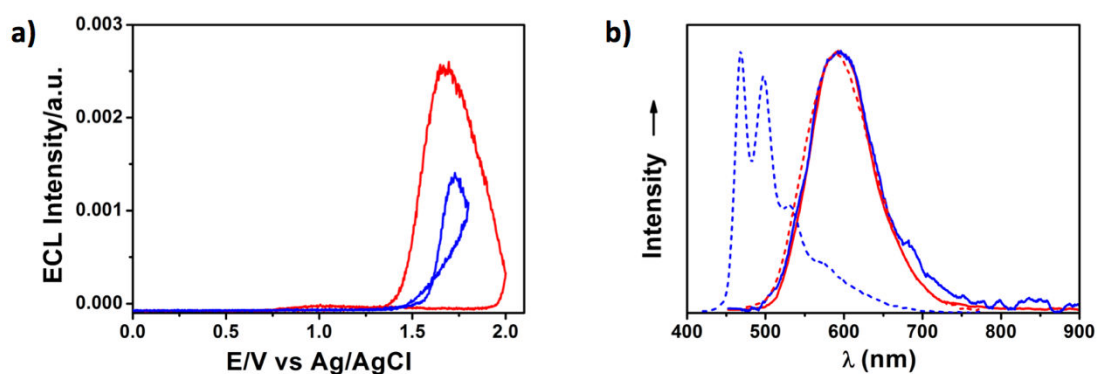


**Figure 2.9.** **a)** ECL emission recorded during a cyclic voltammetry at scan rate  $0.2 \text{ V s}^{-1}$  in aqueous  $0.1 \text{ M LiClO}_4$  solution of Pt-amide physically transferred (blue trace) and drop casted from acetone (red traces) onto SPE using  $10 \text{ mM TPrA}$  as co-reactant. Ag/AgCl as reference electrode and pt wire as counter electrode; **b)** PL (dashed traces) and ECL (solid traces) emissions of Pt-amide physically transferred onto spe (blue trace) and drop casted from acetone (red traces) onto SPE.

By physical transfer, the complex powder on the electrode surface emits upon photoexcitation in the blue region showing the typical profile observed in solution when it is in monomeric form (figure 2.5). However, the electrochemical excitation gives an emission centered at 600 nm (see figure 2.9b blue traces) identical to the one seen for the drop casting, demonstrating that TPrA<sup>•</sup> can reduce by electron-transfer the oxidised Pt-Amide only where it forms aggregates that produce the MMLCT excited state. To gain further information on the possible mechanism, the emission changes on the electrode surface was monitored by cycling the applied potential several times. The results show that orange emission arises upon oxidation (Figure 2.10). On first approximation, the co-reactant (TPrA) is oxidised in the same potential range as the  $\text{Pt}^{2+}$  species, the oxidised TPrA then generates a radical product TPrA<sup>•</sup> that reacts with  $\text{Pt}^{4+}$  to generate the excited state, which



subsequently produces light. This simple mechanism is based on reported ECL experiments on Pt complexes,<sup>17,40</sup> however in this case it results a bit more complex because the formation of the aggregate appears during a potential scan. In fact, upon oxidation of  $\text{Pt}^{2+}$  it is evident the formation onto the SPE surface of an aggregate form (possibly a dimer) with a more stabilised LUMO able to be reduced from  $\text{TPrA}^\bullet$  (Figure 2.10).

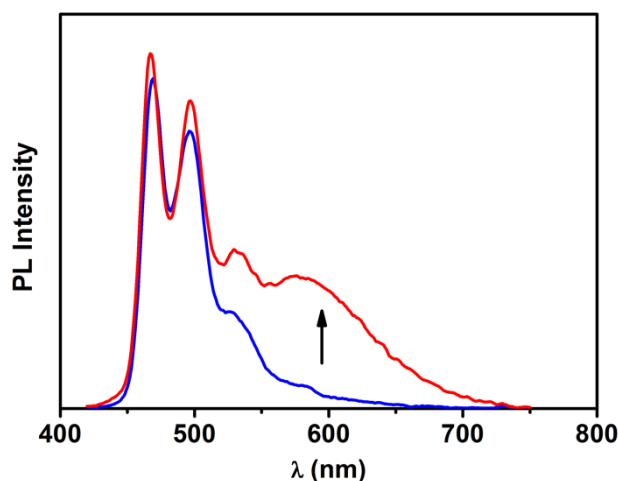


**Figure 2.10.** PL emission of Pt-Amide physically transferred onto SPE before (blue trace) and after oxidation (red trace).

We can hypothesise two different ECL mechanisms. The first implies a bi-electronic oxidation of  $\text{Pt}^{2+}$  to  $\text{Pt}^{4+}$  with a subsequent *in situ* aggregation with a vicinal  $\text{Pt}^{2+}$ . The interaction between these two vicinal platinum complexes is of a metallophilic nature and it is responsible of the formation of the MMLCT transition, therefore suitable for the electron transfer from  $\text{TPrA}^\bullet$  that generates the excited state. The second possibility is that two  $\text{Pt}^{2+}$  are oxidised to  $\text{Pt}^{3+}$ . Comparing to the 4+, the 3+ oxidation state of platinum is much less common<sup>41-43</sup> due to the reactive nature of the unpaired electron residing in a sterically-exposed  $d_z^2$  orbital. In fact, only Pt (III) compounds with metal-metal covalent bonds are relatively common.<sup>44,45</sup> After oxidation, their instability lead them to interact forming a dimer that can be excited by  $\text{TPrA}^\bullet$  to give the emission at 600 nm. In both cases, the process requires an aggregation with the consequent formation of the MMLCT, therefore the phenomenon can be classified as AIECL (see Figure 2.11). For each case, it is likely that oxidation during redox cycling leads to dissolution and re-precipitation on the electrode. The re-precipitated form is the  $\text{Pt}\cdots\text{Pt}$  aggregate which undergoes solid state AIECL.

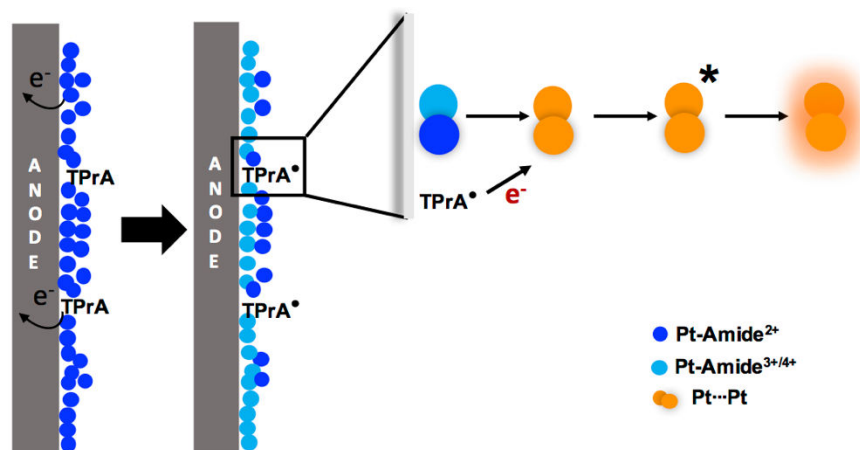


**Figure 2.11.** Schematic representation of AIECL upon physical transfer of Pt-Amide onto SPE.

SEM images of the electrodes surfaces were acquired to assess the aggregation of the metal complex upon drop casting and physical transfer. The results show that two different aggregates are formed upon drop casting, namely quasi-spheres and fibers (Figure 2.12a-b). The quasi-spheres could be the responsible for the orange emission, as reported elsewhere.<sup>29</sup> Concerning the physical transfer, the SEM images (Figure 2.12c-d) show crystals and not spherical aggregation.

Finally, taking inspiration from the work published recently by the same group in Nature Chemistry,<sup>29</sup> a 0.1 mM solution of Pt-Amide in 1,4-Dioxane was flash-injected in PBS, giving an orange emitting suspension with a PLQY of 69%. However, the ECL intensity obtained with this suspension was very low (Figure 2.13a), possibly due to the larger size of the particles (see TEM in Figure 2.13b), which diffuse slower comparing to a single complex.<sup>46</sup> The importance of diffusivity in ECL will be treated better in chapter 5.

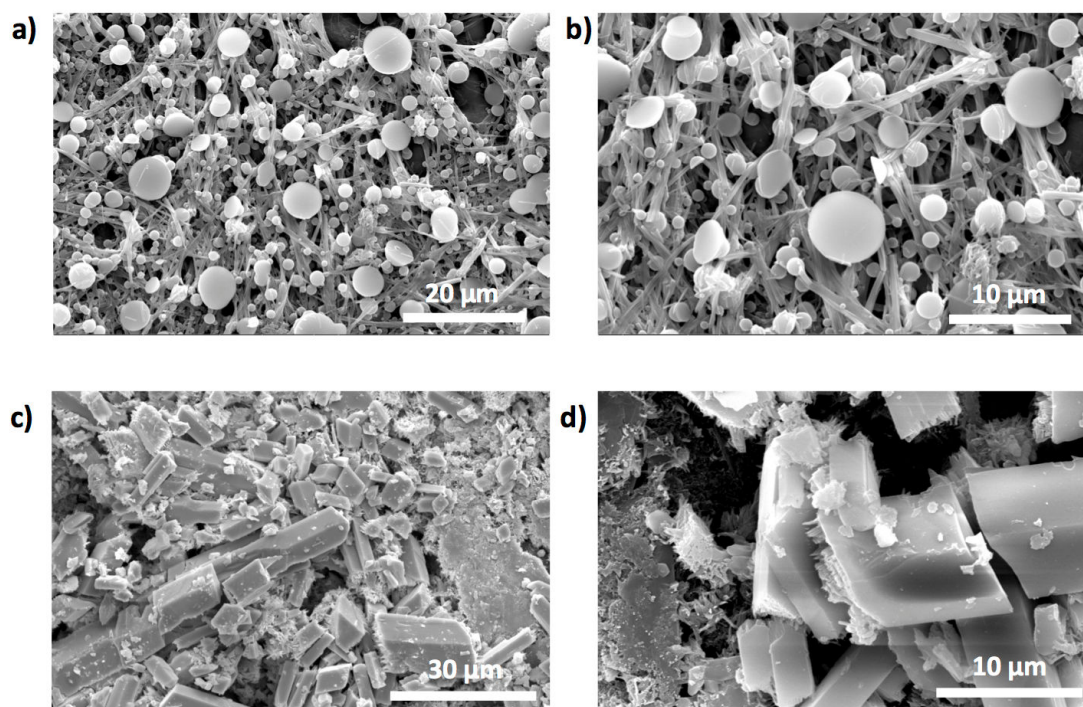


Figure 2.12. SEM images of *a-b*) drop casted Pt-Amide from acetone onto SPE, *c-d*) physical transfer of Pt-Amide onto SPE.

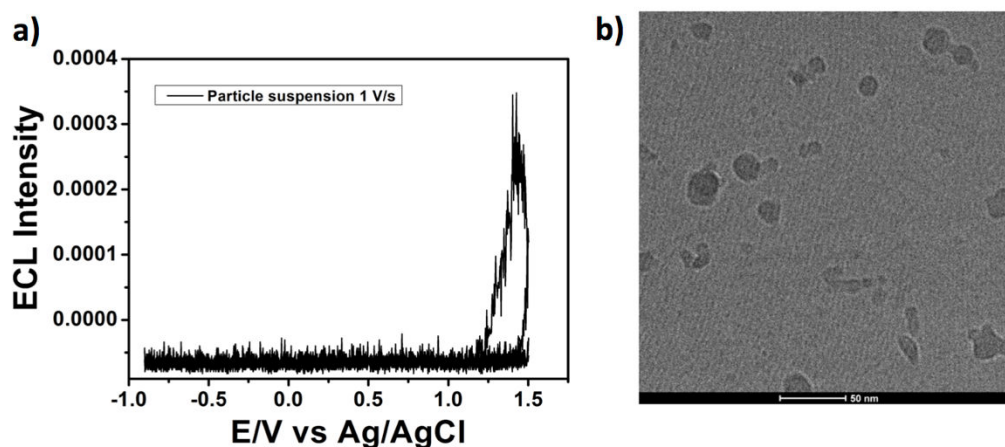
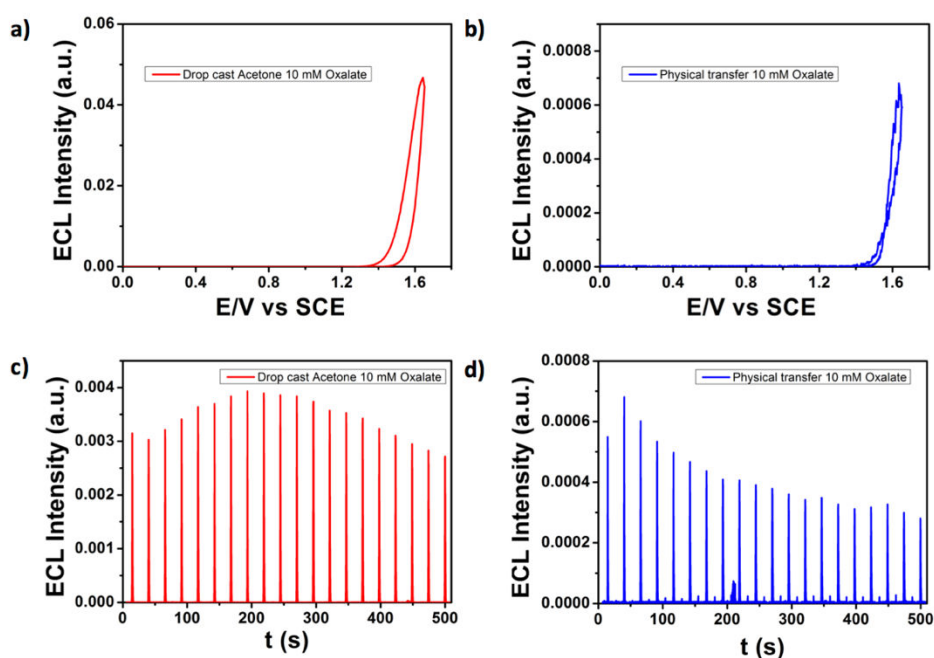


Figure 2.13. *a*) ECL emission of Pt-Amide particles suspension solution recorded during a cyclic voltammetry at scan rate  $1 \text{ V s}^{-1}$  in PBS solution upon addition of  $10 \text{ mM TprA}$ ; *b*) TEM image of particles suspension (scale bar =  $50 \text{ nm}$ ).

In order to improve the signal-to-noise ratio in the above measurement, we tried to employ oxalate ( $\text{C}_2\text{O}_4^{2-}$ ), which is known to stabilise  $\text{Pt}^{4+}$ .<sup>47</sup> Under such conditions, ECL emission recorded during a cyclic voltammetry show repeatability and constant peak potential (Figure 2.14). The emission peak is at  $+1.6 \text{ V}$  in agreement with the results with TPrA.

Both working electrodes could be cycled numerous times, as shown in figure 2.14 c-d over 20 cycles. This can open up an avenue for Pt-based solid state ECL platforms.



**Figure 2.14.** **a)** ECL emission recorded during a cyclic voltammetry at scan rate  $0.2 \text{ V s}^{-1}$  in  $0.1 \text{ M}$  aqueous  $\text{LiClO}_4$  after drop casting of Pt-Amide on SPE from acetone solution using  $\text{Na}_2\text{C}_2\text{O}_4$  as co-reactant; **b)** ECL emission recorded during a cyclic voltammetry at scan rate  $0.2 \text{ V s}^{-1}$  in  $0.1 \text{ M}$  aqueous  $\text{LiClO}_4$  after physical transfer of Pt-Amide on SPE using  $\text{Na}_2\text{C}_2\text{O}_4$  as co-reactant; **c-d)** 20 CV cycles of both electrodes.

## 2.4.2 Pt-PEG

Electrochemical properties of Pt-PEG were studied in DCM, where the complex was dissolved at  $1 \text{ mM}$ . Results, in figure 2.15, show only the onset of the oxidation peak due to the narrow electrochemical window of DCM and a quasi-reversible peak in reduction centered at  $-1.4 \text{ V}$  vs SCE.

In solution, any kind ECL experiment was unsuccessful. In DCM, we observed a very low emission similar to the Pt-Amide case, while in water after flash-injection it was not possible to collect any light because of the size of the formed aggregates, around  $130 \text{ nm}$  as reported elsewhere.<sup>29</sup>

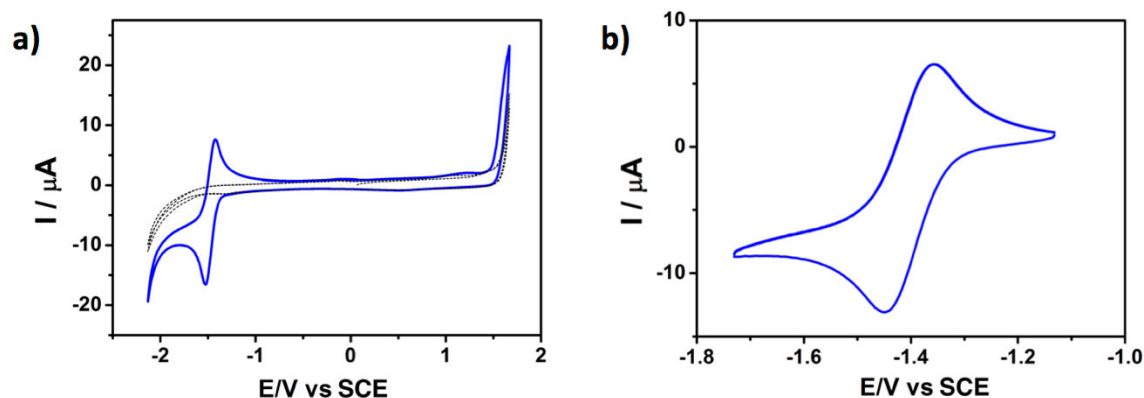


**Figure 2.15.** a) Cyclic voltammograms of 1 mM (blue trace) of Pt-PEG in 0.1 M TBAPF<sub>6</sub> DCM solution (blank in dotted black trace) at GC electrode. Scan rate 0.1 V s<sup>-1</sup>. SCE as reference electrode and Pt wire as counter electrode; a) Cathodic scan of the same solution.

Therefore, Pt-PEG was grafted onto an electrode in the same ways described for Pt-Amide. In both cases, physical transfer and drop casting produced a blue-emitting layer. In this case, the ECL was very low in intensity using oxalate as co-reactant. It is straightforward thinking that the mechanism is the same described for Pt-Amide, that means the local aggregation between few complexes upon oxidation is responsible of the formation of the MMLCT transition suitable for the electron transfer from TprA<sup>•</sup> in order to generate the excited state.

Besides that, Pt (II) complexes like this one are known for being mechanochromic materials thanks to their peculiar tunability of the luminescence spectrum as a function of metal-metal distance.<sup>32,48</sup> Luminescence mechanochromism is defined as a change of emission spectrum upon mechanical stresses.<sup>49-52</sup> Therefore, upon mechanical stress with a gentle grinding using a small pestle, it is possible to convert the spot onto the electrode surface from blue to orange bright emitter energetically favourable for ECL co-reactant experiments. ECL potential curves and ECL emission before and after mechanical stress are shown in figure 2.16.

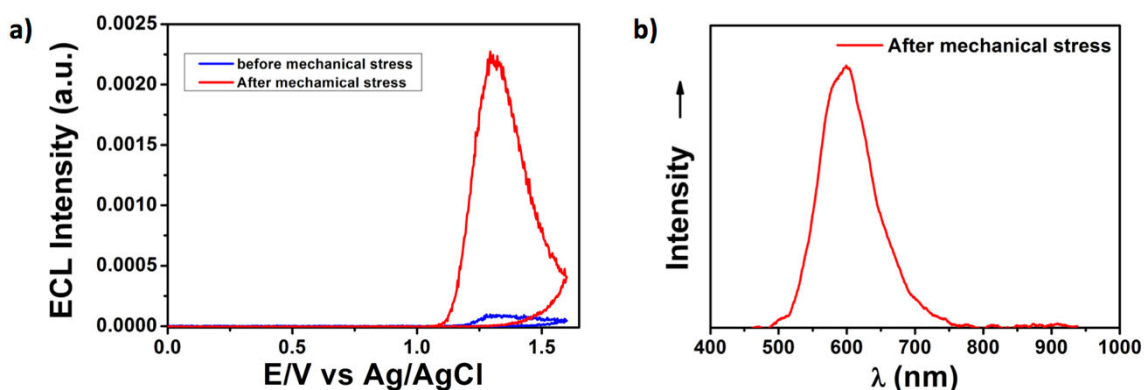


**Figure 2.16.** a) ECL emission recorded during a cyclic voltammetry at scan rate  $0.2 \text{ V s}^{-1}$  in  $0.1 \text{ M LiClO}_4$  water solution of Pt-PEG physically transferred onto SPE before (blue trace) and after (red trace) mechanical stress using  $10 \text{ mM Na}_2\text{C}_2\text{O}_4$  as co-reactant. Ag/AgCl as reference electrode and pt wire as counter electrode; b) ECL emission of Pt-PEG after mechanical stress onto SPE.

From the figure 2.16a it is clear that upon mechanical stress the ECL emission from Pt aggregates is twenty times higher than the blue solid (figure 2.16a, blue trace) that emits in a quite weak way according to the proposed mechanism in section 2.4.1.

### 2.4.3 Pt-2PEG

Pt-2PEG is soluble in DCM and it forms a stable micellar-like suspension in water, as pointed out in section 2.3. Accordingly, electrochemical features were explored in these two solvents. Pt concentration in both case was  $1 \text{ mM}$ . In DCM (figure 2.17a), Pt-2PEG exists as monomeric form and its oxidation should fall at potential higher than the electrochemical window of DCM, therefore no oxidations are seen during a potential scan. A reduction is seen at  $-2.3 \text{ V}$  vs SCE and it should be linked to the ligand. When the complex is dissolved in water, an oxidation peak arises at  $+1.33 \text{ V}$  vs Ag/AgCl (figure 2.17b) and it is due to the oxidation of  $\text{Pt}^{2+}$  to  $\text{Pt}^{4+}$  that takes places at lower potential since there is the formation of the MMLCT band with a destabilised HOMO. Unfortunately, in water it is not possible to investigate the reduction because of its limited electrochemical window.

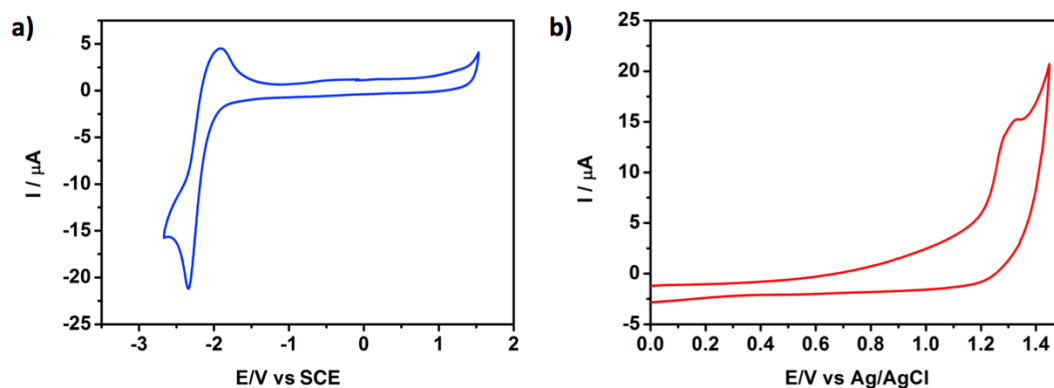


**Figure 2.17.** Cyclic voltammograms of Pt-2PEG in **a)** DCM at concentration 1 mM using 0.1 M TBAPF<sub>6</sub> as supporting electrolyte, **b)** in water at concentration 1 mM using 0.1 M LiClO<sub>4</sub> as supporting electrolyte. GC as working electrode, SCE and Ag/AgCl as reference electrodes and Pt wire as counter electrode. Scan rate 0.1 V s<sup>-1</sup>.

ECL properties were investigated in aqueous solutions (water and Procell) and after immobilisation on SPE. Ru(bpy)<sub>3</sub><sup>2+</sup> was used as standard with the aim of calculating the ECL efficiency. To compare water with Procell, an amount of 100 mM TPrA was added in order to get the ECL emission. In addition, oxalate was evaluated as co-reactant since it gave for the other complexes a better result because of improved capacities in stabilizing the oxidised species. All solutions were prepared with a concentration of 10<sup>-5</sup> M.

In water, ECL emission of Pt-2PEG and Ru(bpy)<sub>3</sub><sup>2+</sup> using 100 mM TPrA as co-reactant are of the same intensity (figure 2.18a). The shapes of the curves are quite different one from each other. From what it emerges, an emission appears around +0.9 V that can be attributed to the oxidation of TPrA and it peaks +1.6 V, showing emission during all the anodic scan. The profile for Ru(bpy)<sub>3</sub><sup>2+</sup> can be explained easily taking into account the two mechanisms reported by Bard and Miao.<sup>53</sup> Potentiostatic measurements were done in order to calculate the efficiency. In water solution, the efficiency is equal to 1.45 (figure 2.18b) and it is visible that Pt-2PEG is still quite active at the second potential step respect to Ru(bpy)<sub>3</sub><sup>2+</sup>.



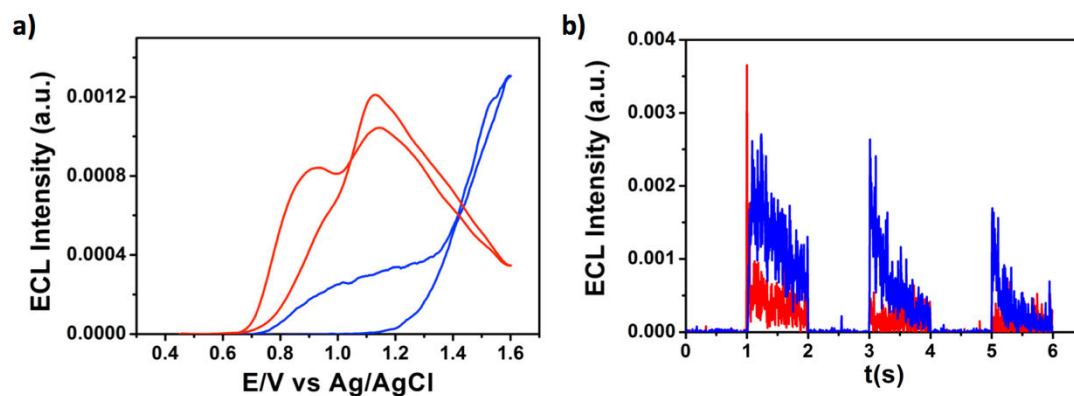


**Figure 2.18.** a) ECL intensity during a potential scan of  $10^{-5}$  M water solution of  $\text{Ru}(\text{bpy})_3^{2+}$  (red trace) and Pt-2PEG (blue trace) using 0.1 M  $\text{LiClO}_4$  as supporting electrolyte, upon addition of 0.1 M of TPrA. Scan rate  $0.05 \text{ V s}^{-1}$ . GC as working electrode, Ag/AgCl as reference electrode and Pt wire as counter electrode; b) ECL Intensities in time of  $\text{Ru}(\text{bpy})_3^{2+}$  (red trace) and Pt-2PEG (blue trace) in 0.1 M  $\text{LiClO}_4$  water solution using 0.1 M TPrA as co-reactant. GC as working electrode, Ag/AgCl as reference electrode and Pt wire as counter electrode. Pulse at +1.4 V.

In Procell, the emission during a potential scan changes shape, as it is possible to visualise in figure 2.19. Comparing to Ru, the emission is more than 50 times lower and it is due to the fact that  $\text{Ru}(\text{bpy})_3^{2+}$  ECL emission is favoured in Procell since the surfactants protect its emission from oxygen and water quenching forming a micelle around them.<sup>54,55</sup> On the contrary, Pt complexes could suffer of the presence of surfactants for an unfavourable intercalation between the complexes that minimizes Pt...Pt interactions.

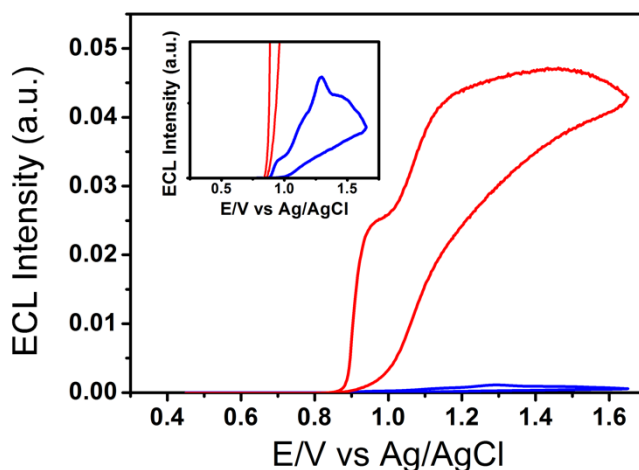


**Figure 2.19.** ECL intensity during a potential scan of  $10^{-5}$  M Procell solution of  $\text{Ru}(\text{bpy})_3^{2+}$  (red trace) and Pt-2PEG (blue trace). Scan rate  $0.05 \text{ V s}^{-1}$ . GC as working electrode, Ag/AgCl as reference electrode and Pt wire as counter electrode. **Inset:** zoom of ECL intensity vs potential.



Since we demonstrated that oxalates stabilize  $\text{Pt}^{4+}$ , we performed the same experiments in 0.1 M  $\text{LiClO}_4$  water solution with 10 mM  $\text{Na}_2\text{C}_2\text{O}_4$  as co-reactant. Potentiodynamic and potentiostatic results are shown in figure 2.20.

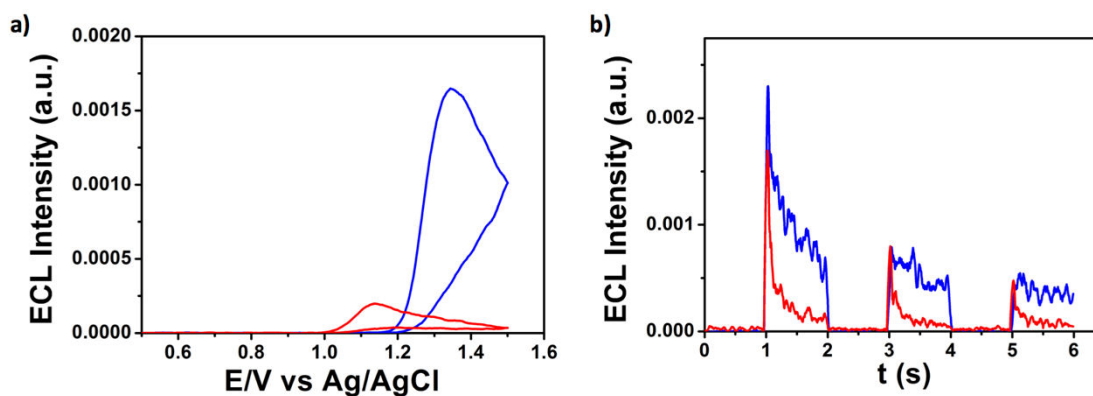


**Figure 2.20.** a) ECL intensity during a potential scan of  $10^{-5}$  M water solution of  $\text{Ru}(\text{bpy})_3^{2+}$  (red trace) and Pt-2PEG (blue trace) using 0.1 M  $\text{LiClO}_4$  as supporting electrolyte, upon addition of 10 mM of  $\text{Na}_2\text{C}_2\text{O}_4$ . Scan rate  $0.05 \text{ V s}^{-1}$ . GC as working electrode, Ag/AgCl as reference electrode and Pt wire as counter electrode; b) ECL Intensities in time of  $\text{Ru}(\text{bpy})_3^{2+}$  (red trace) and Pt-2PEG (blue trace) in 0.1 M  $\text{LiClO}_4$  water solution using 10 mM of  $\text{Na}_2\text{C}_2\text{O}_4$  as co-reactant. GC as working electrode, Ag/AgCl as reference electrode and Pt wire as counter electrode. Pulse at +1.4 V.

Surprisingly, the ECL intensity of such Pt complex results much higher than  $\text{Ru}(\text{bpy})_3^{2+}$ . The ECL intensity during a potential scan shows the emission peak at +1.3 V in agreement with the oxidation potential of Pt-2PEG.  $\text{Ru}(\text{bpy})_3^{2+}$  shows a peak at +1.15 V, typical of the simultaneous oxidation of it and co-reactant. The relative efficiency ( $\text{Ru}(\text{bpy})_3^{2+} = 1$ ) calculated from chronoamperograms in figure 2.20b is equal to 14. This is the first example of Pt (II) complex out-performing  $\text{Ru}(\text{bpy})_3^{2+}$  in ECL intensity.

Finally, we tested the complex in solid phase onto the SPE after physical transfer. The emission was very intense as shown by the results in figure 2.21.

As visible in Figure 2.21a, the emission peak falls at +1.3 V, exactly at the oxidation potential of this complex in aggregate form in water. Figure 2.21b shows the emission of this complex onto the SPE surface, centered at 600 nm and it is the same obtained by photo-excitation, as shown in section 2.3. Therefore, both TPrA and  $\text{C}_2\text{O}_4^{2-}$  can be used as co-reactant for the generation of the excited state responsible for the emission typical of MMLCT transitions.

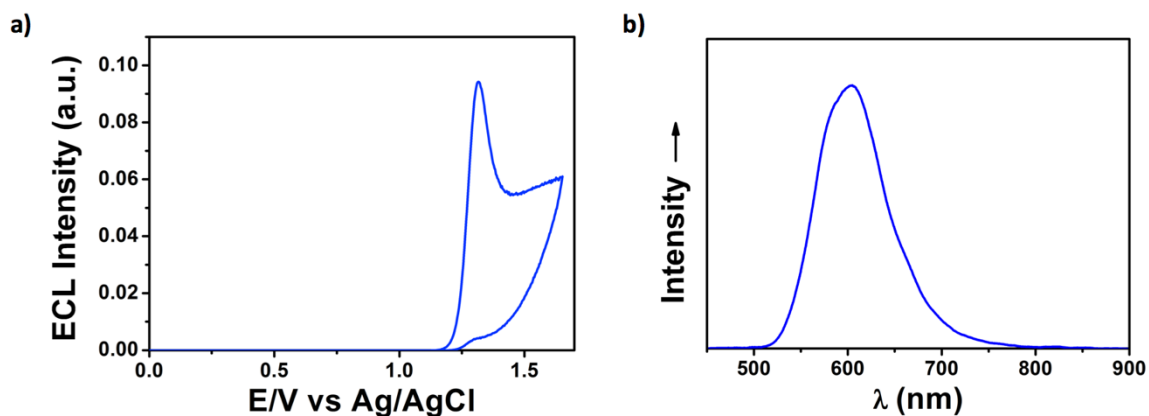


**Figure 2.21.** a) ECL intensity during a potential scan of physical transfer of Pt-2PEG onto SPE, using 10 mM  $C_2O_4^{2-}$  as co-reactant and 0.1 M  $LiClO_4$  as supporting electrolyte. Scan rate  $0.05 V s^{-1}$ . SPE as working electrode, Ag/AgCl as reference electrode and Pt wire as counter electrode; b) ECL spectrum during a potential scan of Pt-2PEG physically transferred onto SPE, using 10 mM  $C_2O_4^{2-}$  as co-reactant and 0.1 M  $LiClO_4$  as supporting electrolyte. Scan rate  $0.05 V s^{-1}$ . SPE as working electrode, Ag/AgCl as reference electrode and Pt wire as counter electrode.

## 2.5 CONCLUSION

The study of ECL properties of Pt(II) complexes with self-assembled functional structures was reported both in solid state and in solution. All of the complexes show intense ECL upon aggregation via co-reactant pathway, using both TPrA and oxalate. For this reason, the phenomenon has been named *Aggregation-Induced ECL* in similarity with Aggregation-Induced Emission behaviour in photoluminescence of the same complexes. Oxalate as co-reactant stabilised more the oxidised  $Pt^{4+}$  by coulombic interactions, resulting more suitable for future applications in biosensing. Interestingly, Pt-2PEG aggregated forming micelles in water, displaying more intense emission than the  $Ru(bpy)_3^{2+}$  benchmark. Such findings open the possibility not only to deeper study the mechanisms behind the ECL generation of this class of metal complexes, that is still unexplored, but also to prepare functional structures able to substitute the  $Ru(bpy)_3^{2+}$  for biosensing and immunoassay applications.

## 2.6 EXPERIMENTAL SECTION

### Materials

Pt-Amide<sup>28</sup> and Pt-PEG<sup>29</sup> were synthesised according to previously reported methods. All the chemicals were purchased and used as received. Ultrapure fresh water was obtained from a Millipore water purification system ( $>18M\Omega$  Milli-Q, Millipore) and Acetonitrile (MeCN) and Dichloromethane (DCM) were purchased at Acros organics and used without

any purification. All the reactions were carried out under inert atmosphere (Schlenk technique). The compounds were purified by column chromatography by using silica gel 60 (230–400 mesh) as stationary phase.  $^1\text{H}$ ,  $^{13}\text{C}$  and  $^{19}\text{F}$  NMR spectra were recorded on a Bruker Avance 400 spectrometer. The  $^1\text{H}$  NMR chemical shifts ( $\delta$ ) are given in ppm and referred to residual protons on the corresponding deuterated solvent. All deuterated solvents were used as received without any further purification. All coupling constants ( $J$ ) are given in Hertz (Hz). Electrospray ionisation mass (ESI-MS) spectra were recorded on a Bruker Daltonics (Bremen, Germany) MicroTof with loop injection. NMR measurements were performed in Institut de Science et d'Ingénierie Supramoléculaires (ISIS), University of Strasbourg. Elemental analyses were recorded by the analytical service of physical measurements and optical spectroscopy at the University of Strasbourg.

### Synthesis Procedure of Pt-2PEG

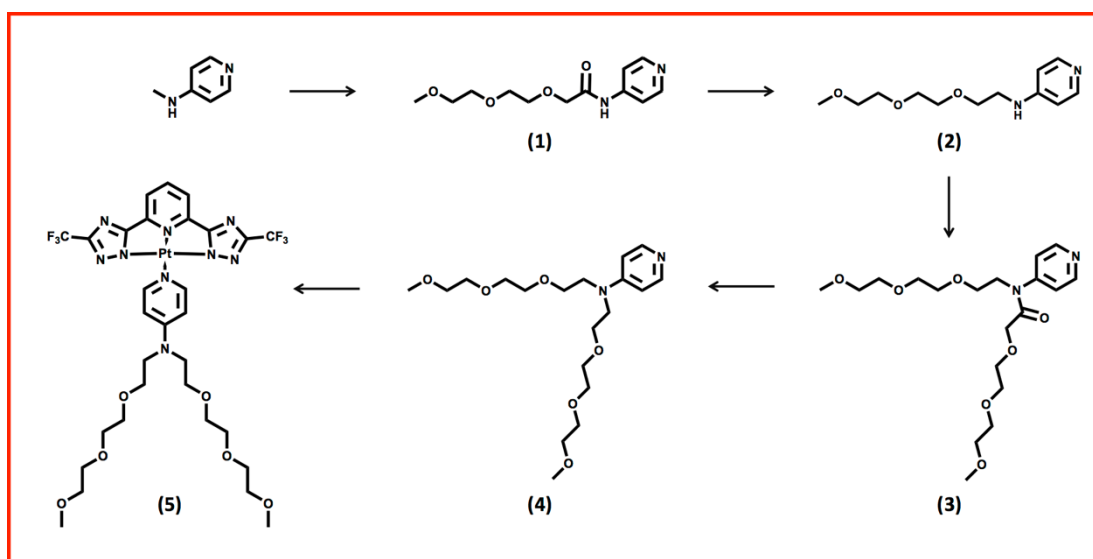


**Figure 2.22.** Schematic synthetic pathway used for the preparation of platinum(II) complex Pt-2PEG.

### *N*-(4-pyridyl)2-[2-(2-methoxyethoxy)ethoxy]acetic acid amide (1)

According to literature procedure,<sup>29</sup> briefly 2-[2-(2-methoxyethoxy)ethoxy]acetic acid (19.88 g, 111.57 mmol) and 4-aminopyridine (7.0 g, 74.38 mmol) were dissolved in 150 mL of  $\text{CHCl}_3$ , then *N,N'*-dicyclohexylcarbodiimide (DCC), (23.0 g, 111.57 mmol) was added in consecutive little aliquots. During the addition, the solution warmed up and a white precipitate was formed. The solution was stirred for one hour at room temperature then refluxed for four hours. After cooling down to room temperature, the solution was filtered and the filtrate concentrated in vacuo. The crude yellow oil was purified by column

chromatography on silica gel using AcOEt to AcOEt:MeOH 9:1 obtaining the pure product as light yellow oil. Yield 12.0 g, 63%.

<sup>1</sup>H NMR (CD<sub>2</sub>Cl<sub>2</sub>, 400 MHz, ppm) δ: 9.04 (s, broad, 1H), 8.51 (d, J = 8 Hz, 2H), 7.62 (d, J = 8Hz, 2H), 4.14 (s, 2H), 3.72–3.80 (m, 6H), 3.60–3.62 (m, 2H), 3.38 (s, 3H); <sup>13</sup>C NMR (CD<sub>2</sub>Cl<sub>2</sub>, 100 MHz, ppm) δ: 169.92, 151.18, 145.10, 114.28, 72.27, 72.00, 71.24, 70.94, 70.52, 59.15. HR-ESI-MS (m/z): C<sub>12</sub>H<sub>18</sub>N<sub>2</sub>O<sub>4</sub> [M+Na]<sup>+</sup>, calcd. 277.115, found 277.115.

*Synthesis of N-(2-(2-(2-methoxyethoxy)ethoxy)ethyl)pyridin-4-amine (2)*

According to literature procedure,<sup>29</sup> briefly under strong nitrogen flux, a solution of **1** (5.5 gr, 21.62 mmol) in anhydrous THF (5 mL) was dropwise added to 30 mL suspension of LiAlH<sub>4</sub> in THF 1 M at 0 °C. After the addition, the ice bath was removed and the mixture was stirred overnight. Then the solution was cooled down at 0 °C and methanol was added slowly (30 mL) under strong flux of nitrogen. The resulting suspension was filtered through a pad of neutral alumina and the filtrate was evaporated under reduced pressure. The product was obtained as yellowish oil purifying the crude by column chromatography on neutral alumina using acetone/10%MeOH as eluent. Yield 2.5 g (48%).

<sup>1</sup>H NMR (CD<sub>2</sub>Cl<sub>2</sub>, 400 MHz, ppm) δ: 8.12 (d, J = 8 Hz, 2H), 6.45 (d, J = 8 Hz, 2H), 4.74 (s, broad, 1H), 3.65–3.70 (m, 2H), 3.64–3.58 (m, 6H), 3.52–3.50 (m, 2H), 3.34–3.28 (m, 5H); <sup>13</sup>C NMR (CD<sub>2</sub>Cl<sub>2</sub>, 100 MHz, ppm) δ: 154.01, 150.53, 108.16, 72.52, 71.02, 70.94, 69.61, 59.18, 42.86. HR-ESI-MS (m/z): C<sub>12</sub>H<sub>20</sub>N<sub>2</sub>O<sub>3</sub> [M+H]<sup>+</sup>, calcd. 241.154, found 241.115.

*2-(2-(2-methoxyethoxy)ethoxy)-N-(2-(2-(2-methoxyethoxy)ethoxy)ethyl)-N-(pyridin-4-yl)acetamide (3)*

Intermediate **2** (1.4 gr, 5.83 mmol) and 2-[2-(2-Methoxyethoxy)ethoxy]acetic acid (2.07 gr, 11.65 mmol) were dissolved in CHCl<sub>3</sub> (30 mL), then N,N'-dicyclohexylcarbodiimide (DCC) (3.6 g, 11.65 mmol) was added in consecutive little aliquots. During the addition, the solution warmed up and a white precipitate was formed. The solution was then refluxed overnight. After cooling down to room temperature, the solution was filtered and the filtrate concentrated in vacuo. The crude yellow oil was purified by column chromatography on neutral allumina with pure DCM then DCM/MeOH 99/1. Yield 1.5 g, 64%.

$^1\text{H}$  NMR ( $\text{CD}_2\text{Cl}_2$ , 400 MHz, ppm)  $\delta$ : 8.6 (d,  $J = 6$  Hz, 2H), 7.27 (d,  $J = 6$  Hz, 2H), 3.97 (s, 2H), 3.87 (t,  $J = 5.5$  Hz, 2H), 3.64–3.45 (m, 18H), 3.32 (s, 3H), 3.31 (s, 3H); ESI-MS ( $m/z$ ):  $\text{C}_{19}\text{H}_{33}\text{N}_2\text{O}_7$   $[\text{M}+\text{H}]^+$ , calcd. 401.23, found 400.9.

*N,N*-bis(2-(2-(2-methoxyethoxy)ethoxy)ethyl)pyridin-4-amine (**4**)

Intermediate **3** (540 mg, 1.35 mmol) dissolved in 2 mL of dry THF was stirred at 0 °C under nitrogen, then borane tetrahydrofuran complex solution (1 M in THF, 3 mL) was added slowly at 0°C and stirred overnight to RT. The reaction was quenched with careful addition of MeOH. After drying the crude was purified on silica with pure ethyl acetate then ethyl acetate MeOH 95/5. Yield 69 mg, 13%.

$^1\text{H}$  NMR ( $\text{CD}_2\text{Cl}_2$ , 400 MHz, ppm)  $\delta$ : 7.97 (d,  $J = 6.7$  Hz, 2H), 6.65 (d,  $J = 6.7$  Hz, 2H), 3.65 (s broad, 8H), 3.59–3.53 (m, 12H), 3.48–3.45 (m, 4H), 3.31 (s, 6H); ESI-MS ( $m/z$ ):  $\text{C}_{19}\text{H}_{35}\text{N}_2\text{O}_6$   $[\text{M}+\text{H}]^+$ , calcd. 387.25, found 386.88

*Platinum Complex: Pt-2PEG (5)*

According to the previous procedure,<sup>29</sup> in a 100 mL round bottom flask the tridentate ligand 2,6-bis(3-(trifluoromethyl)-1H-1,2,4-triazol-5-yl)pyridine (250 mg, 0.71 mmol) and  $\text{PtCl}_2(\text{DMSO})_2$  (302 mg, 0.71 mmol) were dissolved in 50 mL of acetonitrile, then *N,N*-diisopropylethylamine (DIPEA) (249  $\mu\text{L}$ , 1.43 mmol) was added and the resulting suspension stirred for 10 minutes. Compound **4** (331 mg, 0.85 mmol) dissolved in a minimum amount of MeCN was added to the solution and the resulting mixture stirred overnight at 80 °C under nitrogen. Then the solution was dried and extracted with DCM and water, the organic part is then washed with brine and dried with sodium sulfate. The residue is purified on silica pure ethyl acetate then ethyl acetate 5%MeOH. Yield 25 mg 4%.

$^1\text{H}$  NMR ( $\text{CD}_2\text{Cl}_2$ , 400 MHz, ppm)  $\delta$ : 9.07 (d,  $J = 7.2$  Hz, 2H), 8.06 (t,  $J = 7.9$  Hz, 1H), 7.83 (d,  $J = 7.9$  Hz, 2H), 6.81 (d,  $J = 7.2$  Hz, 2H), 3.74 (s broad, 8H), 3.64–3.54 (m, 12H), 3.50–3.45 (m, 4H), 3.31 (s, 6H);  $^{19}\text{F}$  NMR ( $\text{CD}_2\text{Cl}_2$ , 376 MHz, ppm)  $\delta$ : 64.52 (s) HR-ESI-MS ( $m/z$ ):  $\text{C}_{30}\text{H}_{37}\text{F}_6\text{N}_9\text{NaO}_6\text{Pt}$   $[\text{M}+\text{Na}]^+$ , calcd. 951.2313, found: 951.2366.

*Electrochemistry*

The electrochemical characterisations of Pt-Amide, Pt-PEG and Pt-2PEG were performed in MeCN or DCM with 0.1M TBAPF<sub>6</sub> as supporting electrolyte. Pt-2PEG was also tested

in 0.1 M aqueous  $\text{LiClO}_4$ . For electrochemical experiments, a CHI750C Electrochemical Workstation (CH Instruments, Inc., Austin, TX, USA) was used and the experiments were performed in a glass cell under an argon atmosphere. Feedback correction was employed in order to minimise the ohmic drop between the working and reference electrodes. A glassy carbon electrode (GC, 3 mm diameter 66-EE047 Cypress Systems) was employed as the working electrode (WE), while platinum and silver wires were used as counter (CE) and quasi-reference (QRE) electrodes, respectively. The GC electrode was stored in ethanol and polished with a 0.05  $\mu\text{m}$  diamond suspension (Metadi Supreme Diamond Suspension, Buehler) before the experiments, then ultrasonically rinsed with water for 10 minutes and ethanol for 10 minutes. The WE was electrochemically activated in the electrolyte solution by means of several voltammetric cycles at 0.5  $\text{Vs}^{-1}$  between the anodic and cathodic solvent/electrolyte discharges. The RE was separated from the catholyte by glass frits and was calibrated at the end of each experiment against the ferrocene/ferricenium ( $\text{Fc}/\text{Fc}^+$ ) couple, whose formal potential is 0.460 V against KCl-saturated SCE. For reversible and quasi-reversible processes, the standard potentials were calculated as the average value between cathodic and anodic peak potentials.

### *Electrochemiluminescence*

A custom system was used for ECL characterisation, consisting in an electrochemical cell based on screen printed electrodes (Zensor TE100) or glassy carbon (GC-Tokai Inc.) disk electrode (3 mm diameter) as the WE, which were closely facing (a few millimetres) the photomultiplier tube detector (PMT, Hamamatsu, H10723-01, Japan) controlled by an Autolab electrochemical workstation PGSTAT101 (Metrohm, The Netherlands). The RE employed was an Ag/AgCl (1M KCl) from CHI-Instruments and was separated from the catholyte by a glass frit. A platinum wire served as the CE. For potentiodynamic measurements (Cyclic Voltammetry), the solution was scanned at 0.05 V/s from +0.5 V to +1.45 V. For chrononamperometric experiments, the pulsing potential was set at +1.4 V vs Ag/AgCl (1M KCl) with 1 s pulse width. Transients and the faradic currents were managed by using the software NOVA provided with the Autolab unit. The ECL spectrum was acquired using a calibrated electron multiplying charge couple device camera (A-DU970N-UVB Andor technology, Newton EM-CCD) coupled with a spectrograph (Andor Technology, Shamrock 163). The GC working electrode was mechanically cleaned before each run as mentioned above for the electrochemical measurements.

### *Photophysical Measurements*

Absorption spectra were measured on a Shimadzu UV-3600 double-beam UV-Vis-NIR spectrometer and baseline corrected. Steady-state emission spectra were recorded on a HORIBA Jobin–Yvon IBH FL-322 Fluorolog 3 spectrometer equipped with a 450W xenon-arc lamp, double-grating excitation and emission monochromators (2.1 nm/mm dispersion, 1200 grooves/mm blazed at 500 nm) and a TBX-04 detector. Emission and excitation spectra were corrected for source intensity (lamp and grating) and emission spectral response (detector and grating) by standard correction curves. Time-resolved measurements were performed on a PicoQuant FluoTime 300 (PicoQuant GmbH, Germany). Quantum yield measurements were performed with an absolute photoluminescence quantum yield spectrometer Quantaaurus C11347 (Hamamatsu, Japan) exciting the sample at  $\lambda_{\text{exc}} = 300\text{-}500$  nm.

### *SEM analysis*

SEM characterisation was performed employing a FEI scanning electron microscope Quanta FEG 250, at an acceleration voltage of 10 kV. The characterisation was done on SPEs after a plasma-induced deposition of a 5-nm thick layer of Au.

### *TEM analysis*

Transmission Electron Microscopy (TEM) images were obtained with a Jeol-JEM 2011 system operated at 200 kV equipped with a Cs-probe corrector and a GIF Tridiem filter. Drop cast of Pt-Amide from water solution on a lacey carbon grid was used as general procedure.

## **2.7 REFERENCES**

- (1) Houlding, V. H.; Miskowski, V. M. *Coord. Chem. Rev.* **1991**, *111* (1), 145.
- (2) Pyykkö, P. *Chem. Rev.* **1997**, *97* (3), 597.
- (3) Roundhill, D. M.; Gray, H. B.; Che, C. M. *Acc. Chem. Res.* **1989**, *22* (2), 55.
- (4) Lehn, J.-M. *Angew. Chem. Int. Ed.* **1990**, *29* (11), 1304.
- (5) Lehn, J.-M. *Supramol. Chem. Self-Assembly* **2002**, 295, 2400.
- (6) Whitesides, G. M.; Grzybowski, B. *Science*. **2002**, *295* (5564), 2418.
- (7) Vezzu, D. A. K.; Lu, Q.; Chen, Y. H.; Huo, S. *J. Inorg. Biochem.* **2014**, *134*, 49.

- (8) Cusumano, M.; Di Pietro, M. L.; Giannetto, A. *Inorg. Chem.* **2006**, *45* (1), 230.
- (9) Ratilla, E. M. A.; Brothers II, H. M.; Kostic, N. M. *J. Am. Chem. Soc.* **1987**, *109* (4), 4592.
- (10) Strassert, C. A.; Chien, C. H.; Galvez Lopez, M. D.; Kourkoulos, D.; Hertel, D.; Meerholz, K.; De Cola, L. *Angew. Chem. - Int. Ed.* **2011**, *50* (4), 946.
- (11) Taneda, M.; Yasuda, T.; Adachi, C. *Appl. Phys. Express* **2011**, *4* (7).
- (12) Chen, Y.; Li, K.; Lu, W.; Chui, S. S. Y.; Ma, C. W.; Che, C. M. *Angew. Chem. - Int. Ed.* **2009**, *48* (52), 9909.
- (13) Che, C.-M.; Chow, C.-F.; Yuen, M.-Y.; Roy, V. A. L.; Lu, W.; Chen, Y.; Chui, S. S.-Y.; Zhu, N. *Chem. Sci.* **2011**, *2* (2), 216.
- (14) Yuen, M. Y.; Roy, V. A. L.; Lu, W.; Kui, S. C. F.; Tong, G. S. M.; So, M. H.; Chui, S. S. Y.; Muccini, M.; Ning, J. Q.; Xu, S. J.; Che, C. M. *Angew. Chem. - Int. Ed.* **2008**, *47* (51), 9895.
- (15) Chen, Z.; Wong, K. M.; Kwok, E. C.; Zhu, N.; Zu, Y.; Yam, V. W. *Inorg. Chem.* **2011**, *50*, 2125.
- (16) Li, C.; Wang, S.; Huang, Y.; Zheng, B.; Tian, Z.; Wen, Y.; Li, F. *Dalt. Trans.* **2013**, *42*, 4059.
- (17) Reid, E. F.; Cook, V. C.; Wilson, D. J. D.; Hogan, C. F. *Chem. A Eur. J.* **2013**, *19*, 15907.
- (18) Tokel-Takvoryan, N. E.; Bard, A. J. *Chem. Phys. Lett.* **1974**, *25* (2), 235.
- (19) Kim, J.; Fan, F. F.; Bard, A. J.; Che, chi-M.; Gray, B. *Chem. Phys. Lett.* **1985**, *121* (6), 543.
- (20) Kane-Maguire, N. A. P.; Wright, L. L.; Guckert, J. A.; Tweet, W. S. *Inorg. Chem.* **1988**, *27* (17), 2905.
- (21) Canty, P.; Väre, L.; Håkansson, M.; Spehar, A. M.; Papkovsky, D.; Ala-Kleme, T.; Kankare, J.; Kulmala, S. *Anal. Chim. Acta* **2002**, *453* (2), 269.
- (22) Liu, Z.; Qi, W.; Xu, G. *Chem. Soc. Rev.* **2015**, *44* (10), 3117.
- (23) Fernandez-Hernandez, J. M.; Longhi, E.; Cysewski, R.; Polo, F.; Josel, H.-P.; De Cola, L. *Anal. Chem.* **2016**, *88* (8), 4174.
- (24) Barbante, G. J.; Doeven, E. H.; Francis, P. S.; Stringer, B. D.; Hogan, C. F.; Kheradmand, P. R.; Wilson, D. J. D.; Barnard, P. J. *Dalt. Trans.* **2015**, *44* (18), 8564.



- (25) Bard, A. J. *Electrogenerated Chemiluminescence*; Marcel Dekker, Inc.: New York., **2004**.
- (26) Hong, Y.; Lam, J. W. Y.; Tang, B. Z. *Chem. Soc. Rev.* **2011**, *40* (11), 5361.
- (27) Mydlak, M.; Mauro, M.; Polo, F.; Felicetti, M.; Leonhardt, J.; Diener, G.; Cola, L. De; Strassert, C. A.; Neutral, A.; Ii, P. *Chem. Mater.* **2011**, *23*, 3659.
- (28) Sinn, S.; Biedermann, F.; Vishe, M.; Aliprandi, A. *ChemPhysChem* **2016**, *17*, 1829.
- (29) Aliprandi, A.; Mauro, M.; Cola, L. De. *Nat. Chem.* **2016**, *8* (January), 10.
- (30) Ma, B.; Li, J.; Djurovich, P. I.; Yousufuddin, M.; Bau, R.; Thompson, M. E. *J. Am. Chem. Soc.* **2005**, *127* (1), 28.
- (31) Mauro, M.; Aliprandi, A.; Cebrián, C.; Wang, D.; Kübel, C.; De Cola, L. *Chem. Commun.* **2014**, *50* (55), 7269.
- (32) Aliprandi, A.; Genovese, D.; Mauro, M.; De Cola, L. *Chem. Lett.* **2015**, *44* (9), 1152.
- (33) Septiadi, D.; Aliprandi, A.; Mauro, M.; De Cola, L. *RSC Adv.* **2014**, *4* (49), 25709.
- (34) Funabiki, K.; Noma, N.; Kuzuya, G.; Matsui, M.; Shibata, K. *J. Chem. Res.* **1999**, No. 5, 300.
- (35) Huixia, X.; Yan, Y.; Litao, Q.; Yuying, H.; Hua, W.; Liuqing, C.; Bingshe, X. *Dye. Pigment.* **2013**, *99* (1), 67.
- (36) Cebrián, C.; Mauro, M.; Kourkoulos, D.; Mercandelli, P.; Hertel, D.; Meerholz, K.; Strassert, C. A.; De Cola, L. *Adv. Mater.* **2013**, *25* (3), 437.
- (37) Yam, V. W. W.; Wong, K. M. C.; Zhu, N. *J. Am. Chem. Soc.* **2002**, *124* (23), 6506.
- (38) Po, C.; Tam, A. Y. Y.; Wong, K. M. C.; Yam, V. W. W. *J. Am. Chem. Soc.* **2011**, *133* (31), 12136.
- (39) Krikorian, M.; Liu, S.; Swager, T. M. *J. Am. Chem. Soc.* **2014**, *136* (8), 2952.
- (40) Li, C.; Wang, S.; Huang, Y.; Zheng, B.; Tian, Z.; Wen, Y.; Li, F. *Dalt. Trans.* **2013**, *42* (11), 4059.
- (41) Uson, R.; Fornies, J.; Tomas, M.; Casas, J. M.; Cotton, F. A.; Falvello, L. R.; Feng, X. *J. Am. Chem. Soc.* **1993**, *115*, 4145.
- (42) Bontchev, P. R.; Mitewa, M.; Geutcheva, G. *Pure Appl. Chem.* **1989**, *61* (5), 897.
- (43) Stephen, E.; Blake, A. J.; Davies, E. S.; McMaster, J.; Schröder, M. *Chem. Commun. (Camb).* **2008**, 5707.
- (44) O'Halloran, T. V.; Lippard, S. J. *Isr. J. Chem.* **1985**, *25* (2), 130.

- (45) Wilson, J. J.; Lippard, S. J. *Inorg. Chem.* **2012**, *51* (18), 9852.
- (46) Zanarini, S.; Rampazzo, E.; Bonacchi, S.; Juris, R.; Marcaccio, M.; Montalti, M.; Paolucci, F.; Prodi, L. *J. Am. Chem. Soc.* **2009**, *131* (40), 14208.
- (47) Wilson, J. J.; Lippard, S. J. *Chem. Rev.* **2014**, *114* (8), 4470.
- (48) Genovese, D.; Aliprandi, A.; Prasetyanto, E. A.; Mauro, M.; Hirtz, M.; Fuchs, H.; Fujita, Y.; Uji-I, H.; Lebedkin, S.; Kappes, M.; De Cola, L. *Adv. Funct. Mater.* **2016**, *26* (29), 5271.
- (49) Sagara, Y.; Kato, T. *Nat. Chem.* **2009**, *1* (8), 605.
- (50) Zhang, X.; Chi, Z.; Zhang, Y.; Liu, S.; Xu, J. *J. Mater. Chem. C* **2013**, *1* (21), 3376.
- (51) Sun, H.; Liu, S.; Lin, W.; Zhang, K. Y.; Lv, W.; Huang, X.; Huo, F.; Yang, H.; Jenkins, G.; Zhao, Q.; Huang, W. *Nat. Commun.* **2014**, *5* (April), 3601.
- (52) Okazaki, M.; Takeda, Y.; Data, P.; Pander, P.; Higginbotham, H.; Monkman, A. P.; Minakata, S. *Chem. Sci.* **2017**, *0*, 1.
- (53) Miao, W.; Choi, J.-P.; Bard, A. J. *J. Am. Chem. Soc.* **2002**, *124* (48), 14478.
- (54) Factor, B.; Muegge, B.; Workman, S.; Bolton, E.; Bos, J.; Richter, M. M. *Anal. Chem.* **2001**, *73* (19), 4621.
- (55) Workman, S.; Richter, M. M. *Anal. Chem.* **2000**, *72* (22), 5556.



# Chapter 3

## **Solid-state ECL Films based on Iridium(III) Complexes**

### **Abstract**

Solid-state electrochemiluminescence (ECL) based on  $\text{Ru}(\text{bpy})_3^{2+}$  system has been widely explored for biosensing purposes. In order to broaden the scope of solid-state ECL, iridium(III) complexes were chosen as new ECL probes due to their outstanding luminescent properties and tunable emission wavelength. In this chapter, the synthesis of a novel electropolymerizable Ir(III) complex is reported, and its use in the facile preparation of a bright solid ECL emitting surface is described.

### 3.1 INTRODUCTION

Iridium complexes have been widely used in many applications such as OLED, catalysis, water splitting and solar cells.<sup>1-4</sup> Their remarkable luminescent properties originate from their high quantum efficiency, long excited state lifetime, large Stock shift, and emission wavelength that is tunable from blue to red through a tailored ligand design. In particular, research on blue emitting iridium(III) complexes plays a crucial role in OLED study nowadays.<sup>5</sup>

The use of Ir (III) complexes for chemo- and ECL-based sensing has only recently gained momentum. Despite their excellent luminescence characteristics, issues such as oxygen quenching and poor solubility in aqueous media have posed significant challenges to the development of sensing applications for ECL-active iridium complexes. However, their significant potential and unique properties continue to drive researchers to overcome these issues.

The majority of early ECL systems involved solubilised species with emission occurring in the diffusion layer near the electrode surface. The advent of chemically modified electrodes allowed ECL to be generated in - or from - films constrained to the surface of an electrode. The ability to modify electrode surfaces with ECL-producing complexes has greatly increased the potential of ECL applications within biomedical sensor design.

Immobilisation of  $\text{Ru}(\text{bpy})_3^{2+}$  on the electrode to develop regenerable solid-state ECL sensors has attracted significant interest, and many different methods and materials have been reported.<sup>6-9</sup> To cite a few examples: the use of Nafion as an ion exchange matrix for the luminophore,<sup>10,11</sup> synthesis and drop casting of electrochemiluminescent metallopolymer on electrodes,<sup>12</sup> electropolymerisation of an electrochemiluminescent compound on the electrode,<sup>13</sup> electrografting of complexes directly on the electrode,<sup>14</sup> immobilisation of the luminophore on indium tin oxide electrode via citrate-capped gold nanoparticles,<sup>15</sup> as well as encapsulation into ultrathin Langmuir-Shaefer<sup>16</sup> and Langmuir-Blodgett Nafion films.<sup>17</sup>

One of the first approaches for immobilisation of  $\text{Ru}(\text{bpy})_3^{2+}$  was the loading in Nafion films.<sup>10</sup> Nafion is a perfluorinated, sulfonated ion-exchange polymer with excellent chemical and mechanical stability. Therefore, it was largely used for polymer-modified electrodes and  $\text{Ru}(\text{bpy})_3^{2+}$  was immobilised through electrostatic interactions. Nevertheless,

its use is actually limited by the instability in the long term. When it is stored overnight in PBS buffer a decrease of the ECL intensity can be observed, likely due to the partitioning of  $\text{Ru}(\text{bpy})_3^{2+}$  into hydrophobic regions of Nafion.<sup>18</sup>

Electropolymerised  $\text{Ru}(\text{vinyl-bpy})_3^{2+}$ -modified electrodes, have attractive ECL properties<sup>19,20</sup> but their use in analytical applications is limited due to inhibited mass transport and poor analyte permeation.

$\text{Ru}(\text{bpy})_3^{2+}$  immobilisation in silica sol-gel films has been also reported.  $\text{Ru}(\text{bpy})_3^{2+}$  and TPrA were trapped in a porous silicate host matrix providing high optical quality, good photochemical and electrochemical stability.<sup>21</sup> An important requirement was that the ECL gel-entrapped chemiluminescent precursors were able to diffuse and react in the gel at the local scale. Depending on the preparation procedure, thin (~200 nm) silica films can be also obtained, allowing both rapid diffusion of the complex molecule to and from the electrode surface and rapid permeation of the analyte from the external solution.  $\text{Ru}(\text{bpy})_3^{2+}$  can be also covalently incorporated within the silica. This leads to the formation of  $\text{Ru}(\text{bpy})_3^{2+}$  gel film that was used to develop stable and sensitive ECL sensors.<sup>22</sup>

Another approach consisted in the adsorption of metallopolymeric films onto the surface of the electrode. Dennany, Forster and Rusling reported direct ECL detection of DNA in 10 nm-thick films of  $\text{Ru}(\text{bpy})_2(\text{PVP})_{10}^{2+}$  cationic polymer and DNA prepared using layer-by-layer deposition.<sup>23</sup> The system was applied to detect DNA hybridisation or damage. Furthermore, the same ruthenium metallopolymer was previously used for detection of oxalates in a flow injection analysis system.<sup>24</sup>

The same group also reported that ECL can be obtained directly from the reaction of oxidised guanines of DNA in thin films using the catalytic metallopolymer  $\text{Os}(\text{bpy})_2(\text{PVP})_{10}^{2+}$ .<sup>25</sup> Moreover, the combination of the latter with  $\text{Ru}(\text{bpy})_2(\text{PVP})_{10}^{2+}$  within the films allowed the simultaneous detection of both chemical and oxidative DNA damage.<sup>25</sup>

Solid state ECL is mostly based on the use  $\text{Ru}(\text{bpy})_3^{2+}$ , and only few iridium(III) complexes have been tested using a method that allows modify the working electrode.<sup>26-29</sup> These methods all rely on the direct immobilisation of iridium(III) complexes by adsorption onto the electrode surface<sup>26-28</sup> or its immobilisation after encapsulation in organosilica

nanoparticles.<sup>29</sup> As far as we are aware, there are no reports on the electropolymerisation of such complexes on electrode surfaces.

Reductive electropolymerisation of vinyl-substituted polypyridine transition-metal complexes is a well-established method for the in-situ deposition of metallopolymeric films on electrode surfaces,<sup>19,20,30-32</sup> and Ir(III) complexes bearing one or more vinyl groups on the ligand backbone are suitable candidates for electropolymerisation.<sup>31</sup>

Hence, we herein report the synthesis of a novel iridium(III) complex bearing a vinyl moiety, the procedure of its electrodeposition as well as its photophysical, electrochemical and ECL properties in solution and after electropolymerisation onto Pt and Fluorine doped Thin Oxide (FTO) surface. We demonstrate the simplicity of the method to obtain robust and stable solid-state device usable of ECL purposes.

### 3.2 SYNTHESIS OF Ir(pphen)<sub>2</sub>(mVbpy)

The synthesis of iridium dimer in figure 3.1 (reagent) was achieved by modification of a previous report (See 3.7 Experimental Section for detail).<sup>33</sup> The iridium dimer was refluxed for 18 hours with two equivalent of 4-methyl-4'-vinyl-2,2'-bipyridine (N<sup>^</sup>N) in 2-ethoxyethanol/water (3:1, v/v). After column chromatography and recrystallization, orange-brown iridium complex was obtained with 90% product yield, and characterised by <sup>1</sup>H NMR, mass spectrometry and elemental analysis (See 3.7 Experimental Section for detail).

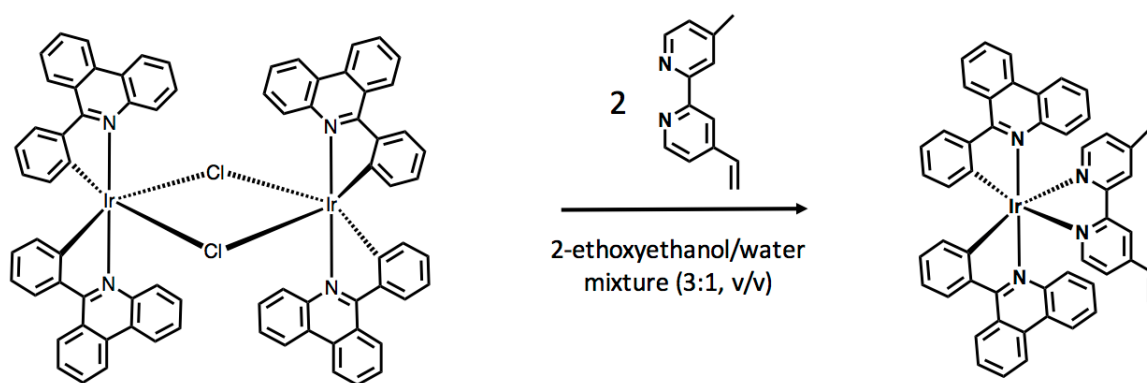


Figure 3.1. Scheme of synthesis of Ir(pphen)<sub>2</sub>(mVbpy).

### 3.3 ABSORPTION AND EMISSION SPECTROSCOPY

The UV-vis absorption spectrum of Ir(pphen)<sub>2</sub>(mVbpy) was recorded on a 10<sup>-5</sup> M solution in CH<sub>3</sub>CN at room temperature (Figure 3.21, black trace) and Table 3.1. The absorption

band at 250 nm can be assigned to the ligand-centered ( $^1\text{LC}$ )  $^1\pi\text{-}\pi^*$  transition, while the broad band at 300-400 nm can be ascribed to singlet-manifold ligand-to-ligand charge transfer ( $^1\text{LLCT}$ ) and metal-to-ligand charge transfer ( $^1\text{MLCT}$ ) transitions. The less intense band centered at ca450 nm can be instead attributed to singlet and triplet metal-to-ligand charge transfer transition ( $^1\text{MLCT}$  and  $^3\text{MLCT}$ ) respectively. The absorption band extends up to 525 nm due to the presence of large conjugated ligands ( $\text{C}^{\wedge}\text{N}$ ).

The emission spectra were recorded on samples at concentration of  $10^{-5}$  M in aerated and degassed  $\text{CH}_3\text{CN}$  (Figure 3.2, red trace and Table 3.1). The complex exhibits red emission in both aerated and degassed solutions with  $\lambda_{\text{max}}$  at 650 nm.

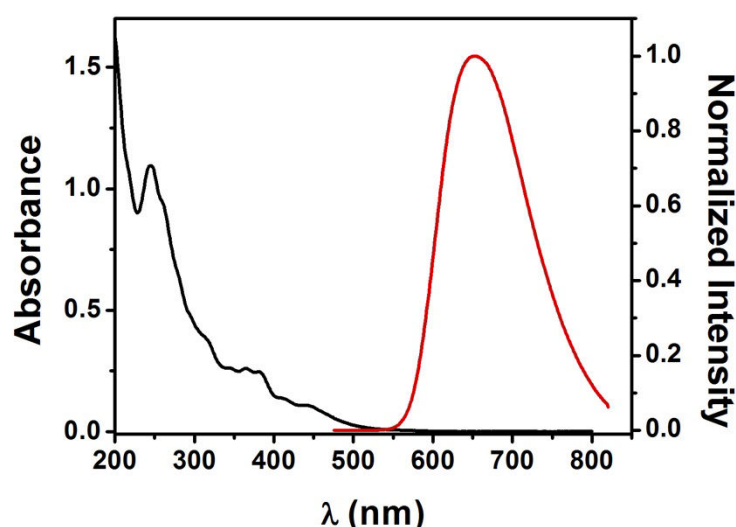


**Figure 3.2.** UV-Vis and emission spectra of  $\text{Ir}(\text{pphen})_2(\text{mVbpy})$ . The measurements were performed on  $10^{-5}$  M  $\text{CH}_3\text{CN}$  solution.

Generally, bis-cyclometalated Ir(III) compounds such as  $[\text{Ir}(\text{C}^{\wedge}\text{N})_2(\text{L}^{\wedge}\text{X})]$  ( $\text{L}^{\wedge}\text{X}$  = pic or acac) exhibit room-temperature phosphorescence spectra that have a character mainly metal to ligand charge transfer. The energy of the emission is dictated by the LUMO and HOMO localised on the  $\text{Ir}(\text{C}^{\wedge}\text{N})_2$  fragment, when the energy gap of the  $\text{L}^{\wedge}\text{X}$  ligand is sufficiently higher compared to the  $\text{C}^{\wedge}\text{N}$  ligand.<sup>34,35</sup> Therefore, the substitution of the cyclometalated ligand with a more extended  $\pi$ -electron system of the N-heterocycle causes a red shift on the emission wavelengths compared to the analogous phenylpyridine complex, centered at 596 nm.<sup>31</sup> The excited state lifetime ( $\lambda_{\text{exc}}$  at 405 nm) in deaerated solutions showed a monoexponential decay it was found to be 2.6  $\mu\text{s}$  (Table 3.1), a value typical for this type of complexes.<sup>34-36</sup> Photoluminescence emission quantum yield (PLQY)



in deaerated CH<sub>3</sub>CN is 25% and it results with a lower PLQY due to the “energy gap law” comparing to other similar complexes,<sup>37</sup> since it is red-shifted.

In aerated solutions, both the excited state lifetime and the PLQY decrease, compared with the deaerated conditions, due to the triplet nature of the emitting state quenched by dioxygen.

**Table 3.1.** Photophysical data for Ir(pphen)<sub>2</sub>(mVbpy) in both aerated and degassed conditions. The measurements were performed on 10<sup>-5</sup> M CH<sub>3</sub>CN solution.

	$\lambda_{\text{abs}}$ (nm)	$\lambda_{\text{em}}$ (nm)	t (ns) ( $\chi^2=1$ )	PLQY (%)
<b>ACN (aer)</b>	245, 364, 380, 416, 445	650	305	4
<b>ACN (degas)</b>		650	2594	25

### 3.4 REDUCTIVE ELECTROPOLYMERISATION OF Ir(pphen)<sub>2</sub>(mVbpy)

In order to assess the redox properties of Ir(pphen)<sub>2</sub>(mVbpy), cyclic voltammetry measurements were performed before the electrodeposition process. Two different working electrodes were employed, Pt and Fluorine doped Tin Oxide (FTO), even though no differences were visible during the potential scan. Results are shown in Figure 3.3. In acetonitrile, consistent with the previous report,<sup>37</sup> we observed an irreversible peak at +1.08 V vs SCE, related to the oxidation of Ir<sup>3+/4+</sup>, while a new small peak emerges at +1.28 V vs SCE and it could be associated to the ancillary ligand oxidation, as reported elsewhere.<sup>31</sup> In reduction, the peaks at -1.67 V and -2.10 V vs SCE can be associated to the N-heterocyclic rings of the cyclometalated ligand and to the ancillary ligand.<sup>31,35</sup> The current intensity on FTO results higher than on Pt most probably due to larger electrode area, exactly 0.42 cm<sup>2</sup> and 0.0314 cm<sup>2</sup> respectively.

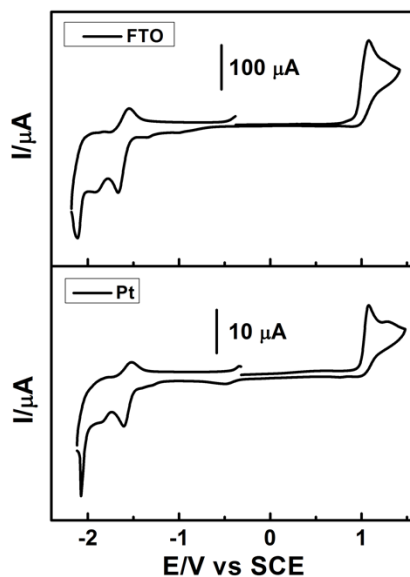


**Figure 3.3.** CVs of 1 mM  $\text{Ir}(\text{pphen})_2(\text{mVbpy})$  in  $\text{CH}_3\text{CN}$ , using 0.1 M  $\text{TBAPF}_6$  as supporting electrolyte and FTO (upper part) or Pt (bottom part) as working electrode. Scan rate  $0.1 \text{ V s}^{-1}$ .

Encouraged by the similar response during a potential scan, both Pt and FTO electrodes were chosen for electropolymerisation process. When a clean electrode is placed into a degassed solution of  $\text{Ir}(\text{pphen})_2(\text{mVbpy})$  in 0.1 M  $\text{TBAPF}_6/\text{CH}_3\text{CN}$  and the potential is scanned between  $-0.98 \text{ V}$  and  $-2.2 \text{ V}$  vs SCE, the electrochemical waves at  $-1.67 \text{ V}$  and  $-2.11 \text{ V}$  gradually start to grow, as shown in Figure 3.4. This is true except for the first reduction peak on FTO electrode. This peak decreases from the 1<sup>st</sup> scan to the 15<sup>th</sup>, while it starts to grow again from the 16<sup>th</sup> on with a shift in potential, as it is shown in Figure 3.5. This suggests that during the potential scans chemical reactions take place. It is also supported by the fact that during polymerisation, the growth cycles are characterised by an enhanced oxidation current at  $-1.55 \text{ V}$  vs SCE suggesting that there may be a catalytic electrochemical/chemical reaction taking place only on FTO surface.<sup>38</sup> All the peaks show a shift to higher potential in absolute value indicating an increased difficulty in reducing the species on the electrode surface.

Currents on the first potential cycle are quite small, then they increase with an increasing number of voltammetric scans.

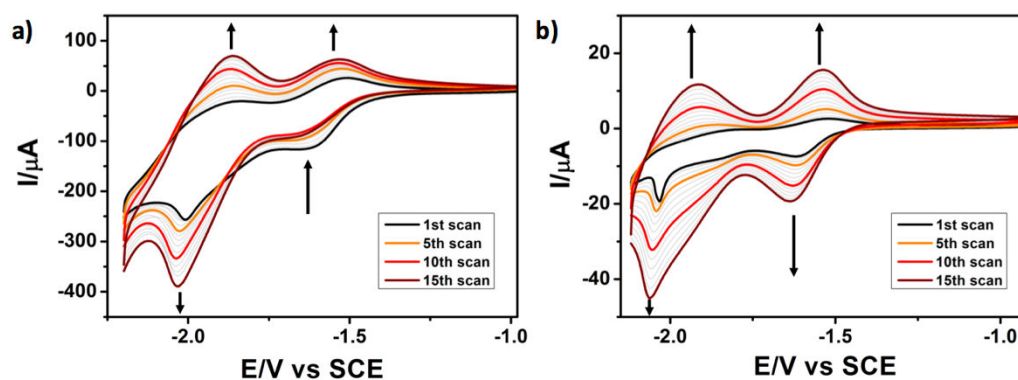


**Figure 3.4.** Interfacial electropolymerisation from a 1 mM solution of  $\text{Ir}(\text{pphen})_2(\text{mVbpy})$  on **a)** FTO electrode ( $A=0.42\text{ cm}^2$ ), **b)** Pt electrode ( $A=0.0314\text{ cm}^2$ ) for 15 scans at a scan rate of  $0.1\text{ V s}^{-1}$ . The deposition medium was  $0.1\text{ M TBAPF}_6$  in  $\text{CH}_3\text{CN}$ .

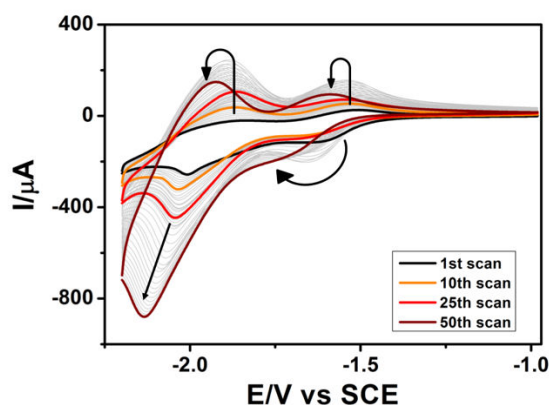


**Figure 3.5.** Interfacial electropolymerisation from a 1 mM solution of  $\text{Ir}(\text{pphen})_2(\text{mVbpy})$  on FTO electrode ( $A=0.42\text{ cm}^2$ ) for 50 scans at a scan rate of  $0.1\text{ V s}^{-1}$ . The deposition medium was  $0.1\text{ M TBAPF}_6$  in  $\text{CH}_3\text{CN}$ .

Deposition of a polymeric electroactive film of the complex, **poly-Ir**, on the electrode surface, which gives rise to the larger currents, is demonstrated by transferring the electrodes, after thorough rinsing, to clean supporting electrolyte solution, where reduction and oxidation waves (Figure 3.6) remain observable.

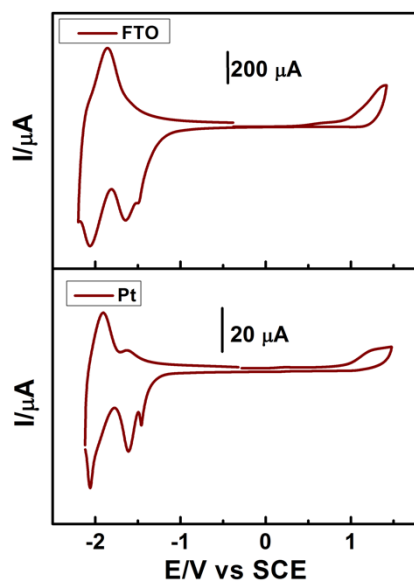


**Figure 3.6.** CVs of poly-Ir on FTO (upper part) or Pt (bottom part) in  $\text{CH}_3\text{CN}$ , using  $0.1 \text{ M TBAPF}_6$  as supporting electrolyte. Scan rate  $0.1 \text{ V s}^{-1}$ .

Many more electroactive sites are present in the films than in a monomolecular layer. In order to determine whether an increase of the number of scan cycles would increase the thickness of the formed film, the number of scans cycles was increased keeping the  $\text{Ir}(\text{pphen})_2(\text{mVbpy})$  concentration constant. Each time, after the set number of scans, the electrode was removed from the cell, thoroughly washed and placed in a cell containing blank electrolyte solution. The surface coverage  $\Gamma$  of the electrodeposited film, in each case, was determined at  $0.1 \text{ Vs}^{-1}$  using Equation 3.1 (see experimental section 3.7). The various surface coverages obtained for different scan numbers using the 2<sup>nd</sup> reduction peak is given in Table 3.2.

**Table 3.2.** Apparent film coverages for the reductive electropolymerisation of  $\text{Ir}(\text{pphen})_2(\text{mVbpy})$  on FTO and Pt electrodes with different numbers of scan cycles at scan rate  $0.1 \text{ V s}^{-1}$ .

	$\Gamma \text{ (nmolcm}^{-2}\text{) on FTO}$	$\Gamma \text{ (nmolcm}^{-2}\text{) on Pt}$
<b>1<sup>st</sup> scan</b>	1.52	0.42
<b>5<sup>th</sup> scan</b>	1.70	0.61
<b>10<sup>th</sup> scan</b>	1.85	0.95
<b>15<sup>th</sup> scan</b>	2.17	1.20

The coverage of deposited polymer can be readily and reproducibly adjusted by varying the number of cyclical potential scans and sweep rate. The increment of polymer per scan is approximately constant for both electrodes as shown in Figure 3.7.

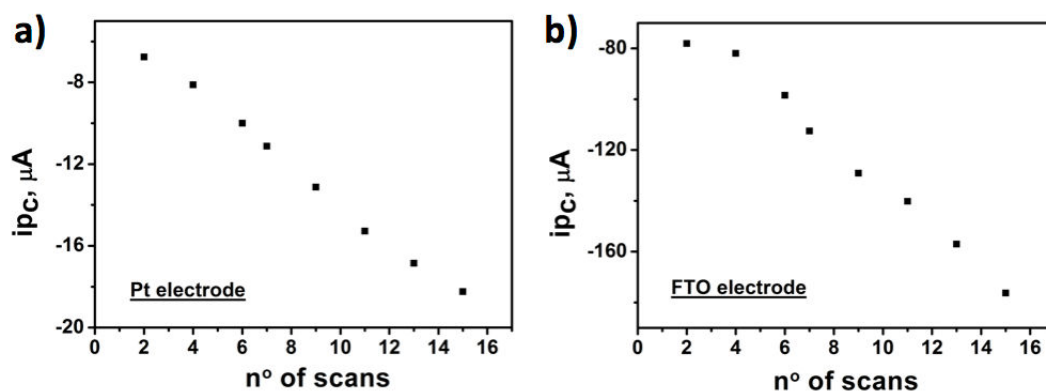


**Figure 3.7.** Peak current as a function of number of scans for **a)** Pt electrode (1<sup>st</sup> reduction peak), **b)** FTO electrode (2<sup>nd</sup> reduction peak). Data collected from graphs in Figure 3.4.

Electrodeposition can be carried out as well potentiostatically. We did not observe any substantial difference in the electrochemistry of potential scanning and potentiostatically deposited films, however some differences in the structure may exist.

The electrode surfaces appear yellow-brown after polymerisation and this color is due to optical absorbance (Figure 3.8a). Under UV lamp, the surface emits an intense red light, typical of the iridium complex employed (Figure 3.8b). Then photophysical characterisation of the FTO coated electrode have been carried out to point out the optical properties of the new poly-Ir (Figure 3.8c).

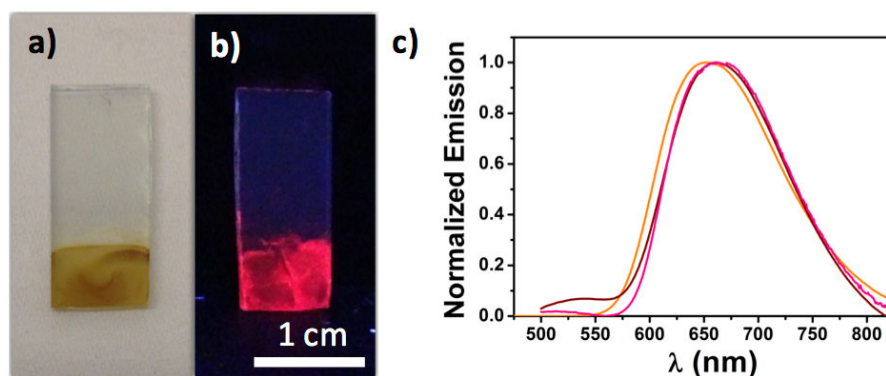


**Figure 3.8.** **a)** Electropolymerised FTO electrode after 15 scans, **b)** under UV lamp, **c)** emission spectra of  $10^{-5}$  M  $\text{Ir}(\text{pphen})_2(\text{mVbpy})$  in  $\text{CH}_3\text{CN}$  (orange trace), poly-Ir on FTO electrode after 15 scans (brown trace) and poly-Ir on FTO electrode after 50 scans (pink trace).  $\lambda_{\text{exc}} = 450$  nm.

It is worth noticing that the emission peak of the iridium complex shift from 650 nm to 662 nm (for the film after 15 cycles) to 676 nm (for the film after 50 cycles). Also, the PLQY decreases drastically, down to 2.9 % after 15 cycles and <1 % after 50 cycles. This is a typical effect observed when the iridium complex is deposited on thin films and the latter acquire more rigidity.<sup>39</sup>

### 3.5 ECL PROPERTIES OF Ir(pphen)<sub>2</sub>(mVbpy) AND POLY-Ir

One of the key objectives of this work was to investigate if electropolymerised film exhibits any ECL respect to the iridium complex in solution and to prove that it does not deteriorate after several cycles, supporting its use for solid-state ECL sensors.

The ECL signal of the monomer Ir(pphen)<sub>2</sub>(mVbpy) was recorded in CH<sub>3</sub>CN at a GC electrode by sweeping to positive potentials in presence of TPrA at low concentration (10 mM) as co-reactant. During the anodic potential scan (Figure 3.9a), the emission rises at +0.75 V vs SCE to peak at +1.20 V vs SCE, indicating oxidation of both TPrA ( $E_{ox} \sim +0.85$  V vs SCE) and iridium complex ( $E_{ox} \sim +1.1$  V vs SCE). A representative ECL emission spectrum is shown in Figure 3.9b. It is similar to the PL spectrum reported in Figure 3.2-3.8c (orange trace). Therefore, the same MLCT excited state is formed using both photoexcitation and electrochemistry.

After electropolymerisation on FTO, the ECL properties of the new formed film were investigated immersing it into a 0.1 M LiClO<sub>4</sub> water solution in presence as well of 10 mM TPrA. It is important to notice that the medium in which ECL experiments were carried out is typical of biosensing media. Poly-Ir demonstrated dramatically lower ECL emission than the monomer during a potential scan (Figure 3.9c), although the intensity is still considerable. This could be due to the rigidity of complexes onto the surface that generally decrease the luminescence yield, as we already discussed in section 3.4.<sup>39</sup> Finally, Figure 3.9d shows the ECL intensity from the poly-Ir film under continuous potential scanning for 10 cycles. The response loses out an intensity drop of almost 50 % within the first 3 cycles then it settles to a constant value, suggesting that improvements on its emission stability have to be done in order to use it for biosensing applications. Nevertheless, the proof of principle of its functioning is clearly demonstrated.

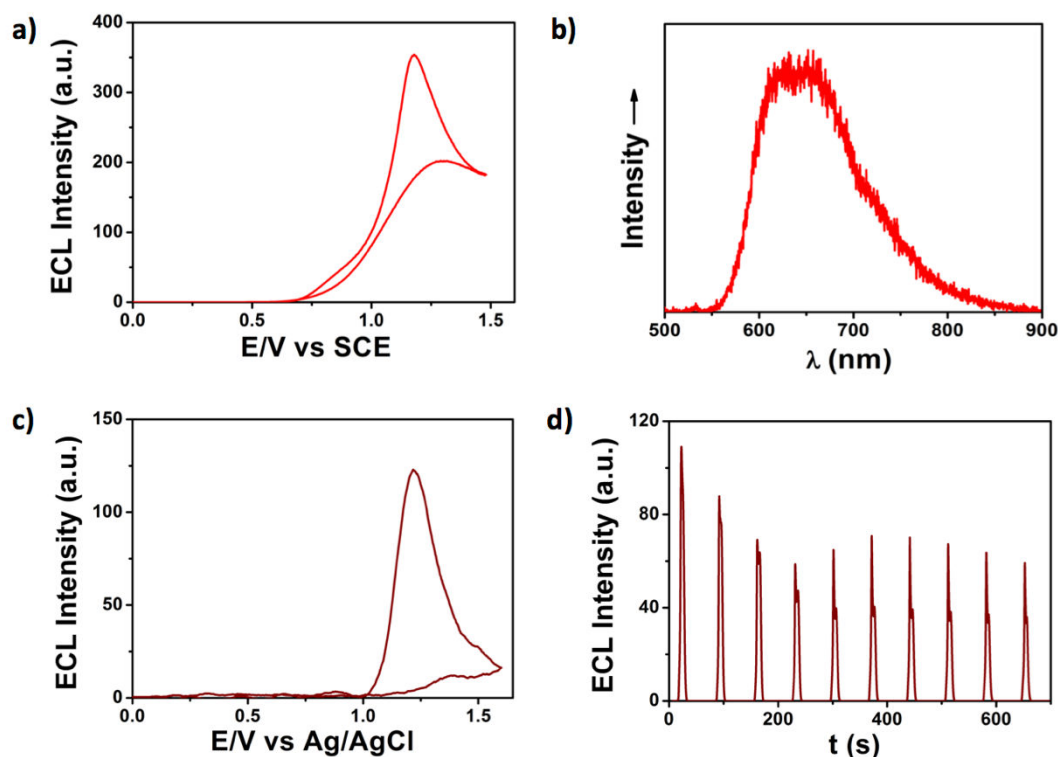


**Figure 3.9.** **a)** ECL intensity during a potential scan at  $0.05 \text{ V s}^{-1}$  and **b)** ECL emission spectrum of  $1 \text{ mM CH}_3\text{CN}$  solution of  $\text{Ir}(\text{pphen})_2(\text{mVbpy})$  upon addition of  $10 \text{ mM TPrA}$  at a GC electrode; **c)** ECL intensity during a potential scan of poly-Ir film on FTO electrode at  $0.05 \text{ V s}^{-1}$  and **d)** ECL response obtained during a continuous potential scan between  $+1.25 \text{ V}$  and  $-0.9 \text{ V}$ . (10 cycles under scan rate  $0.05 \text{ V/s}$ ) upon addition of  $10 \text{ mM TPrA}$ .

### 3.6 CONCLUSIONS

The synthesis of a new cyclometalated iridium complex based on phenyl phenanthridine and methyl-vinyl-bipyridine, as well as its photophysical properties and its electropolymerisation onto different electrode surfaces was explored. In particular, the results have shown that electropolymerisation proceeds in acetonitrile and smooth emitting films, which cover the entire electrode surface, can be obtained. Surface coverage calculation proved that it increases with the number of scans. This electropolymerised film exhibit considerable ECL when oxidised together with TPrA, which acts as co-reactant. However, its ECL emission decreases over the cycles, showing up that it is still necessary an attentive work to render the film more stable in terms of emission.

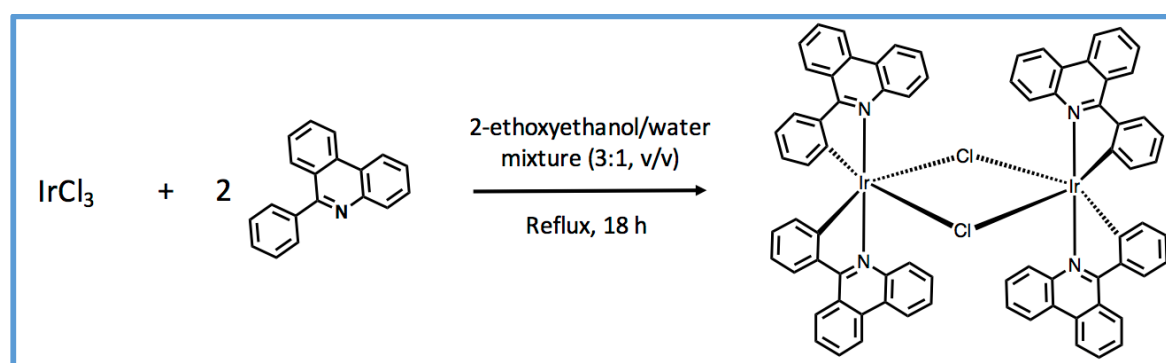
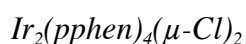
### 3.7 EXPERIMENTAL DETAILS

#### *General information and materials*

All the reagents were used as received from commercial sources, unless otherwise stated. The ligand 6-phenylphenanthridine (pphen) was purchased from SYNTHON Chemicals-GmbH. Ligand 4-methyl-4'-vinyl-2,2'-bipyridine (mVbpy) was purchased from Ark Pharm, Inc. Anhydrous solvents were distilled under N<sub>2</sub> atmosphere and used directly. Silica column chromatography was performed using silica gel (Merck, 250–430 mesh).

NMR was acquired on a Bruker AV400 (400 MHz) at 25 °C with the deuterated solvent as the lock and residual solvent as the internal reference. Chemical shifts are reported in ppm units with residual protons from the deuterated solvents as an internal standard. Mass spectrometry measurements and element analysis measurements were performed in the Department of Chemistry, University of Strasbourg. NMR measurements were performed in Institut de Science et d'Ingénierie Supramoléculaires (ISIS), University of Strasbourg.

#### *Synthetic Procedure*



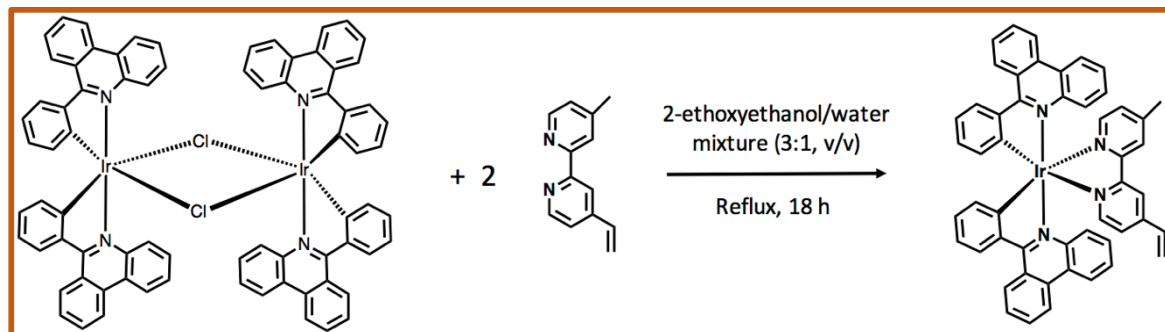
The Ir(III) dimer,  $[\text{Ir}_2(\text{pphen})_4(\mu\text{-Cl})_2]$ , was prepared by a former group member following a similar procedure as reported by Nonoyama<sup>32</sup> and used by the former group in another publication.<sup>33</sup>

$\text{IrCl}_3 \cdot x\text{H}_2\text{O}$  and 2-2.5 equivalent of the corresponding C^N ligand (pphen) were heated at 140 °C for 18 h under nitrogen in a 2-ethoxyethanol/water mixture (3:1, v/v). After cooling to room temperature, the precipitate was filtered off and successively washed with water, methanol and diethylether. The solid was used without further purification. Dimers



$[\text{Ir}_2(\text{C}^{\wedge}\text{N})_4(\mu\text{-Cl})_2]$ , ( $\text{C}^{\wedge}\text{N} = \text{pq}, \text{piq}$ ) were synthesised following the procedures described in the literature.

$\text{Ir}(\text{pphen})_2(\text{mVbpy})$



The complex  $\text{Ir}(\text{pphen})_2(\text{mVbpy})$  was synthesised following a modified procedure described in the literature.<sup>31</sup>

A mixture of the dimer  $[\text{Ir}_2(\text{pphen})_4(\mu\text{-Cl})_2]$  (50.0 mg, 34  $\mu\text{mol}$ ;) and 4-methyl-4'-vinyl-2,2'-bipyridine (mVbpy) (14.66 mg, 75  $\mu\text{mol}$ ) in  $\text{CH}_2\text{Cl}_2$  (10 mL) and methanol (6 mL) was stirred at 55 °C for 16 h. After cooling to room temperature, the  $\text{CH}_2\text{Cl}_2$  was removed under reduced pressure, and a saturated water solution (2 mL) of ammonium hexafluorophosphate ( $\text{NH}_4\text{PF}_6$ ) (75 mg, 460  $\mu\text{mol}$ ) was added, and the resulting suspension was stirred for 20 min. The solid was isolated by filtration and successfully washed with water and hexanes. It was re-precipitated by diethylether diffusion to afford  $\text{Ir}(\text{pphen})_2(\text{mVbpy})$  as an orange-brown solid in 90% yield (60 mg, 66.9  $\mu\text{mol}$ ).

$^1\text{H}$  NMR (400 MHz,  $\text{CD}_2\text{Cl}_2$ )  $\delta$  [ppm]= 9.20 (m, 2H), 8.65 (m, 3H), 8.57 (m, 2H), 8.44 (m, 4H), 7.99 (m, 4H), 7.70 (q, 4H), 7.50 (t, 2H), 7.31 (m, 3H), 7.15 (d, 1H), 7.09 (m, 2H), 6.91 (m, 4H), 6.60 (m, 1H), 6.01 (d, 1H), 5.62 (d, 1H), 2.34 (s, 3H)

HR-ESI-MS (m/z):  $[\text{M}]^+$  calculated 897.2567; found 897.2538

Microanalysis: %N=5.30 (calculated=5.31), %C=58.28 (calculated=58.46), %H=3.38 (calculated=3.41)

**3.8 REFERENCES**

- (1) Lalrempuia, R.; McDaniel, N. D.; Müller-Bunz, H.; Bernhard, S.; Albrecht, M. *Angew. Chem. - Int. Ed.* **2010**, *49* (50), 9765.
- (2) Lo, K. K. W.; Louie, M. W.; Zhang, K. Y. *Coord. Chem. Rev.* **2010**, *254* (21–22), 2603.
- (3) Mattos, L. V.; Jacobs, G.; Davis, B. H.; Noronha, F. B. *Chem. Rev.* **2012**, *112* (7), 4094.
- (4) Ning, Z.; Zhang, Q.; Wu, W.; Tian, H. *J. Organomet. Chem.* **2009**, *694* (17), 2705.
- (5) Darmawan, N.; Yang, C.-H.; Mauro, M.; Raynal, M.; Heun, S.; Pan, J.; Buchholz, H.; Braunstein, P.; De Cola, L. *Inorg. Chem.* **2013**, *52*, 10756.
- (6) Zhang, M.; Ge, S.; Li, W.; Yan, M.; Song, X.; Yu, J.; Xu, W.; Huang, J. *Analyst* **2012**, *137* (3), 680.
- (7) Xu, Y.; Lv, Z.; Xia, Y.; Han, Y.; Lou, B.; Wang, E. *Anal. Bioanal. Chem.* **2013**, *405* (11), 3549.
- (8) Díaz-Ortega, I. F.; Ballesta-Claver, J.; Martín, M. C.; Benítez-Aranda, S.; Capitán-Vallvey, L. F. *RSC Adv.* **2014**, *4* (100), 57235.
- (9) Milutinovic, M.; Sallard, S.; Manojlovic, D.; Mano, N.; Sojic, N. *Bioelectrochemistry* **2011**, *82* (1), 63.
- (10) Rubinstein, I.; Bard, A. J. *J. Am. Chem. Soc.* **1981**, *103* (3), 5007.
- (11) Su, M.; Liu, S. *Anal. Biochem.* **2010**, *402* (1), 1.
- (12) Devadoss, A.; Dennany, L.; Dickinson, C.; Keyes, T. E.; Forster, R. J. *Electrochem. commun.* **2012**, *19* (1), 43.
- (13) Venkatanarayanan, A.; Spehar-Délèze, A. M.; Dennany, L.; Pellegrin, Y.; Keyes, T. E.; Forster, R. J. *Langmuir* **2008**, *24* (19), 11233.
- (14) Piper, D. J. E.; Barbante, G. J.; Brack, N.; Pigram, P. J.; Hogan, C. F. *Langmuir* **2011**, *27* (1), 474.
- (15) Sun, X.; Du, Y.; Dong, S.; Wang, E. *Anal. Chem.* **2005**, *77* (24), 8166.
- (16) Bertocello, P.; Dennany, L.; Forster, R. J.; Unwin, P. R. *Anal. Chem.* **2007**, *79* (19), 7549.
- (17) Moretto, L. M.; Kohls, T.; Badocco, D.; Pastore, P.; Sojic, N.; Ugo, P. *J. Electroanal. Chem.* **2010**, *640* (1–2), 35.

- (18) Lee, W. *Microchim. Acta* **1997**, 39, 19.
- (19) Abrufia, H. D.; Bard, A. J. *J. Am. Chem. Soc.* **1982**, 104 (7), 2641.
- (20) Maness, K. M.; Terrill, R. H.; Meyer, T. J.; Murray, R. W.; Wightman, R. M. *J. Am. Chem. Soc.* **1996**, 118 (43), 10609.
- (21) Collinson, M. M.; Taussig, J.; Martin, S. A. *Chem. Mater.* **1999**, 11, 2594.
- (22) Lee, J. K.; Lee, S. H.; Kim, M.; Kim, H.; Kim, D. H.; Lee, W. Y. *Chem. Commun.* **2003**, 9 (13), 1602.
- (23) Dennany, L.; Forster, R. J.; Rusling, J. F. *J. Am. Chem. Soc.* **2003**, 125 (17), 5213.
- (24) Forster, R. J.; Hogan, C. F. *Anal. Chem.* **2000**, 72 (22), 5576.
- (25) Dennany, L.; Forster, R. J.; White, B.; Smyth, M.; Rusling, J. F. *J. Am. Chem. Soc.* **2004**, 2 (20), 8835.
- (26) Muegge, B. D.; Richter, M. M. *Luminescence* **2005**, 20 (2), 76.
- (27) Sun, S. Q.; Song, Q. J.; Yuan, H. F.; Ding, Y. Q. *Chinese Chem. Lett.* **2008**, 19 (12), 1509.
- (28) Li, M. J.; Shi, Y. Q.; Lan, T. Y.; Yang, H. H.; Chen, G. N. *J. Electroanal. Chem.* **2013**, 702, 25.
- (29) Liu, Y.; Song, Q. *Anal. Methods* **2014**, 6 (14), 5258.
- (30) Nie, H. J.; Shao, J. Y.; Wu, J.; Yao, J.; Zhong, Y. W. *Organometallics* **2012**, 31 (19), 6952.
- (31) Metz, S.; Bernhard, S. *Chem. Commun.* **2010**, 46 (40), 7551.
- (32) Denisevich, P.; Abruna, H. D.; Leidnerd, C. R.; Meyer, T. J.; Murray, R. W. *Inorg. Chem.* **1982**, 21 (6), 2153.
- (33) Nonoyama, M. *Bulletin of the Chemical Society of Japan.* **1974**, pp 767–768.
- (34) Lamansky, S.; Djurovich, P.; Murphy, D.; Abdel-Razzaq, F.; Kwong, R.; Tsyba, I.; Bortz, M.; Mui, B.; Bau, R.; Thompson, M. E. *Inorg. Chem.* **2001**, 40 (7), 1704.
- (35) Shin, I.; Kim, J. Il; Kwon, T.; Hong, J.; Lee, J.; Kim, H. *J. Phys. Chem. C* **2007**, 111, 2280.
- (36) Kim, J. Il; Shin, I.; Kim, H.; Lee, J. *J. Am. Chem. Soc.* **2005**, 127 (Iii), 1614.
- (37) Fernandez-Hernandez, J. M.; Longhi, E.; Cysewski, R.; Polo, F.; Josel, H.-P.; De Cola, L. *Anal. Chem.* **2016**, 88 (8), 4174.
- (38) Bard, A. J.; Faulkner, L. R. *Electrochemical Methods: Fundamentals and*

*Applications*; **2001**.

- (39) Chen, H.-F.; Wu, C.; Kuo, M.-C.; Thompson, M. E.; Wong, K.-T. *J. Mater. Chem.* **2012**, 22 (19), 9556.



# Chapter 4

## **Amine-rich Nitrogen-doped Carbon NanoDots (NCNDs): Revealing and Tailoring Co-reactant Properties**

### **Abstract**

Amine-rich nitrogen-doped carbon nanodots (NCNDs) have been successfully used as co-reactant in electrochemiluminescence (ECL) processes. Primary and tertiary amino groups on NCNDs have been studied as co-reactant sites for  $\text{Ru}(\text{bpy})_3^{2+}$ , showing their eligibility as powerful alternatives to the toxic tripropylamine (TPrA). As a proof-of-concept application, the detection of a bioanalyte, L-epinephrine, is reported.

The work presented in this chapter has been accomplished with the aid of *Ms. Francesca Arcudi* from *Prof. Maurizio Prato* research group (University of Trieste).

Part of the work discussed in this chapter has been accepted as “Amine-Rich Nitrogen-Doped Carbon NanoDots as Platform for Self-Enhancing Electrochemiluminescence” in *Angewandte Chemie* **2017** (DOI: 10.1002/anie.201611879R1).

## 4.1 INTRODUCTION

Carbon nanodots (CNDs), quasi-spherical nanoparticles with size below 10 nm,<sup>1-3</sup> are expected to have a huge impact in biotechnological and environmental applications, due to their potential as a nontoxic, fluorescent alternative to more traditional semiconductor-based quantum dots (QDs).<sup>4,5</sup> CNDs were first discovered during the purification of single-walled carbon nanotubes through preparative electrophoresis in 2004<sup>6</sup> and, due to their interesting features, have gradually become a prominent new member of the nanocarbon family.<sup>2,4,5</sup> In addition, properties such as aqueous solubility, robust chemical inertness, facile modification and high resistance to photobleaching,<sup>3,4,7,8</sup> have been explored in their use in biomedicine, biosensing, optronics and catalysis.<sup>1,4,5,9-17</sup>

ECL is a redox-induced light emission in which high-energy species, generated at the electrodes, undergo a high-energy electron transfer reaction forming an excited state that emits light.<sup>18-20</sup> The excited state can be produced through the reaction of radicals generated from the same chemical species (emitter), in the so-called annihilation mechanism, or from two different precursors (emitter and co-reactant), via co-reactant ECL (see Chapter 1-Section 1.2.2). that is strongly coupled with the energies of the HOMO and LUMO levels of the emitter. The main advantage of the co-reactant pathway is that the formation of radicals and the consequent generation of ECL in aqueous solutions is attainable without potential cycling and at less extreme potentials than common organic solvents, opening up a wide range of bioanalytical applications.

Tripropylamine (TPrA) is the most employed co-reactant providing the optimum ECL signal when used in combination with Ru(bpy)<sub>3</sub><sup>2+</sup>.<sup>21</sup> However, TPrA has several disadvantages, being toxic, corrosive, volatile; moreover, needs to be used in high concentrations (usually up to 100 mM) to obtain good sensitivity.<sup>22</sup> Alternative co-reactant species have to obey to some stringent requirements: matching redox potentials, fast charge transfer kinetics and rapid degradation routes to produce a high-energy radical capable to initiate the ECL process.<sup>23</sup> Additionally, good solubility and high chemical stability are two crucial conditions.

Some recent studies reports other tertiary amines, such as 2-(dibutylamino)ethanol (DBAE)<sup>22</sup> and N- butyldiethanolamine (BDAE),<sup>24</sup> as more efficient co-reactants than TPrA. However, they are still toxic and volatile compounds, thus their use is hampered due to the same drawbacks of TPrA.

On the other hand, in some applications, the addition of TPrA (or in general co-reactants) is not needed, since its role is played by the analyte itself, generally an amine, for example, sarcosine,<sup>25</sup> dopamine,<sup>26</sup> NADH,<sup>27</sup> other organic compounds,<sup>28</sup> or with the generation of the co-reactant in situ.<sup>29</sup> Furthermore, suitably designed fluorophores with groups acting as co-reactant have attracted a lot of attention.<sup>30–34</sup> They would not only avoid the addition of TPrA, but also provide a self-enhanced ECL emission thanks to an intramolecular and thus more efficient electron transfer.

Another way to overcome at this inconvenience rely on the use of supported alkyl amines, thus avoiding or limiting their volatility. In this context, amine-rich nitrogen-doped CNDs (NCNDs) bearing amines supported on a carbonaceous scaffold, which in turn are water soluble and of small dimensions, i.e. with a potential high diffusivity, can be a valuable candidate.

The use of CNDs as co-reactant is still in its infancy.<sup>35–37</sup> However, apart from a recent study in which benzylic alcohol moieties were identified as co-reactant sites,<sup>35</sup> the identification of the functional group responsible of their co-reactant behavior is complicated, but pivotal.

Since amino functional groups are the best and most used co-reactant units in combination with  $\text{Ru}(\text{bpy})_3^{2+}$ , we evaluated the performance as co-reactant of NCNDs bearing primary and tertiary alkyl amino groups on the surface as alternative to TPrA for  $\text{Ru}(\text{bpy})_3^{2+}$  ECL generation (Figure 4.1).

The discussion will start with a description of the NCNDs characterisation and their alkylation in order to obtain methylated-NCNDs (mNCNDs). A morphological study will be presented for the evaluation of the shape and the size of these dots, followed by a photophysical characterisation, functional for studying their emission spectral range, in order to avoid overlap with the one of  $\text{Ru}(\text{bpy})_3^{2+}$ . Therefore, electrochemical experiments based on cyclic voltammetry will shed light on the type of amino groups on the surface and will give information about their redox potentials. Through these measurements, a deep investigation of the NCNDs effect in  $\text{Ru}(\text{bpy})_3^{2+}$  ECL, which in turn will drive towards a proposed a reaction mechanism, is reported.



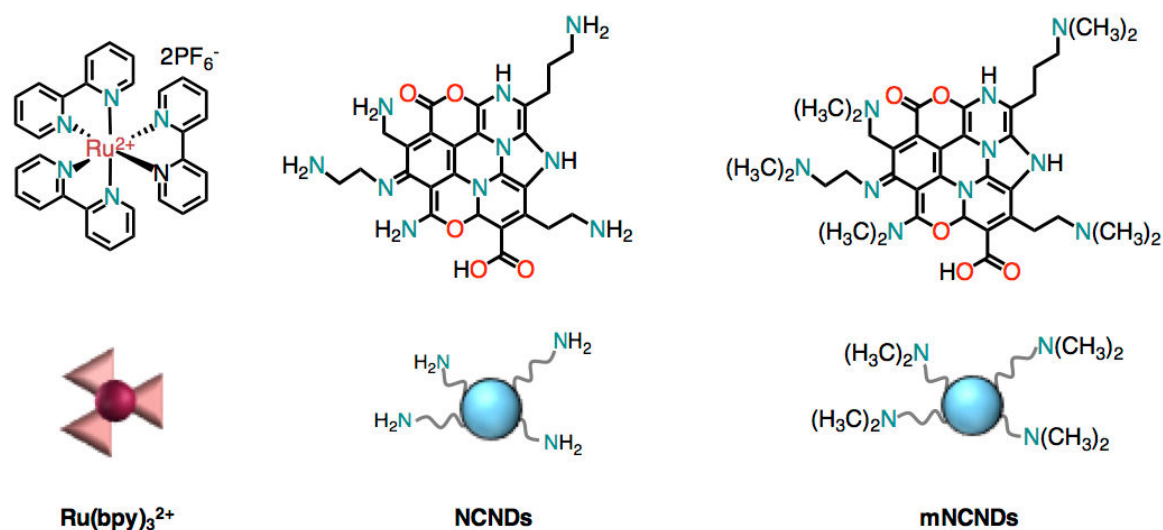


**Figure 4.1.** Tris(2,2'-bipyridine)ruthenium(II) ( $Ru(bpy)_3^{2+}$ ) on the left, nitrogen-doped carbon nanodots (NCNDs) in the middle and methylated-NCNDs (mNCNDs) on the right.

## 4.2 SYNTHESIS AND CHARACTERISATION OF PRIMARY AND TERTIARY NCNDs

NCNDs were kindly supplied by the research group of Prof. M. Prato (University of Trieste). They were synthesised according to a reported procedure, by using a microwave reactor under controlled conditions.<sup>38</sup> As shown in Figure 4.2a-c, they show a rather homogeneous size distribution with an average size of  $2.5 \pm 0.8$  nm, multiple oxygen and nitrogen functional groups on their surface, which foster their excellent solubility in water (up to 80 mg/mL). In particular, the presence of functional groups such as amines was revealed through a positive Kaiser test and by FT-IR and XPS measurements (Figure 4.2d-g). From the full-scan XPS spectrum of NCNDs (Figure 3.2e), C, N, O atoms were detected with peaks at 286.8 eV (C1s), 400.33 eV (N1s), and 532.34 eV (O1s), respectively. To determine the C and N configurations, a detailed peak fitting analysis was performed (Figure 4.2f-g). The C1s XPS spectrum can be deconvoluted into five surface components corresponding to  $sp^2$  (C=C) at 284.5 eV,  $sp^3$  (C-C, and C-H) at 285.5 eV, C-O/C-N at 286.2 eV, C=O/C=N at 288.3 eV, as well as COOH at 290.5 eV. The N1s spectrum can be deconvoluted into four peaks centered at 398.3, 399.6, 400.5, and 401.9 eV corresponding to C=N,  $NH_2$ , C-N-C and N-C<sub>3</sub> respectively. The presence of amino groups on their surface, in an estimated concentration of 1350  $\mu\text{mol/g}$  (based on Kaiser test), can allow easy insertion of interesting molecules through standard organic chemistry procedures.

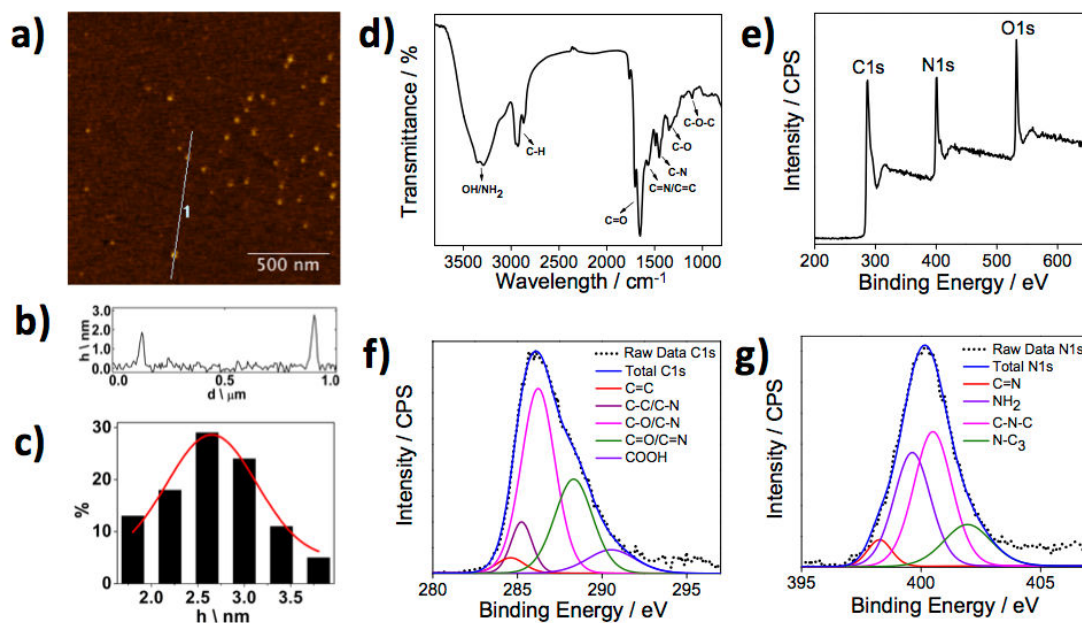


**Figure 4.2.** *a)* Tapping mode AFM images of NCNDs ( $1.7 \times 1.7 \mu\text{m}$ ) on a mica substrate; *b)* Height profiles NCNDs; *c)* size histograms of NCNDs with curves fit to the data using a Gaussian model; *d)* FTIR spectra of NCNDs; *e)* XPS survey of NCNDs; *f)* deconvoluted C1s spectra of NCNDs; *g)* deconvoluted N1s spectra of NCNDs.

We alkylated primary amino groups of NCNDs to tertiary amines through an Eschweiler-Clarke methylation reaction (see experimental condition in Section 4.7). The reaction was monitored with the Kaiser test (Figure 4.3) and the as obtained NCNDs, denoted as mNCNDs, were fully characterised.

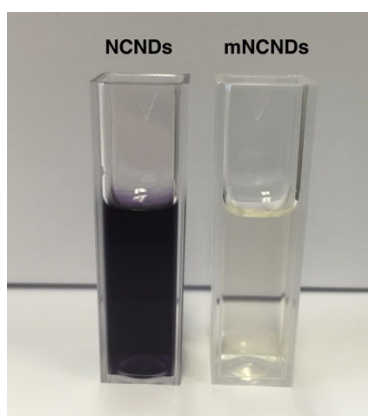


**Figure 4.3.** Photograph of colorimetric Kaiser Test of NCNDs (left) and mNCNDs (right).

The UV-Vis spectrum of ap-NCNDs show an absorption band at 286 nm, ascribed to the  $\pi$ - $\pi^*$  transition of the conjugated C=C units from the carbon core (Figure 4.4a).<sup>38</sup>

Fluorescence (FL) is one of the most fascinating features of CNDs. Spectrally broad FL emission with excitation wavelength dependence is a common phenomenon observed in CNDs.<sup>3,39</sup> CNDs produce multi-fluorescence colors under different excitation wavelengths and this behavior may arise not only from particles of different size but also from a distribution of different emissive domains on each carbon dots.

This property implies that the emission of CNDs can be tuned by changing the excitation wavelength since the emission arises from different surface emissive traps. NCNDs exhibit clear excitation-dependent emission spectra, showing their optimal emission for a characteristic excitation wavelength, revealing the presence of different energy levels corresponding to the maximum transition probability (Figure 3.4). A broad emission peak at 356 nm is observed when the sample is excited at the optimal excitation wavelength (300 nm, Figure 4.4b). The fluorescence peaks shift from 356 nm to 474 nm when the excitation wavelength changes from 300 to 420 nm and the fluorescence intensity decreased as the peak red shifts. The many kinds of functional groups present on the surface of ap-NCNDs have different surface state energy levels, which result in a series of emissive traps that dominate the emission at different excitation wavelengths and explain the excitation wavelength-dependent phenomenon of NCNDs. The PLQY was found to be 17%.

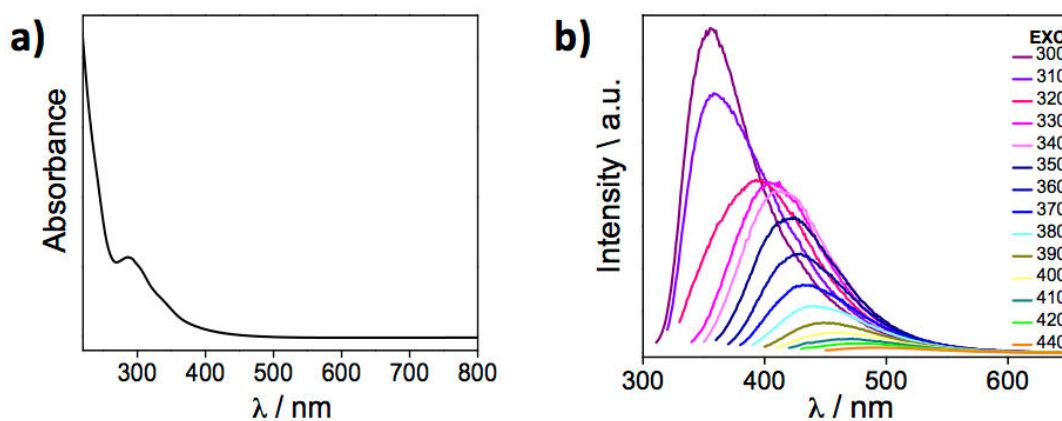


**Figure 4.4.** a) UV-Vis absorption spectra of NCNDs in water; b) FL spectra of NCNDs in water (298 K) at different excitation wavelengths.

Upon methylation, the changes observed in the photophysical properties of mNCNDs are consistent with the NCNDs surface modification (Figure 4.5), since they strongly depend to the trapping of excitons under excitation. mNCNDs shows its most intense emission at 395 nm, upon excitation at 330 nm, and the PLQY decrease from 17% to 8%.

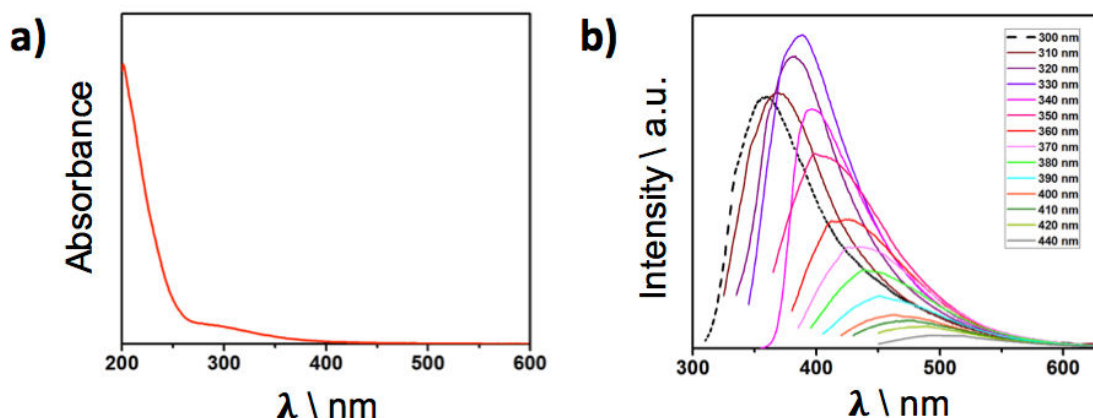


**Figure 4.5.** a) UV-Vis absorption spectra of mNCNDs in water; b) FL spectra of mNCNDs in water (298 K) at different excitation wavelengths.

### 4.3 ELECTROCHEMICAL PROPERTIES

The cyclic voltammogram (CV) of NCNDs (Figure 4.6a black trace) was recorded to evaluate their electrochemical features in oxidation and reduction. It shows an irreversible peak attributable to the oxidation of amino groups (+1.15 V vs SCE).<sup>38</sup> The intense current and the steep slope of this peak, demonstrate that many amino groups on the NCNDs surface can be easily oxidised. Additionally, the process is a mono-electron oxidation, taking as reference the CV of ferrocene at same concentration. Indeed, it is well known that ferrocene has a reversible oxidation peak associated to a mono-electron oxidation.<sup>40</sup> Figure 4.6 reports the CV of a system 1:1 Ferrocene: NCNDs. From the area under the peaks (at +0.52 V and at +1.14 V) it is possible to calculate the same charge (in Coulomb- as reported in the figure 4.6) for both the oxidation processes and, thus, to conclude that the oxidation of NCNDs is a one-electron event, in analogies with amine oxidation.

To be active as ECL co-reactant, the amino functional groups should have a hydrogen in  $\alpha$  position in order to have a strongly reducing intermediate. This intermediate supplies chemical energy for the emissive excited state generation.<sup>41</sup>

To gain further information on the amino groups present on the NCNDs surface we have measured the CV of a variety of amine derivatives (Figure 4.7): aromatic, aliphatic, primary, secondary and tertiary, in the same solvent and at the same concentration. Oxidation potentials  $E_{ox}$  are listed in table 4.1.

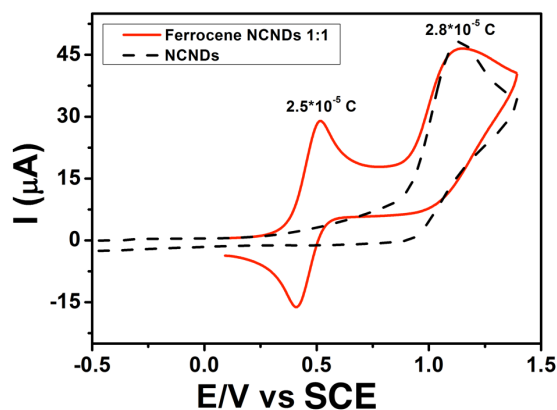


**Figure 4.6.** Cyclic Voltammetry of 1 mg/mL NCNDs (black dashed trace) and of Ferrocene: NCNDs 1:1 mg/mL (red trace) in DMF solution using 0.1 M TBAPF<sub>6</sub> as supporting electrolyte on GC. Scan rate 0.1 V s<sup>-1</sup>, SCE as reference electrode and platinum wire as counter electrode.

Among the amines investigated, the cyclic voltammogram of NCNDs shows strong similarities with those of phenethylamine and benzylamine (Figure 4.7a brown and green trace). These results suggest that the amino groups on NCNDs have a hydrogen atom attached to the  $\alpha$ -carbon, in agreement with previous NMR studies.<sup>38</sup> Therefore, they should be capable of forming reductive or oxidative species during an unidirectional voltammetric scan.<sup>20,42</sup>

**Table 4.1.** Electrochemical data of NCNDs, mNCNDs and different amines:  $E_{ox}$  (V) vs SCE, 0.1 M TBAPF<sub>6</sub>/DMF. GC working electrode, 298 K, scan rate 0.1 Vs<sup>-1</sup>.

	$E_{ox}$ (V)
<b>NCNDs</b>	+1.15
<b>Phenethylamine</b>	+1.15
<b>Benzylamine</b>	+1.16
<b>Piperidine</b>	+1.20
<b>Aniline</b>	+1.08
<b>Tripropylamine</b>	+0.87
<b>mNCNDs</b>	+0.80; +1.20

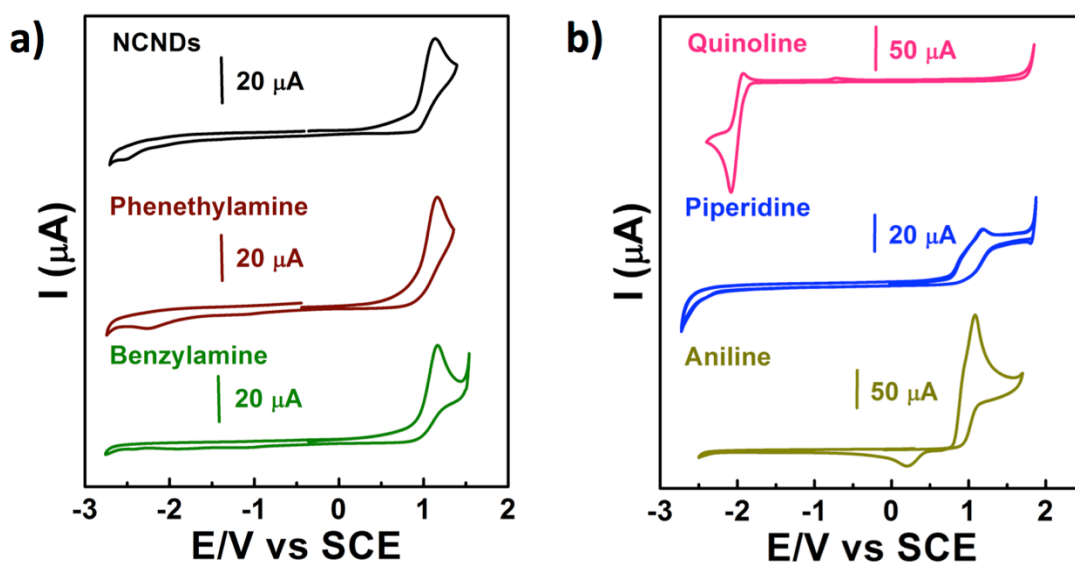


**Figure 4.7.** Cyclic Voltammetry of **a)** 1 mg/mL NCNDs (black trace), 1 mg/mL phenethylamine (brown trace), benzylamine (green trace), **b)** 1 mg/mL quinolone (pink trace), 1 mg/mL piperidine (blue trace), 1 mg/mL aniline (dark yellow trace), in DMF using TBAPF<sub>6</sub> as supporting electrolyte on GC. Scan rate 0.1 V s<sup>-1</sup>.

The CV of mNCNDs shows a new peak at +0.8 V vs SCE that matches with that one of TPrA (Figure 4.8) and can be attributed to the formation of tertiary amines on their surface.

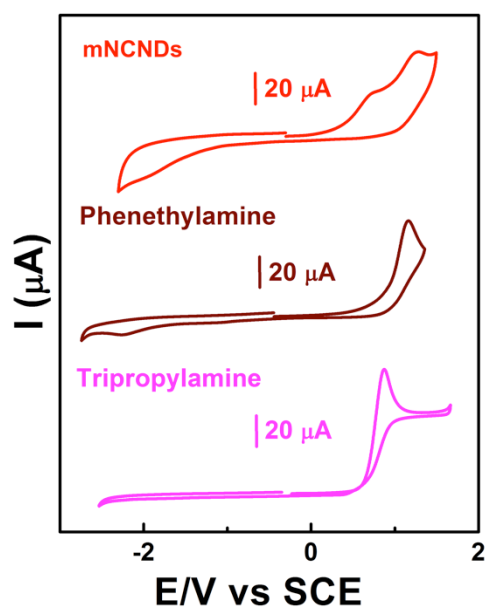


**Figure 4.7.** Cyclic Voltammetry of 1 mg/mL mNCNDs (red trace), 1 mg/mL phenethylamine (brown trace), 1 mg/mL Tripropylamine (pink trace) in DMF using TBAPF<sub>6</sub> as supporting electrolyte on GC. Scan rate 0.1 V s<sup>-1</sup>.

It was also determined the diffusion coefficient of NCNDs and mNCNDs (Figure 4.9 and Table 4.2) assuming that for both species the processes are diffusion controlled. In order to

determine the diffusion coefficient, cyclic voltammetric experiments (CVs) at different scan rate from 0.01 to 1 V s<sup>-1</sup> were performed and the Randles–Sevcik equation was applied (see experimental section 4.7).<sup>43</sup> More so, we compared them with the one of TPrA.<sup>44</sup>

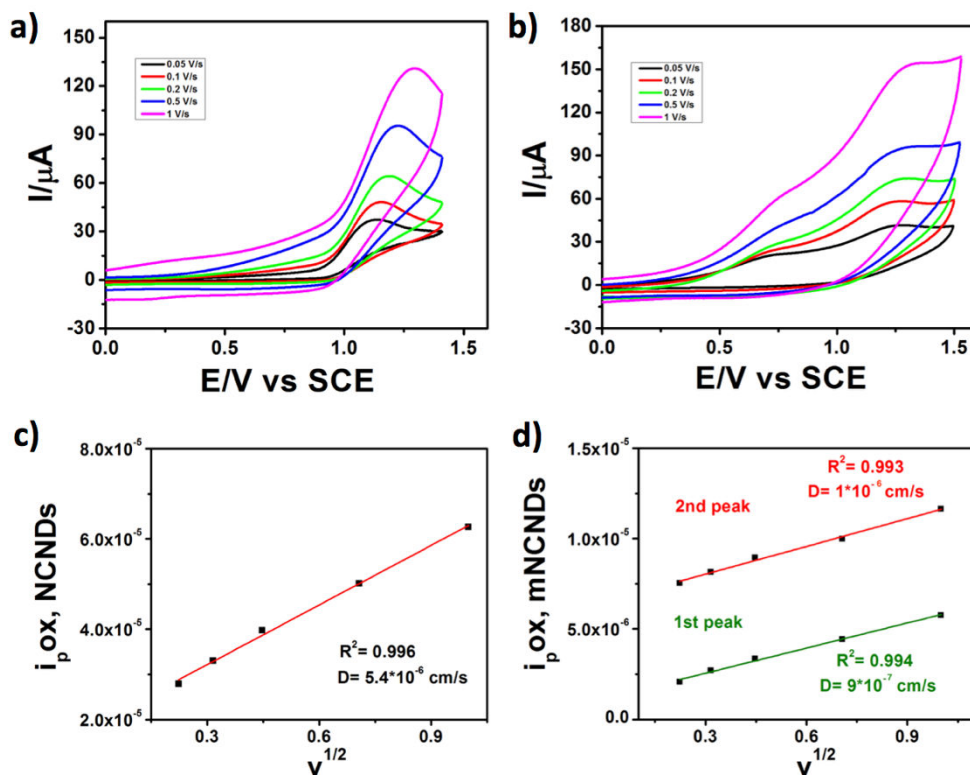


**Figure 4.8.** **a)** CVs of 1 mg/mL NCNDs in DMF, **b)** CVs of 1 mg/mL mNCNDs in DMF, using 0.1 M TBAPF<sub>6</sub> as supporting electrolyte and GC as working electrode, SCE as reference electrode and platinum as counter electrode. Scan rate from 0.05 V s<sup>-1</sup> to 1 V s<sup>-1</sup>. **c)**  $i_p$  vs  $v^{1/2}$  of **c)** CVs of NCNDs and **d)** CVs of mNCNDs.

**Table 4.2.** Diffusion coefficients of NCNDs and mNCNDs, calculated with Randles-Sevcik equation, and of TPrA.<sup>44</sup>

	<b>D ( cm<sup>2</sup>/s)</b>
<b>NCNDs</b>	$5.4 \cdot 10^{-6}$
<b>mNCNDs</b>	$1 \cdot 10^{-6}$ $9 \cdot 10^{-7}$
<b>Tripropylamine</b>	$5 \cdot 10^{-6}$

#### 4.4 EFFECT OF (m)NCNDs ON THE ECL OF Ru(bpy)<sub>3</sub><sup>2+</sup>

Since Ru(bpy)<sub>3</sub><sup>2+</sup> and NCNDs have almost the same HOMO values (-6.1 and -5.7 eV respectively),<sup>21,45</sup> both species can be oxidised at the electrode surface upon applying a positive voltage (Figure 4.10).



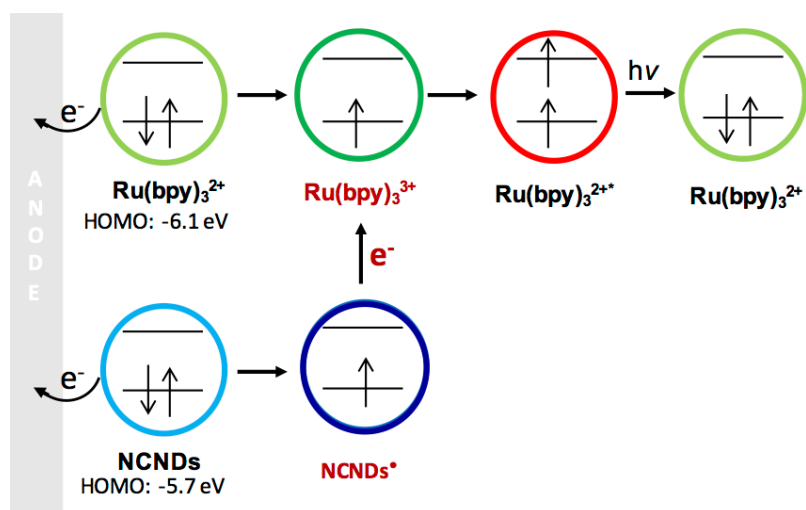


**Figure 4.9.** Schematic diagram showing the general principle of  $\text{Ru}(\text{bpy})_3^{2+}$  electrochemiluminescence using NCNDs as co-reactant.

Thus, the  $\text{Ru}(\text{bpy})_3^{2+}$  ECL signal of a 0.1 mM  $\text{Ru}(\text{bpy})_3^{2+}$  solution in PBS (pH=7.4) was recorded upon addition of NCNDs (0.1 mg/mL) at a glassy carbon electrode (during a cyclic voltammetry between +0.5 V and +1.4 V), and compared to the one recorded without NCNDs (Figure 4.11a, bottom part).

$\text{Ru}(\text{bpy})_3^{2+}$  background ECL emission (Figure 4.11a, bottom part, black trace) in aqueous solutions can be attributed to a light-emitting reduction of  $\text{Ru}(\text{bpy})_3^{3+}$  by  $\text{OH}^-$  ions (chemiluminescence) or other reducing agents, rather than the annihilation reaction.<sup>46–49</sup>

The presence of NCNDs (Figure 4.11a, bottom part, red trace) results in a four-time intensity enhancement of the  $\text{Ru}(\text{bpy})_3^{2+}$  ECL signal rising at +1 V and peaking at +1.1 V (Figure 4.11a, black trace). This result confirms the NCNDs co-reactant behavior during the oxidation process, which can be further corroborated by the higher ECL signal of  $\text{Ru}(\text{bpy})_3^{2+}$  upon increasing the concentration of NCNDs from 0.002 to 0.1 mg/mL (Figure 4.11b). In order to prove the efficiency of our system over time, several cycles were performed, scanning between +1.1 V and -0.9 V, at a rate of 0.05 V/s. In contrast to TPrA, the ECL response with NCNDs is relatively constant (within 10%) for more than 15 cycles (Figure 4.11c), revealing their great electrochemical stability, the abundant presence of available amino groups for further ECL cycles and their consequent eligibility for biosensing platforms.



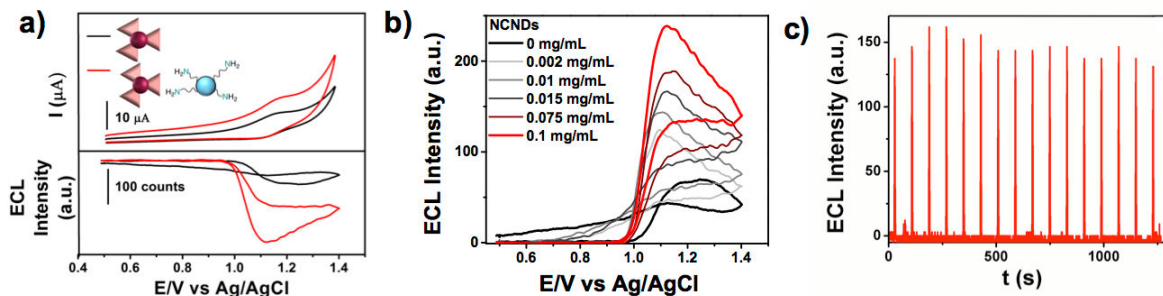


**Figure 4.10.** **a)** CV (upper part) and ECL (bottom part) potential curves of 0.1 mM  $\text{Ru}(\text{bpy})_3^{2+}$  (black curves) and  $\text{Ru}(\text{bpy})_3^{2+}/\text{NCNDs}$  system (red curves) in PBS (pH=7.4) on GC electrode. Scan rate  $0.05 \text{ V s}^{-1}$ ; **b)** ECL intensity during a potential scan of 0.1 mM PBS solution of  $\text{Ru}(\text{bpy})_3^{2+}$  upon addition of different concentration of NCNDs; **c)** ECL responses of  $\text{Ru}(\text{bpy})_3^{2+}/\text{NCNDs}$  (red trace) system obtained during a continuous potential scan between +1.1 V and -0.9 V. (16 cycles under scan rate  $0.05 \text{ V s}^{-1}$ ).

CV measurements were performed to shed light on the co-reactant mechanism. The CV of a PBS (pH=7.4) solution 0.1 mM of  $\text{Ru}(\text{bpy})_3^{2+}$  shows the typical reversible oxidation peak at +1.1 V vs  $\text{Ag}/\text{AgCl}$ .<sup>45</sup> However, upon addition of 0.1 mg/mL NCNDs (Figure 3.11a) the intensity of the oxidation peak of  $\text{Ru}(\text{bpy})_3^{2+}$  became higher, while the reduction peak becomes lower. This behavior is commonly observed in the system  $\text{Ru}(\text{bpy})_3^{2+}/\text{TPrA}$  and suggests an NCND catalytic effect on the  $\text{Ru}(\text{bpy})_3^{2+}$  oxidation.<sup>21,50</sup>

Therefore, the following mechanism can be proposed (Figure 4.12). Upon oxidation, the amino groups of NCNDs become a reducing unstable intermediate able to generate the excited state  $\text{Ru}(\text{bpy})_3^{2+*}$  through highly energetic electron transfer. The excited metal complex emits light and produces  $\text{Ru}(\text{bpy})_3^{2+}$  which can be reoxidised for a new cycle.

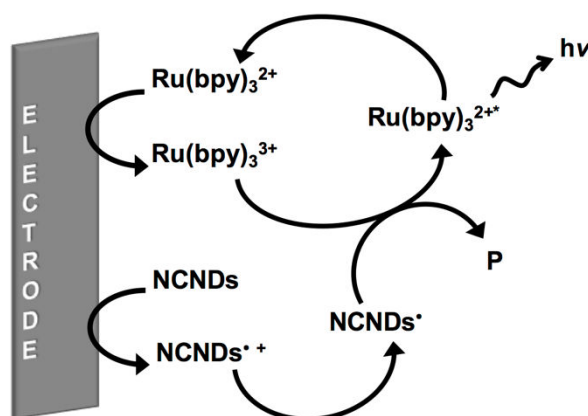


**Figure 4.11.** ECL proposed mechanism for  $\text{Ru}(\text{bpy})_3^{2+}/\text{NCNDs}$  system.

After methylation to tertiary amines, mNCNDs have been tested as co-reactant of  $\text{Ru}(\text{bpy})_3^{2+}$  ECL. The experiments were carried out on solutions with the same optical density of  $\text{Ru}(\text{bpy})_3^{2+}$ , and revealed an ECL activity ten times higher for mNCNDs with respect to NCNDs (Figure 4.13a, green and red traces). In addition, as in the case of NCNDs, stronger ECL signals for  $\text{Ru}(\text{bpy})_3^{2+}$  were observed upon increasing the concentration of mNCNDs (Figure 4.13b) while constant ECL responses (within 10%) were obtained for over 20 cycles (Figure 4.13c). Thus, tertiary amines on the mNCNDs surface provide an enhanced ECL activity with respect to primary amines, as usually observed with all the alkyl amines commonly used as “oxidative-reductive” co-reactants.<sup>44,51</sup> Moreover, a comparison with the widely used TPrA clearly demonstrated the potential of the nanodots as alternative co-reactant species. Interestingly, a small amount of mNCNDs (0.1 mg/mL, corresponding to concentration around 0.13 mM in amines) gave the same  $\text{Ru}(\text{bpy})_3^{2+}$  ECL intensity as the one recorded using TPrA 20 mM (2.86 mg/mL), which corresponds to an improvement of ca. 150 times (Figure 4.13a, green and black traces) despite of the slower diffusion coefficient of the mNCNDs vs TPrA (Figure 4.9b-d and Table 4.2).<sup>44</sup>

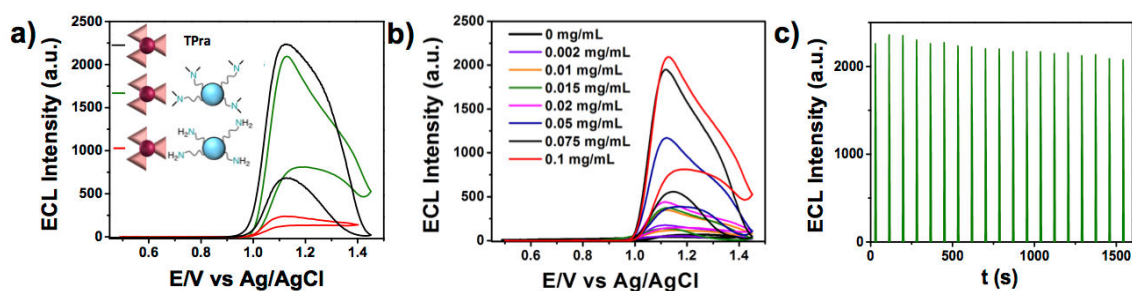


**Figure 4.12.** *a)* ECL emission of  $\text{Ru}(\text{bpy})_3^{2+}$  enhanced by 0.1 mg/mL NCNDs (red trace), 0.1 mg/mL mNCNDs (green trace) and 20 mM TPrA (black trace); *b)* ECL intensity during a potential scan of  $\text{Ru}(\text{bpy})_3^{2+}$  0.1 mM PBS solution upon addition of different concentration of mNCNDs (0.002-0.1 mg/mL); *c)* ECL responses of  $\text{Ru}(\text{bpy})_3^{2+}$ /mNCNDs system obtained during a continuous potential scan between +1.1 V and -0.9 V. (20 cycles under scan rate 0.05 V s<sup>-1</sup>).

## 4.5 EPINEPHRINE SENSING

To explore the sensing ability of the studied system  $\text{Ru}(\text{bpy})_3^{2+}$ /(m)NCNDs, we investigated the quantification of a chemical species able to quench  $\text{Ru}(\text{bpy})_3^{2+}$  emission. In particular, we used epinephrine (EP), also known as adrenaline. EP is an important catecholamine neurotransmitter in the mammalian central nervous systems involved in Parkinson’s disease and its quantification is relevant for the diagnosis of nerve diseases and in the development of their physiology. For this reason, a variety of analytical methods

have been employed so far for its detection, such as capillary electrophoresis,<sup>52</sup> fluorimetry,<sup>53</sup> electrochemistry and ECL.<sup>54–56</sup>

Our strategy is based on the quenching, by electron transfer, of the emission of the Ru(bpy)<sub>3</sub><sup>2+</sup>/NCNDs system by EP. Indeed, it is well known that this catecholamine forms an ortho-benzoquinone derivative by electro-oxidation (at around +0.2 V vs SCE), which quenches the luminescence of Ru(bpy)<sub>3</sub><sup>2+</sup>\* due to an electron transfer from the excited state of the metal complex to the quinone derivative.<sup>55</sup>

EP detection experiments were performed (in a PBS solution at pH=7.4) by means of chronoamperometry coupled with PMT tube. The measurements were performed with 0.1 mg/mL NCNDs, varying the concentration of EP from 0.5 to 15 μM. It was found a linear dependence of  $I_0/I$  on the concentration ( $R^2=0.993$ ) (Figure 4.14a). The limit of detection (LOD) and limit of quantification (LOQ) have been determined based on the standard deviation of the response and the slope (see experimental section 4.6 for details), and were found to be 0.2 μM and 0.6 μM (S/N=3), respectively (S/N=3). It should be highlighted that, the obtained LOD is lower as compared to other methodologies reported (for instance, capillary electrophoresis and fluorimetry)<sup>52,53</sup>, because the slow diffusion toward the electrode surface for an ECL sensor in solution, which is a crucial point in the formation of an excited state, should be taken in account. However, the performance of our system is really competitive with respect to other ECL-based systems already reported using nanoparticles, such as other CNDs.<sup>35,36</sup> For instance, a LOD of 0.3 μM for the quantification of dopamine employing oxygen-doped CNDs was recently reported.<sup>35</sup>

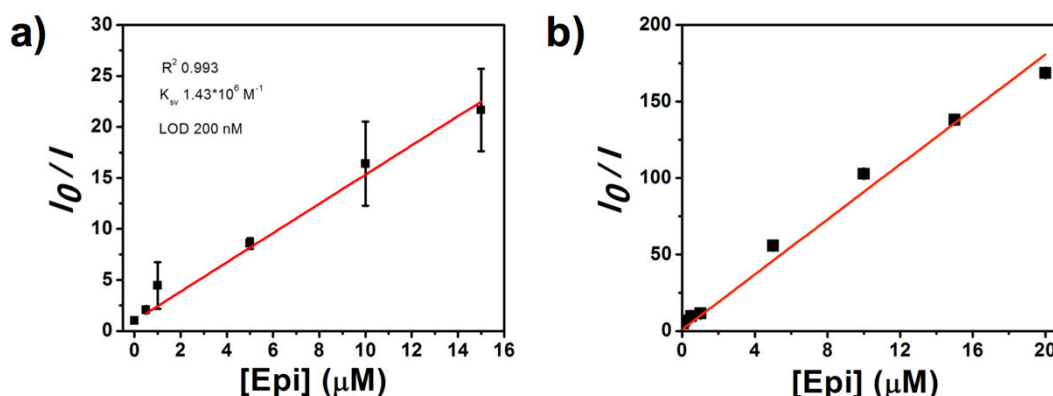


Figure 4.13. Linear fitting of  $I_0/I$  versus the concentration of EP when a) NCNDs and b) mNCNDs are employed as co-reactant in the concentration of 0.1 mg/mL. Error bars are of the same size of the square symbol for b).

By using the same analytical procedure, the employment of 0.1 mg/mL mNCNDs as co-reactant, decreasing the minimum concentration of EP to 0.05  $\mu\text{M}$ , was investigated. The linear dependence is shown in figure 4.14b ( $R^2=0.994$ ).

As compared to NCNDs, lower LOD and LOQ values by a factor 10 values were estimated, namely 30 nM and 110 nM ( $S/N=3$ ), respectively. Notably, we achieved a ca. ten times higher sensitivity as compared to the other reported nanodots-based systems,<sup>35,37</sup> and really competitive performance, for instance as compared to the detection of bisphenol with N doped CNDs,<sup>36</sup> reaching comparable limit of detection to the ones achieved employing other types of techniques, as discussed above.<sup>52-56</sup>

We believe that the better result obtained employing mNCNDs could be ascribed to the tertiary amino groups, that enhance the luminescence of  $\text{Ru}(\text{bpy})_3^{2+}$ , and in turn result in a detection of lower quantities of analytes.

## 4.6 CONCLUSION

To conclude, in this chapter we demonstrated that NCNDs carrying amino groups on the surface, act as powerful co-reactant species to promote  $\text{Ru}(\text{bpy})_3^{2+}$  ECL.

In detail, NCNDs carrying primary and tertiary amino groups on the surface were studied as co-reactants to promote ECL. Their simple and cost effective production, high aqueous solubility and low toxicity have inspired us to investigate the possible use of NCNDs as user-friendly alternative to the conventional co-reactant species. The primary or tertiary amino groups, which are known to provide great efficiency as “oxidative-reduction” co-reactants, present on the NCNDs surface, have shown powerful co-reactants ability for  $\text{Ru}(\text{bpy})_3^{2+}$  ECL generation. The co-reactant mechanism was investigated proving a NCNDs catalytic effect on the  $\text{Ru}(\text{bpy})_3^{2+}$  oxidation.

Our results showed how the use of alkyl amines on a carbon nanodots for  $\text{Ru}(\text{bpy})_3^{2+}$  ECL, would allow to circumvent most of the aforementioned drawbacks related to the use of the standard alkyl amines such as TPrA, which is toxic, corrosive, volatile and scarcely soluble and need to be used in high concentrations. Notably, it was recorded the same  $\text{Ru}(\text{bpy})_3^{2+}$  ECL intensity using a small amount of NCNDs and a concentration of TPrA 20 mM such as to achieve an improvement of ca 150 times by using nanodots.

We proposed a mechanism in which, upon oxidation, the amino groups of NCNDs become a reductive unstable intermediate able to form the excited-state  $\text{Ru}(\text{bpy})_3^{2+*}$ , through highly energetic electron transfer. Then  $\text{Ru}(\text{bpy})_3^{2+*}$  emits light and produces  $\text{Ru}(\text{bpy})_3^{2+}$ , which in

turn can be re-oxidised for a new cycle. Impressively, it was observed that, in contrast to TPrA, our NCNDs can be used for further cycles. Indeed, NCNDs provide constant ECL response for more than ca. 20 cycles due to a great electrochemical stability and abundant presence of amines for further cycles.

In light of these results, we finally explored the use of our  $\text{Ru}(\text{bpy})_3^{2+}/\text{NCNDs}$  ECL system for biosensing, reporting a simple methodology for the detection of L-epinephrine which show competitive performance compared to other systems already reported. Therefore, the use of our NCNDs can pave the route towards sensitive biosensing platform for the detection of interesting bioanalytes.

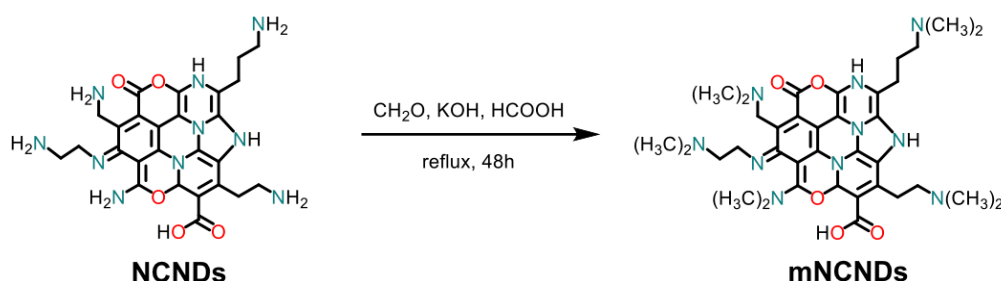
## 4.7 EXPERIMENTAL SECTION

### Materials

NCNDs were synthesised according to previously reported method.<sup>38</sup> Ruthenium- tris(2,2'-bipyridyl) dihexafluorophosphate  $\text{Ru}(\text{bpy})_3(\text{PF}_6)_2$ , tetra-butylammonium hexafluorophosphate ( $\text{TBAPF}_6$ ), piperidine, phenethylamine, benzylamine, aniline, quinoline, tripropylamine, L-epinephrine, paraformaldehyde (95%), potassium hydroxide ( $\geq 85\%$ ) and formic acid ( $\geq 96\%$ ) and Phosphate Buffer Saline (PBS, pH=7.4) were purchased from Sigma-Aldrich and used without purification.

Kaiser test kits were purchased from Sigma-Aldrich. Dialysis tubes with molecular weight cutoff 0.5-1 KDa were bought from Spectrum Labs. Ultrapure fresh water obtained from a Millipore water purification system ( $>18\text{M}\Omega$  Milli-Q, Millipore). N,N-dimethylformamide (DMF) was purchased at Acros organics and used without any purification.

### Synthesis of methylated-NCNDs (mNCNDs)



The synthetic procedure was adapted from the literature.<sup>57-59</sup> NCNDs (80 mg, 0.108 mmol amines) were dissolved in formalin (37 % w/v, 3 mL, 0.01 mol) and formic acid (99 %, 4 mL, 106 mmol). The solution was heated to reflux for 48 h and cooled to room temperature.

Volatiles were removed under vacuum together with the solvent and the residue was taken up in water and dialysed against pure water through a dialysis membrane for 2 days. The aqueous solution of NCNDs was lyophilised, yielding a slightly brownish solid (mNCNDs: 47.5 mg). Kaiser Tests performed on NCNDs and mNCNDs results respectively in 1350  $\mu\text{mol/g}$  and 26  $\mu\text{mol/g}$  of amines, respectively (see figure 4.3).

### *Electrochemistry*

The electrochemical characterisations of NCNDs, mNCNDs and the different amines at a concentration of 1 mg/mL were performed in DMF with 0.1M TBAPF<sub>6</sub> as supporting electrolyte, whereas the electrochemistry on the Ru(bpy)<sub>3</sub><sup>2+</sup>(0.1 mM)/NCNDs (0.1 mg/mL) system has been studied in PBS (pH=7.4). For electrochemical experiments, a CHI750C Electrochemical Workstation (CH Instruments, Inc., Austin, TX, USA) was used and the experiments were performed in a glass cell under an argon atmosphere. Feedback correction was employed in order to minimize the ohmic drop between working and reference electrodes. A glassy carbon electrode (GC, 3 mm diameter 66-EE047 Cypress Systems) was employed as the working electrode (WE), while platinum and silver wires were used as counter (CE) and quasi-reference (QRE) electrodes, respectively. The GC electrode was stored in ethanol and polished with a 0.05  $\mu\text{m}$  diamond suspension (Metadi Supreme Diamond Suspension, Buehler) before the experiments, then ultrasonically rinsed with water for 10 minutes and ethanol for 10 minutes. It was electrochemically activated in the electrolyte solution by means of several voltammetric cycles at 0.5 Vs<sup>-1</sup> between the anodic and cathodic solvent/electrolyte discharges. The RE was separated from the catholyte by glass frits. It was calibrated at the end of each experiment against the ferrocene/ferricenium (Fc|Fc<sup>+</sup>) couple, whose formal potential is 0.460 V against KCl-saturated calomel electrode (SCE). The standard potentials were calculated as the average value between cathodic and anodic peak potentials for reversible or quasi-reversible processes.

We determined the diffusion coefficients of NCNDs and mNCNDs, Ru(bpy)<sub>3</sub><sup>2+</sup> through cyclic voltammetric experiments at different scan rate (from 0.05 to 1 V s<sup>-1</sup>) and applying the Randles–Sevcik equation (eq. 4.1):<sup>43</sup>

$$i_p = 2.69 \cdot 10^5 n^{3/2} AD^{1/2} C\nu^{1/2} \quad (4.1)$$

where  $n$  is the number of electrons transferred in the redox event (usually 1),  $A$  the electrodic surface ( $\text{cm}^2$ ),  $D$  the diffusion coefficient ( $\text{cm}^2/\text{s}$ ),  $v$  the scan rate ( $\text{V}/\text{s}$ ) and  $C$  the concentration ( $\text{mol}/\text{cm}^3$ ). The cyclic voltammetric experiments for NCNDs/mNCNDs and the diffusion coefficients ( $D$ ) were determined on the oxidation peaks. It was observed that the peak currents are proportional to the square root of the scan rate ( $v^{1/2}$ ), indicating that all the oxidation/reduction processes were diffusion controlled and no adsorption phenomena on the electrode surface were occurring (Figure 4.9).

#### *Electrochemiluminescence*

A custom system was used for ECL characterisation, consisting in an electrochemical cell based on a glassy carbon (Tokai Inc.) disk electrode (3 mm diameter) as the WE, which was closely facing (a few millimetres) the photomultiplier tube detector (PMT, Hamamatsu, H10723-01, Japan) controlled by an Autolab electrochemical workstation PGSTAT101 (Metrohm, The Netherlands). The RE employed was an Ag/AgCl (1M KCl) from CHI-Instruments and it was separated from the catholyte by a glass frit. A platinum wire served as the CE. For potentiodynamic measurements (Cyclic Voltammetry), the solution was scanned at 0.05 V/s from +0.5 V to +1.45 V. For chronamperometric experiments, used for the detection of EP, the pulsing potential was set at +1.4 V vs Ag/AgCl (1M KCl). The pulse width was 1 s. The transients and the faradic currents were managed by using the software NOVA provided with the Autolab unit. The ECL spectrum was acquired using a calibrated electron multiplying charge couple device camera (A-DU970N-UVB Andor technology, Newton EM-CCD) coupled with a spectrograph (Andor Technology, Shamrock 163). For EP detection the values of ECL intensity are the average of three different measurements. The working electrode was mechanically cleaned before each run as mentioned above for the electrochemical measurements.

#### *Photophysical Measurements*

Absorption spectra were measured on a Shimadzu UV-3600 double-beam UV-Vis-NIR spectrometer and baseline corrected. Steady-state emission spectra were recorded on a HORIBA Jobin-Yvon IBH FL-322 Fluorolog 3 spectrometer equipped with a 450W xenon-arc lamp, double-grating excitation and emission monochromators (2.1 nm/mm dispersion, 1200 grooves/mm blazed at 500 nm) and a TBX-04 detector. Emission and excitation spectra were corrected for source intensity (lamp and grating) and emission

spectral response (detector and grating) by standard correction curves. Quantum yield measurements were performed with an absolute photoluminescence quantum yield spectrometer Quantaaurus C11347 (Hamamatsu, Japan) exciting the sample at  $\lambda_{\text{exc}} = 350$  nm.

#### 4.8 REFERENCES

- (1) Sun, Y. P.; Zhou, B.; Lin, Y.; Wang, W.; Fernando, K. a S.; Pathak, P.; Meziani, M. J.; Harruff, B. a.; Wang, X.; Wang, H.; Luo, P. G.; Yang, H.; Kose, M. E.; Chen, B.; Veca, L. M.; Xie, S. Y. *J. Am. Chem. Soc.* **2006**, *128* (24), 7756.
- (2) Georgakilas, V.; Perman, J. a.; Tucek, J.; Zboril, R. *Chem. Rev.* **2015**, *115* (11), 4744.
- (3) Baker, S. N.; Baker, G. A. *Angew. Chem. - Int. Ed.* **2010**, *49* (38), 6726.
- (4) Lim, S. Y.; Shen, W.; Gao, Z. *Chem. Soc. Rev.* **2015**, *44* (1), 362.
- (5) Roy, P.; Chen, P.-C.; Periasamy, A. P.; Chen, Y.-N.; Chang, H.-T. *Mater. Today* **2015**, *18* (8), 447.
- (6) Xu, X.; Ray, R.; Gu, Y.; Ploehn, H. J.; Gearheart, L.; Raker, K.; Scrivens, W. A. *J. Am. Chem. Soc.* **2004**, *126*, 12736.
- (7) Yang, S. T.; Cao, L.; Luo, P. G.; Lu, F.; Wang, X.; Wang, H.; Meziani, M. J.; Liu, Y.; Qi, G.; Sun, Y. P. *J. Am. Chem. Soc.* **2009**, *131* (32), 11308.
- (8) Cao, L.; Wang, X.; Meziani, M. J.; Lu, F.; Wang, H.; Luo, P. G.; Lin, Y.; Harruff, B. a.; Veca, L. M.; Murray, D.; Xie, S. Y.; Sun, Y. P. *J. Am. Chem. Soc.* **2007**, *129* (37), 11318.
- (9) Tang, J.; Kong, B.; Wu, H.; Xu, M.; Wang, Y.; Wang, Y.; Zhao, D.; Zheng, G. *Adv. Mater.* **2013**, *25* (45), 6569.
- (10) Zheng, M.; Liu, S.; Li, J.; Qu, D.; Zhao, H.; Guan, X.; Hu, X.; Xie, Z.; Jing, X.; Sun, Z. *Adv. Mater.* **2014**, *26* (21), 3554.
- (11) Lei, J.; Yang, L.; Lu, D.; Yan, X.; Cheng, C.; Liu, Y.; Wang, L.; Zhang, J. *Adv. Opt. Mater.* **2015**, *3* (1), 57.
- (12) Li, H.; He, X.; Kang, Z.; Huang, H.; Liu, Y.; Liu, J.; Lian, S.; Tsang, C. H. A.; Yang, X.; Lee, S.-T. *Angew. Chemie* **2010**, *122* (26), 4532.
- (13) Wang, F.; Chen, Y.; Liu, C.; Ma, D. *Chem. Commun.* **2011**, *47* (12), 3502.
- (14) Zhang, X.; Zhang, Y.; Wang, Y.; Kalytchuk, S.; Kershaw, S. V.; Wang, Y.; Wang,



- P.; Zhang, T.; Zhao, Y.; Zhang, H.; Cui, T.; Wang, Y.; Zhao, J.; Yu, W. W.; Rogach, A. L. *ACS Nano* **2013**, 7 (12), 11234.
- (15) Yu, X.; Liu, J.; Yu, Y.; Zuo, S.; Li, B. *Carbon N. Y.* **2014**, 68, 718.
- (16) Zhao, A.; Chen, Z.; Zhao, C.; Gao, N.; Ren, J.; Qu, X. *Carbon N. Y.* **2015**, 85, 309.
- (17) Luo, P. G.; Yang, F.; Yang, S.-T.; Sonkar, S. K.; Yang, L.; Broglie, J. J.; Liu, Y.; Sun, Y.-P. *RSC Adv.* **2014**, 4 (21), 10791.
- (18) Bard, A. J. *Electrogenerated Chemiluminescence*; **2004**.
- (19) Hu, L.; Xu, G. *Chem. Soc. Rev.* **2010**, 39 (8), 3275.
- (20) Miao, W. *Chem. Rev.* **2008**, 108 (7), 2506.
- (21) Miao, W.; Choi, J.-P.; Bard, A. J. *J. Am. Chem. Soc.* **2002**, 124 (48), 14478.
- (22) Liu, X.; Shi, L.; Niu, W.; Li, H.; Xu, G. *Angew. Chem. - Int. Ed.* **2007**, 46 (3), 421.
- (23) Richter, M. M. *Chem. Rev.* **2004**, 104 (6), 3003.
- (24) Han, S.; Niu, W.; Li, H.; Hu, L.; Yuan, Y.; Xu, G. *Talanta* **2010**, 81 (1–2), 44.
- (25) Valenti, G.; Rampazzo, E.; Blavardi, E.; Villani, E.; Fracasso, G.; Marcaccio, M.; Bertani, F.; Ramarli, D.; Dalcanale, E.; Paolucci, F.; Prodi, L. *Faraday Discuss.* **2015**, 185, 299.
- (26) Stewart, A. J.; Hendry, J.; Dennany, L. *Anal. Chem.* **2015**, 87, 11847.
- (27) Poulpiquet, A. De; Diez-buitrago, B.; Milutinovic, M. D.; Sentic, M. *Anal. Chem.* **2016**, 88, 6585.
- (28) Kebede, N.; Francis, P. S.; Barbante, G. J.; Hogan, C. F. *Analyst* **2015**, 140, 7142.
- (29) Irkham; Watanabe, T.; Fiorani, A.; Valenti, G.; Paolucci, F.; Einaga, Y. *J. Am. Chem. Soc.* **2016**.
- (30) Liang, P.; Dong, L.; Martin, M. T. *J. Am. Chem. Soc.* **1996**, 7863 (96), 9198.
- (31) Li, P.; Jin, Z.; Zhao, M.; Xu, Y.; Guo, Y.; Xiao, D. *Dalton Trans.* **2015**, 44 (5), 2208.
- (32) Wang, H.; He, Y.; Chai, Y.; Yuan, R. *Nanoscale* **2014**, 6, 10316.
- (33) Wang, H.; Yuan, Y.; Zhuo, Y.; Chai, Y.; Yuan, R. *Anal. Chem.* **2016**, 88, 2258.
- (34) Liang, W.; Zhuo, Y.; Xiong, C.; Zheng, Y.; Chai, Y.; Yuan, R. *Anal. Chem.* **2015**, 87, 12363.
- (35) Long, Y.-M.; Bao, L.; Zhao, J.-Y.; Zhang, Z.-L.; Pang, D.-W. *Anal. Chem.* **2014**, 86 (15), 7224.
- (36) Li, L.; Yu, B.; Zhang, X.; You, T. *Anal. Chim. Acta* **2015**, 895, 104.

- (37) Xu, Z.; Yu, J.; Liu, G. *Sensors Actuators B Chem.* **2013**, *181*, 209.
- (38) Arcudi, F.; Đorđević, L.; Prato, M. *Angew. Chem. - Int. Ed.* **2016**, *55*, 2107.
- (39) Strauss, V.; Margraf, J. T.; Dolle, C.; Butz, B.; Nacken, T. J.; Walter, J.; Bauer, W.; Peukert, W.; Spiecker, E.; Clark, T.; Guldi, D. M. *J. Am. Chem. Soc.* **2014**, *136*, 17308.
- (40) Evans, D. H. *Chem. Rev.* **2008**, *108*, 2113.
- (41) Knight, A. W.; Greenway, G. M. *Analyst* **1996**, *121* (November), 101R.
- (42) Liu, Z.; Qi, W.; Xu, G. *Chem. Soc. Rev.* **2015**, *44* (10), 3117.
- (43) Bertram, R. *Electrochemistry at solid electrodes. Monographs in Electroanalytical Chemistry and Electrochemistry*; Marcel Dekker, I., Ed.; Marcel Dekker, Inc., New York, **1969**; Vol. 1 Aufl., XI.
- (44) Kanoufi, F.; Zu, Y.; Bard, A. J. *J. Phys. Chem. B* **2001**, *105*, 210.
- (45) Tokel-Takvoryan, N. E.; Hemingway, R. E.; Bard, A. J. *J. Am. Chem. Soc.* **1973**, *95* (20), 6582.
- (46) Hercules, D. M.; Lytle, F. E. *J. Am. Chem. Soc.* **1966**, *88* (20), 4745.
- (47) Lytle, F. E.; Hercules, D. M. *Photochem. Photobiol.* **1971**, *13*, 123.
- (48) Wallace, W. L.; Bard, A. J. *J. Phys. Chem.* **1979**, *83* (10), 1350.
- (49) Jonah, C. D.; Matheson, M. S.; Meisel, D. *J. Am. Chem. Soc.* **1978**, *100* (5), 1449.
- (50) Kerr, E.; Doeven, E. H.; Wilson, D. J. D.; Hogan, C. F.; Francis, P. S. *Analyst* **2016**, *141*, 62.
- (51) Leland, J. K.; Powell, M. J. *J. Electrochem. Soc.* **1990**, *137*, 3127.
- (52) Kang, J.; Yin, X. B.; Yang, X.; Wang, E. *Electrophoresis* **2005**, *26* (9), 1732.
- (53) Guo, Y.; Yang, J.; Wu, X.; Du, A. *J. Fluoresc.* **2005**, *15* (2), 131.
- (54) Babaei, A.; Mirzakhani, S.; Khalilzadeh, B. *J. Braz. Chem. Soc.* **2009**, *20* (10), 1862.
- (55) Guo, Z. H.; Dong, S. J. *Electroanalysis* **2005**, *17* (7), 607.
- (56) Li, F. *Talanta* **2003**, *59* (3), 627.
- (57) Martin, L. J.; Koegl, M.; Bader, G.; Cockcroft, X.; Fedorov, O.; Fiegen, D.; Gerstberger, T.; Hofmann, M. H.; Hohmann, A. F.; Kessler, D.; Knapp, S.; Knesl, P.; Kornigg, S.; Mu, S.; Nar, H.; Rogers, C.; Rumpel, K.; Schaaf, O.; Tallant, C.; Vakoc, C. R.; Zeeb, M.; Zoephel, A.; Pearson, M.; Boehmelt, G.; McConnell, D. *J. Med. Chem.* **2016**, *59*, 4462.

- (58) Tomassoli, I.; Gündisch, D. *Bioorg. Med. Chem.* **2015**, *23* (15), 4375.
- (59) Moegling, J.; Benischke, A. D.; Hammann, J. M.; Vepr, N. A.; Zoller, F.; Rendenbach, B.; Hoffmann, A.; Sievers, H.; Schuster, M.; Knochel, P.; Herrespawlis, S. *European J. Org. Chem.* **2015**, 7475.

# Chapter 5

## Transition Metal Complex-Nanoparticle Hybrid Nanostructures for ECL Applications

### Abstract

We report, for the first time, a nitrogen-doped carbon nanodots (NCNDs) covalently-linked system with transition metal complexes for ECL applications.

The preparation, as well as the morphological, photophysical and electrochemical characterizations of ruthenium and iridium complexes-NCNDs hybrids is discussed. To a deep investigation on their ECL properties, follow their evaluation as self-enhanced and multi-labels ECL platforms.

The work presented in this chapter has been accomplished with the aid of *Ms. Francesca Arcudi* from *Prof. Maurizio Prato* research group (University of Trieste).

Part of the work discussed in this chapter has been accepted as “Amine-Rich Nitrogen-Doped Carbon NanoDots as Platform for Self-Enhancing Electrochemiluminescence” in *Angewandte Chemie* **2017** (DOI: 10.1002/anie.201611879).

## 5.1 INTRODUCTION

In recent years, electrochemiluminescence (ECL) has been widely exploited in the design of powerful analytical assays, that allow unprecedented selectivity and sensitivity coupled with ease of use and low costs.<sup>1,2</sup> In commercial ECL analytical platforms the presence of the ECL label indicates the presence of the analyte and the total intensity of the ECL signal can be correlated to the concentration of the latter.<sup>1,3</sup> In order to endow the assays with high sensitivity, a lot of effort has been devoted to the design of labels (both organic molecules and metal complexes) with high ECL efficiencies.<sup>2</sup> In this context, different strategies have been pursued to achieve this goal.

One of the possible strategies is to increase the label-per-analyte-molecule ratio, achieving an increased number of photons generated during the analyses.<sup>4-6</sup> However, when the ECL properties of a label are probed in solution, i.e. without the immobilization on an electrode surface, the whole process finds its bottleneck in the labels diffusion. In this case, increasing the size of a multi-label system may not bring any improvement in the ECL efficiency, due to a slow diffusion towards the electrode.<sup>5,7</sup>

In a different approach, fluorophores bearing organic moieties that can act as intramolecular co-reactants have attracted a lot of attention.<sup>8-12</sup> When an emitter and a suitable co-reactant are bound in the same molecular unit, a new ECL reaction pattern, termed self-enhanced ECL, is observed. Here, the electron transfer between luminophore and the co-reactant group occurs intramolecularly, showing several advantages as compared with the usually used intermolecular ECL reaction, such as shorter electronic transmission distance, improved luminous stability, simpler operation, decreased measurement error, and use of less reagent. Moreover, the intramolecular self-enhanced ECL reaction reduces the loss of energy caused by the relaxation effect in the intermolecular reaction when the co-reactants diffuse to the electrode surface, resulting in a significative luminous efficiency enhancing.<sup>8,10,11,13</sup>

Nanomaterials are nowadays considered a viable alternative to molecules for ECL applications. Nanomaterials properties are often described as intermediate between those of individual molecules and bulk materials, so that they can be used in different ways in ECL assays. Some representative examples include their employment for the electrode surface modification, as ECL-active chromophores or as scaffolds to carry other ECL-

active species.<sup>14,15</sup> Indeed, there have been various reports of ECL probes loaded on metal, silica, polymeric nanoparticles or single-wall nanotubes.<sup>5-7,14,16-19</sup> Up to now, most studies report on nanomaterials with sizes between 100 and 7 nm. They display diffusion coefficients that are usually orders of magnitude lower than that of free molecules and result in lower ECL efficiencies.<sup>20</sup> Some studies reported that the encapsulation of ruthenium or iridium complexes in silica nanoparticles does not promote ECL enhancement because of the large size, even if the silica shell protects them from water and oxygen quenching.<sup>5,7</sup> Additionally, their encapsulation prevents the contact with the electrode surface, causing a difficult tunneling of electrons and co-reactants in the structure (Figure 5.1a).<sup>5,7</sup> In other reports, nanoparticles functionalized with chromophores can display affected optical properties, resulting for example in emission quenching phenomena. For example, Cui *et al.* reported a strong quenching effect of gold nanoparticles on the PL and ECL intensities of ruthenium-decorated nanoparticles compared to those of the isolated complex, as shown in Figure 5.1b.<sup>6</sup>

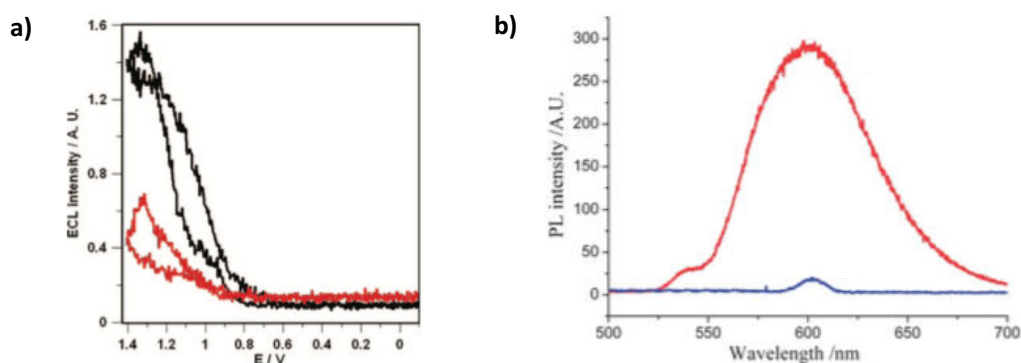


**Figure 5.1.** a) ECL profiles of a  $Ru(bpy)_3^{2+}$  (black line) and  $Ru(bpy)_3^{2+}$  covalently doped silica nanoparticles (red line) solutions at the same optical density of ruthenium complex ( $2 \cdot 10^{-5} M$ ). Reprinted from reference (7) b) photoluminescence spectra of  $Ru(bpy)_2(NH_2-phen)^{2+}$  (red trace) and AuNPs synthesized with  $Ru(bpy)_2(NH_2-phen)^{2+}$  (blue trace). Reprinted from reference (6)

In this chapter, in order to overcome the typical slow diffusion of nanostructured systems, that hinders ECL efficiency improvements, we built on the use of nanomaterials having sizes in the range of 1.5-5 nm. In particular, we describe, for the first time, the ECL application of nitrogen-doped carbon nanodots (NCNDs, with size below 3 nm) decorated with transition metal complexes. The following paragraphs describe the preparation, as well as the structural and morphological characterizations, of nanohybrid materials consisting of ruthenium and iridium complexes covalently bound to NCNDs scaffolds. Their photophysical behavior in solution by means of absorption, steady-state and time-

resolved fluorescence spectroscopy were evaluated in order to investigate the occurrence of possible quenching phenomena once the complexes are attached to the nanoparticle surface. Moreover, electrochemical studies were performed to shed light on the hybrids mobility in solution through the determination of their diffusion coefficients. Finally, the ECL properties in solution of these novel nanohybrids were studied.

To conclude, since the NCNDs can effectively act as co-reactant, as discussed in chapter 4, we evaluated their simultaneous employment as ECL carrier and co-reactant, aiming to a self-enhanced ECL system. Additionally, upon immobilization on an electrode surface, we evaluate our hybrid systems as platform for more signal-generating units, in an attempt to propose a strategy for signal amplification.

## **5.2 RUTHENIUM(II) AND IRIIDIUM(III) COMPLEXES- NCNDs NANOSTRUCTURED MATERIALS**

NCNDs were kindly provided by the group of Prof. Maurizio Prato (University of Trieste). Their synthesis and characterization are discussed in chapter 4.<sup>21</sup>

### **5.2.1 Grafting of metal complexes onto NCNDs**

The presence of amino groups on the NCNDs surface allow easy insertion of the metal complexes through standard organic chemistry procedures.

The hybrids were prepared through condensation reactions of the NCNDs amino groups with the commercially available NHS-activated carboxylic acid of the ruthenium complex (bis-(2,2-bipyridyl)(4-carboxypropyl, 4'-methyl- 2,2'-bipyridine)ruthenium(II) chloride (Ru-COOSu)) or the carbodiimide-activated carboxylic acid of the iridium complex (iridium (6-phenylphenanthridine)<sub>2</sub>-(carboxyethylphenyl) pyridine-2-carboxylic acid (Ir-COOH)).<sup>22</sup> The hybrid materials, indicated as Ru-NCNDs and Ir-NCNDs (Figure 5.2), were purified by using size exclusion chromatography and obtained as orange solids.

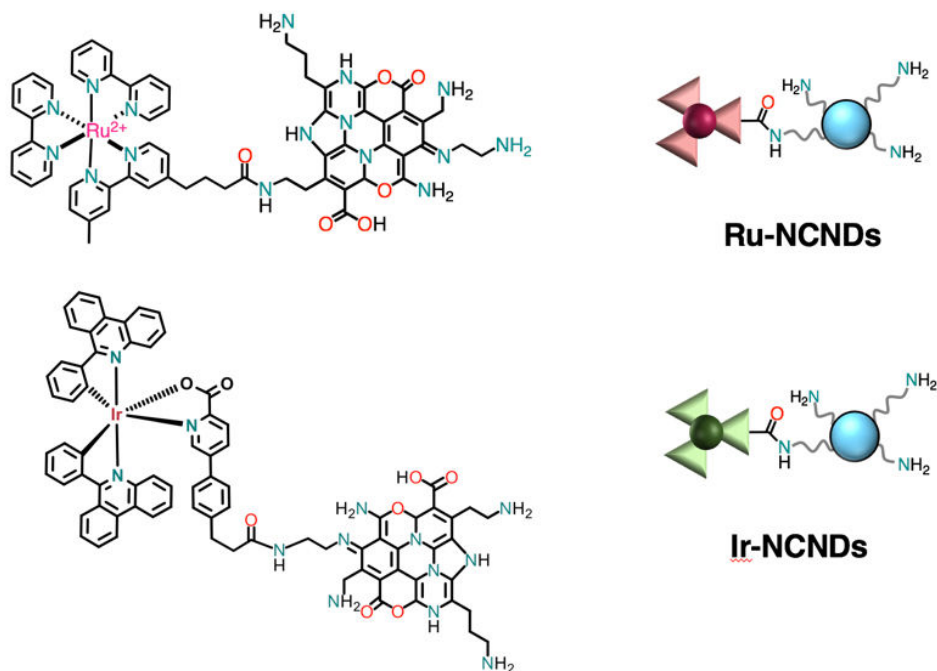


**Figure 5.2.** Covalently linked ruthenium-NCNDs nanoconjugate on the top and covalently linked iridium-NCNDs nanoconjugate on the bottom.

## 5.2.2 Characterization

### *Transmission electron microscopy*

Transmission electron microscopy (TEM) was employed to probe the morphological features of the conjugates. TEM images show that the quasi-spherical shape of NCNDs is retained in the hybrids, while the average size increases from  $2.5 \pm 0.8$  nm of the bare NCNDs to  $4.5 \pm 0.6$  nm and  $3.2 \pm 0.9$  nm for Ru-NCNDs and Ir-NCNDs (Figure 5.3), respectively. These values suggest the presence of c.a. 3 ruthenium complexes and c.a. 2 iridium complexes for each dot and was found in accordance to the ICP-MS measurements (details in experimental section 5.4).



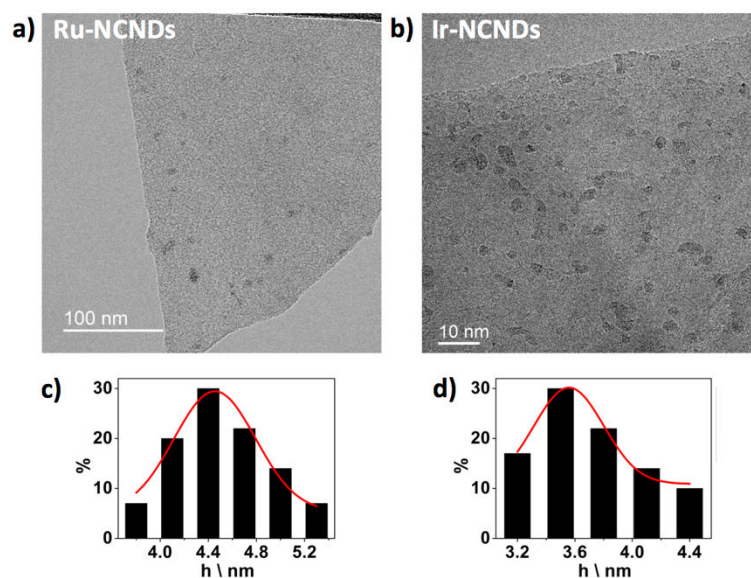


**Figure 5.3.** Representative TEM image of **a)** Ru-NCNDs and **b)** Ir-NCNDs hybrid drop-casted on a lacey carbon grid; **c-d)** Size histograms with curve fit to the data using a Gaussian model for each hybrid, respectively.

### FT-IR spectroscopy

The formation of the hybrids was monitored by FT-IR spectroscopy. The FT-IR spectrum of Ru-NCNDs (Figure 5.4, red trace) shows the typical bands of NCNDs (Figure 5.4, black trace),<sup>21</sup> as well as the bands characteristic of the metal complexes (grey trace),<sup>23</sup> and confirm the amide bond formation.

Regarding the ruthenium-based system, in Figure 5.4 the three peaks corresponding to the vibrations of the NHS-ester bonds at 1814, 1783, and 1736  $\text{cm}^{-1}$  observed for Ru-COOSu disappear in the hybrid spectrum for the benefit of two characteristic vibrations of amide I (at 1653  $\text{cm}^{-1}$ ) and amide II (1547  $\text{cm}^{-1}$ ).

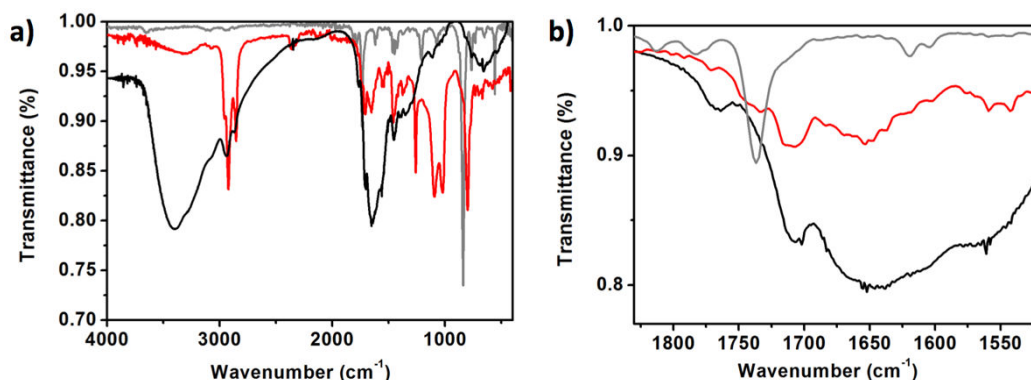


**Figure 5.4.** *a)* FT-IR spectra of NCNDs (black trace), Ru-COOSu (grey trace) and Ru-NCNDs (red trace); *b)* zoom of the spectra in the region 1900-1400  $\text{cm}^{-1}$ .

Similarly, in the Ir-NCNDs spectrum (Figure 5.5) new peaks related to the amidation reaction can be detected (at 1630 and 1555  $\text{cm}^{-1}$ ), together with the disappearance of the C=O stretching mode of the carboxylic acid at 1722  $\text{cm}^{-1}$ .

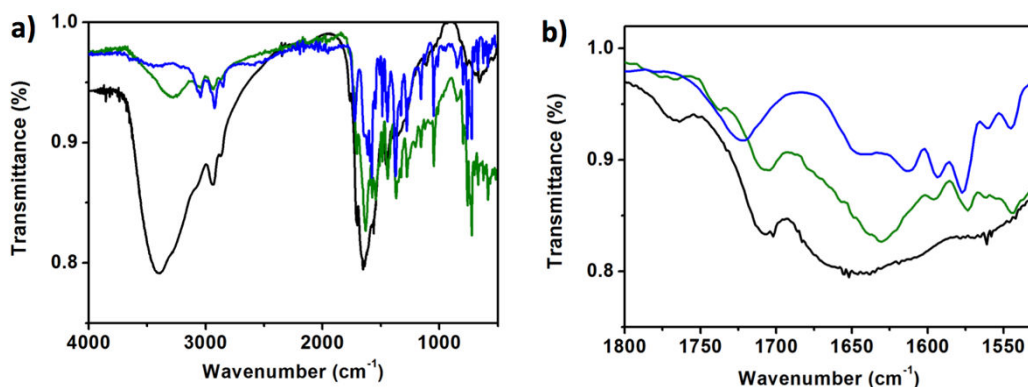


**Figure 5.5.** *a)* FT-IR spectra of NCNDs (black trace), Ir-COOH (blue trace) and Ir-NCNDs (green trace); *b)* zoom of the spectra in the region 1900-1200  $\text{cm}^{-1}$ .

### 5.2.3 Photophysical properties

For the sake of utilization in practical bionalalytical settings, both photophysical and ECL measurements were performed in a buffer solution (ProCell®) specially designed for commercial immunoassay system. ProCell® solution was provided by Roche and consists

in a phosphate buffer enriched of TPrA and different surfactants with a confidential specific chemical composition.

The absorption and fluorescence spectra of the Ru-NCNDs and Ir-NCNDs hybrids, together with the free metal complexes and the bare NCNDs as references, are reported in figures 5.6 and 5.7.

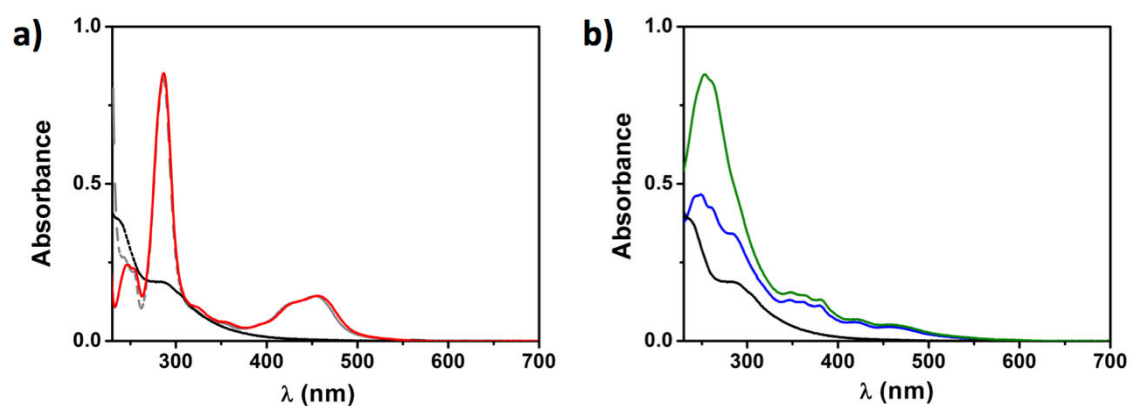


**Figure 5.6.** UV-Vis absorption spectra of **a)** Ru(bpy)<sub>3</sub><sup>2+</sup> (grey trace), NCNDs (black trace) and Ru-NCNDs (red trace), **b)** Ir-COOH (blue trace), NCNDs (black trace) and Ir-NCNDs (green trace), in ProCell® solution. (Metal complexes concentration: 10<sup>-5</sup>M).

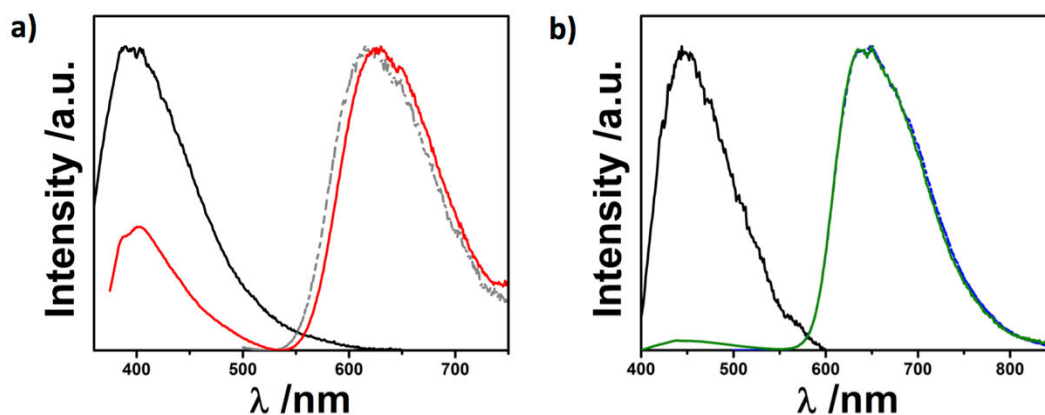


**Figure 5.7.** PL emission spectra of **a)** Ru(bpy)<sub>3</sub><sup>2+</sup> (grey trace), NCNDs (black trace) and Ru-NCNDs (red trace),  $\lambda_{exc}=340$  nm, **b)** Ir-COOH (blue trace), NCNDs (black trace) and Ir-NCNDs (green trace),  $\lambda_{exc}=380$  nm, in ProCell® solution. (Metal complexes concentration: 10<sup>-5</sup>M).

The absorption spectra of the hybrid materials show the main features of both its parent components, with a slight shift of the metal to ligand charge transfer (<sup>1</sup>MLCT) band of Ru-NCNDs at lower energy (Figure 5.6a). The UV-visible spectra of Ru(bpy)<sub>3</sub><sup>2+</sup> and Ru-NCNDs exhibit the expected features of most ruthenium-based metal complexes.<sup>24–26</sup> They

are characterized by intense transitions at high energy (200 – 350 nm) and weaker bands in the visible region (400 –500 nm). In particular, The band at 285 nm in the UV range is assigned to bipyridil-based  $\pi$ - $\pi^*$  -allowed ligand centered ( $^1$ LC) transitions. The two bands at 240 and 453 nm are assigned to  $^1$ MLCT d- $\pi^*$  transitions. The shoulders visible at 320 and 340 nm are related to MC transitions. The maximum at 450 nm results slightly red-shifted probably due to a rigidity of the hybrid system respect to the free metal complex.

For Ir-COOH and Ir-NCNDs, the UV band at wavelength around 250 nm is assigned to the ligand centered ( $^1$ LC)  $\pi$ - $\pi^*$  transition, while the bands at 300-400 nm are a mixture of singlet-manifold ligand-to-ligand charge transfer ( $^1$ LLCT) and metal-to-ligand charge transfer ( $^1$ MLCT) transitions. The band at 456 nm is attributed to both singlet and triplet metal to ligand charge transfer transition,  $^1$ MLCT and  $^3$ MLCT, respectively.

In figure 5.7a, the PL spectrum of Ru-NCNDs ( $\lambda_{exc}=340$  nm) exhibits two distinct contributions at 400 nm and at 630 nm, corresponding to the NCNDs-centered emission and the  $^3$ MLCT of the ruthenium-bipyridine complex, respectively. The latter contribution also appears shifted to lower energy, in respect to the free complex. For Ir-NCNDs, the fluorescence peak at 650 nm ( $\lambda_{exc}=380$  nm) does not show any bathochromic shift (Figure 5.7b).

The PL excited state lifetimes of the hybrid materials are mono-exponentials when detected in the metal complex emission band, while a more complex (tri-exponential) decay is observed for the NCNDs emission, without significant variations from the free components (Table 5.1). The absolute photoluminescence quantum yield (PLQY) of the metal complexes in the hybrid were found to be the same of the complexes alone, respectively 4% and 12%, indicating that no quenching processes occur due to the attachment on the NCNDs. From the analysis of the data, we can conclude that the optical properties of the redox centers are not affected after the coupling, which is a crucial requirement for their effective use in ECL.

**Table 5.1.** Photophysical data in ProCell® solution: **a)**  $\lambda_{exc}$  375 nm/  $\lambda_{em}$  420 nm; **b)**  $\lambda_{exc}$  440 nm/  $\lambda_{em}$  625 nm; **c)**  $\lambda_{exc}$  440 nm/  $\lambda_{em}$  640 nm; **d)**  $\lambda_{exc}$  300 nm; **e)**  $\lambda_{exc}$  460 nm; **f)**  $\lambda_{exc}$  380 nm.

	<b>Lifetime / ns</b>	<b>PLQY / %</b>
<b>NCNDs</b>	$\tau_1=14.0$ (2.3%) $\tau_2=5.1$ (34%) $\tau_3=2.1$ (63.7%) <sup>a</sup>	8 <sup>d</sup>
<b>Ru-COOSu</b>	329.1 <sup>b</sup>	4 <sup>e</sup>
<b>Ru-NCNDs</b>	$\tau_1=11.7$ (11.8%) $\tau_2=3.6$ (26.3%) $\tau_3=1.0$ (61.9%) <sup>a</sup>	4 <sup>d,e</sup>
	363.0 <sup>b</sup>	
<b>Ir-COOH</b>	734.4 <sup>c</sup>	14 <sup>f</sup>
<b>Ir-NCNDs</b>	$\tau_1=9.9$ (21.9%) $\tau_2=3.6$ (62.7%) $\tau_3=1.1$ (15.4%) <sup>a</sup>	12 <sup>f</sup>
	785.5 <sup>c</sup>	

Fluorescence anisotropy measurements were carried out to further demonstrate the increased size of the hybrids in comparison to the bare NCNDs (Figure 5.8). This technique is commonly used for rotational time measurements, in association with the emission transition moment that lies along the fluorophore structure.<sup>27,28</sup> The rotational time depends on the viscosity of the solvent and on the size of the fluorophore.<sup>27</sup> The bigger is the fluorophore, longer is the rotational time necessary to get a depolarized emission. As expected, the rotational time of the anisotropic emission of NCNDs increases from 1.45 ns to 2.3 ns, for the free NCNDs and the hybrid Ru-NCND, and from 1.45 ns to 2.2 ns for the free NCNDs and the hybrid Ir-NCNDs.

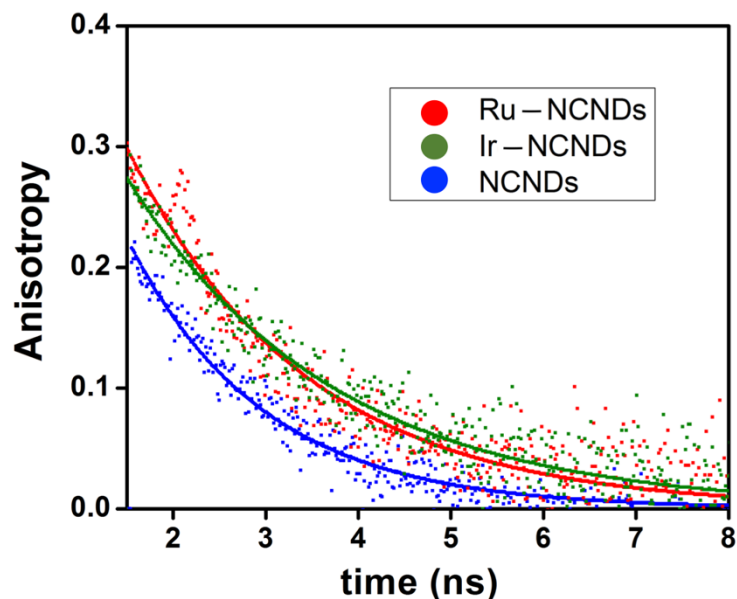


**Figure 5.8.** Anisotropy of Ru-NCNDs (red dots), Ir-NCNDs (green dots) and NCNDs (blue dots) in Ethylene Glycol at room temperature.

## 5.2.4 Electrochemistry

To gain deeper insight on the electronic properties of the new systems, an extensive electrochemical investigation of NCNDs, Ru(bpy)<sub>3</sub><sup>2+</sup>, Ru-NCNDs, Ir-COOH and Ir-NCNDs in DMF was carried out. Electrochemistry, like ECL, is a diffusion limited process and, as such, is greatly influenced by the size and mobility of the electrochemically active species in solution. In order to determine the diffusion coefficients of the functionalized nanoparticles and investigate their influence on the ECL process, cyclic voltammetric experiments (CV) at different scan rates (from 0.01 to 1 V/s) were performed and the Randles–Sevcik equation was applied (see experimental section 5.4).<sup>29</sup>

### 5.2.4.1 Ru-NCNDs

As illustrated in Figure 5.9, the CV of Ru-NCNDs (at scan rate 0.1 V/s) shows the electrochemical features of both NCNDs and Ru(bpy)<sub>3</sub><sup>2+</sup>. In the anodic region two distinctive oxidation peaks are present, at +1.09 V assigned to the oxidation of the free amine on the NCNDs surface and at +1.30 V related to the oxidation of Ru<sup>2+</sup> to Ru<sup>3+</sup>, as discussed in chapter 4. The occurrence of only a single oxidation wave for Ru(bpy)<sub>3</sub><sup>2+</sup> suggests that all the complexes in the proximity of the electrode are electrochemically

equivalent. On the other hand, the three peaks in the cathodic region (at -1.24; -1.42 and -1.71 V) correspond to the reduction of the three bipyridine ligands.<sup>30,31</sup>

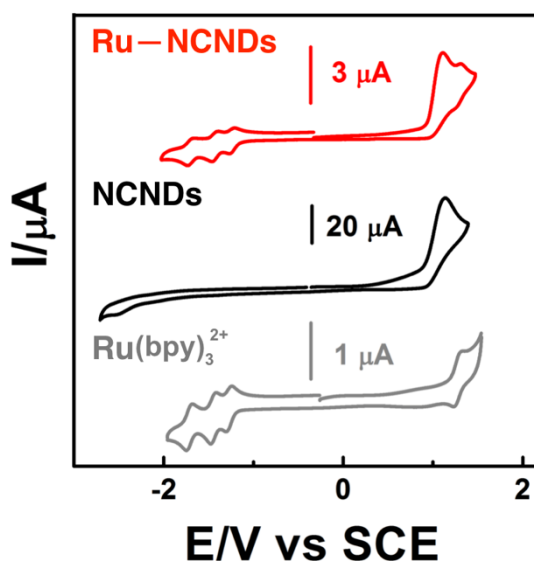


**Figure 5.9.** CVs of Ru-NCNDs (red trace), NCNDs (black trace, 1 mg/mL) and Ru(bpy)<sub>3</sub><sup>2+</sup> (grey traces) at the same concentration of chromophores (0.26 mM) in 0.1 M TBAPF<sub>6</sub> DMF solution. Scan rate 0.1 V s<sup>-1</sup>, potential referred to SCE at room temperature using platinum wire as counter electrode.

Further experiments were carried out at different scan rates to determine the diffusion coefficients of Ru(bpy)<sub>3</sub><sup>2+</sup> and Ru-NCNDs, as shown in figure 5.10a-b. NCNDs diffusion coefficients were already calculated in the previous chapter. The peak current intensities for the studied samples ( $I_p$ ) were found to be proportional to the square root of the scan rate ( $\nu^{1/2}$ ), as shown in Figure 5.10c-d. The intercept of the linear plots  $I_p$  vs  $\nu^{1/2}$ , are very close to zero, suggesting that oxidation and reduction processes were diffusion controlled and no adsorption phenomena on the electrode surface were occurring. The diffusion coefficient (D) can be therefore determined by using Randles–Sevcik equation on the oxidation peak related to Ru<sup>2+</sup>/Ru<sup>3+</sup>. The calculated values (Figure 5.10e) are in agreement with those reported in the literature for zero dimensional (spherical) nanoparticles with diameters ranging from 1 to 5 nm.<sup>32,33</sup> The diffusion coefficient found for Ru-NCNDs is about one sixth that of the free Ru complex, as expected from the increased size.

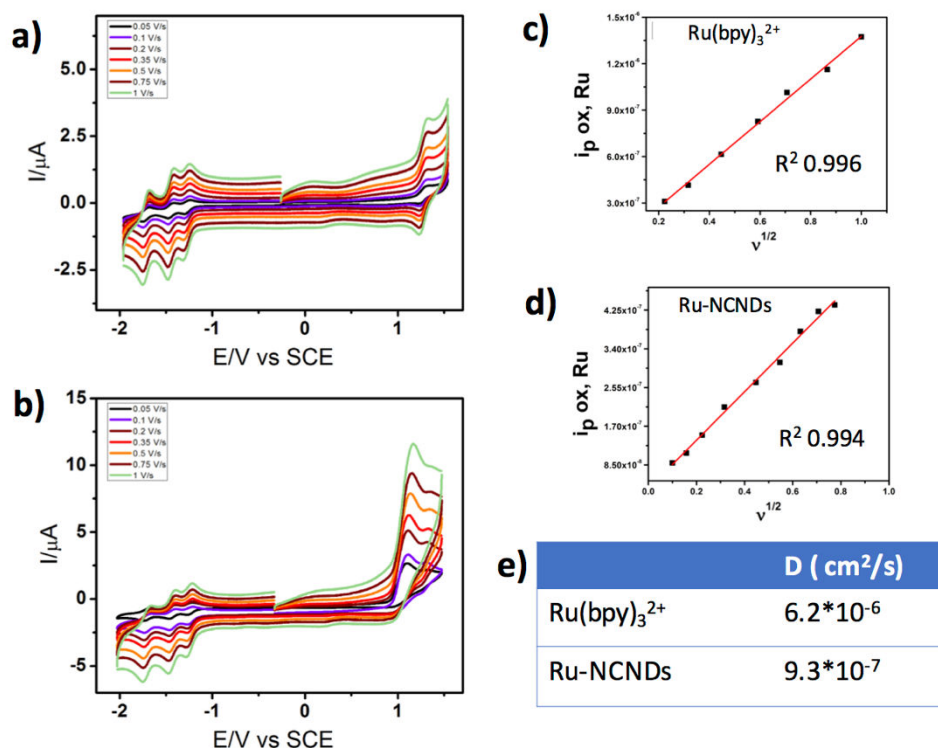


**Figure 5.10.** **a)** CVs of  $\text{Ru}(\text{bpy})_3^{2+}$ , **b)** CVs of Ru-NCNDs at the same concentration of chromophores (0.26 mM) in 0.1 M TBAPF<sub>6</sub> DMF solution and GC (1 mm) as working electrode. Scan rate from 0.05 V s<sup>-1</sup> to 1 V s<sup>-1</sup>;  $i_p$  vs  $v^{1/2}$  of **c)** CVs of  $\text{Ru}(\text{bpy})_3^{2+}$  and **d)** CVs of Ru-NCNDs. **e)** table reporting the diffusion coefficients ( $D$ , cm<sup>2</sup>/s) calculated by using Randles-Sevcik equation for  $\text{Ru}(\text{bpy})_3^{2+}$  and Ru-NCNDs.

#### 5.2.4.2 Ir-NCNDs

While in the case of Ru-NCNDs the features of the bare NCNDs and the free metal complex can be clearly told in the anodic part of the voltammogram, for Ir-NCNDs (Figure 5.11) just one peak could be identified due to the proximity of the oxidation peaks of NCNDs and Ir-COOH, +1.09 V and +1.12 V, respectively. The peaks in reduction are observed at -1.43 V, -1.74 V and -2.26 V, the latter being slightly less pronounced in the hybrid in respect to the free complex, probably correlated to the picolinic ligand which is the one who binds the amino group on the surface of the nanodots. As for the ruthenium hybrid discussed above, CV experiments were performed with scan rates ranging from 0.05 V s<sup>-1</sup> to 1 V s<sup>-1</sup>. Given the linear dependence of  $I_p$  on  $v^{1/2}$  (Figure 5.12c-d), the diffusion coefficients of the species were calculated and shown the same trend found for ruthenium-based hybrid (Figure 5.12e).



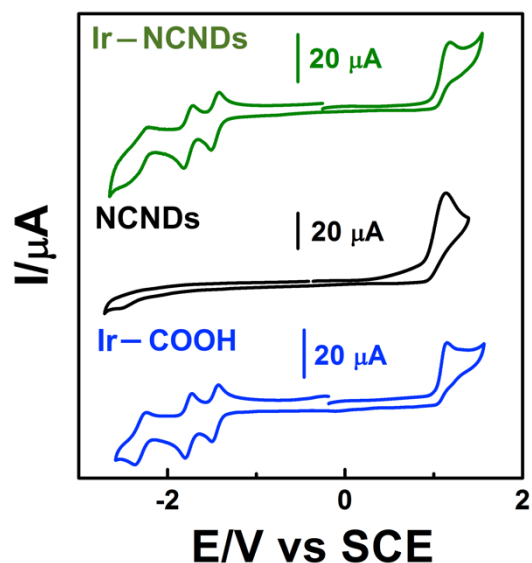


**Figure 5.11.** CVs of Ir-NCNDs (green trace), NCNDs (black trace, 1 mg/mL) and Ir-COOH (blue traces) at the same concentration of chromophores (1 mM) in 0.1 M TBAPF<sub>6</sub> DMF solution. Scan rate 0.1 V s<sup>-1</sup>, potential referred to SCE at room temperature using platinum wire as counter electrode.

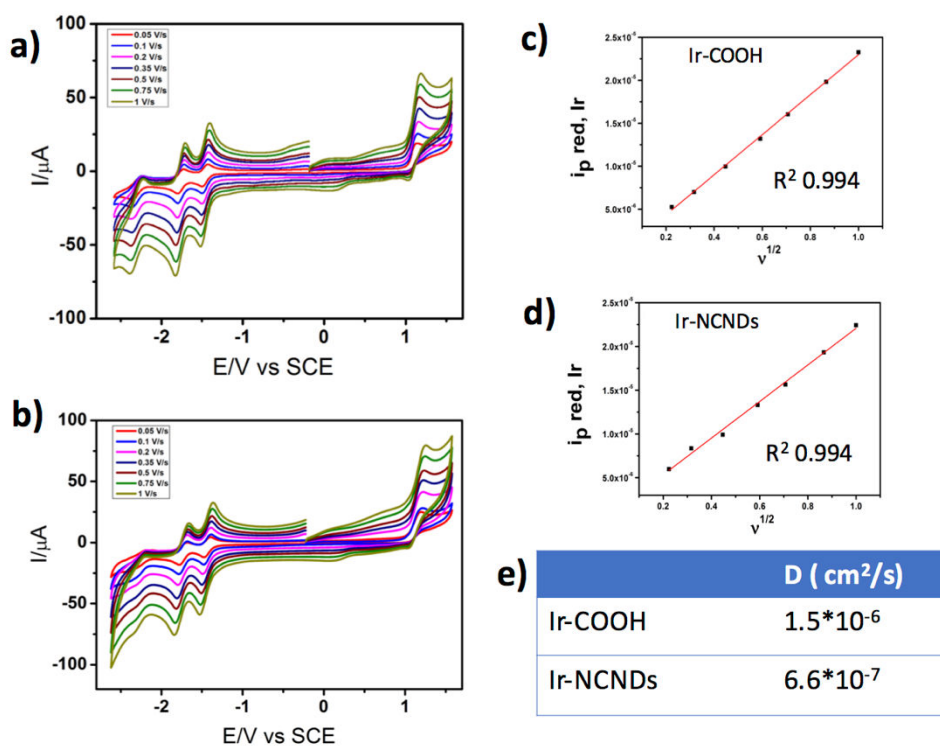


**Figure 5.12.** a) CVs of Ir-COOH, b) CVs of Ir-NCNDs at the same concentration of chromophores (1 mM) in 0.1 M TBAPF<sub>6</sub> DMF solution and GC (1 mm) as working electrode. Scan rate from 0.05 V s<sup>-1</sup> to 1 V s<sup>-1</sup>;  $i_p$  vs  $v^{1/2}$  of c) CVs of Ir-COOH and d) CVs of Ir-NCNDs. e) table reporting the diffusion coefficients ( $D$ , cm<sup>2</sup>/s) calculated by using Randles-Sevcik equation for Ir-COOH and Ir-NCNDs.

Therefore, both nanohybrids promise a mobility towards the electrode surface comparable to the one of the single label, which should result in an unaffected electrochemical process efficiency.

### 5.2.5 Electrochemiluminescence

The ECL activity of both hybrids was evaluated as function of voltage applied, time and emission profile in comparison to isoabsorbing (at 450 nm) reference solutions of the free complexes. In agreement with a previous report by Bard *et al.*<sup>31</sup> on the  $\text{Ru}(\text{bpy})_3^{2+}/\text{TPrA}$  system in aqueous solution, for a concentration  $10 \mu\text{M}$   $\text{Ru}(\text{bpy})_3^{2+}$ , two waves at  $+0.93 \text{ V}$  and  $+1.18 \text{ V}$  vs  $\text{Ag}/\text{AgCl}$  ( $1\text{M}$   $\text{KCl}$ ) are observed in the grey trace in figure 5.13a, both contributing to the generation of the excited state of  $\text{Ru}(\text{bpy})_3^{2+}$ . According to the oxidative-reduction mechanism I in Figure 5.13c, the first wave involves the electrochemical oxidation of  $\text{TPrA}$  to  $\text{TPrA}^{\bullet+}$ , which then oxidizes  $\text{Ru}(\text{bpy})_3^+$  to  $\text{Ru}(\text{bpy})_3^{2+*}$ . This latter species then decays to the ground state with emission of a photon. The second wave is instead ascribed to the classic oxidative-reduction mechanism II that occurs when electrogenerated  $\text{Ru}(\text{bpy})_3^{3+}$  reacts with  $\text{TPrA}$  (Figure 5.13d).  $\text{Ir-COOH}$  behaves likewise, showing a peak at  $+0.9 \text{ V}$ , associated to mechanism I, then reaching the maximum ECL intensity at around  $+1.25 \text{ V}$  with a small bump at  $+1.1 \text{ V}$  correlated to mechanism II (Figure 5.13b, blue traces).

Performing the same experiment on the hybrid materials yields different ECL profiles.  $\text{Ru-NCNDs}$  is characterized by a broader emission between  $+0.95 \text{ V}$  and  $+1.2 \text{ V}$  (Figure 5.13a, red trace), while for  $\text{Ir-NCNDs}$  two peaks at higher intensity than  $\text{Ir-COOH}$  appear at  $+0.9 \text{ V}$  and at  $+1.05 \text{ V}$  followed by a plateau (Figure 5.13b, green traces). These evidences could be correlated to the generation of the excited state of  $\text{Ru-NCNDs}^*$  and  $\text{Ir-NCNDs}^*$  coming from a mixed contribution of  $\text{TPrA}$  and the uncoupled amino groups that are oxidized within this range and they act as co-reactant, as previously demonstrated (see Chapter 4).

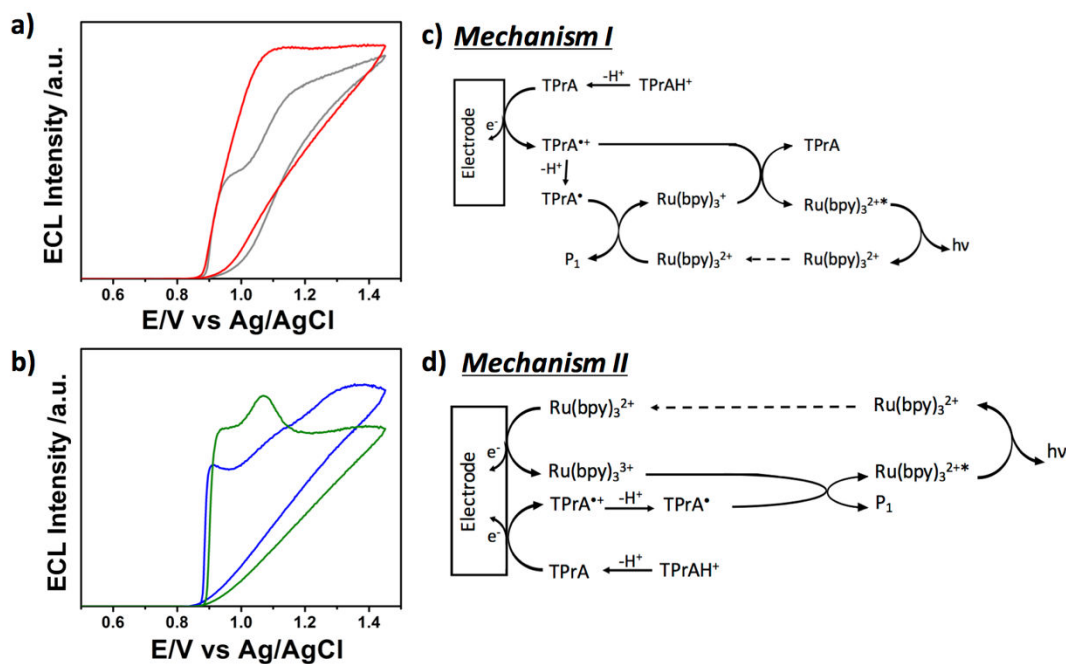


**Figure 5.13.** ECL Intensities recorded during a CV in Procell of **a)** Ru(bpy)<sub>3</sub><sup>2+</sup> (grey trace) and Ru-NCNDs (red trace), **b)** Ir-COOH (blue traces), Ir-NCNDs (green traces), using GC as working electrode. (Metal complexes concentration: 10<sup>-5</sup>M). Potential scan rate 0.05 V s<sup>-1</sup>. **c)** Mechanism I and **d)** Mechanism II reported by Bard et al.<sup>31</sup> for the system Ru(bpy)<sub>3</sub><sup>2+</sup>/TPrA in aqueous solution containing Ru(bpy)<sub>3</sub><sup>2+</sup> in low concentration.

The ECL efficiency of Ru-NCNDs and Ir-NCNDs were quantified by means of chronoamperometric experiments, referring to an iso-absorptive solution of [Ru(bpy)<sub>3</sub>]<sup>2+</sup> standard (details in experimental section 5.4). In this experiment, ECL was generated by a chronoamperometry pulse at +1.4 V for 1 s (Figure 5.14). Notably, the ECL intensities of the conjugated systems is the same of the single labels. Up to now, this represents the highest result for ECL labels-coupled nanoparticles that further demonstrate the absence of quenching phenomena (as previously reported for gold),<sup>6</sup> of diffusional problems typical

of nanostructured systems,<sup>7</sup> confirming that the 100% of the redox center are electrochemically and ECL active, and not only a percentage.<sup>5</sup>

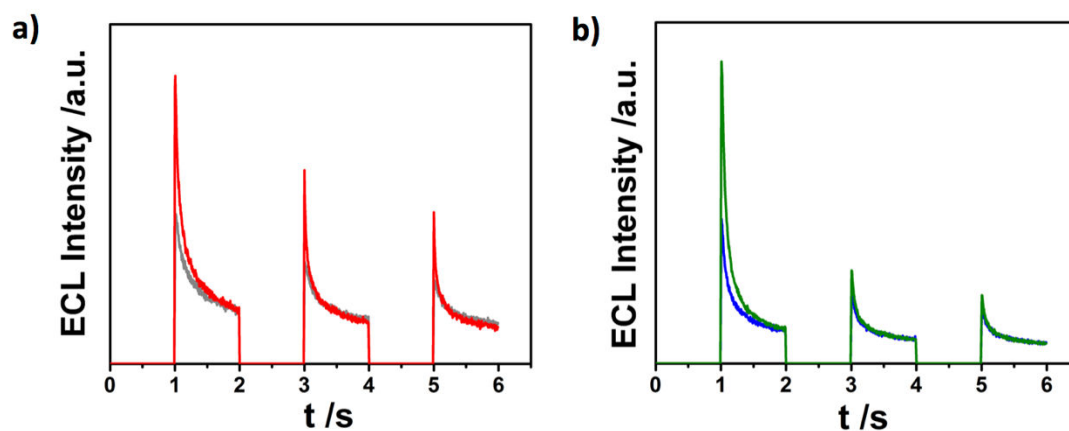


**Figure 5.14.** ECL Intensities in time in Procell of **a)**  $\text{Ru}(\text{bpy})_3^{2+}$  (grey trace) and  $\text{Ru-NCNDs}$  (red trace), **b)**  $\text{Ir-COOH}$  (blue traces),  $\text{Ir-NCNDs}$  (green traces), using GC as working electrode. (Metal complexes concentration:  $10^{-5}\text{M}$ ). Pulse at +1.4 V for 1 s.

Finally, the wavelength-resolved ECL spectra of the conjugates were recorded to investigate the nature of the electrogenerated emissive excited state. In this experiment, the ECL signal was collected during 5 chronoamperometry pulses of 1 s between 0 V and +1.4 V vs Ag/AgCl and the spectra were collected using a cooled EMCCD camera with an accumulation time of 10 s. Under these conditions, the ECL spectra well resemble the PL spectra measured in ProCell® (Figure 5.15), confirming that the photogenerated and the electrogenerated emitting excited state of each label are the same.

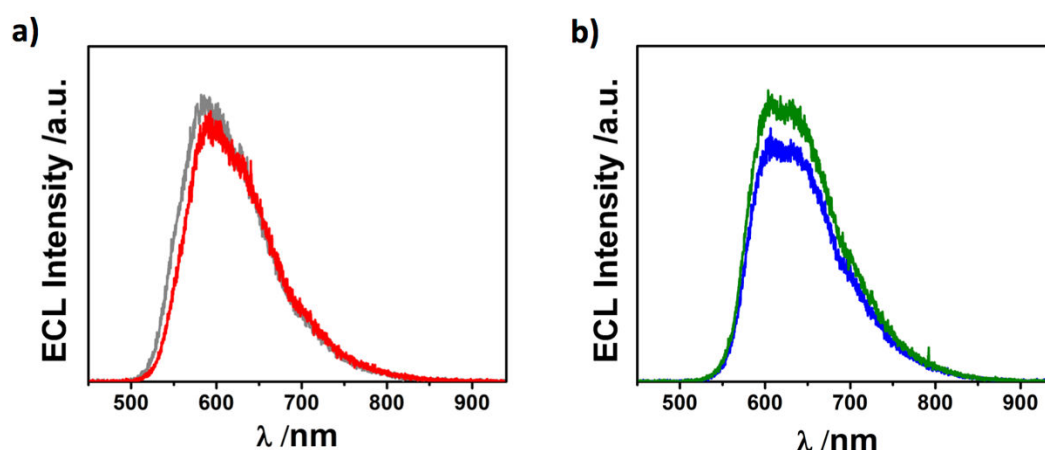


**Figure 5.15.** ECL emission spectra in Procell of **a)**  $\text{Ru}(\text{bpy})_3^{2+}$  (grey trace) and  $\text{Ru-NCNDs}$  (red trace), **b)**  $\text{Ir-COOH}$  (blue traces),  $\text{Ir-NCNDs}$  (green traces), using GC as working electrode. (Metal complexes concentration:  $10^{-5}\text{M}$ ).

### 5.2.6 Nanohybrids as self-enhancing and multi-label for ECL platforms

In light of the above considerations, we moved forward in the study of the previously discussed systems as ECL self-enhanced nanohybrids and we investigated the effect of their immobilization on the electrode surface on the ECL emission.

Since it was demonstrated the presence of NCNDs free amines in the hybrids and, as discussed in chapter 4, their effect as co-reactant for  $\text{Ru}(\text{bpy})_3^{2+}$  ECL emission, we investigated these novel hybrids as ECL self-enhanced platform. For this purpose, the ECL generation of the Ru-NCNDs hybrid in PBS solution, without the presence of additional co-reactant species such as TPrA, was studied.

In particular, we focused on the ruthenium-based hybrid due to its improved solubility in aqueous medium compared to the iridium-based system.

On the other hand, the ECL efficiency of Ir-NCNDs after immobilization on a gold surface was evaluated, to investigate if the exceptional finding of the totality of metal complexes ECL active in the nanohybrids, results in the expected increased ECL efficiency, that is proportional to the number of redox centers for nanodots.

#### 5.2.6.1 Self-enhancing ECL platform

To evaluate the co-reactant behavior of the NCNDs in Ru-NCNDs, we recorded the ECL curve of the hybrid in PBS solution, comparing those obtained for  $\text{Ru}(\text{bpy})_3^{2+}$  or for the uncoupled system NCNDs/  $\text{Ru}(\text{bpy})_3^{2+}$  (Figure 5.16b).

All experiments were performed in the same conditions and with the same optical density of  $\text{Ru}(\text{bpy})_3^{2+}$  (Figure 5.16a) to ensure the same overall content of complex in the three system. The ECL emission intensity of Ru-NCNDs was found to be two times higher respect to the uncoupled components (Figure 5.16b, blue and red traces), thus suggesting an ECL self-enhanced emission in the case of the covalently-linked hybrid system. Indeed, as previously reported for other self-enhanced systems,<sup>8,9,11-13</sup> we hypothesize that, in Ru-NCNDs, the intramolecular electron transfer is more efficient compared to the intermolecular reaction, due to a shorter electron-transfer path and consequent reduced energy loss.

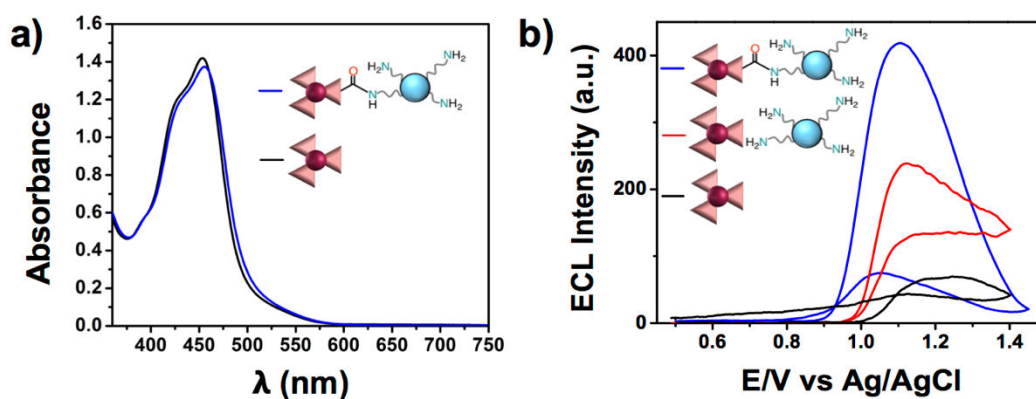


**Figure 5.16.** **a)** Absorption spectra at MLCT of  $\text{Ru}(\text{bpy})_3^{2+}$  (black trace) and  $\text{Ru-NCNDs}$  (blue trace) in PBS at the same concentration of chromophore (0.1 mM); **b)** ECL intensity during a potential scan of a PBS solution (pH=7.4) of  $\text{Ru}(\text{bpy})_3^{2+}$  (black trace), upon addition of 0.1 mg/mL of NCNDs (red trace) and of  $\text{Ru-NCNDs}$  (blue trace). (Metal complexes concentration:  $10^{-4}$  M). Scan rate  $0.05 \text{ V s}^{-1}$ . Potential referred to  $\text{Ag/AgCl}$  (KCl sat.) at room temperature. Platinum wire as counter electrode.

### 5.2.6.2 Multi-label ECL platform

$\text{Ir-NCNDs}$  were immobilized onto a gold electrode surface, mediated by a SAM (Figure 5.17b; detailed procedure in experimental section). For comparison, also the free metal complex was immobilized using the same procedure starting from a solution with the same optical density of the hybrid (Figure 5.17a; detailed procedure in experimental section). The ECL behavior for the two modified electrodes was evaluated in a PBS/Triton X 100 solution with TPrA 10 mM as co-reactant. The ECL curves obtained for the two surface-confined system showed an ECL enhancement for the  $\text{Ir-NCNDs}$  nano hybrid (Figure 5.17c, green trace) respect to the metal complex alone (Figure 5.17d, black trace). In particular, it was observed an ECL emission intensity two times higher for the nanoconjugate with respect to the reference, in agreement with the ICP calculation, and thus confirming that the totality of the redox centers covalently linked to the nanodots are ECL active.

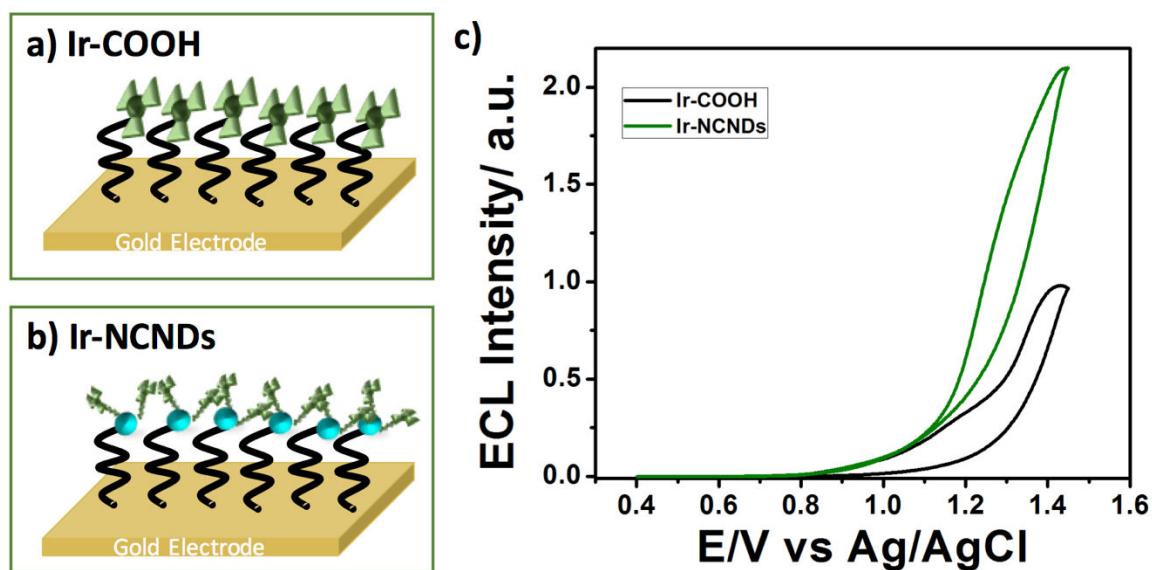


**Figure 5.17.** Schematic representation of **a)** Ir-COOH and **b)** Ir-NCNDs immobilization onto gold electrodes; **c)** ECL Intensities recorded during a CV in PBS/ Triton X 100/ TPrA 10 mM of Ir-NCNDs (green trace) and Ir-COOH (black traces) after immobilization. Scan rate  $0.05 \text{ V s}^{-1}$ .

### 5.3 CONCLUSION

In the framework of ECL systems based on nanomaterials, this chapter focused on the investigation of the largely unexplored application of NCNDs in ECL technology.

We reported for the first time the use of NCNDs in covalently-linked systems with ECL labels. We prepared NCND-based nanohybrids bearing ruthenium or iridium complexes with a straightforward synthetic strategy in order to assemble more signal-generating units into the nanodots platform. Notably, a deep spectroscopic and electrochemical investigation demonstrated the totality of the redox centers retain their properties in the nanohybrids.

The optical characterizations showed that no quenching phenomena for the redox centers occur after their immobilization onto NCNDs. The electrochemical studies shed light on the mobility of the hybrids towards the electrode through the determination of the diffusion coefficients. It was observed that due to the small dimensions of the nanoconjugates, the electron transfer kinetics in ECL should not be significantly modified compared to the bare metal complexes.

These results have prompted us to investigate the ECL behaviors of the nanohybrids. From ECL spectra and chronoamperometries, no significant difference in ECL efficiency of the nanoconjugates and the metal complexes references at the same concentration of redox

units were observed. These evidences substantiate the effective use of these nanohybrids as ECL platform. In particular, these results achieved are the highest for ECL labels-coupled nanoparticles ever reported, since in nanostructured architectures both the optical properties of the redox centers and their accessibility to the electrode surface can be affected. To summarize, it was in fact demonstrated that the totality of the redox centers in the presented hybrids are ECL actives, in close contact with the electrode and able to diffuse towards it.

Furthermore, we probed for the first time that our NCNDs-based hybrids exhibit great self-enhanced ECL without the addition of co-reactants such as TPrA. Our nanohybrids provide an ECL emission intensity two times higher with respect to the uncoupled components.

The observed ECL enhancement is due to the presence of NCNDs amino groups in the hybrids, which act as co-reactants. Therefore, the luminophores and its co-reactive groups are integrated in a single nanohybrids entity. Thus, in contrast to the common intermolecular ECL reaction, the electrons are transferred intramolecularly to the redox centers, leading to enhanced ECL intensity due to shorter electron-transfer path and less energy loss. Our results provide a new method for signal amplification, opening interesting possibilities towards self-enhanced systems which would extend bionalytical applications. Finally, since our NCNDs have shown good matrix ability in ECL label-derivatized systems through the independence of each redox unit, we evaluated the direct effect on the ECL signal of the more signal-generating units assembly into the same nanometric object. Thus, it was investigated the immobilization of the hybrids on an electrode to overcome diffusion limitation and provide ECL signal amplification. It was observed a signal enhancement proportional to the number of ECL probes present in each NCNDs due their raised density on the electrode surface. Therefore, the use of NCNDs as novel platform for higher ECL efficiency was demonstrated and we believe that our encouraging results would offer the possibility to make outstanding steps forward in this field.



## 5.4 EXPERIMENTAL SECTION

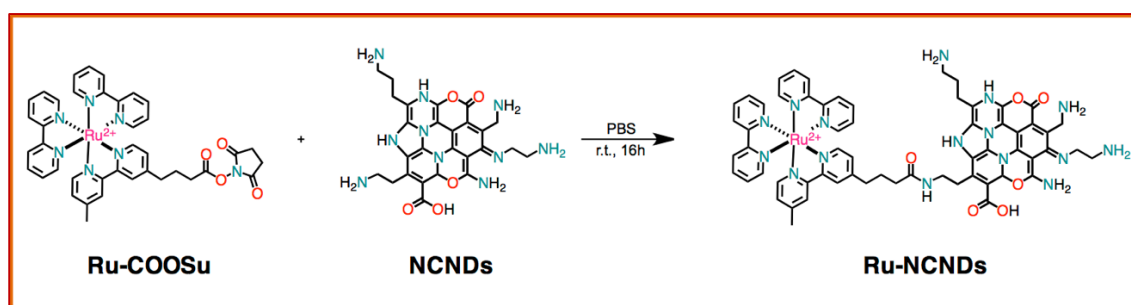
### Materials

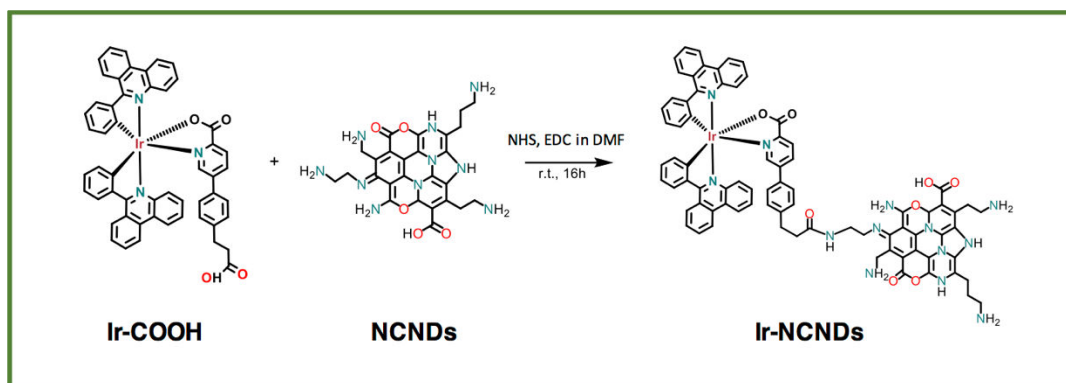
NCNDs were synthesized according to our previously reported method.<sup>21</sup> Bis(2,2'-bipyridine)-4'-methyl-4-carboxybipyridine-ruthenium N-succinimidyl ester- Chloride, (Ru-COOSu), was supplied by Roche diagnostics. Ir(6-phenylphenanthridine)<sub>2</sub> 2-(Carboxyethyl-phenyl)pyridine-2-carboxylic acid (Ir-COOH) was synthesized as reported elsewhere from a former member.<sup>22</sup>

Ruthenium- tris(2,2'-bipyridyl) dihexafluorophosphate (Ru(bpy)<sub>3</sub>(PF<sub>6</sub>)<sub>2</sub>), sulfo-N-hydroxy succinimide (NHS), 1-ethyl-3-[3-dimethylaminopropyl] carbodiimide hydrochloride (EDC), 16-mercaptohexadecanoic acid (MHDA), 11-Amino-1-undecanethiol (AUDT) and Phosphate Buffer Saline (PBS, pH=7.4) were purchased at Sigma-Aldrich and used without purification. Size exclusion chromatography was carried out using Sephadex TMLH-20 (Amersham Biosciences). Ultrapure fresh water obtained from a Millipore water purification system (>18MΩ Milli-Q, Millipore) was used in all experiments.

ProCell® solution was acquired from Roche (Product number, 1662988) and consists in a solution of phosphate buffer (PBS, pH = 6.8) 300 mmol/l, tripropylamine 180 mmol/l, a proprietary surfactant (0.1%) and preservative.

### Synthesis of Ru-NCNDs and Ir-NCNDs





For Ru-NCNDs, NCNDs (40.0 mg, 1 eq) were added into a solution of Ru-COOSu (39.0 mg, 1.4 eq) in MeOH (1.5 mL), then PBS (2 mL) was added. For Ir-NCNDs, NCNDs (40.0 mg, 1 eq) were added into a solution of a NHS activated Ir(6-phenylphenanthridine)<sub>2</sub>-2-(Carboxyethyl-phenyl)pyridine-2-carboxylic acid (Ir-COOSu) (30.34 mg, 1 eq) in DMF (5 mL). The mixtures were then stirred at room temperature for 16 h. The solvent was removed under reduced pressure and the crude mixture was dissolved in MeOH (1.5 mL) and separated by Gel Filtration Chromatography using a column packed with Sephadex LH-20 (eluent: MeOH). Finally, methanol was removed under reduced pressure, to obtain orange-red solids as the final products, Ru-NCNDs and Ir-NCNDs.

#### *Transmission Electron Microscopy*

Transmission electron microscopy images were obtained with a a Jeol-JEM 2011 microscope operated at 200 kV, equipped with a Cs-probe corrector, an Energy Dispersive X-ray Spectrometer and a GIF Tridiem filter. Samples were prepared by drop-casting the sample directly from methanol, at concentrations of few mg/mL on a lacey carbon grid and drying at ambient conditions.

#### *ICP-MS measurements*

ICP-MS experiments were performed to evaluate the amount of ruthenium complexes in Ru-NCNDs. The instrument employed was a "X series II" from Thermo Electron. From the determination of the absolute ruthenium and iridium content in Ru-NCNDs and Ir-NCNDs, a loading of 200 mg/g for ruthenium complex and 440 mg/g for iridium complex were calculated. Through the following calculations, it was estimated a number of three ruthenium and iridium complexes for each NCNDs. The ICP-MS measurement of a Ru-NCNDs and Ir-NCNDs sample with a concentration of respectively 0.0096 mg/mL and 0.0330 mg/mL in nitric acid, revealed a concentration (**C**) of NCNDs and Ru equal to

0.0074 and 0.0022 mg/mL (corresponding to  $2.3 \cdot 10^{-9}$  mol/mL), respectively, and of NCNDs and Ir equal to 0.0290 and 0.0054 mg/mL (corresponding to  $5.5 \cdot 10^{-9}$  mol/mL). By assuming NCNDs as spherical nanoparticles with a diameter equal to 2.47 nm,<sup>21</sup> and considering the density of amorphous carbon as  $2 \text{ g/cm}^3$ ,<sup>5</sup> it was calculated the mass ( $m$ ) of a single NCNDs:

$$V = 4/3 \pi r^3 = 7,89 \cdot 10^{-21} \text{ cm}^3 \quad (5.1)$$

$$m = d \cdot V = 2 \cdot 7,9 \cdot 10^{-21} = 1,58 \cdot 10^{-20} \text{ g} \quad (5.2)$$

From the ratio between the concentration ( $C$ ) of NCNDs in the sample and the mass ( $m$ ) of one NCNDs it was calculated the number ( $N_0$ ) of NCNDs in the Ru-NCNDs nanohybrid:

$$\frac{0,0074 \cdot 10^{-3}}{1,58 \cdot 10^{-20}} = 4,7 \cdot 10^{14} \text{ } N_0 \text{ of NCNDs in Ru-NCNDs} \quad (5.3)$$

$$\frac{0,029 \cdot 10^{-3}}{1,58 \cdot 10^{-20}} = 1,8 \cdot 10^{15} \text{ } N_0 \text{ of NCNDs in Ir-NCNDs} \quad (5.4)$$

The number ( $N_0$ ) of Ru in the Ru-NCNDs and Ir in the Ir-NCNDs nanohybrid was calculated as follow:

$$n \cdot N_A = N_0 \quad (5.5)$$

$$2,3 \cdot 10^{-9} \cdot 6,022 \cdot 10^{23} = 1,4 \cdot 10^{15} \text{ } N_0 \text{ of Ru in Ru-NCNDs} \quad (5.6)$$

$$5,5 \cdot 10^{-9} \cdot 6,022 \cdot 10^{23} = 3,4 \cdot 10^{15} \text{ } N_0 \text{ of Ir in Ir-NCNDs} \quad (5.7)$$

where  $N_A$  is the Avogadro number and  $n$  are the number of moles of Ru and Ir in the nanohybrid. From the  $N_0$  as calculated, it was estimated the number of ruthenium and iridium complexes on each NCNDs:

$$\frac{1,4 \cdot 10^{15}}{4,7 \cdot 10^{14}} = 2,98 \text{ Ru/NCNDs} \quad (5.8)$$

$$\frac{3,4 \cdot 10^{15}}{1,8 \cdot 10^{15}} = 1,88 \text{ Ir/NCNDs} \quad (5.9)$$

*ATR FT-IR*

Fourier transform infrared spectroscopy was performed in the solid state using an attenuated total reflectance (ATR-FTIR) accessory on a Shimadzu IRAffinity-1 spectrometer.

*Ir-COOH and Ir-NCNDs -modified gold electrodes*

Figure 5.18 illustrates the fabrication process of the modified electrodes. Gold working electrodes (2 mm in diameter) were polished repeatedly with 0.3 and 0.05 mm alumina slurry, followed by sonication in acetone, ethanol and distilled water (5 min each) and dried in air. The electrodes were then modified in two different ways: in order to graft Ir-COOH on the gold surface, the electrode was treated with a 1 mM ethanol solution of 11-Amino-1-undecanethiol. and for the Ir-NCNDs with a 1 mM ethanolic solution of 16 mercapto-decanodic acid for 48 hours. Electrodes were then washed in PBS at pH 7.4, then the carboxy-terminated parts were immersed in a mixture of EDC and NHS (1:3) PBS solution for approximately 15 minutes at room temperature (Ir-COOH and SAM for Ir-NCNDs). Following activation, the electrode was immersed in activated Ir-COOH or Ir-NCNDs PBS solution ( $[Ir]=10^{-4}$  M) for approximately 1 hour at 37°C. Each electrode was then washed with PBS at 0.05% v/v (called PBS tween), three times and PBS three times.

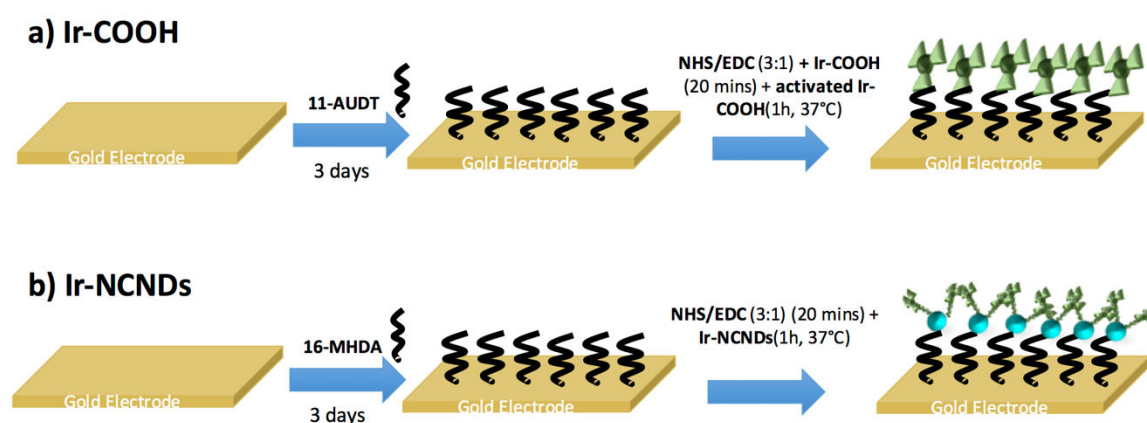


**Figure 5.18.** Schematic representation of modified Ir-COOH and modified Ir-NCNDs electrodes.

*Electrochemistry*

The electrochemical characterizations of NCNDs, Ru-NCNDs, Ir-NCNDs,  $\text{Ru}(\text{bpy})_3^{2+}$  and Ir-COOH were performed in DMF with 0.1M tetra-butylammonium hexafluorophosphate ( $\text{TBAPF}_6$ ) as supporting electrolyte. A CHI750C Electrochemical Workstation (CH

Instruments, Inc., Austin, TX, USA) was used throughout. All experiments were performed in a glass cell under argon atmosphere. Feedback correction was employed in order to minimize the ohmic drop between the working and reference electrodes. A glassy carbon electrode (GC, 3 mm diameter 66-EE047 Cypress Systems) was employed as the working electrode (WE), while a platinum and a silver wires were used as counter (CE) and quasi-reference (QRE) electrodes. The GC electrode was stored in ethanol and polished with a 0.05  $\mu\text{m}$  diamond suspension (Metadi Supreme Diamond Suspension, Buehler) and ultrasonically rinsed with water for 10 minutes and ethanol for 10 minutes, before each experiment. The WE was electrochemically activated in the electrolyte solution by means of several voltammetric cycles at 0.5  $\text{V s}^{-1}$  between the anodic and cathodic solvent/electrolyte discharges. The RE was separated from the catholyte by glass frits. It was calibrated at the end of each experiment against the ferrocene/ferricenium ( $\text{Fc}/\text{Fc}^+$ ) couple, whose formal potential is 0.460 V against KCl-saturated calomel electrode (SCE). Throughout the chapter, all potential values are reported against SCE. The standard potentials were calculated as the average value between cathodic and anodic peak potentials, when the processes are reversible or quasi-reversible.

### *Electrochemiluminescence*

A custom system was used for ECL characterization, consisting of an electrochemical cell based on a glassy carbon (Tokai Inc.) disk electrode (3 mm diameter) WE, closely facing (a few millimetres) the photomultiplier tube (PMT, Hamamatsu, H10723-01, Japan) detector controlled by a PGSTAT101 Autolab electrochemical workstation (Metrohm, The Netherlands). The RE was an Ag/AgCl (1M KCl) by CHI-Instruments, separated from the catholyte by a glass frit. A platinum wire served as the CE. For potentiodynamic measurements (cyclic voltammetry), the solution was scanned at 0.05 V/s from +0.5 V to +1.45 V. In chronamperometric experiments, the pulsing potential was set at +1.4 V vs Ag/AgCl (1M KCl), with 1 s the pulse width. The transients and the faradic currents were managed by using the software NOVA provided with the Autolab unit. The ECL spectrum was acquired using a calibrated electron multiplying charge couple device (EM-CCD) camera (A-DU970N-UVB Andor technology, Newton EM-CCD) coupled with a Shamrock 163 spectrograph (Andor Technology). The relative ECL intensity of the complexes is compared to Rubpy, ( $I/I_{\text{Ru}}$ ), where  $I$  is the integrated signal of the complex for 1s and  $I_{\text{Ru}}$  is the integrated signal of Rubpy under the same conditions. The  $I$  values are

the average of three different measurements. The working electrode was mechanically cleaned before each run as above mentioned for the electrochemical measurements. A Ru(bpy)<sub>2</sub>PF<sub>6</sub> solution (10<sup>-5</sup> M in Procell) was used as reference.

#### *Photophysical Measurements*

Absorption spectra were recorded on a Shimadzu UV-3600 double-beam UV-Vis-NIR spectrometer and baseline corrected. Steady-state emission spectra were recorded on an HORIBA Jobin-Yvon IBH FL-322 Fluorolog 3 spectrometer equipped with a 450W xenon-arc lamp, double-grating excitation and emission monochromators (2.1 nm/mm dispersion, 1200 grooves/mm blazed at 500 nm), and a TBX-04 detector. Emission and excitation spectra were corrected for source intensity (lamp and grating) and emission spectral response (detector and grating) by standard correction curves. The quantum yield measurements were performed by using an absolute photoluminescence quantum yield spectrometer Quantaaurus C11347 (Hamamatsu, Japan) exciting the sample at 350 nm. Time-resolved measurements were performed using time-correlated single-photon counting (TCSPC) electronics PicoHarp300 of a PicoQuant FluoTime 300 (PicoQuant GmbH, Germany), equipped with a PDL 820 laser pulse driver. The excitation wavelength was 375 nm (NCNDs and the hybrids) or 440 nm ([Ru(bpy)<sub>3</sub>]<sup>2+</sup>, Ir-COOH and the hybrids) using a LDH-P-C-375 laser diode. The laser was mounted directly on the sample chamber at 90° to a Czerny-Turner type emission monochromator (2.7 nm mm<sup>-1</sup> of dispersion; 1200 grooves mm<sup>-1</sup>). The photons were collected with a PMA-C-192 photomultiplier single-photon-counting detector. Ethylene glycol was used as the solvent for anisotropy measurements. The polarization was in the configuration VV (vertical-vertical) and VH (vertical-horizontal). The data were acquired with the commercially-available software EasyTau (PicoQuant GmbH, Germany), and data analysis was performed by using the FluoFit (PicoQuant GmbH, Germany). The goodness-of-fit was assessed by minimizing the reduced chi-square function ( $\chi^2$ ) and visual inspection of the weighted residuals.

## **5.5 REFERENCES**

- (1) Miao, W. *Chem. Rev.* **2008**, *108* (7), 2506.
- (2) Liu, Z.; Qi, W.; Xu, G. *Chem. Soc. Rev.* **2015**, *44* (10), 3117.
- (3) Hsueh, Y.; Collins, S. D.; Smith, R. L. *Sensors Actuators B. Chem.* **1998**, *49*, 1.
- (4) Staffilani, M.; Höss, E.; Giesen, U.; Schneider, E.; Hartl, F.; Josel, H. P.; De Cola,

- L. Inorg. Chem.* **2003**, *42* (24), 7789.
- (5) Zanarini, S.; Rampazzo, E.; Ciana, L. Della; Marcaccio, M.; Marzocchi, E.; Montalti, M.; Paolucci, F.; Prodi, L. *J. Am. Chem. Soc.* **2009**, *131* (6), 2260.
- (6) Yu, Y.; Zhou, M.; Cui, H. *J. Mater. Chem.* **2011**, *21* (34), 12622.
- (7) Zanarini, S.; Rampazzo, E.; Bonacchi, S.; Juris, R.; Marcaccio, M.; Montalti, M.; Paolucci, F.; Prodi, L. *J. Am. Chem. Soc.* **2009**, *131* (40), 14208.
- (8) Liang, P.; Dong, L.; Martin, M. T. *J. Am. Chem. Soc.* **1996**, 7863 (96), 9198.
- (9) Swanick, K. N.; Ladouceur, S.; Zysman-Colman, E.; Ding, Z. *Angew. Chem. - Int. Ed.* **2012**, *51* (44), 11079.
- (10) Li, P.; Jin, Z.; Zhao, M.; Xu, Y.; Guo, Y.; Xiao, D. *Dalton Trans.* **2015**, *44* (5), 2208.
- (11) Wang, H.; He, Y.; Chai, Y.; Yuan, R. *Nanoscale* **2014**, *6*, 10316.
- (12) Wang, H.; Yuan, Y.; Zhuo, Y.; Chai, Y.; Yuan, R. *Anal. Chem.* **2016**, *88*, 2258.
- (13) Liang, W.; Zhuo, Y.; Xiong, C.; Zheng, Y.; Chai, Y.; Yuan, R. *Anal. Chem.* **2015**, *87*, 12363.
- (14) Qi, H.; Peng, Y.; Gao, Q.; Zhang, C. *Sensors* **2009**, *9* (1), 674.
- (15) Deng, S.; Ju, H. *Analyst* **2013**, 43.
- (16) Wang, H.; Zhang, C.; Li, Y.; Qi, H. *Anal. Chim. Acta* **2006**, *575* (2), 205.
- (17) Miao, W.; Bard, A. J. *Production* **2004**, *76* (23), 7109.
- (18) Miao, W.; Bard, a. J. *Anal. Chem.* **2004**, *76* (18), 5379.
- (19) Li, Y.; Qi, H.; Fang, F.; Zhang, C. *Talanta* **2007**, *72* (5), 1704.
- (20) Valenti, G.; Rampazzo, E.; Bonacchi, S.; Khajvand, T.; Juris, R.; Montalti, M.; Marcaccio, M.; Paolucci, F.; Prodi, L. *Chem. Commun.* **2012**, *48*, 4187.
- (21) Arcudi, F.; Đorđević, L.; Prato, M. *Angew. Chem. - Int. Ed.* **2016**, *55*, 2107.
- (22) Cysewski, R.; De Cola, L.; Fernandez Hernandez, J. M.; Josel, H.-P.; Lopez-Calle, E.; Zarnt, T. Iridium-based complexes for ECL. US 8835637 B2, 2014.
- (23) Morailon, A.; Gouget-Laemmel, A. C.; Ozanam, F.; Chazalviel, J. N. *J. Phys. Chem. C* **2008**, *112* (18), 7158.
- (24) Juris, A.; Balzani, V.; Barigelletti, F.; Campagna, S.; Belser, P.; von Zelewsky, A. *Coord. Chem. Rev.* **1988**, *84* (C), 85.
- (25) De Cola, L.; Belser, P. *Coord. Chem. Rev.* **1998**, *177* (1), 301.
- (26) Kalyanasundaram, K. *Coord. Chem. Rev.* **1982**, *46*, 159.

- (27) Ameloot, M.; Acuña, A. U.; Valeur, B.; Hasselt, U.; Building, C. *Pure Appl. Chem.* **2013**, 85 (3), 589.
- (28) Barbero, N.; Napione, L.; Quagliotto, P.; Pavan, S.; Barolo, C.; Barni, E.; Bussolino, F.; Viscardi, G. *Dye. Pigment.* **2009**, 83 (2), 225.
- (29) Bertram, R. *Electrochemistry at solid electrodes. Monographs in Electroanalytical Chemistry and Electrochemistry*; Marcel Dekker, I., Ed.; Marcel Dekker, Inc., New York, 1969; Vol. 1 Aufl., XI.
- (30) Tokel-Takvoryan, N. E.; Hemingway, R. E.; Bard, A. J. *J. Am. Chem. Soc.* **1973**, 95 (20), 6582.
- (31) Miao, W.; Choi, J.-P.; Bard, A. J. *J. Am. Chem. Soc.* **2002**, 124 (48), 14478.
- (32) Bhatt, P. A.; Pratap, A.; Jha, P. K. *AIP Conf. Proc.* **2013**, 1536 (2013), 237.
- (33) Roberts, J. J. P.; Vuong, K. T.; Murray, R. W. *Langmuir* **2013**, 29 (1), 474.





# Chapter 6

## **Electrochemical Impedance Spectroscopy and Electrochemiluminescence for the detection of Troponin I**

### **Abstract**

This chapter describes an electrochemical bio-sensing device for Troponin I cardiac biomarker with enhanced properties using a novel, brighter Ir (III) based metal complex that can substitute the typical  $\text{Ru}(\text{bpy})_3^{2+}$ . Using the highly sensitive electrochemical techniques, impedance and ECL, and confocal microscopy an LOD of 10 and 0.42 mg/mL, respectively, is observed. Such low concentration is clinically relevant for early-stage detection, thus allowing to coincide this device as promising platform for future point of care health monitoring.

The work presented in this chapter has been accomplished at Biomedical Diagnostics Institute (BDI) in Dublin College University (DCU) with the help of *Dr. Kellie Adamson* and *Dr. Elaine Spain* under the supervision of *Prof. Robert Forster*.

## 6.1. INTRODUCTION

### 6.1.1 Cardiac Biomarkers: Troponin I, the gold standard

Cardiovascular disease (CVD) is a major cause of human death in both developing and developed countries. According to the World Health Organization (WHO) an estimated 17.5 million (30%) of all global deaths in 2005 are associated with CVD and it is estimated that by 2015, CVD may be the leading cause of death in the developing countries.<sup>1</sup>

Among all the mortal CVD,<sup>2</sup> Acute Myocardial Infraction (AMI) is the most common type and occurring when a part of the heart muscle is damaged following blockage of a coronary artery. The management of AMI is extremely time-sensitive and its rapid diagnosis, e.g., through a molecular biomarker, is very urgent.<sup>3</sup> There are several important characteristics that an ideal cardiac biomarker should exhibit including: (a) high clinical sensitivity and specificity, (b) quick release of biomarker in the blood enabling early diagnosis, (c) capability to remain elevated for a time in the blood, and (d) ability to be assayed quantitatively.<sup>4</sup> Many biomarkers have been investigated for the detection of AMI such as myoglobin, creatine kinase MB (CK-MB) and cardiac Troponin (cTn).<sup>5</sup>

Myoglobin is released into the bloodstream as early as 1 h after the onset of symptoms and several hours earlier than CK-MB and cardiac troponins. With its rapid kinetics and clearance, myoglobin provides a good non-invasive marker of coronary perfusion in patients undergoing thrombolysis or angioplasty. Unfortunately, the clinical specificity of myoglobin is poor owing to its abundant presence in skeletal muscle.<sup>5</sup>

The appearance of the second marker, CK-MB isoform, in the bloodstream is highly sensitive for myocardial injury. However, diagnostic specificity of CK-MB is compromised as well when skeletal muscle is involved, such as in the case of trauma, cardiac surgery, or extreme exercise. In addition, CK-MB cannot be regarded as a true early marker of AMI owing to its release kinetics.<sup>5,6</sup>

Cardiac Troponins have been suggested as preferred biomarkers for acute coronary syndrome. Cardiac Troponin exists as a complex between three single chain polypeptides (Figure 6.1): Troponin T (cTnT) binds the other troponin components to tropomyosin,

Troponin I (cTnI) inhibits ATP activity when bound to actin, Troponin C (cTnC) contains binding sites for calcium. Typically, upon AMI, the Troponin complex is broken and the individual protein components are released in the bloodstream. Among the three types of Troponin, cTnI is chosen for the detection because of its superior cardiac specificity and selectivity.<sup>3</sup> The concentration of cTnI increases within 2-6h and reaches a peak of 53 ng/mL during the next 24h.<sup>7</sup>

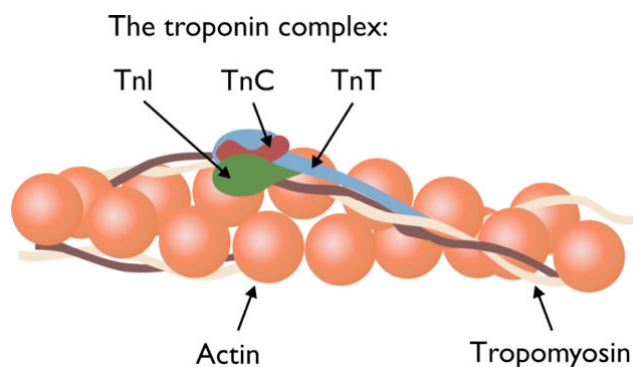


**Figure 6.1.** Components of the Troponin Complex. Three subunits: Troponin I (TnI), Troponin C (TnC) and Troponin T (TnT) interact with Tropomyosin located along the Actin filaments on the striated muscles. Image reprinted from reference (8).

Fast, accurate determination of cTnI is very important for early diagnosis and treatment of AMI. Given the urgent need for early diagnosis, clinicians should perform cTnI testing within 3-4h after the suspected onset of AMI. To date, many different techniques have been reported for cTnI detection including enzyme-linked immunosorbent assay (ELISA),<sup>9</sup> optomagnetism,<sup>10</sup> field-effect transistor,<sup>11</sup> fluorescence immunoassay,<sup>12</sup> and electrochemiluminescence (ECL) based biosensors.<sup>13-16</sup> While these techniques have proven to be sensitive and selective, they require lengthy sample pre-treatment/enrichment steps such as signal amplification to detect low concentrations and are generally challenging to develop into a point-of-care device. Consequently, the approach reported here is expected to have significant applications for the detection of low levels of cTnI as a promising, fast and accurate alternative to current time-consuming, conventional methods.

### 6.1.2 Electrochemical Impedance Spectroscopy (EIS) as sensing technique

Electrochemical impedance spectroscopy (EIS) has long been employed for studying electrochemical systems,<sup>17,18</sup> including those involved in corrosion, electrodeposition,<sup>19</sup>

batteries<sup>20</sup> and fuel cells.<sup>21</sup> For impedance measurements, a small sinusoidal AC voltage probe (typically 2–10 mV) is applied, and the current response is determined.

A sinusoidal voltage can be expressed as:

$$e = E \sin \omega t \quad (6.1)$$

where  $\omega$  is the angular frequency and  $E$  the amplitude. The current  $i$  will not be in phase with  $e$  and it will be separated by a phase angle  $\phi$ , according to the equation 6.2:

$$i = I \sin(\omega t + \phi) \quad (6.2)$$

The relationship between  $e$  and  $i$  remains constant, hence  $\phi$  is constant.

This concept can be applied for some simple circuits. For a pure resistance,  $R$ , the response is always in phase with the perturbation ( $\phi = 0$ ), then for the Ohm's law:

$$i = e/R \quad (6.3)$$

The relationship between the voltage across a resistor and the current through it is shown in Figure 6.2a.

For a pure capacitance,  $C$ , the fundamental relation of interest is  $q=CE$  or  $i=C(dE/dt)$ , therefore:

$$i = \omega CE \cos \omega t = \frac{E}{X_C} \sin \left( \omega t + \frac{\pi}{2} \right) \quad (6.4)$$

where  $X_C$  is the capacitive reactance,  $1/\omega C$ . The phase angle is equal to  $\pi/2$  and current and voltage are now expanded to a plane (Figure 6.2x). It is the convenient to represent them in terms of complex notation, and in particular the in-phase current response determines the real (resistive) component of the impedance, while the out-of-phase current response determines the imaginary (capacitive) component (Figure 6.2) and it is multiplied by  $j = \sqrt{-1}$ , resulting in:

$$E = -jX_C I \quad (6.5)$$

Therefore, the voltage is linked to the current through a vector  $Z$ , called Impedance.<sup>18</sup> The variation of Impedance with frequency can be displayed in different ways, in a *Bode plot*,

$\log|Z|$  and  $\phi$  against  $\log\omega$ , and in a Nyquist plot, composed of an imaginary ( $Z''$ ) and real ( $Z'$ ) impedance (Figure 6.3b).

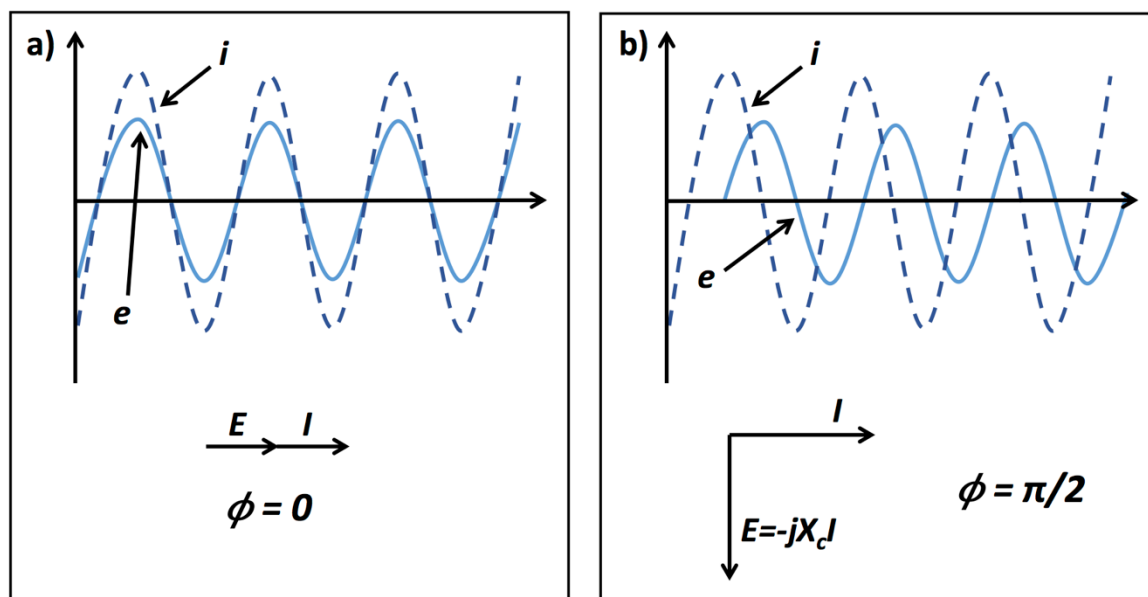


Figure 6.2. a) Voltage and current in phase through a resistor; b) Voltage and current out-of-phase ( $\pi/2$ ) through a capacitor.

Impedance methods are quite powerful as they are capable of characterizing physicochemical processes of widely differing time constants, e.g., sampling electron transfer at high frequency and mass transfer at low frequency. For instance, the Randles equivalent circuits of resistors and capacitors (Figure 6.3a),<sup>22</sup> often used to interpret simple electrochemical systems, yields the Nyquist plot in Figure 6.3b.

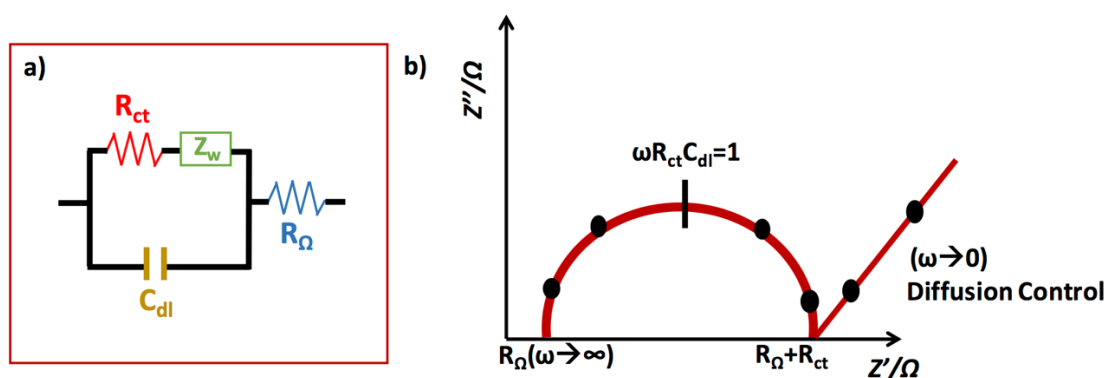


Figure 6.3. a) Randles equivalent circuit for a simple electrochemical system; b) Nyquist plot arising from the Randles circuit.

In Figure 6.3,  $R_{ct}$  is the charge-transfer resistance, which is inversely proportional to the rate of electron transfer;  $C_{dl}$ , is the double-layer capacitance;  $R_{\Omega}$  is the solution-phase resistance; and,  $Z_w$  is the Warburg impedance, which arises from mass-transfer limitations. If an analyte affects one or more of these equivalent circuit parameters and these parameters are not affected by interfering species, then impedance methods can be used for analyte detection.

The equivalent circuit elements in Figure 6.3 that are most often useful for analyte detection are  $R_{ct}$  and  $C_{dl}$ . The measured capacitance usually arises from the series combination of several elements, such as analyte binding ( $C_{anal}$ ) to a sensing layer ( $C_{sens}$ ) on an Au electrode ( $C_{Au}$ ). In this case, the measured capacitance is:

$$\frac{1}{C_{dl}} = \frac{1}{C_{Au}} + \frac{1}{C_{sens}} + \frac{1}{C_{anal}} \quad (6.6)$$

for a sensing layer densely packed. One difficulty with capacitive sensors is that their sensitivity depends on obtaining the proper thickness of the original sensing layer.<sup>23</sup> If the original sensing layer is too thin, then the underlying electrode surface may be partially exposed, allowing for non-specific interactions from interfering species. However, if the original sensing layer is too thick, then the AC impedance current that is detected is dramatically reduced, as is the change in capacitance upon analyte binding.  $R_{ct}$  can also be quite sensitive to analyte binding, particularly for detection of large species, such as proteins or cells, which significantly impede electron transfer. For analyte binding ( $R_{anal}$ ) to a sensing layer ( $R_{sens}$ ) on an Au electrode ( $R_{Au}$ ) the measured resistance is:

$$R_{ct} = R_{Au} + R_{sens} + R_{anal} \quad (6.7)$$

The resistance at the interface between the Au electrode and the sensing layer is typically negligible. Measurement of  $R_{ct}$  requires the presence of redox-active species in the electrolyte. Many of the examples of impedance sensors monitor  $R_{ct}$  as a measure of analyte concentration.<sup>24,25</sup>

So far, the discussion was focused on *Faradaic* Impedance, which uses a redox probe such as potassium ferri/ferrocyanide.

*Non-Faradaic* Impedance does not require a probe, which could alter the system, and it is particularly useful for cell detection or biological detection with the aim to improve detection sensitivity and reproducibility.

In this latter case, the circuit employs a constant phase element ( $Z_{CPE}$ ) correlated to surface defects on the monolayer/antibody/antigen/antibody layer. It is represented by:

$$Z_{CPE} = Q^{-1}(j\omega)^{-\alpha} \quad (6.8)$$

where  $Q$  is the magnitude of the capacitance of the CPE,  $\omega$  is the angular frequency, and  $\alpha$  is a real number between 1 and 0 (the closer  $\alpha$  gets to 1 the more ideal the capacitive behaviour of the CPE).

CPE does not have any physical significance and it is a non-intuitive circuit element typical of real chemical systems. Due to inhomogeneous distribution of the system, depressed semicircles or arcs will be observed in impedance spectroscopy plots, in these case the data cannot be fitted as an ideal capacitor, because there should not be any depression of the impedance plots (only exact semi circles are required). Using CPE, it is possible to get  $C$  values.

One of the most significant advantages of impedance detection for biosensing is that antibody-antigen binding can be directly detected. The main drawback of impedance methods for biosensors is the need for interfacial engineering to reduce non-specific adsorption since there is no label to discriminate non-specifically and specifically bound material. One well-studied method to minimize non-specific interactions is to embed the probe agent into a composite film that contains the biomolecule of interest interspersed with a protein-resistant species, such as molecules containing ethylene-glycol moieties. This approach has been widely studied by the research group of Whitesides,<sup>26-28</sup> and such reagents are now commercially available. Limits of detection (LODs) have been reported for impedance biosensors in the nM–pM range in controlled laboratory conditions.<sup>29-33</sup>

### 6.1.3 ECL biosensors and immunoassays

Electrochemiluminescence, ECL, involves a label that emits detectable light when oxidised/reduced in a solution of appropriate composition. It is of great interest in the field of biosensing and immunoassays due to its high sensitivity, low background and wide dynamic range.<sup>34,35</sup> Therefore, in the context of medical diagnostics, ECL is known



to offer better performance than many other analytical techniques, as discussed in Chapter 1.<sup>36</sup>

The first ECL immunoassay (ECLIA) was reported by Bard and Whiteside in 1997,<sup>37</sup> using a newly synthesized Ru-chelate having an N-hydroxysuccinimide (NHS) residue. The availability of such systems to generate ECL in the presence of a co-reactant such as tripropylamine (TPrA) or oxalate, and the ability to label protein moieties, has contributed to the significant interest and ability to develop highly sensitive ECL assays.<sup>35,38</sup>

Several ECL biosensors have been developed for the determination of proteins with high sensitivity, up to  $\text{fg ml}^{-1}$ .<sup>39</sup> In addition, it is relatively easy to conjugate the luminescent species to biomolecules like antibodies or DNA.<sup>40-42</sup> The conventional ECL system involves  $\text{Ru}(\text{bpy})_3^{2+}$  as the light-emitting species and TPrA as the co-reactant and it is the basis of several commercial based ECL immunoassays.<sup>35,43</sup>

#### 6.1.4 Aim of the work

The work presented in this chapter aims to improve cTnI detection sensitivity using EIS and ECL with a common goal of improving point-of-care health monitoring. This is an important objective since it would allow AMI to be diagnosed earlier. Currently, cTnI assays have limits of detection in the 80-100  $\text{fg/mL}$  range using ECL<sup>13</sup> which compares favourably with other analytical methods (see Table 6.1).<sup>9-12</sup>

**Table 6.1.** cTnI detection limits (LOD) of immunoassays based on different types of materials using electrochemiluminescent detection.

Types	LOD
ELISA	0.5 $\text{ng/mL}$ <sup>9</sup>
Au particles label-free	0.03 $\text{ng/mL}$ <sup>16</sup>
Peptide-based	4.5 $\text{pg/mL}$ <sup>14</sup>
Functionalized Au Particles	2 $\text{pg/mL}$ <sup>15</sup>
Self-enhanced Ru(II) complex	83 $\text{fg/mL}$ <sup>13</sup>

Efforts have been made to improve the sensitivity of ECL assays and even to obtain different emission colors for multiplexing in diagnostics.<sup>44,45</sup> To improve the ECL

intensity of  $\text{Ru}(\text{bpy})_3^{2+}$ , many researchers have explored the effects of alternative co-reactants, as 2-(dibutylamino)ethanol DBAE and histidine.<sup>46-48</sup> Another promising strategy is to replace  $\text{Ru}(\text{bpy})_3^{2+}$  with cyclometalated Ir(III) complexes.<sup>49-51</sup> They generally show higher photoluminescence efficiency and easy tunability of the emission wavelength which is extremely useful for multiplexed detection of several biomarkers without separation.

Inspired by these findings, this work aims to use an Ir(III) complex to improve cTnI detection using an ECL immunoassay sensor. The sensor, compared to those reported previously for cardiac biomarker detection,<sup>13-16</sup> replaces the conventional  $\text{Ru}(\text{bpy})_3^{2+}$ , by using a brighter Ir(II) metal complex, patented by the former group and used in Chapter 5, that presents higher sensitivity, permitting fast, reliable and inexpensive detection of lower quantities of antigen. The Ir-MAb conjugate is described along with its photophysical characterization, supported by confocal microscopy. EIS and ECL will be the two techniques used for analytical purposes.

## **6.2 ELECTROCHEMICAL SENSOR BASED ON LABELED ANTIBODIES WITH IR(III) COMPLEXES (MAb-Ir)**

Herein we report the use of Ir-COOH (see Chapter 5) as label of three antibodies that capture cTnI. The antibodies investigated are:

- **MAB 19c7** – Epitope 41 – 49
- **Mab228** - Epitope 26 – 35
- **MAB 20b3** – Epitope 24-39 (NYRAYATEPHAKKSKI)

The firsts two are commercially available (see experimental section 6.5), whereas 20b3 is a custom antibody produced in-house by the group of Prof. O' Kennedy at DCU, Dublin. The in-house MAb 20b3 and commercially available MAb 228 have the same epitope region which prevents the fabrication of an immunoassay using them as a couple, i.e., primary and secondary antibody. The idea is to compare their efficiency as capture-antibody and detection-antibody when coupled with Mab19c7.

### **6.2.1 Labeling of MABs with Ir(III) complexes**

Labelling of MAb19c7/MAB 228/MAB 20b3 with Ir-COOH complex was done by mixing the activated NHS complex (see experimental Section 6.5) with a DPBS solution

(pH = 7.4) of the antibody for 4 hrs. After that, the reaction mixture was purified by different cycles of centrifuges and characterized by means of photophysics (details in experimental Section 6.5).

### 6.2.1.1 Photophysical characterization

The conjugates were characterized by time-resolved fluorescence, in particular excited-state lifetime and anisotropy. The latter technique is commonly used for rotational time measurements associated to the emission transition moment that lies along the fluorophore structure.<sup>52</sup> The rotational time depends on the viscosity of the solvent and on the size of the fluorophore.<sup>53</sup> The bigger the fluorophore is, the longer is the rotational time necessary to get a depolarized emission. Lifetime shows the effective binding since it increased and anisotropy rotational time  $\theta$  as well (Table 6.2), since the complex alone does not show it. The fundamental anisotropy,  $r_0$ , ranges from 0.4 (parallel transition dipoles) to -0.2 (perpendicular dipoles) and from this value it is possible to calculate the angle  $\beta$  between the absorption and emission transition moment by using the following equation:

$$r_0 = \frac{2}{5} \frac{3\langle \cos^2 \beta \rangle - 1}{2} \quad (6.9)$$

The value found in PBS solution is equal to  $63^\circ$ , showing a high anisotropy of Ir-COOH when attached to a big molecule like these antibodies.

**Table 6.2.** Lifetime and anisotropy rotational time  $\theta$  in ns of Ir-COOH and the conjugates.

	<b>Lifetime (ns)</b>	<b><math>\theta</math> (ns)</b>
<b>Ir-COOH</b>	430 (56%) 150 (44%)	0
<b>Ir-19c7</b>	470	480 ( $r_0=-0.02$ )
<b>Ir-228</b>	466	760 ( $r_0=0.009$ )
<b>Ir-20b3</b>	924	490 ( $r_0=-0.014$ )

### 6.2.2 Immunoassay configuration

Figure 6.4 illustrates the combinations of capture antibody and detection antibody (Ir-MAb) that have been used for the fabrication of cTnI electrochemical immunoassay. Details on the preparation are reported in experimental Section 6.5. Capture antibodies have been linked to the gold surface through self-assembled monolayers (SAM) of alkane thiols (16-MHDA, see Experimental Section 6.5).

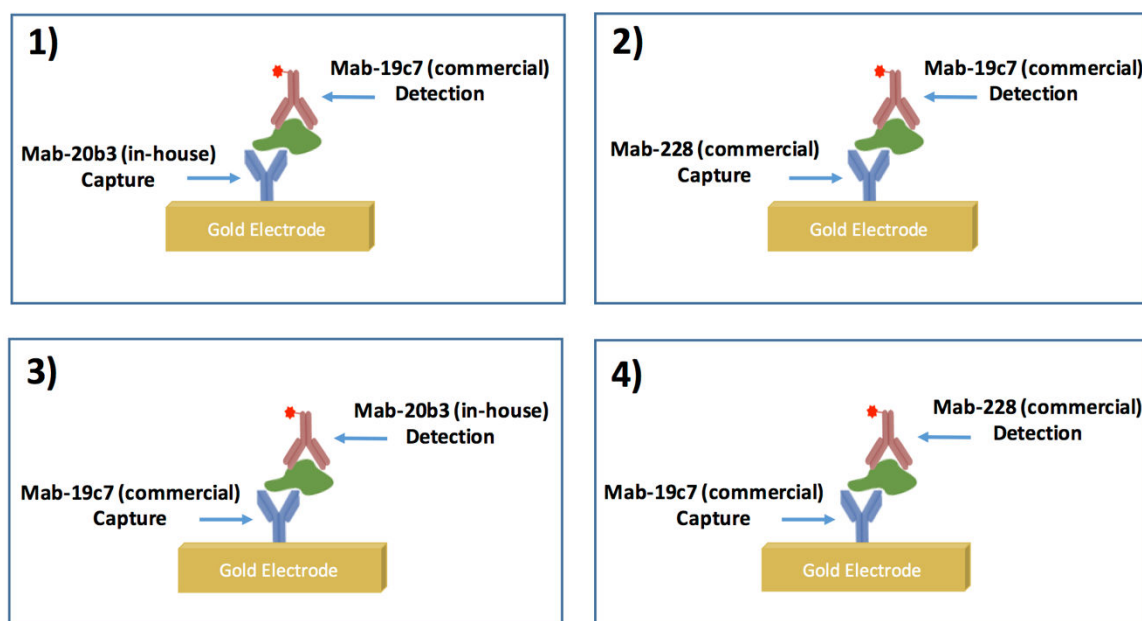


Figure 6.4. Schematic representation of fabricated immunoassays for the detection of cTnI.

The capture-detection MAb are listed in Figure 6.4. From now on, we will report:

- 1 → 20b3/Ir-19c7 (range 1 ag/mL-1 mg/mL)
- 2 → 228/Ir-19c7 (range 1 ag/mL-1 ng/mL)
- 3 → 19c7/Ir-20b3 (range 1 ag/mL-1 ng/mL)
- 4 → 19c7/Ir-228 (range 1 ag/mL-1 ng/mL)

### 6.2.3 Electrochemistry

An insight on the electrochemical properties at each the state of surface-confinement has been carried out to investigate the extent of surface coverage.

Cyclic voltammetry of the immunoassay with a cTnI concentration of 1 ag/mL, 1 ng/mL and 1  $\mu$ g/mL for sensor **1** is presented in Figure 6.5. From the peak in reduction related to the Iridium complex the surface coverage  $\Gamma$  has been calculated using the peak at -0.90 V vs Ag/Ag<sup>+</sup>, according to equation 6.10:

$$\Gamma = Q/nFA \quad (6.10)$$

Where Q (C) is the charge passed during the reduction process, n is the number of electrons involved in the electron transfer process (for SAM=1), F (C/mol) is the Faradic Constant and A is the electrode area equal to 0.0314 cm<sup>2</sup>. The results for each of the curves are shown in Table 6.5b. We report only the couple **1** since it is the most studied.

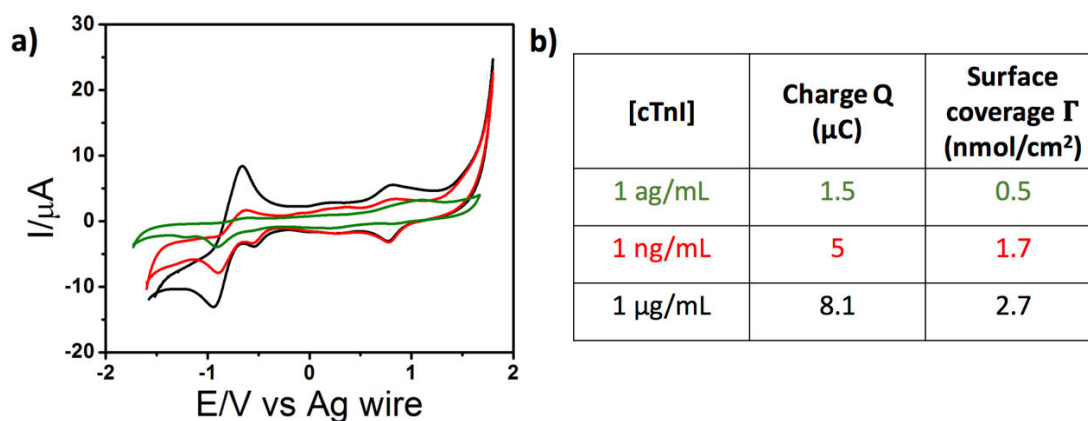


**Figure 6.5.** a) Cyclic Voltammetry of the ECL biosensor at different concentration of cTnI: green trace 1 ag/mL, red trace 1 ng/mL and black trace 1  $\mu$ g/mL; Scan rate 0.1 V s<sup>-1</sup> b) Table reporting the charge passed during the reduction of Ir-COOH and the surface coverage for each concentration, according to equation 6.10.

#### 6.2.4 Confocal microscopy

Confocal luminescence microscopy was employed to assess Troponin (cTnI) surface coverage and labelling efficiency of Ir-MAb. Figures 6.6 to 6.9 present confocal luminescence images of the 20b3/228/19c7 antibody modified electrodes after exposure to suspensions of Troponin at concentrations ranging from 1ag/mL to 1mg/mL, following labelling with Ir-MAb for 1 hour at 37°C. Troponin was successfully captured and labelled with all three Ir-MAb, and as illustrated in Figures 6.6 to 6.9, the surface concentration depends on the concentration in suspension. In agreement with the electrochemical studies presented in Figure 6.5, an increase in surface coverage with

increasing cTnI concentration is observed. Beneficially, a wide range of surface coverages over which the electrochemical response can be measured is presented.

In Particular, when Ir-19c7 is used as detection antibody, the confocal images in Figure 6.6 and 6.7 show increasing fluorescent intensity of Ir-COOH after incubation with increasing concentrations of captured troponin for both the MAb-20B3 and MAb-228 functionalized electrode surface. In particular, the fluorescence intensity profile of 1 ng cTnI/Ir-19C7 electrode showed approximately a 30 % increase for the in-house generated MAb-20B3 compared to the Hytest MAb228 capturing antibody surface. This significant increasing fluorescence intensity is an indication of the high capture efficiency of the in-house generated antibody and demonstrates its capability as an imperative biomarker of cTnI.

When used as detection antibody, Ir-20b3 shows too a good affinity to bind to troponin following the same increasing profile in terms of fluorescence. However, compared to Ir-228, the intensity results lower maybe due to a lower quantity of iridium complexes in the sample.

Significantly, in control experiments where the 16-MHDA monolayer modified gold electrodes, i.e., the capture antibody and cTnI complex is absent, are exposed to Ir-mAb (100 $\mu$ g/mL stock concentration) for 1 hour at 37°C, the surface coverage, as shown in Figure 6.10, is minimal compared to that found at the antibody modified surfaces, suggesting that non-specific binding is not a significant issue for these capture surfaces.

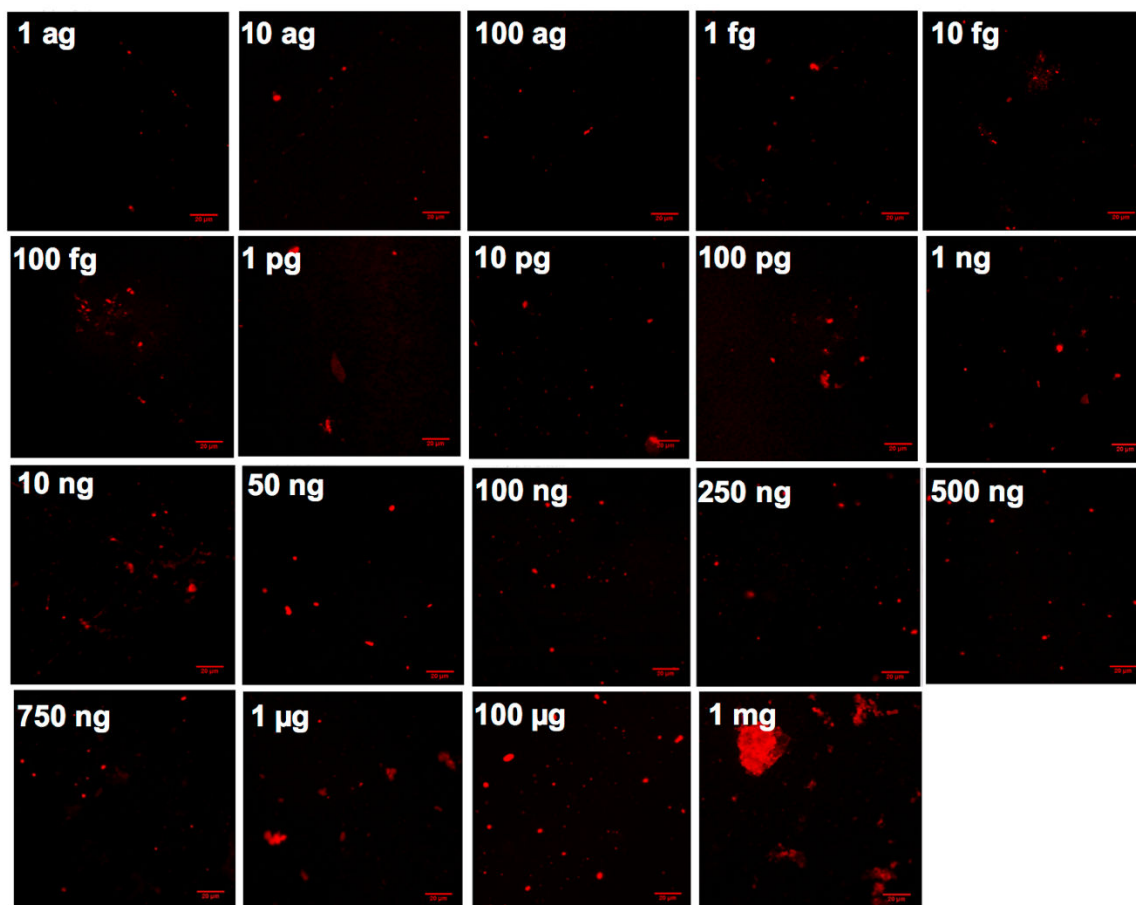


**Figure 6.6.** Confocal Images of the couple 1 (concentrations 1 ag/mL-1mg/mL). Scale bar 20  $\mu$ m. Luminescence images were recorded live on a Zeiss LSM510 Meta confocal microscope using a 40 $\times$  oil immersion objective lens (NA 1.4) and a 488 nm argon ion laser applied for Iridium labelled antibody imaging.

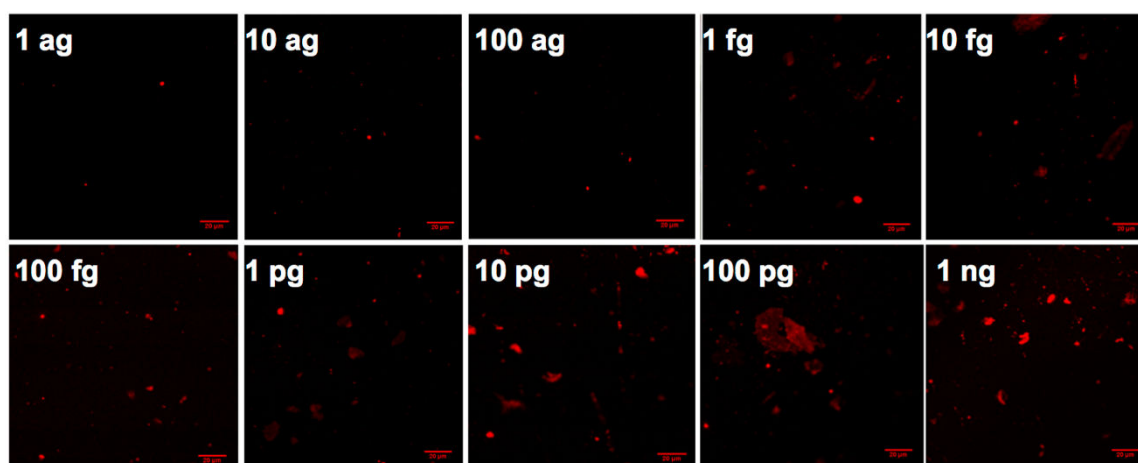


**Figure 6.7.** Confocal Images of the couple 2 (concentrations 1 ag/mL-1ng/mL). Scale bar 20  $\mu$ m. Luminescence images were recorded live on a Zeiss LSM510 Meta confocal microscope using a 40 $\times$  oil immersion objective lens (NA 1.4) and a 488 nm argon ion laser applied for Iridium labelled antibody imaging.

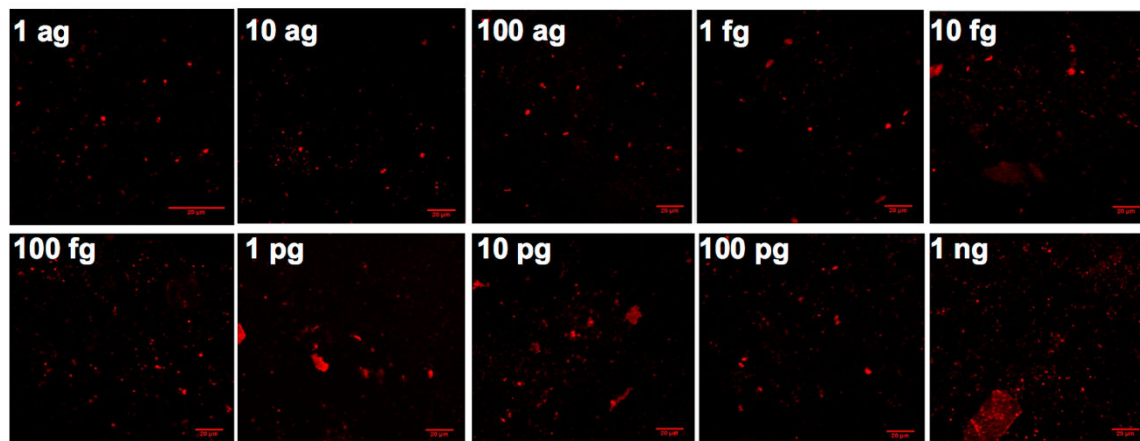


**Figure 6.8.** Confocal Images of the couple 3 (concentrations 1 ag/mL-1ng/mL). Scale bar 20  $\mu$ m. Luminescence images were recorded live on a Zeiss LSM510 Meta confocal microscope using a 40 $\times$  oil immersion objective lens (NA 1.4) and a 488 nm argon ion laser applied for Iridium labelled antibody imaging.

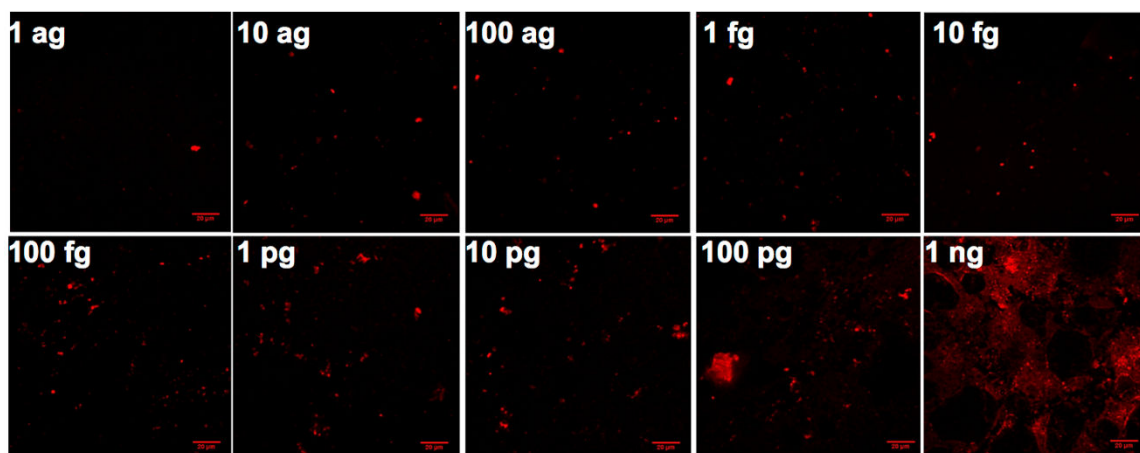


**Figure 6.9.** Confocal Images of the couple 4 (concentrations 1 ag/mL-1ng/mL). Scale bar 20  $\mu$ m. Luminescence images were recorded live on a Zeiss LSM510 Meta confocal microscope using a 40 $\times$  oil immersion objective lens (NA 1.4) and a 488 nm argon ion laser applied for Iridium labelled antibody imaging.

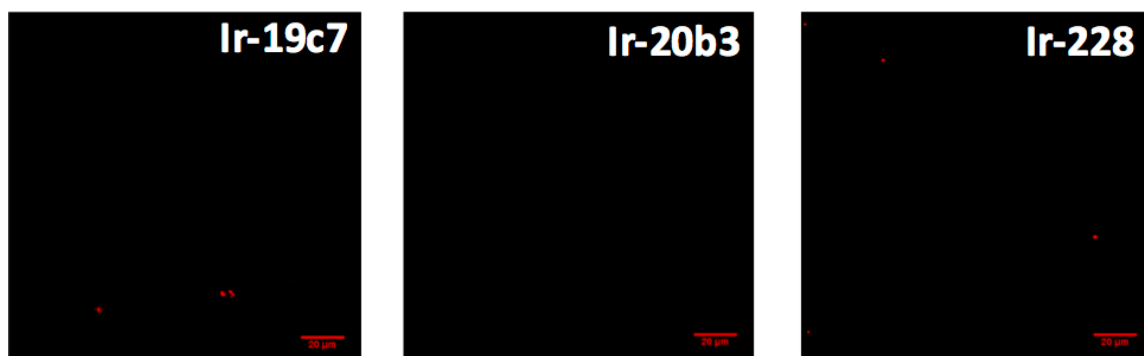


**Figure 6.10.** Confocal Images of the control experiments (monolayer, capture antibody and detection antibody when cTnI complex is absent). Scale bar 20  $\mu$ m. Luminescence images were recorded live on a Zeiss LSM510 Meta confocal microscope using a 40 $\times$  oil immersion objective lens (NA 1.4) and a 488 nm argon ion laser applied for Iridium labelled antibody imaging.



### 6.3. TROPONIN I SENSING

#### 6.3.1 EIS Measurements

The impedance response was measured in a solution of 1 mM DPBS at open circuit potential, at ac amplitude of 25 mV with a frequency range from 0.01 Hz to 100 kHz. The electric behaviour of each fabrication step of the gold impedance sensor can be represented by the simple equivalent circuit model presented in Figure 6.11. The dilute electrolyte (DPBS) was chosen so that the double layer thickness was comparable to the thickness of the antibody-target-secondary antibody/Iridium layer thus making the measurement sensitivity to changes occurring within that film.<sup>25</sup> This can ensure both the cell resistance (intersection of the right-hand side of the Nyquist semicircle with the  $x$ -axis) and the capacitances are strongly dependent on the antigen concentration.

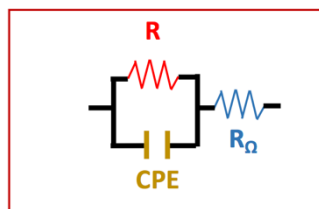


*Figure 6.11. Equivalent circuit model representing the cTnI immunoassays.*

$R_{\Omega}$  represents the electrolyte solution resistance and  $R$  represents the resistance of the modified gold sensor surface, whereas CPE is the charge of constant phase element, presented in section 6.1.2.

The cell resistance obtained for the bare gold is 237  $\Omega$ . The  $R$  value further increased to 1995  $\Omega$  for 16-MHDA SAM electrode indicating that the 16-MHDA layer blocked the mass transport of  $H^+$  from the solution to the surface. As proton is involved in the electron transfer process of Ir-COOH, if the proton transport from the buffer solution is blocked, the electron transfer process of the adsorbed Ir-COOH will be slowed and the  $R$  value will be increased. After the immobilization of the capture antibodies (100  $\mu\text{g/mL}$ ) on the Au/MHDA/ EDC/NHS electrode, the  $R$  value further increased (Table 6.3). The presence of antibodies hindered the efficiency of electron transfer, indicating the successful immobilization of them on the modified sensor surface.<sup>54</sup>

**Table 6.3.** R in  $\Omega$  of gold bares modified with SAM and capture antibodies. The EIS were recorded in the presence of 1 mM DPBS at a frequency range between 0.01 Hz and 100,000 Hz using an ac amplitude of 25 mV amplitude and the dc potential set to the open circuit potential.

Antibody (MAb)	R of SAM+MAb ( $\Omega$ )
20b3	6800
228	9000
19c7	11700

From Table 6.3 it is possible to evidence that the MAb-19c7 show a R that is too high compared to the others. Since they have been prepared in the same way and using the same concentration, this value needs to be evaluated carefully for real argumentations.

The R value, which exhibits the charge transfer kinetics of the surface attached Ir-COOH redox couple, could be used to prove the existence of biomolecular layers on the modified electrode. Generally, the R value can be determined by fitting the experimental data to the model circuit. However, R could also be determined from the diameter of the semicircle part at higher frequencies in the Nyquist plot.

Nyquist plots were utilized to study resistance changes when cTnI I concentration is varied from 1 ng/mL to 1 ag/mL. A dilute electrolyte, 1 mM DPBS, was utilised for EIS so that the double layer thickness was comparable to the thickness of the antibody-target-secondary antibody layer thus making the measurement sensitive to changes occurring within that film.<sup>55</sup> In particular, this dilute concentration of electrolyte ensures both the cell resistance (intersection of the right-hand side of the Nyquist semicircle with the x-axis) and the capacitances are strongly dependent on the cTnI concentration (surface coverage).

The effect of MAb20b3 and MAb228 (same epitope region) as capturing antibodies was initially evaluated (in both cases Ir-19c7 was employed as detection antibody). Nyquist plots of both couples compared to SAM+MAb (no cTnI/Ir-19c7 present on the surface) is presented in Figure 6.12a-b. The two antibodies MAb20b3 and MAb228 alone presented R values of 6800  $\Omega$  and 9000  $\Omega$  (see table 6.3) respectively. Significantly, incubating the antibody modified sensors with increasing concentrations of cTnI labelled with Mab19c7-Ir (100  $\mu\text{g/mL}$ ), Figure 6.12a-b clearly show that the R increases with increasing cTnI

concentration. This increase is attributed to the binding of cTnI to the immobilized MAb20b3 and Mab228 on the electrode, producing a barrier layer that inhibits charge transfer. Significantly, changes in the total impedance can be reliably detected for the couple **1** in the range 10 ag/mL-1 ng/mL, while for the couple **2** the increase is only seen for concentrations above 100 pg/mL resulting in a difficulty of creating a calibration curve for the studied range. Consequently, the custom synthesised Mab20b3 (couple **1**) is suggested as the better capture antibody with respect to the commercial MAb288. The low LOD equal to 10 mg/mL observed for the couple **1** and its ideal regression curve ( $R^2=0.92$ ) demonstrate that this couple may be potentially useful for early detection in AMI diseases. An electrochemical sensor that detect cTnI has been available called i-STAT© cardiac troponin I (cTnI) from Abbott, USA that has excellent portability but has low detection sensitivity ( $0.02 \text{ ng mL}^{-1}$ ) in view of early detection.<sup>56</sup>

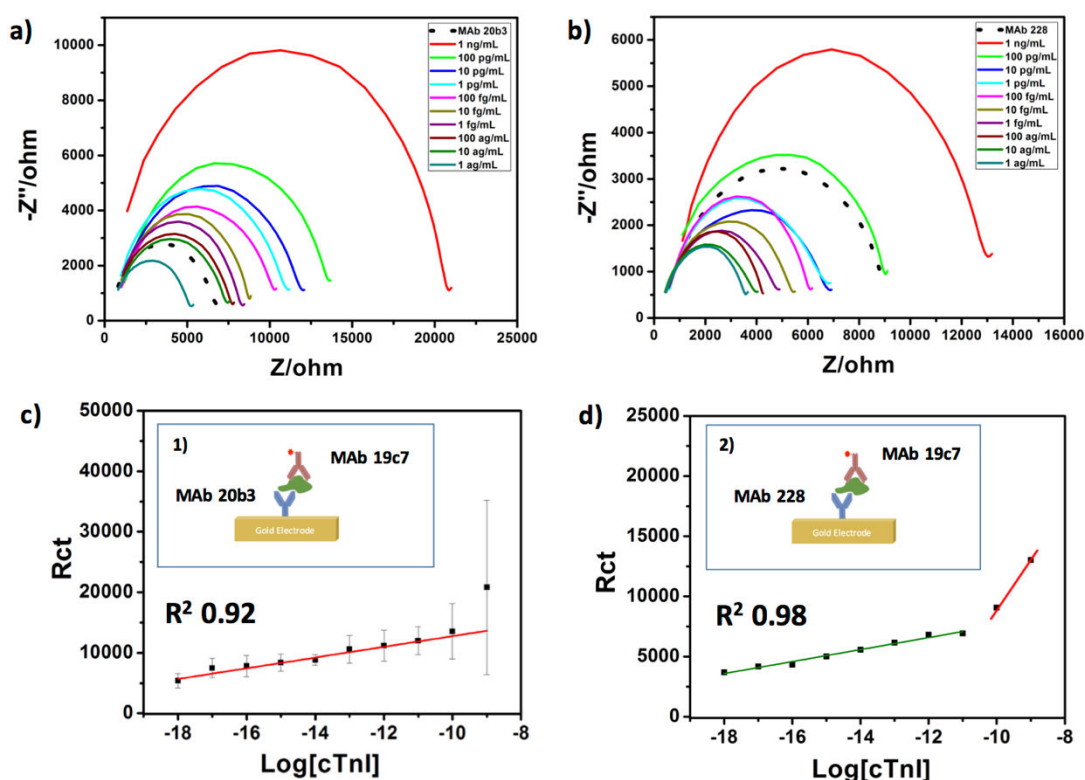


**Figure 6.12.** Nyquist plots of a) 20b3\_cTnI\_19c7-Ir and b) 228\_cTnI\_19c7-Ir bound to modified gold electrodes with the concentration of cTnI systematically varied from 1 ag/mL to 1 ng/mL in 1 mM DPBS ( $N=3$ ). The frequency range was between 0.01 and 100000 Hz; the ac amplitude was 25 mV amplitude and the dc potential set to the open circuit potential. Linear regression of  $R_{ct}$  c) 20b3\_cTnI\_19c7-Ir and d) 228\_cTnI\_19c7-Ir.

The effect of MAb20b3 and MAb228 as detection antibodies was also evaluated using Mab19c7 as capture antibody, as seen in Figure 6.13. In this case the detection for the

couple **3** has a limit (LOD) of 10 pg/mL because of the increase of  $R_c$ , while for the couple **4** an inverse behaviour is observed. In this case the  $R_c$  for each concentration of cTnI is below the value obtained for the monolayer/capture antibody surface. Two possible conclusions exist; (1) this couple impedance is not a suitable technique to detect low concentration of cTnI, (2) the couple is not reliable and physically not formed, giving as result something not realistically explainable.

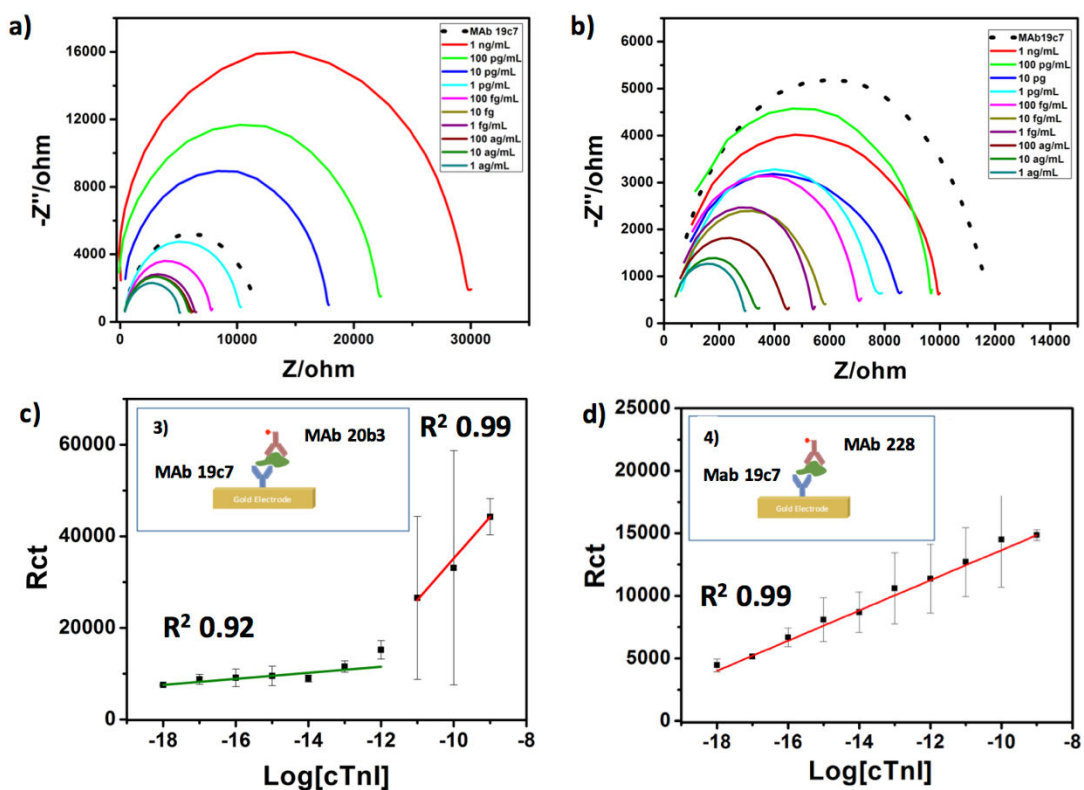


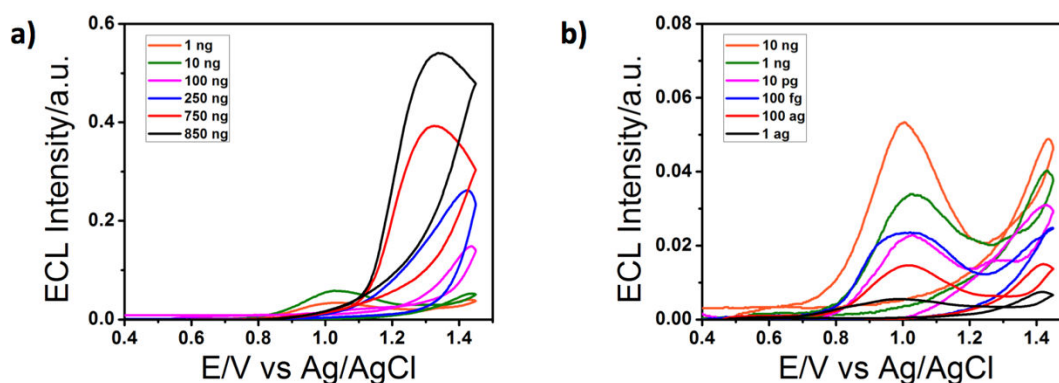
**Figure 6.13.** Nyquist plots of a) 19c7\_cTnI\_20b3-Ir and b) 19c7\_cTnI\_228-Ir bound to modified gold electrodes with the concentration of cTnI systematically varied from 1 ag/mL to 1 ng/mL in 1 mM DPBS ( $N=3$ ). The frequency range was between 0.01 and 100000 Hz; the ac amplitude was 25 mV amplitude and the dc potential set to the open circuit potential. Linear regression of  $R_{ct}$  c) 19c7\_cTnI\_20b3-Ir and d) 19c7\_cTnI\_228-Ir.

### 6.3.2 Electrochemiluminescence

ECL detection was carried out for couple **1** using 100  $\mu\text{M}$  TPrA as co-reactant. cTnI concentrations ranged from 1 ag/mL-1mg/mL, that converted in terms of molarity is 0.042 aM-0.042 mM.

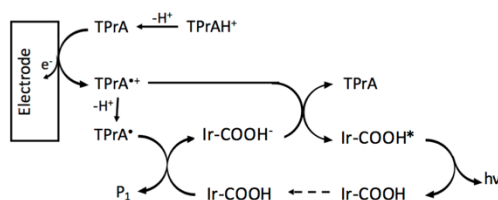
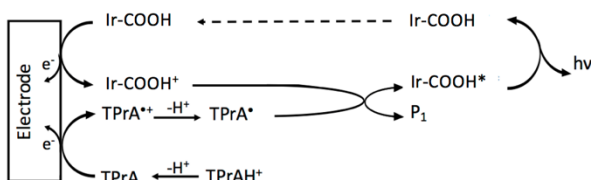
The ECL responses are shown in Figure 6.14. Looking at higher concentrations (Figure 6.14a), the emission observed at approximately +1.35 V vs Ag/AgCl is attributed to the simultaneous oxidation of TPrA and iridium complex, according to the mechanism

reported by Miao and Bard for  $\text{Ru}(\text{bpy})_3^{2+}$  and shown for iridium complex in Figure 6.15b.<sup>57</sup>



**Figure 6.14.** Dependence of ECL Intensity on the cTnI concentration **a)** for high concentration of Ir-MAb (850 ng/mL to 1 ng/mL) and **b)** for low concentration (10 ng/mL to 1 ag/mL) of couple **1**. Measurements carried out upon addition of 100  $\mu\text{M}$  TPrA as co-reactant in 0.33 mM Triton-X 100 PBS solution. Ag/AgCl as reference electrode and a Pt wire as counter electrode. Scan rate 0.1  $\text{V s}^{-1}$ . For clarity, not all the ECL curves for each concentration are shown.

When the iridium concentration is high there is more probability that some iridium complexes are located on the electrode surface, resulting in the simultaneous oxidation of Ir and the co-reactant. After oxidation,  $\text{TPrA}^\bullet$ , reductive unstable radical, reduce by electron-transfer the iridium complex forming its excited state that finally emits light. Passing from higher to lower protein concentrations the emission profile disposes of two peaks (Figure 6.14b), and in this case the peak observed at +1 V vs Ag/AgCl is related to the direct oxidation of TPrA on the electrode surface (Figure 6.15a), termed generally as the “revisited route”. This wave usually merges into the foot of the second peak when the concentration of Iridium complex increases, then it is only visible for lower concentration of label.

**a) Mechanism I****b) Mechanism II**

**Figure 6.15.** **a)** mechanism involving the oxidation of TPrA (mechanism I); **b)** mechanism involving the simultaneous oxidation of the system Ir-COOH/TPrA in aqueous solution containing the iridium complex at low concentration (mechanism II).

The excellent sensitivity of the presented sensor at really low concentration is due to the fact that iridium centers are surface-confined on the electrode. Therefore, the radical TPrA<sup>•</sup> diffuses over short distances and reacts with the luminophores to generate its excited state. This happens at a potential 400 mV lower than for the first mechanism. The path is the typical “oxidative-reductive” one, in which both label and co-reactant are oxidized at the electrode surface. The short-lived TPrA radical cation (TPrA<sup>•+</sup>) loses a proton generating a strongly reducing radical species that can reduce Ir-COOH<sup>•+</sup> in Ir-COOH\*.

Figure 6.16 shows the dependence of ECL intensity on the log[cTnI] over the entire concentration range of couple **1**. From this plot the  $K_D$  (dissociation constant) value of Mab20b3 may be obtained and is found to be approximately  $10^{-8}$  M, which is in close agreement with the  $K_D$  reported in solution for the same in-house synthesized MAb20b3 ( $10^{-9}$  M)<sup>58</sup> and suggests that the antibody demonstrates great affinity towards cTnI.

The ECL intensity increases linearly in two different regions with different slopes. The analytical limit of detection (LOD) has been evaluated for the lower concentration using the formula  $[3 \times \text{SD lowest concentration} / \text{slope of the curve}]$  and was calculated to be 0.42 ag/mL, corresponding to  $1.76 \times 10^{-20}$  M (S/N=4). Such a low LOD is attributed to the employed Ir label, and presents significantly enhanced sensitivity compared to the gold standard  $\text{Ru}(\text{bpy})_3^{2+}$  label in terms of efficiency.<sup>13</sup> This work presents the highest

sensitivity for cTnI detection in comparison to those currently reported in literature using the ECL technique.<sup>13–16</sup>

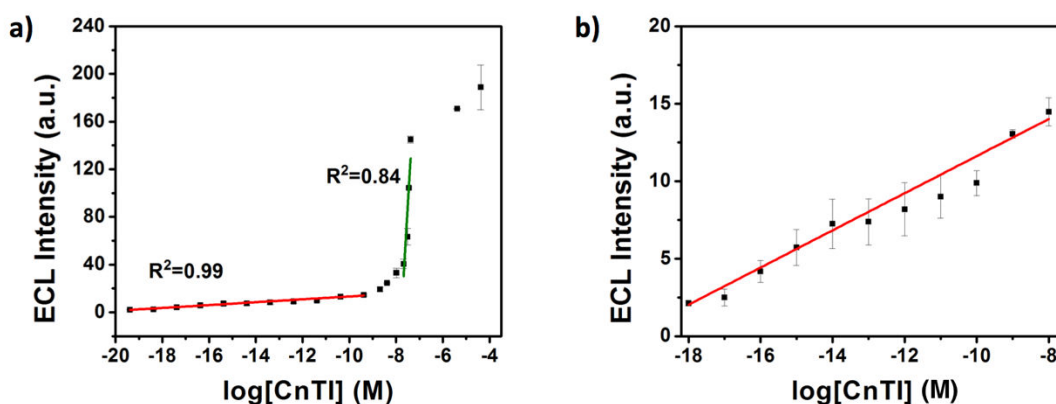


**Figure 6.16.** a) Dependence of the ECL Intensity Area on  $\log[cTnI]$  (full range concentration) and linear regression of the two different zone of concentration. The error bars are comparable to, or smaller, than the size of the symbols; b) linear regression of the low concentration range data (1 ag/mL – 1 ng/mL).

#### 6.4. CONCLUSION

In summary, this work highlights a proof-of-concept example for a new, robust and highly sensitive ECL immunoassay for the detection of Troponin I, which is a biomarker for myocardial infarction. We have combined recombinant antibody technology with EIS and ECL to produce a powerful assay for the determination of the cardiac biomarker at the ag level, which to our knowledge is the first reported bioassay capable of detecting cTnI at these detection levels. Significantly, a bright Ir (III) complex was employed as label for the detection as substitution of the most common used  $Ru(bpy)_3^{2+}$ , since its ECL efficiency is higher than this standard. This example paves the way for a broader application of recombinant antibody engineering across other biologically relevant biomarkers and we are currently pursuing this possibility. In combining recombinant antibody engineering with low background detection techniques such as ECL, there exists much potential for the development of a new generation of sensitive, selective and rapid biosensors as well as significant scope for the improvement of existing systems, all with a common goal of improving point-of-care health monitoring.



## 6.5. EXPERIMENTAL SECTION

### Materials

MAB19c7 (epitope region 41-49) and MAb228 (epitope region 26-35) were purchased from HyTest company. Mab20b3 (epitope 24-39) was synthesized in laboratory (Richard O' Kennedy laboratory at DCU, Dublin). Sulfo-N-hydroxy succinimide (NHS), 1-ethyl-3-[3-dimethylaminopropyl] carbodiimide hydrochloride (EDC), 16-mercaptohexadecanoic acid (MHDA), Dulbecco's phosphate buffered saline (DPBS), dimethylsulfoxide (DMSO), N,N-Dimethylformamide (DMF), tetrabutylammonium tetrafluoroborate (TBABF<sub>4</sub>), Triton X-100 and tri-n-propylamine (TPrA) were purchased from Sigma–Aldrich and used as received. Ir(6-phenylphenanthridine)<sub>2</sub> 2-(Carboxyethyl-phenyl)pyridine-2-carboxylic acid (Ir-COOH) was synthesized as reported elsewhere.<sup>59</sup>

### Immunoassays fabrication

Figure 6.16 illustrates the fabrication process of the cTnI electrochemical immunoassay. A Gold working electrode (Au, 2 mm in diameter) was polished repeatedly with 0.3 and 0.05 mm alumina slurry, followed by successive sonication in acetone, ethanol and distilled water for 5 min and dried in air. The electrodes were then modified with a thiol C16 monolayer by immersion in a 1 mM ethanolic solution of 16-mercaptohexadecanoic acid for 48 hours (step 1 Figure 6.17). Electrodes were then washed in phosphate buffered saline (PBS), pH 7.4, before being immersed in a mixture of EDC and NHS (1:3) DPBS solution for approximately 15 minutes at room temperature (step 2 Figure 6.17).

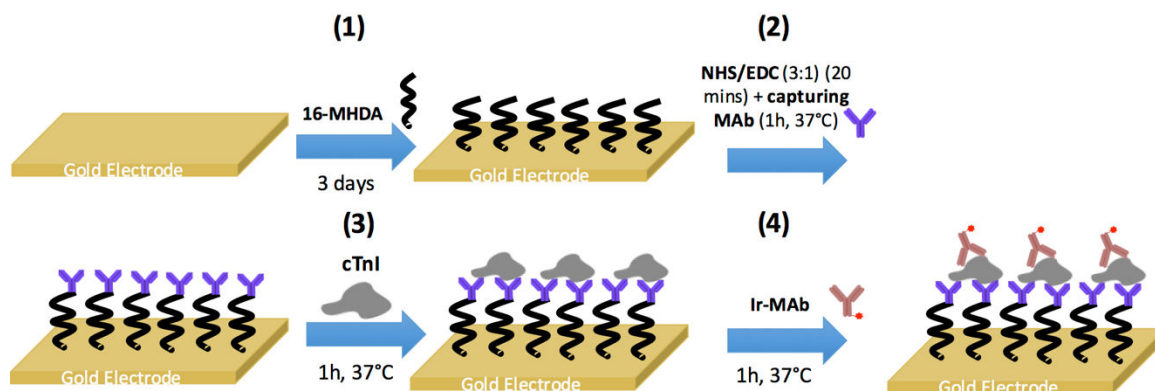


Figure 6.17. Schematic representation of immunoassay fabrication.



Following monolayer modification, the electrode was immersed in capture antibody PBS solution (100 $\mu$ g/mL stock concentration) for approximately 1 hour at 37°C (step 2 Figure 6.17). Each electrode was then washed with PBS Tween (PBST 0.05% v/v), three times and PBS three times. After coating with the capture MAb, the electrodes were incubated in various concentrations of Troponin in PBS for an approximately 1 hour at 37°C followed by washing (PBST x 3 and PBS x 3) (step 3 Figure 6.17). The electrodes were washed even with ethanolamine three times in order to block the non-specific binding sites. After incubation, the electrodes were immersed in a PBS solution containing the soluble labelled Ir-MAb (100 $\mu$ g/mL stock concentration) for 1 hour at 37°C and again washed, (PBST x 3 and PBS x 3), prior to electrochemical and ECL analysis (step 4 Figure 6.17).

### *Electrochemistry*

Voltammetry and EIS were performed using a CH Instruments, Model 760E electrochemical workstation. A three-electrode electrochemical cell was used at a temperature of 22 $\pm$ 2 °C. The working electrode was a 2 mm diameter planar gold disc, modified as previous described, a platinum and a silver wires were used as counter (CE) and quasi-reference (QRE) electrodes for cyclic voltammetries (CVs), while for EIS an Indium Thin Oxide (ITO) electrode as RE and a gold electrode as CE. CVs of the bioassays were performed in DMF with 0.1M tetra-butylammonium hexafluorophosphate (TBAPF6) as supporting electrolyte, whereas the EIS has been done in 1 mM DPBS (pH=7.4). EIS measurements were carried out at the open circuit potential in the frequency range of 0.01–100,000 Hz, with a 25 mV ac amplitude using a conventional three-electrode cell placed inside a Faraday cage. Voltammetry was employed to know the surface coverage by scanning the electrode between +1.8 and -1.6 V.

### *Electrochemiluminescence*

In order to obtain enhanced analytical performance, the medium proposed for the ECL measurements has been a PBS solution of 0.33 mM Triton X-100.

Potentials were measured versus a standard Ag/AgCl aqueous reference electrode (3M KCL). Measurements involving simultaneous detection of light and current utilized a CH instrument model 760B connected to an Oriel 70680 photomultiplier tube (PMT). The PMT was biased at -850 V by a high voltage power supply (Oriel, model 70705) and an

amplifier/recorder (Oriel, model 70701) was used in all the experiments. During the experiments, the cell was kept in a light-tight box in a specially designed holder where the working electrode was positioned directly opposite to the fiber optic bundle, the other end of which was coupled to the PMT.

### *Photophysical Measurements*

Time-resolved emission lifetime and anisotropy measurements were carried out on a PicoQuant Fluotime 100 time-correlated single photon counting (TCSPC) system ( $\lambda_{\text{exc}} = 458 \text{ nm}$ ) using a Thurlby Thandar Instruments (TTi) TGP110 10 MHz pulse generator. For anisotropy measurements sheet polarizers were used to select V polarized excitation from the diode source and the G-factor was estimated by tail matching the VV and VH emission decays. An average of three measurements was taken for each sample, and the data were fit using Fluofit software with a single decay function tail fitting. Time resolved luminescence anisotropy measurements were analyzed to yield anisotropy (rotational correlation time,  $\tau_{\text{rot}}$ ) values using the monoexponential model shown in equation 26 using Fluofit software:

$$r(t) = r_0 \exp(-t/\tau_{\text{rot}}) \quad (26)$$

where  $r(t)$  is the time dependent anisotropy,  $r_0$  is the initial anisotropy,  $\tau$  is the luminescent lifetime of the sample. Because of the long time-scale of the anisotropy decay and consequently the relatively low resolution of the data over short time-scales, a tail fit rather than reconvolution was used to fit the anisotropy data according to this model. The  $r_0$  depends on the data point from which the fit commences and therefore is not reliably determined from this method so these values are not quoted here.

### *Confocal microscopy*

The MAb-20b3/228/19c7 antibody modified electrode sensors were fabricated as presented in Figure 6.16. Following incubation with Troponin (cTnI) concentrations ranging from 1 $\mu\text{g/mL}$ -1 $\text{mg/mL}$  and incubation with the Ir-MAb (100 $\mu\text{g/mL}$  stock concentration) conjugate for 1 hour at 37°C, the electrodes were washed thoroughly with DPBS (pH 7.4) prior to confocal microscopy analysis. Non-specificity was also investigated by incubating gold electrodes modified with a 16-MHDA monolayer (no capture antibody) with Ir-MAb (100 $\mu\text{g/mL}$  stock concentration) for 1 hour at 37°C. All

surfaces were rinsed three times with DPBS (pH 7.4) to remove any non-specifically bound Ir-MAb. Luminescence images were recorded live on a Zeiss LSM510 Meta confocal microscope using a 40× oil immersion objective lens (NA 1.4) and a 488 nm argon ion laser applied for Iridium labelled antibody imaging.

## 6.6 REFERENCES

- (1) WHO. WHO, Facts About Cardiovascular Diseases.
- (2) Murray, C. J. L.; Lopez, A. D. *Lancet* **1997**, *349* (9064), 1498.
- (3) Morrow, D. A.; Cannon, C. P.; Jesse, R. L.; Newby, L. K.; Ravkilde, J.; Storrow, A. B.; Wu, A. H. B.; Christenson, R. H. *Circulation* **2007**, *115* (13), 356.
- (4) Martín-ventura, J. L.; Blanco-colio, L. M.; Tuñón, J.; Muñoz-garcía, B. *Rev. Esp. Cardiol.* **2009**, *62* (6), 677.
- (5) Friess, U.; Stark, M. *Anal. Bioanal. Chem.* **2009**, *393* (5), 1453.
- (6) Christenson, R. H.; Azzazy, H. M. E. *Clin. Biochem.* **2009**, *42* (3), 150.
- (7) Mahajan, V. S.; Jarolim, P. *Circulation* **2011**, *124* (21), 2350.
- (8) Hegyi, G.; Kardos, J.; Kovacs, M.; Malnasi-Csizmadia, A.; Nyitray, L.; Pal, G.; Radnai, L.; Remenyi, A.; Venekei, I. *Introduction to Practical Biochemistry*; Eötvös Loránd University, **2013**.
- (9) Cho, I. H.; Paek, E. H.; Kim, Y. K.; Kim, J. H.; Paek, S. H. *Anal. Chim. Acta* **2009**, *632* (2), 247.
- (10) Dittmer, W. U.; Evers, T. H.; Hardeman, W. M.; Huijnen, W.; Kamps, R.; de Kievit, P.; Neijzen, J. H. M.; Nieuwenhuis, J. H.; Sijbers, M. J. J.; Dekkers, D. W. C.; Hefti, M. H.; Martens, M. F. W. C. *Clin. Chim. Acta* **2010**, *411* (11–12), 868.
- (11) Kim, K.; Park, C.; Kwon, D.; Kim, D.; Meyyappan, M.; Jeon, S.; Lee, J. S. *Biosens. Bioelectron.* **2016**, *77*, 695.
- (12) Kar, P.; Pandey, A.; Greer, J. J.; Shankar, K. *Lab Chip* **2012**, *12* (4), 821.
- (13) Zhou, Y.; Zhuo, Y.; Liao, N.; Chai, Y.; Yuan, R. *Talanta* **2014**, *129*, 219.
- (14) Qi, H.; Qiu, X.; Xie, D.; Ling, C.; Gao, Q.; Zhang, C. *Anal. Chem.* **2013**, *85*, 3886.
- (15) Shen, W.; Tian, D.; Cui, H.; Yang, D.; Bian, Z. *Biosens. Bioelectron.* **2011**, *27* (1), 18.

- (16) Li, F.; Yu, Y.; Cui, H.; Yang, D.; Bian, Z. *Analyst* **2013**, *138* (6), 1844.
- (17) Lasia, A. *Electrochemical impedance spectroscopy and its applications, Modern aspects of electrochemistry*; Conway, B. E., Bockris, J., White, R., Eds.; New York, **1999**.
- (18) Bard, A. J.; Faulkner, L. R. *Electrochemical Methods: Fundamentals and Applications*; **2001**.
- (19) Wiart, R. *Electrochim. Acta* **1990**, *35* (10), 1587.
- (20) Huet, F. *J. Power Sources* **1998**, *70*, 59.
- (21) Yuh, C. Y.; Selman, J. R. **1988**, *34* (12), 1949.
- (22) Randles, J. E. B. *Discuss. faradic Soc.* **1947**, *1*, 11.
- (23) Hu, S.; Wu, Z.; Zhou, Y.; Cao, Z.-X.; Shen, G.-L.; Yu, R.-Q. *Anal. Chim. Acta* **2002**, *458*, 297.
- (24) Spain, E.; Gilgunn, S.; Sharma, S.; Adamson, K.; Carthy, E.; Kennedy, R. O.; Forster, R. J. *Biosens. Bioelectron.* **2016**, *77*, 759.
- (25) Nwankire, C. E.; Venkatanarayanan, A.; Glennon, T.; Keyes, T. E.; Forster, R. J.; Ducreé, J. *Biosens. Bioelectron.* **2015**, *68*, 382.
- (26) Lahiri, J.; Isaacs, L.; Tien, J.; Whitesides, G. M. *Anal. Chem.* **1999**, *71* (4), 777.
- (27) Ostuni, E.; Chapman, R. G.; Holmlin, R. E.; Takayama, S.; Whitesides, G. M. *Langmuir* **2001**, *17* (9), 5605.
- (28) Qian, X.; Metallo, S. J.; Choi, I. S.; Wu, H.; Liang, M. N.; Whitesides, G. M. *Anal. Chem.* **2002**, *74* (8), 1805.
- (29) Berggren, C.; Johansson, G. *Anal. Chem.* **1997**, *69* (18), 3651.
- (30) Mirsky, V. M.; Riepl, M.; Wolfbeis, O. S. *Biosens. Bioelectron.* **1997**, *12* (9), 977.
- (31) Zayats, M.; Raitman, O. A.; Chegel, V. I.; Kharitonov, A. B.; Willner, I. *Anal. Chem.* **2002**, *74* (18), 4763.
- (32) Lucarelli, F.; Marrazza, G.; Mascini, M. *Biosens. Bioelectron.* **2005**, *20*, 2001.
- (33) Cai, H.; Lee, T. M.; Hsing, I. *Sensors Actuators B. Chem.* **2006**, *114*, 433.
- (34) Liu, Z.; Qi, W.; Xu, G. *Chem. Soc. Rev.* **2015**, *44* (10), 3117.
- (35) Miao, W. *Chem. Rev.* **2008**, *108* (7), 2506.
- (36) Rampazzo, E.; Bonacchi, S.; Genovese, D.; Juris, R.; Marcaccio, M.; Montalti, M.; Paolucci, F.; Sgarzi, M.; Valenti, G.; Zaccheroni, N.; Prodi, L. *Coord. Chem. Rev.*

- 2012**, 256 (15–16), 1664.
- (37) Bard, A. J.; Whitesides, G. M. PCT.WO86/02734, **1986**.
- (38) Bard, A. J. *Electrogenerated Chemiluminescence*; **2004**.
- (39) Rusling, J. F.; Bishop, G. W.; Doan, N.; Papadimitrakopoulos, F. *J. Mater. Chem. B. Mater. Biol. Med.* **2014**, 2 (1), 12.
- (40) Chikkaveeraiah, B. V.; Bhirde, A. A.; Morgan, N. Y.; Eden, H. S.; Chen, X. *ACS Nano* **2012**, 6 (8), 6546.
- (41) Milutinovic, M.; Sallard, S.; Manojlovic, D.; Mano, N.; Sojic, N. *Bioelectrochemistry* **2011**, 82 (1), 63.
- (42) Deiss, F.; LaFratta, C. N.; Symer, M.; Blicharz, T. M.; Sojic, N.; Walt, D. R. *J. Am. Chem. Soc.* **2009**, 131 (17), 6088.
- (43) Hu, L.; Xu, G. *Chem. Soc. Rev.* **2010**, 39 (8), 3275.
- (44) Doeven, E. H.; Barbante, G. J.; Kerr, E.; Hogan, C. F.; Endler, J. A.; Francis, P. S. *Anal. Chem.* **2014**, 86, 2727.
- (45) Doeven, E. H.; Zammit, E. M.; Barbante, G. J.; Hogan, C. F.; Barnett, N. W.; Francis, P. S. *Angew. Chem. - Int. Ed.* **2012**, 51, 1.
- (46) He, Y.; Chai, Y.; Yuan, R.; Wang, H.; Bai, L.; Cao, Y.; Yuan, Y. *Biosens. Bioelectron.* **2013**, 50, 294.
- (47) Zu, Y.; Bard, A. J. *Anal. Chem.* **2000**, 72 (14), 3223.
- (48) Liu, X.; Shi, L.; Niu, W.; Li, H.; Xu, G. *Angew. Chem. - Int. Ed.* **2007**, 46 (3), 421.
- (49) Swanick, K. N.; Ladouceur, S.; Zysman-Colman, E.; Ding, Z. *Chem. Commun.* **2012**, 48, 3179.
- (50) Barbante, G. J.; Doeven, E. H.; Francis, P. S.; Stringer, B. D.; Hogan, C. F.; Kheradmand, P. R.; Wilson, D. J. D.; Barnard, P. J. *Dalt. Trans.* **2015**, 44 (18), 8564.
- (51) Fernandez-Hernandez, J. M.; Longhi, E.; Cysewski, R.; Polo, F.; Josel, H.-P.; De Cola, L. *Anal. Chem.* **2016**, 88 (8), 4174.
- (52) Ameloot, M.; Acuña, A. U.; Valeur, B.; Hasselt, U.; Building, C. *Pure Appl. Chem.* **2013**, 85 (3), 589.
- (53) Barbero, N.; Napione, L.; Quagliotto, P.; Pavan, S.; Barolo, C.; Barni, E.; Bussolino, F.; Viscardi, G. *Dye. Pigment.* **2009**, 83 (2), 225.
- (54) Katz, E.; Willner, I. *Electroanalysis* **2003**, 15 (11), 913.

- (55) Luna, D. M. N.; Avelino, K. Y. P. S.; Cordeiro, M. T.; Andrade, C. A. S.; Oliveira, M. D. L. *Sensors Actuators B. Chem.* **2015**, 220, 565.
- (56) Use, I.; Explanation, M.; Ingredient, R.; Phosphate, S. A.; Source, B.; Intestine, P.; Igm, M.; Quantity, M. *Abbott Point Care Inc.* **2013**, 1.
- (57) Miao, W.; Choi, J.-P.; Bard, A. J. *J. Am. Chem. Soc.* **2002**, 124 (48), 14478.
- (58) Conroy, P. J.; Okennedy, R. J.; Hearty, S. *Protein Eng. Des. Sel.* **2012**, 25 (6), 295.
- (59) Cysewski, R.; De Cola, L.; Fernandez Hernandez, J. M.; Josel, H.-P.; Lopez-Calle, E.; Zarnt, T. Iridium-based complexes for ECL. US 8835637 B2, **2014**.



# Chapter 7

## Experimental Techniques

### **Abstract**

This chapter briefly describes the major instrumental methods employed in the thesis for the characterization of the compounds both theoretically and practically. UV-Vis absorption, Steady state and time resolved emission techniques are described as well as quantum yield measurements and cyclic voltammetry. Microscopy techniques such as scanning electron microscopy, transmission electron microscopy and fluorescence microscopy are discussed. The conditions for all other commonly used characterizations and experimental techniques (i.e. NMR, mass spectroscopy, sample preparation) are given in the experimental sections of the individual chapters.



## 7.1 ABSORPTION SPECTROSCOPY

In order to measure such quantity with no influences exerted by other phenomena (mainly related to short-term changes in source intensity), a double-beam UV-Vis spectrophotometer is used. A schematic diagram of a double-beam UV-Vis spectrophotometer is shown in Figure 7.1. The monochromator selects a particular wavelength from the light source, which is split into two separate beams. These two beams ( $I_0$ ) are guided through the sample containing and through the pure solvent (reference) using optically transparent cells (generally quartz cuvettes). The intensity of two beams is compared to give respective absorbances.

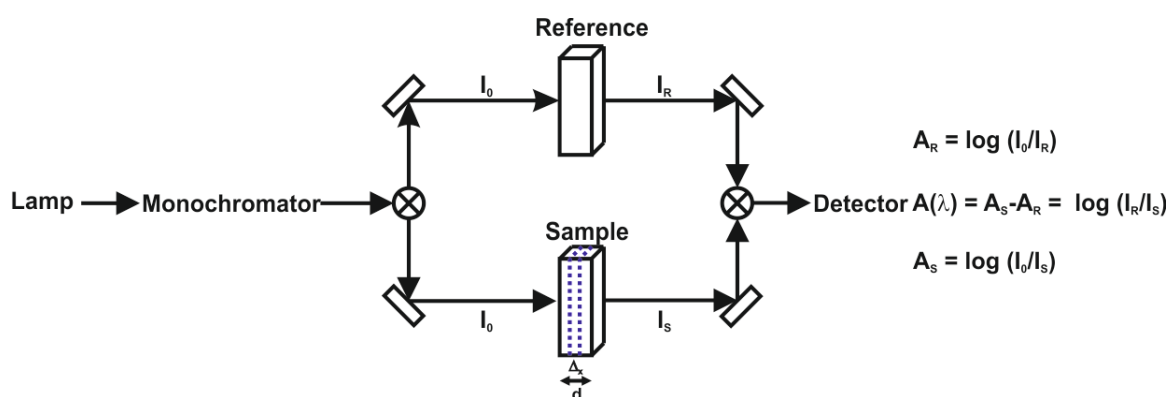


Figure 7.1. Schematic description of a double beam spectrophotometer.

Consider a thin slab of solution of thickness  $dx$  that contains  $n$  light-absorbing molecules/cm<sup>3</sup> (Figure 7.1). If  $\sigma$  is the effective cross-section for absorption in cm<sup>2</sup>, the light intensity  $dI$  absorbed per thickness  $dx$  is proportional to the intensity of the incident light  $I$ ,  $\sigma$  and the number of molecules per cm<sup>3</sup> ( $n$ ):

$$\frac{dI}{dx} = I\sigma n \quad (7.1)$$

Rearrangement and integration, subject to the boundary condition  $I = I_0$  at  $x = 0$ , yields the Beer-Lambert equation, which is generally used in an alternative form:

$$\log \frac{I_0}{I} = \epsilon cd \quad (7.2)$$

where  $\epsilon$  is the molar extinction coefficient (in M<sup>-1</sup> cm<sup>-1</sup>) and  $c$  is the concentration in moles/liter. Also, the transmittance ( $T$ ) is frequently used and it is defined as the ratio between the intensity of light that passes through a medium (transmitted light,  $I$ ) and the intensity of the incident light ( $I_0$ ). In other words, it is defined as the negative logarithm of

the absorbance. Beer's Law predicts that the optical density is directly proportional to the concentration of the absorbing species. However, deviations from Beer's law can result from both instrumental and intrinsic causes. Biological and/or supramolecular systems that contain macromolecules or other large aggregates, can lead to turbid samples that scatter light. The optical density resulting from scatter will be proportional to  $1/\lambda^4$  (Rayleigh scattering), and may thus be easily recognized as a background absorption that increases rapidly with decreasing wavelength. If the optical density of the sample is high, and the absorbing species fluorescent, the emitted light cannot reach the detector. However, this effect can be minimized by keeping the detector distant from the sample, decreasing the efficiency with which the fluorescence emission is collected or with cuvettes having reduced optical path or a different geometry. Aggregation processes can also take place and the resulting supramolecular systems may possess distinct features from the monomers. Depending upon the wavelength chosen for observation, the deviations from Beer's law may be positive or negative. In our experiments the electronic absorption spectra were recorded on a Shimadzu UV-3600 double-beam UV–VIS–NIR spectrophotometer and baseline corrected. Time- and temperature-dependent absorption spectra were recorded on a JASCO V-650 UV–VIS spectrophotometer equipped with cell holder and temperature control. The quartz cuvettes (from Hellma) have an optical path of 1 cm.

## 7.2 FLUORESCENCE SPECTROSCOPY

An emission spectrum is the wavelength distribution of an emission measured at a single constant excitation wavelength. Conversely, an excitation spectrum is the dependence of emission intensity, measured at a single emission wavelength, upon scanning the excitation wavelength. Such spectra can be presented on either a wavelength scale or a wavenumber scale. Light of a given energy can be described in terms of its wavelength  $\lambda$ , frequency  $\nu$ , or wavenumber. The usual units for wavelength are nanometers, and wavenumbers are given in units of  $\text{cm}^{-1}$ . Wavelengths and wavenumbers are easily interconverted by taking the reciprocal of each value. For example, 400 nm corresponds to  $(400 \times 10^{-7} \text{ cm})^{-1} = 25,000 \text{ cm}^{-1}$ . On the contrary of absorption spectroscopy in which a double-beam configuration can get right of many artefacts, there is no ideal spectrofluorometer. The available instruments do not yield true excitation or emission spectra. This is because of the nonuniform spectral output of the light sources and the wavelength-dependent efficiency of the monochromators and detector tubes. The polarization or anisotropy of the emitted

light can also affect the measured fluorescence intensities because the efficiency of gratings depends on polarization. Emission spectra recorded on different instruments can be different because of the wavelength-dependent sensitivities of the instruments. Figure 7.2 shows a schematic diagram of a Fluorolog 3 spectrometer. In this thesis, steady-state emission spectra were recorded on a HORIBA Jobin-Yvon IBH FL-322 Fluorolog 3 spectrometer equipped with a 450 W xenon arc lamp as a source of exciting light which passes through a monochromator (2.1 nm/mm dispersion; 1200 grooves/mm) and is directed to a reference detector and to the sample.

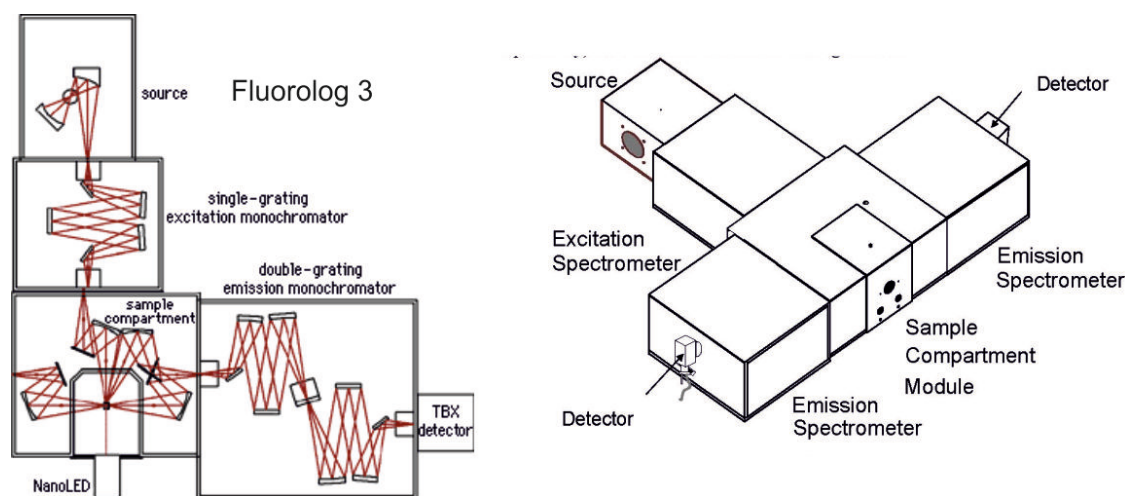


**Figure 7.2.** Schematic representation of the fluorescence spectrophotometer Fluorolog 3 model FL3-12 from Horiba Scientific (source: [www.horiba.com](http://www.horiba.com)).

Emission of the sample, collected at  $90^\circ$  with respect to the incident light, passes through another monochromator (2.1 nm/mm dispersion; 1200 grooves/mm) before reaching the detector. Different detectors were used depending on the considered region of the light spectrum: for the UV-Vis range, a TBX-04 single photon-counting detector was used whereas for the NIR a Hamamatsu R2658P photomultiplier was used. The excitation spectra are corrected for source intensity (lamp and excitation grating) and for detector spectral response and emission grating by standard correction curves. Optical Filters are used, to remove unwanted wavelengths in the excitation beam, or to remove scattered light from the emission channel in particular a 400 nm long pass filter was employed. For anisotropy measurements, a PicoQuant FluoTime 300 (PicoQuant GmbH, Germany) equipped with the Multi-Channel Scaling (MCS) electronics NanoHarp 250 and a xenon lamp as a source of exciting light was used.

### 7.3 LUMINESCENCE QUANTUM YIELD

The luminescence quantum yield was measured for a molecule in solution varies depending on the experimental conditions, including the type of solvent, the concentrations of sample and dissolved oxygen in the solution, temperature, and excitation wavelength. When the physical conditions are fully specified, the absolute quantum yield can, in principle, be precisely determined. However, even if these parameters are specified, a number of pitfalls exist. It must be considered explicitly to determine reliable quantum yields. These include polarization effects, refractive index effects, reabsorption/ reemission effects, internal reflection effects, and the spectral sensitivity of the detection system.<sup>1,2</sup> They can be classified into absolute (or primary) methods and relative (or secondary) methods.<sup>3</sup>

The absolute methods require performing various complex corrections to obtain accurate quantum yields. Therefore, in most laboratories relative (secondary) methods are used to determine quantum yields. In secondary methods, the quantum yield of a sample solution is determined by comparing the integrated fluorescence intensity with a standard solution under identical conditions of incident irradiance. Thus, it is critical to correct for the spectral sensitivity of the instrument, and the measured quantum yield is only as accurate as the certainty of the quantum yield of the fluorescence standard according to the equation:

$$\Phi_S = \Phi_R \frac{I_S OD_R n_S^2}{I_R OD_S n_R^2} \quad (7.3)$$

where  $\Phi$  is the photoluminescence quantum yield (PLQY);  $I$  is the integrated emission intensity;  $OD$  is the optical density, and  $n$  is the refractive index. The subscripts  $S$  and  $R$  refer to the sample and reference fluorophore the latter must have a known quantum yield. In this expression it is assumed that the sample and reference are excited at the same wavelength, so that it is not necessary to correct for the different excitation intensities of different wavelengths.<sup>4</sup>

Many different absolute (or primary) methods for determining PLQY have been developed such as the Vavilov method (using magnesium oxide as a standard)<sup>5</sup>, the Weber and Teale method (using scattering solution as standard)<sup>6</sup>, Calorimetric methods<sup>7-9</sup> and photoacoustic (optoacoustic) methods<sup>10,11</sup> detect the fraction of the absorbed energy which is lost by nonradiative processes in a luminescent sample, i.e., the complement of the luminescence energy yield. These photothermal methods generally require making the assumption that

the relaxation processes of excited molecules involve no photochemical reactions. Another approach consists in the use of an integrating sphere which collects all the emitted photons with a calibrated photodiode and sets them into relation with the number of absorbed photons. In this way, the effects of polarization, scattering and refractive index are eliminated from the measurements. A schematic representation of an integrating sphere setup is shown in Figure 7.3.

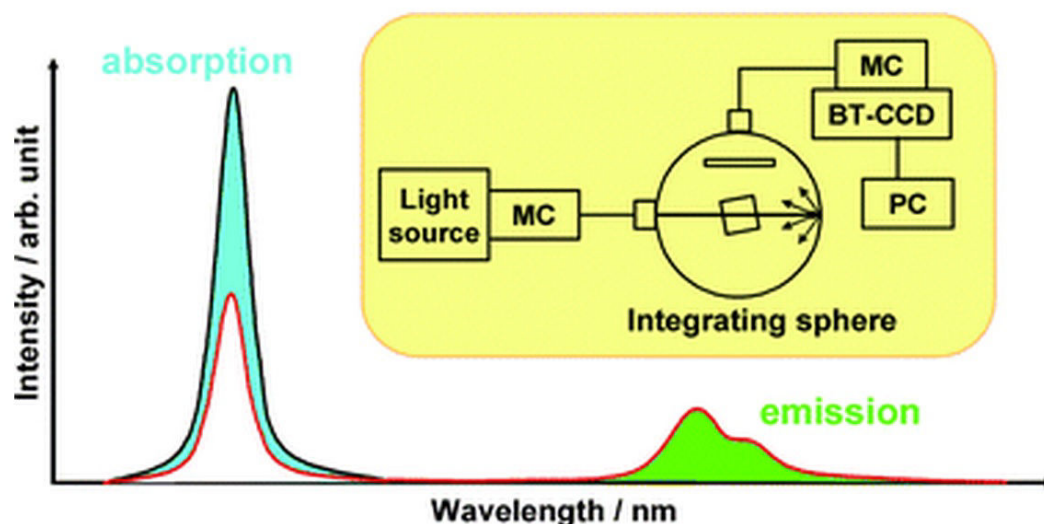


**Figure 7.3.** Schematic representation of an integrating sphere (IS) for measuring absolute luminescence quantum yields. MC stands for monochromator, and BT-CCD is a back thinned CCD. The number of photons absorbed is proportional to the difference of the integrated excitation light profiles, while the number of photons emitted is proportional to the area under its fluorescence spectrum.<sup>3</sup>

Light from a xenon lamp is monochromatized at the selected wavelength and guided by an optical fiber into the IS. The emitted light from the sample is collected by a detector after passing through another optical fiber and a second monochromator. The PLQY ( $\Phi$ ) is then calculated from the number of photons absorbed (difference of the integrated excitation light profiles) and the number of photons emitted (integrated fluorescence spectrum) according to the equation:

$$\Phi = \frac{PN(Em)}{PN(Abs)} = \frac{\int \frac{\lambda}{hc} [I_{em}^{sample}(\lambda) - I_{em}^{reference}(\lambda)] d\lambda}{\int \frac{\lambda}{hc} [I_{exc}^{reference}(\lambda) - I_{exc}^{sample}(\lambda)] d\lambda} \quad (7.4)$$

where PN(Abs) is the number of photons absorbed by a sample and PN(Em) is the number of photons emitted from a sample,  $\lambda$  is the wavelength, h is Planck's constant, c is the

velocity of light,  $I_{exc}^{sample}$  and  $I_{exc}^{reference}$  are the integrated intensities of the excitation light with and without a sample respectively,  $I_{em}^{sample}$  and  $I_{em}^{reference}$  are the photoluminescence intensities with and without a sample, respectively. For this purpose, we used Hamamatsu Photonics absolute PL quantum yield measurement system (C9920-02) equipped with a L9799-01 CW Xenon light source (150 W), monochromator, C7473 photonic multichannel analyzer, integrating sphere and employing U6039-05 PLQY measurement software (Hamamatsu Photonics, Ltd., Shizuoka, Japan).

#### 7.4 LIFETIME MEASUREMENTS

Time-resolved experiments, such as the excited state lifetime determination, were carried out by time-correlated single-photon counting (TCSPC). The schematic diagram of the setup is shown in Figure 7.4. The experiment starts with the excitation pulse (either a flash lamp or a laser) which excites the samples and sends a signal to the electronics. This signal is passed through a constant function discriminator (CFD), which accurately measures the arrival time of the pulse.

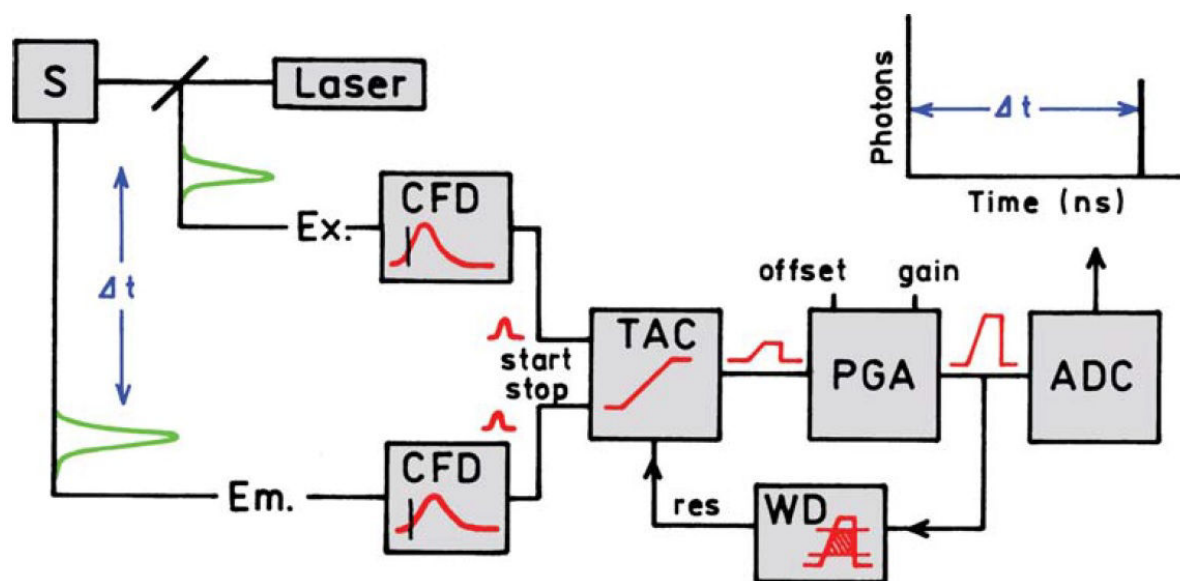


Figure 7.4. Electronic schematic for TCSPC.<sup>4</sup>

The signal (START) is passed to a time-to-amplitude converter (TAC), which starts the charging of the capacitor by generating a voltage ramp. The voltage increases linearly with time on the nanosecond timescale. A second channel detects the pulse from the single detected photon (STOP). The arrival time of the signal is also accurately determined using a CFD, which sends a signal to stop the voltage ramp. TAC now contains a voltage

proportional to the time delay and is stored in a histogram in which the x-axis in the histogram is the time difference between START and STOP signal and the y-axis is the number of photons detected for this time difference. As needed the voltage is amplified by a programmable gain amplifier (PGA) and converted to a numerical value by the analog-to-digital converter (ADC). To minimize false readings the signal is restricted to given range of voltages. If the signal is not within this range the event is suppressed by a window discriminator (WD). The voltage is converted to a digital value that is stored as a single event with the measured time delay. By repetitive measurements a statistical time distribution of emitted photons is obtained.

Time-resolved measurements up to  $\sim 10 \mu\text{s}$  were performed using the TCSPC option (PicoHarp) of a FluoTime 300 “EasyTau” apparatus (PicoQuant) equipped with subnanosecond LDH sources (375, 405, 440, 510 and 640 nm, with 50–100 ps pulse-width) powered by a PicoQuant PDL 820 variable (0.2–80 MHz) pulsed power supply. A PMA-C was employed for detection in the UV-visible (200–900 nm). For excited state lifetimes  $>10 \mu\text{s}$ , NanoHarp 250 MCS (Multi Channel scaler Card) histogram accumulating real-time processor was employed.

The multichannel analyzer consists of a multichannel card. The light input is discriminated for its intensity and if the input pulse amplitude falls within the threshold of the lower level discriminator and the upper level discriminator, the control and logic circuit are enabled and the peak amplitude is stored. In general, the signal intensities are collected in different channels for the duration of a dwell time after which an intensity counter moves to the next channel. After the acquisition time is reached, the collected total light intensities in all channels are counted and correlated to the time frame of each channel giving an intensity-time profile.

The decays were analyzed by means of PicoQuant FluoFit Global Fluorescence Decay Analysis Software (PicoQuant GmbH, Germany). The quality of the fit was assessed by minimizing the reduced  $X^2$  function and by visual inspection of the weighted residuals. For multi-exponential decays, the intensity, namely  $I(t)$ , has been assumed to decay as the sum of individual single exponential decays:

$$I(t) = \sum_{i=1}^n a_i e^{-\frac{t}{\tau_i}} \quad (7.5)$$

where  $\tau_i$  are the decay times and  $a_i$  are the amplitude of the component at  $t = 0$ . The percentages to the pre-exponential factors,  $a_i$ , are listed upon normalization.

## 7.5 SCANNING ELECTRON MICROSCOPY (SEM)

The schematic diagram of a simplified SEM setup is shown in Figure 7.5. The beam of electrons, generated at the top by the electron gun, is accelerated by the anode, which is biased +1 to +50 kV respect to the electron gun, down into the electron column. After being collimated through condenser lens the beam passes through pairs of scanning coils in the electron column, which deflect the beam in the x and y axes so that it scans in a raster fashion over a rectangular area of the sample surface.

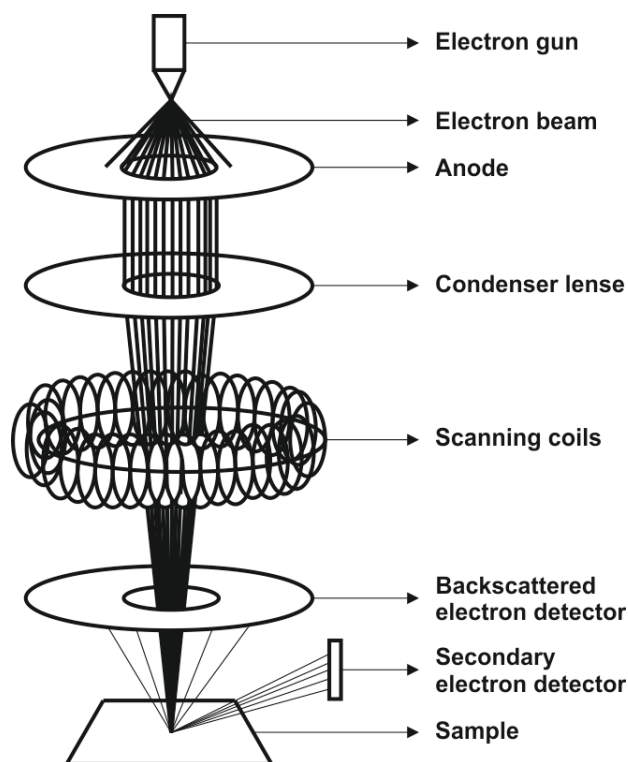


*Figure 7.5 Schematic representation of a SEM setup.*

Generally, the beam is focused in a spot of 1 nm to 5 nm size. The energy exchange between the electron beam and the sample results in the reflection of high-energy electrons by elastic scattering, emission of secondary electrons by inelastic scattering and the emission of electromagnetic radiation, each of which can be detected by specialized detectors.

The most common imaging mode collects low-energy (<50 eV) secondary electrons that are ejected from the k-shell of the specimen atoms by inelastic scattering interactions. The



Backscattered electrons, originated by elastic scattering interactions with specimen atoms can also be used for creating the contrast image of the specific regions of the sample.

For conventional imaging in the SEM, specimens must be electrically conductive, at least on the surface, and electrically grounded to prevent the accumulation of electrostatic charge on the surface. Therefore they are usually coated with an ultrathin coating of electrically conducting material, deposited on the sample either by low-vacuum sputter coating or by high-vacuum evaporation.

In this thesis, the samples were covered by a 5 nm thick gold layer, and finally investigated using a FEI Dual Beam 235: FIB-SEM-STEM with an ion beam (FIB, 5 nm) and electron beam (SEM, 1 nm).

## 7.6 FLUORESCENCE MICROSCOPY

Figure 7.6 shows a simplified setup of a wide-field fluorescence microscope (left) and a laser scanning confocal microscope (right).

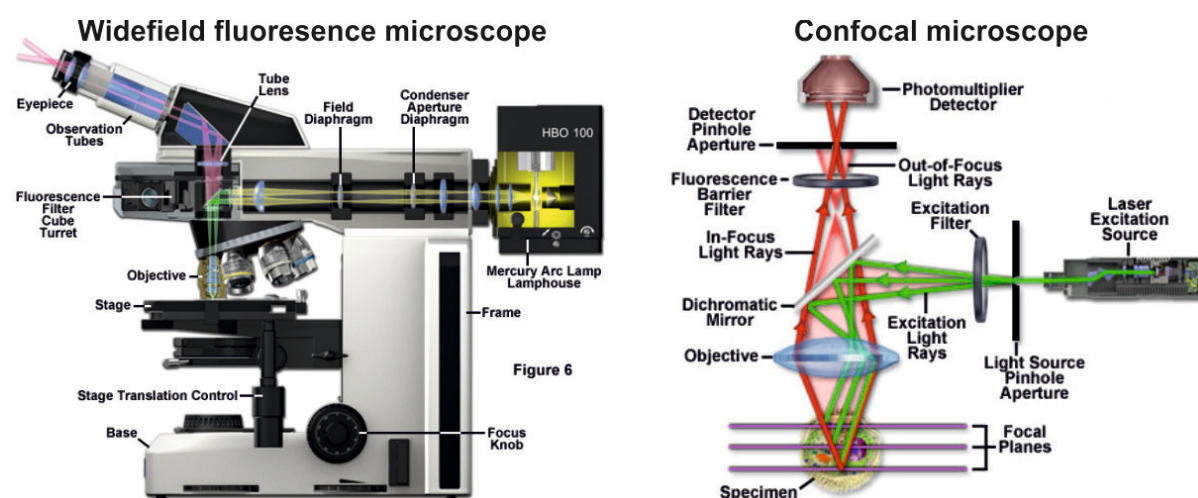


**Figure 7.6.** Simplified setup of a widefield fluorescence microscope (left) and schematic representation of a Laser Scanning Confocal Microscope (right) adapted from [www.zeiss.com](http://www.zeiss.com).

In the wide-field microscopes the light source is usually a xenon arc lamp or mercury-vapor lamp. An excitation filter selects a particular wavelength range, and the excitation beam is deflected at  $90^\circ$  by a dichroic (DIC) mirror, reaching the sample after passing through an emission filter and the objective lens which focuses the light emitted by the sample onto an area array detector system (usually a CCD camera). A shutter system limits the excessive exposure to harmful excitation light. The full aperture of emission light gathered by the

microscope objective maximizes the recorded signal and simultaneously minimizes the required exposure times. Thus, specimens can be imaged with very brief illumination periods. The major drawback of widefield imaging is that fluorescence arising from regions far from the focal plane, as well as background signal, often obscures the features of interest. Therefore, widefield imaging achieves the optimum results when the features of interest are either large (such as an organelle) or highly punctate in nature. Generally, DIC microscopy is used in conjunction with widefield fluorescence to monitor the general morphology while simultaneously investigating phenomena of interest with specifically labeled targets. Thus, the DIC image can be captured from a fluorescently labeled specimen using transmitted light followed by imaging in epi-fluorescence mode and combined during analysis.

Nowadays wide-field microscopes can capture DIC and fluorescence images simultaneously. Multiple fluorophores can be sequentially imaged to elucidate the spatial and temporal relationships between labeled targets.

Laser scanning confocal microscopes (Figure 7.6 right) offer several advantages over conventional wide-field fluorescence microscopes, in particular the possibility to control the depth of field and the elimination of the out-of-focus information. It is also possible to collect series of “optical sections” from thick specimens that can be subsequently used to reconstruct the specimens in three dimensions.

The key to the confocal approach is the usage of spatial filtering to eliminate out-of-focus light or flare in specimens that are thicker than the plane of focus by illuminating the objective through a pinhole. Only if the specimen is in focus, the light can pass through the pinhole and reach a detector (usually a PMT).

As drawback, total signal level is lower even if the specific signal-to-noise ratio for the features of interest is increased.

Magnification can be electronically adjusted by altering the scanning laser sampling period which varies the area scanned by the laser without having to change objectives (zoom factor). Increasing the zoom factor reduces the specimen area scanned and simultaneously reduces the scanning rate. However high zoom factor may lead to increase photobleaching.

In this thesis fluorescence confocal microscopy was performed with a Zeiss LSM510 Meta confocal microscope using a 40× oil immersion objective lens (NA 1.4) and a 488 nm argon ion laser.

## 7.7 TRANSMISSION ELECTRON MICROSCOPY

This microscope technique is used to analyze very small objects, down to the angstrom scale. An electron beam that is produced by an anode under vacuum and passes at a very high speed through the sample and to the cathode. This beam is condensed by electromagnetic lenses, and electrons are stopped or not by the structures they collide with. The lenses then widen the obtained picture and projected on a fluorescent screen.

The vacuum is maintained during the entire experiment to avoid electrons dispersion. Therefore, a cooling system is also used, typically with liquid nitrogen. Nowadays, TEM microscopes are equipped by a camera, allowing a better data acquisition. TEM offers the advantage of pushing the limit of resolution down to 50 pm, with possible magnification in the order of  $10^7$  times, making it possible to work at the atomic scale. A schematic view of the electron path in a TEM instrument is shown in Figure 7.7.

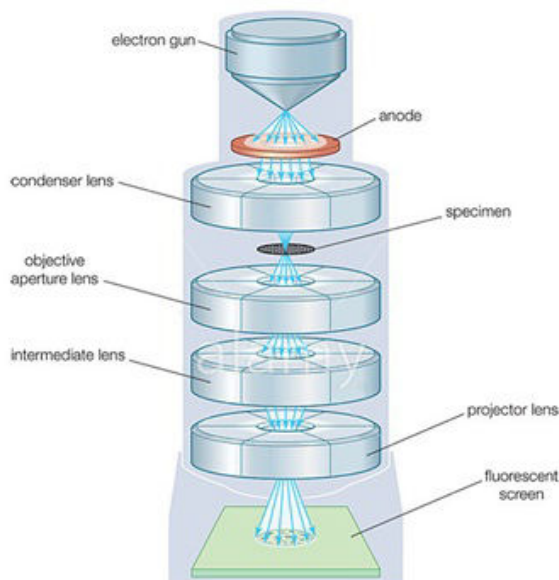


*Figure 7.7. Schematic representation of a TEM setup.*

Once the electron beam passes through the sample, it reaches the objective lens, which generates the first intermediate image of the sample, the quality of which determines the resolution of the final image. The intermediate image is an inverted initial one, which then

is subsequently magnified by the intermediate lens, and produces a second intermediate image. The latter is collected by the projector lens, which forms the final image onto a fluorescent screen or a recording device.

## 7.8 ELECTROCHEMISTRY

### *Cyclic Voltammetry (CV)*<sup>12</sup>

Cyclic voltammetry is the most used electroanalytical technique. It is performed by connecting an electrochemical potentiostat to an electrochemical cell. The cell contains a sample solution and three electrodes: working electrode (WE), reference electrode (RE) and counter electrode (CE). A cyclic voltammogram is obtained by applying the working electrode potential swept linearly between two voltages at a fixed rate. Figure 8 shows the cyclic voltammogram. As the potential is swept back and forth, it crosses the formal potential,  $E_0$ , of an analyte and a current flow through the electrode that either oxidizes or reduces the analyte.

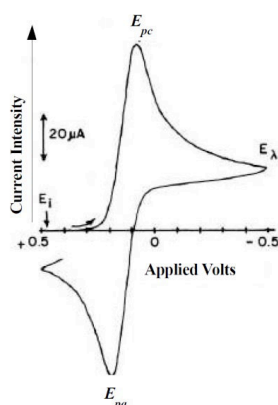


**Figure 7.8.** Example of cyclic voltammogram.

From Figure 7.8, two peaks are obtained when the potential sweep back and forth, the peak potential for the anodic sweep,  $E_{pa}$ , and the peak potential for the cathodic peak,  $E_{pc}$ . The difference between  $E_{pc}$  and  $E_{pa}$ ,  $\Delta E$ , can be calculated, and if the redox couple is reversible, then the relationship  $n\Delta E = 59 \text{ mV}$  holds true, where  $n$  is the number of electrons involved in the redox couple. Also, the anodic peak current,  $i_{pa}$ , is equal to the cathodic peak current,  $i_{pc}$ , so that the relationship  $(i_{pa}/i_{pc}) = 1$  also holds true for the reversible redox couple. Besides, if  $59 \text{ mV} < \Delta E < 100 \text{ mV}$ , the redox couple is described as quasi-reversible, and if

$\Delta E > 100$  mV, the redox couple is described as irreversible. The formal potential  $E_0$  for a reversible redox couple is termed as the average of the two peak potentials as follows:

$$E_0 = \frac{(E_{pa} + E_{pc})}{2} \quad (7.6)$$

### Potentiostatic techniques<sup>12</sup>

In a potential step experiment, two responses can be recorded, whereby the potential of a working electrode is changed instantaneously and the current time (galvanostatic) or the charge time (potentiostatic) is found. In chronoamperometry, the potential is stepped so as to drive a Faradaic reaction. This potential is held while the current with time is monitored at the electrode (Figure 7.9). At the initial potential, no significant current flows. At the final potential, the analyte is consumed at the electrode surface. There is a depletion of the concentration of the analyte near the electrode. The current response is shown by a rapid increase followed by decay as the analyte is exhausted and equilibrium is reached. In this case, the charge for reduction is calculated by integrating the area under the current versus time curve within the limits of the initial to final deposition time.

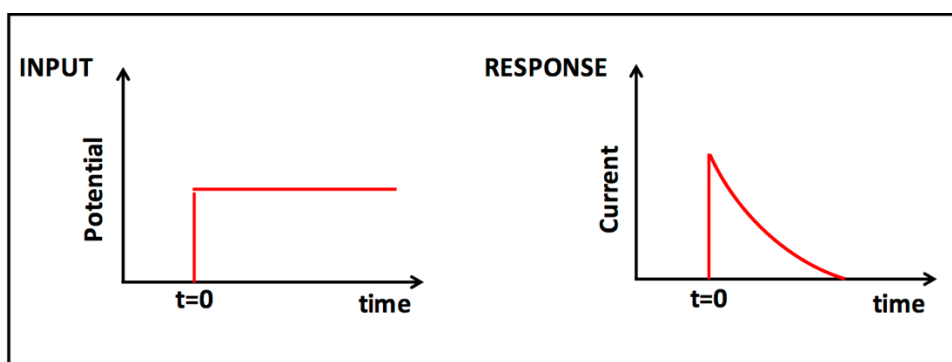


Figure 7.9. Variation of current in potentiostatic method.

## 7.9 REFERENCES

- (1) Crosby, G. A.; Demas, J. N. *J. Phys. Chem.* **1971**, 75, 991.
- (2) Eaton, D. F. *Pure Appl. Chem.* **1988**, 60 (7), 1107.
- (3) Suzuki, K.; Kobayashi, A.; Kaneko, S.; Takehira, K.; Yoshihara, T.; Ishida, H.; Shiina, Y.; Oishi, S.; Tobita, S. *Phys. Chem. Chem. Phys.* **2009**, 11 (42), 9850.
- (4) Lakowicz, J. R. *Principles of Fluorescence Spectroscopy*; **2006**.
- (5) Vavilov, S. I. *Z. Phys.* **1924**, 22, 266.

- (6) Hercules, D. M.; Frankel, H. *Science* (80-. ). **1960**, 131, 1611.
- (7) Gelernt, B.; Findeisen, A.; Stein, A.; Poole, J. A. *J. Chem. Soc. Faraday Trans. 2 Mol. Chem. Phys.* **1974**, 70, 939.
- (8) Mardelli, M.; Olmsted, J. *J. Photochem.* **1977**, 7, 277,285.
- (9) Olmsted, J. *J. Phys. Chem.* **1979**, 83, 2581.
- (10) Braslavsky, S. E.; Heibel, G. E. *Chem. Rev.* **1992**, 92, 1381.
- (11) Adams, M. J.; Highfield, J. G.; Kirkbright, G. F. *Anal. Chem.* **1977**, No. 49, 1850.
- (12) Bard, A. J.; Faulkner, L. R. *Electrochemical Methods: Fundamentals and Applications*; **2001**.



# Summary of the Thesis

Sensitivity and reliability are fundamental requirements in bio- and medical assays. Many analytical techniques and detection methods are based on the use of fluorescence due to the sensitivity and rather inexpensive technology.

**Electrogenerated Chemiluminescence (ECL)** is for many applications more powerful and its use is extended also to sensing and detection of biomolecules. In ECL the light emission is generated by a process in which species generated at electrodes, with the support of a reducing or oxidizing agent, a co-reactant, undergo high-energy electron-transfer reactions to form emissive excited states.<sup>1</sup> Since the light intensity is usually proportional to the concentration of the emitting species, ECL has found wide application in diagnostics as a powerful analytical tool.<sup>2,3</sup>

It offers very sensitive detection, down to sub-picomolar concentrations with an extremely wide dynamic range greater than six order of magnitude. As there is no need of light source, the system is simple and it can be easily combined with other technologies such as microfluidics and capillary electrophoresis to obtain complete detection systems.<sup>2</sup> In all the assay it is necessary to have a luminophore, that will report on the presence of the analyte, in the case of immunoassays, and is coupled with a redox species, a co-reactant.

The most common label for ECL has been a derivative of Ruthenium(II) tris(2,2'-bipyridyl) ( $\text{Ru}(\text{bpy})_3^{2+}$ ) because of its bright emission, an excellent stability, ideal redox properties, and the possibility to use a variety of co-reactants in combination with a positive or negative bias applied to the electrode. Recently however the need for a more sensitive label and the search of multicolor emitters for multiplex assays resulted in the investigation of different metal complexes, such as Ir(III) compounds<sup>4-6</sup> or dendrimers and small polymers that possess more than one label.<sup>7</sup>

Concerning the co-reactant, Tri-(n)-propylamine (TPrA) is the most employed one, providing the optimum ECL signal when used in combination with  $\text{Ru}(\text{bpy})_3^{2+}$ .<sup>8</sup> Even in this case, it is desirable to replace TPrA, which is toxic, corrosive, volatile and needs to be used in high concentrations (usually up to 100 mM) to obtain good sensitivity.<sup>9</sup>

This doctoral dissertation **aims to develop new hybrid materials for ECL applications.**



In particular, the study begins with the ECL properties of new aggregated forms of metal complexes, based Platinum(II) and Iridium(III) complexes, and a new class of co-reactant based on Amine-Rich Carbon Nanodots, to end up in the development of new hybrid materials coming from the combination of nanoparticles and metal complexes. Finally, an approach for realizing immunoassay platforms for the detection of cardiac biomarkers will be presented.

In the first chapter of this thesis the general principles of ECL are presented. In general, ECL excitation pathways are closely related to their corresponding photoluminescent excitation pathways.<sup>10</sup>

The excited state can be produced through the reaction of radicals generated from the same chemical species (emitter), in the so-called **ion annihilation** mechanism, or from two different precursors (emitter and co-reactant), via **co-reactant ECL**.<sup>1,11</sup> (Figure 1). This represent the backbone of the experimental work presented in the other chapters. As the co-reactant ECL has more applications, the most used ECL luminophores and co-reactants are also presented with a critical overview in the latest use of nanomaterials in this field. In the last part of this chapter, the principal applications of ECL are briefly described.

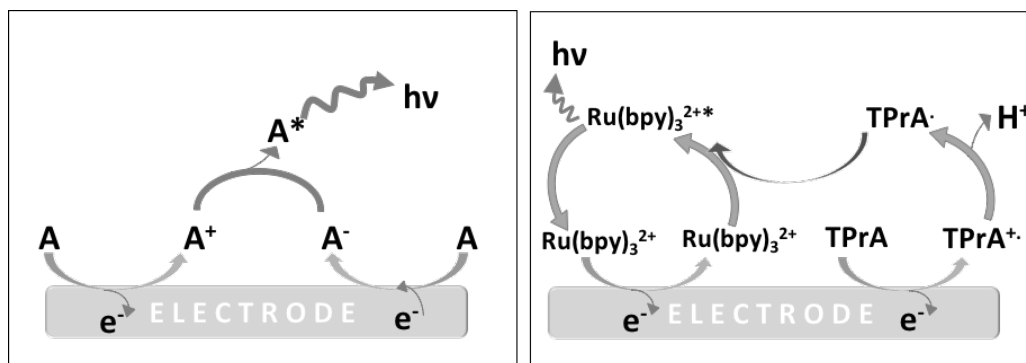


**Figure 1.** Schematic diagram describing the electron transfer reactions responsible for emission during annihilation ECL (left) and co-reactant ECL (right).

The second chapter is dedicated to a new class metal complexes for ECL based on supramolecular self-assembled square-planar Pt(II) complexes. These complexes are capable of forming different supramolecular assemblies depending on the concentration, solvent and temperature.<sup>12,13</sup>

Due to its d8 electronic configuration, platinum (II) complexes have a square planar geometry, allowing them to self-assemble by non-covalent interactions such as  $\pi$ - $\pi$  stacking (between the ligands) or metal-to-metal interactions (by the overlap of the  $5d_{z^2}$  orbitals).<sup>14,15</sup> A new electronic transition is hence formed, so-called triplet metal-metal to ligand charge transfer (MMLCT), as shown in Figure 2. This new transition results in dramatic changes in their luminescent properties.<sup>13,16,17</sup>

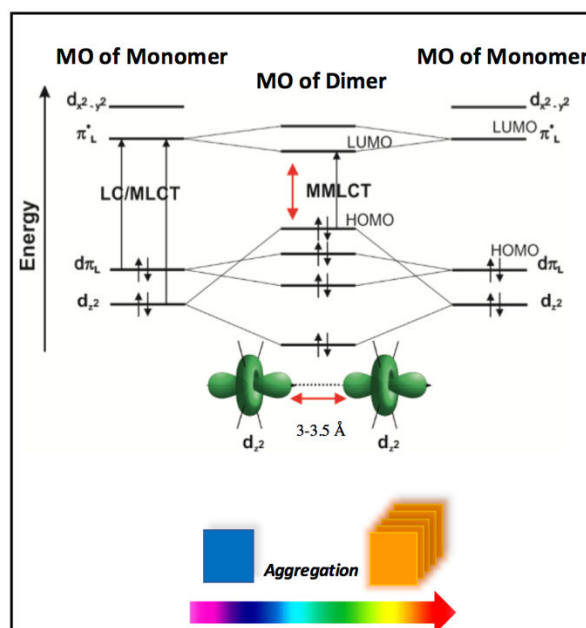


**Figure 2.** Simplified frontier molecular orbital showing the effect of interactions and intermolecular orbital overlap (top); Schematic representation of Pt(II) complex aggregation (bottom).

Despite the great interest in the photophysical properties of luminescent platinum (II) complexes and their assemblies, there are only few reports of their ECL properties.<sup>18–20</sup> Taking inspiration from the phenomenon of Aggregation-Induced Emission (AIE), typical for such self-assemblies,<sup>13,17,21</sup> we classified the ECL emission of these aggregates as **Aggregation-Induced ECL** (AIECL), not yet reported up to now in the field.

The investigated platinum complexes, called for their chemical features Pt-Amide, Pt-PEG and Pt-2PEG (Figure 3a-b-c), display very interesting ability to emit orange phosphorescence via ECL upon aggregation (Figure 3d), which is due to the establishment of Pt $\cdots$ Pt metallophilic interactions by electrical or mechanical stimuli or by spontaneous aggregation.

Notably, Pt-2PEG shows intense orange ECL emission that results higher in efficiency respect to the widely used standard  $\text{Ru}(\text{bpy})_3^{2+}$ , as shown in Figure 4a-b. Since the platinum complex molecularly dissolved displays blue photoluminescence in suitable solvents,<sup>12,13</sup> the orange emission is the result of an aggregation in water solution triggered by energetic requirements.

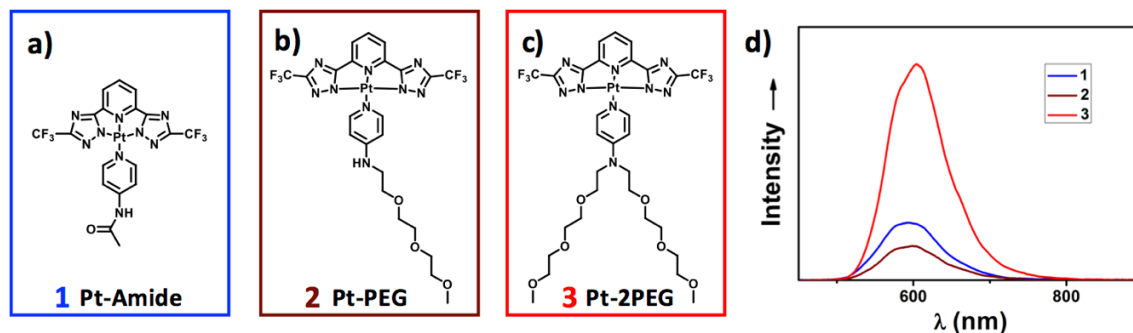


**Figure 3.** a) Pt-Amide structure; b) Pt-PEG structure; c) Pt-2PEG structure; d) ECL spectra during a potential scan of physical transfer of Pt-Amide (blue trace), Pt-PEG (brown trace) and Pt-2PEG (red trace) onto screen printed electrodes, using 10 mM  $\text{C}_2\text{O}_4^{2-}$  as co-reactant and 0.1 M  $\text{LiClO}_4$  as supporting electrolyte. Scan rate  $0.05 \text{ V s}^{-1}$ . Ag/AgCl as reference electrode and Pt wire as counter electrode.

Thanks to its dual hydrophilic/hydrophobic nature, we hypothesize that the complex tries to minimize the interactions between the hydrophobic chelate ligand and the aqueous environment forming a micelle-like structure with the PEG chains heading externally towards the water. Such aggregation forms through metallophilic interactions a new transition called MMLCT, responsible for the bathochromic shift of the emission.

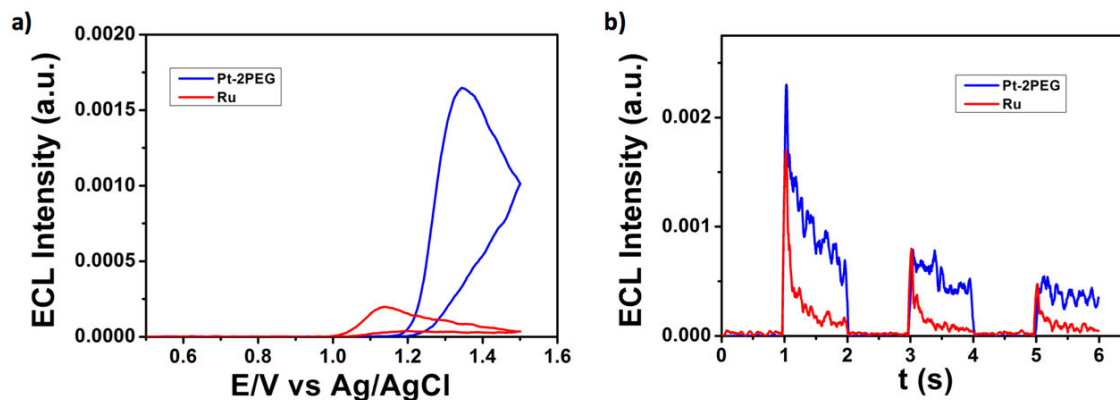


**Figure 4.** *a)* ECL intensity during a potential scan of  $10^{-5}$  M water solution of  $\text{Ru}(\text{bpy})_3^{2+}$  (red trace) and Pt-2PEG (blue trace) using 0.1 M  $\text{LiClO}_4$  as supporting electrolyte, upon addition of 10 mM of  $\text{Na}_2\text{C}_2\text{O}_4$ . Scan rate  $0.05 \text{ V s}^{-1}$ . GC as working electrode, Ag/AgCl as reference electrode and Pt wire as counter electrode; *b)* ECL Intensities in time of  $\text{Ru}(\text{bpy})_3^{2+}$  (red trace) and Pt-2PEG (blue trace) in 0.1 M  $\text{LiClO}_4$  water solution using 10 mM of  $\text{Na}_2\text{C}_2\text{O}_4$  as co-reactant. GC as working electrode, Ag/AgCl as reference electrode and Pt wire as counter electrode. Pulse at +1.4 V.

In search of new complexes, in chapter three we also investigated Ir(III) complexes for the fabrication of **solid-state ECL platforms**.  $[\text{Ir}(\text{pphent})_2(\text{dMe bpy})]$  (pphent= phenyl-phenanthridine; dMe bpy= 4,4' vinyl methyl byridine) contain a ligand that can polymerize due to the vinyl group attached to the bipyridine. The procedures of electrodeposition as well as photophysical, electrochemical and ECL properties are presented (Figure 5). It shows high emission during different voltammetric cycles, even though further improvements are still ongoing to render the electrodeposited film stable over the cycles.

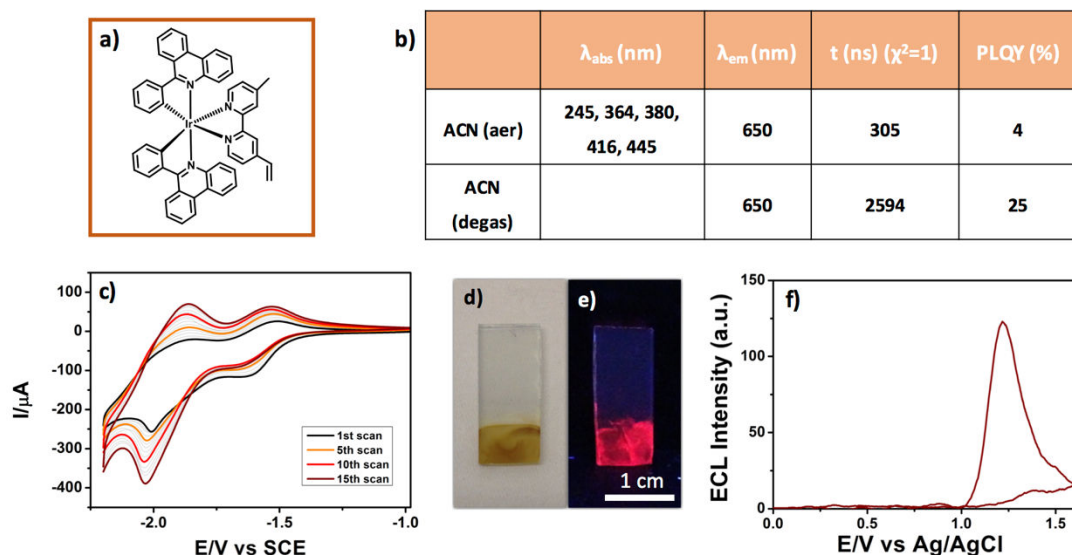


**Figure 5.** **a)**  $[\text{Ir}(\text{pphen})_2(\text{mVbpy})]$  structure; **b)** photophysical properties of the complex in acetonitrile (aerated and degassed solution); **c)** electropolymerization of the complex in 0.1 TBAPF<sub>6</sub> acetonitrile solution on FTO electrode. Scan rate 0.1 V s<sup>-1</sup>; **d-e)** electropolymerized layer of the complex on FTO (left) and under UV-vis irradiation (right); **f)** ECL intensity during a potential scan of poly-Ir film on FTO electrode during a potential scan between +1.6 V and 0 V upon addition of 10 mM TPrA as co-reactant. Scan rate 0.05 V s<sup>-1</sup>.

In the fourth chapter **co-reactant properties** of amine-rich Nitrogen-doped carbon nanodots (NCNDs) are revealed and tailored. As mentioned in the introduction a great challenge is to replace TPrA with something efficient, less volatile and non-toxic. The NCNDs presented show abundant amino groups on their surface. Since these groups are the most efficient and used co-reactant unit in combination with Ru(bpy)<sub>3</sub><sup>2+</sup>, this project focuses on the study of NCNDs bearing primary and tertiary alkyl amine groups on the surface as co-reactant for Ru(bpy)<sub>3</sub><sup>2+</sup> ECL generation (Figure 6). Their facile and low cost synthesis, good solubility in water and biocompatibility, make our NCNDs a promising user-friendly alternative to the toxic TPrA. We demonstrate that from primary to tertiary amines their ability in the generation of the emissive excited state of Ru(bpy)<sub>3</sub><sup>2+</sup> improves. In particular, the Ru(bpy)<sub>3</sub><sup>2+</sup> emission increases of 10 times with tertiary NCNDs (mNCNDs) respect to the NCNDs, showing that the toxic TPrA can be replaced up to a concentration of 20 mM (Figure 6b). Interestingly, constant ECL response (within 10%) were obtained for over 20 cycles, using mNCNDs as co-reactant (Figure 6c).

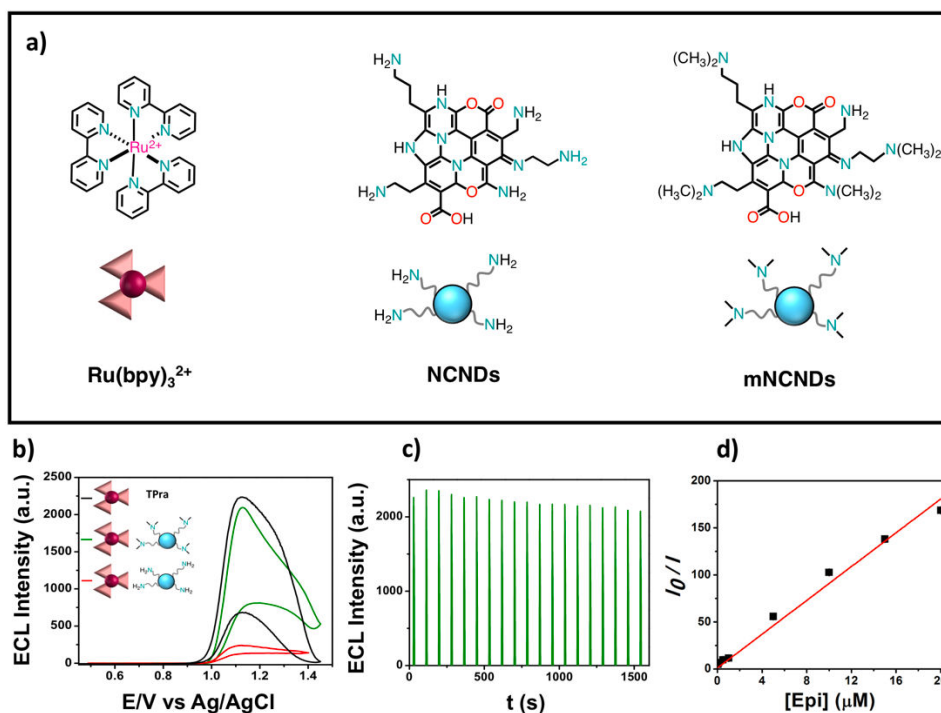


**Figure 6.** *a*) Tris(2,2'-bipyridine)ruthenium(II) ( $Ru(bpy)_3^{2+}$ ), nitrogen-doped carbon nanodots (NCNDs) in the middle and methylated-NCNDs (mNCNDs) on the left; *b*) ECL emission of  $Ru(bpy)_3^{2+}$  enhanced by 0.1 mg/mL NCNDs (red trace), 0.1 mg/mL mNCNDs (green trace) and 20 mM TPrA (black trace). GC electrode ( $d=3$  mm), potential referred to Ag/AgCl (KCl sat.) at room temperature. Platinum wire as counter electrode; *c*) ECL responses of  $Ru(bpy)_3^{2+}$ /mNCNDs system obtained during a continuous potential scan between +1.1 V and -0.9 V (20 cycles under scan rate  $0.05$  V  $s^{-1}$ ). GC electrode ( $d=3$  mm), potential referred to Ag/AgCl (KCl sat.) at room temperature. Platinum wire as counter electrode; *d*) Linear fitting of  $I_0/I$  versus the concentration of EP when mNCNDs are employed as coreactant in the concentration of 0.1 mg/mL. Error bars are of the same size of the square symbol.

Moreover, in an attempt to evaluate the possible use of this novel ECL system NCNDs/ $Ru(bpy)_3^{2+}$  as biosensing platform, the detection of L-Epinephrine, important neurotransmitter studied for diagnosis of neurological disorders, is discussed. Using mNCNDs, the limit of detection (LOD) and quantification (LOQ) decreased of a factor 10 respect to NCNDs, respectively 30 nM and 110 nM ( $S/N=3$ ). This result is ten times higher than the ones reported for different CNDs<sup>22,23</sup> and it reaches the same limit found using other types of techniques (Figure 6d).<sup>24–28</sup>

The fifth chapter is built on the active research field of ECL systems functionalized with nanomaterials. A variety of nanomaterials and in particular nanoparticles, such as gold or

silicon NPs, has been investigated in the framework of ECL hybrid system with transition metal complexes as emitter.<sup>29-32</sup> However, carbon nanodots-based hybrid ECL system has not so far been explored.

For this purpose, in the context of the use of nanoparticles aimed to obtain ECL signal enhancement, which represents the most interesting research line for the development of the ECL technique, we investigate the use of carbon nanodots as carrier for ECL labels. Indeed, our NCNDs presents outstanding advantages over other common nanoparticles. Their easily functionalizable surface without the need of additional treatments after the synthesis and their small size, together with all the above mentioned appealing characteristics, make NCNDs a particularly valuable carrier for ECL active species.

We present **NCND-based nanohybrids** bearing multiple ruthenium or iridium complexes as ECL labels (Figure 7a). An extensive study shows their redox and photophysical properties (Figure 7b-c) in order to evaluate the NCNDs effect on the ECL active units. The major concern about nanomaterial-based hybrid systems is associated to the proximity of the redox centers to the electrode surface, their ability to diffuse to it and the occurrence of quenching phenomena affecting their optical and electrochemical properties.

To conclude, the novel systems demonstrates to be an ECL self-enhancer platform, which is a promising ECL reaction pattern with enhanced luminous efficiency (Figure 7d). Additionally, the immobilization of these hybrids on the electrode surface prove signal intensity enhancement due to the presence of a plurality of signal-generating units on each NCNDs (Figure 7e).

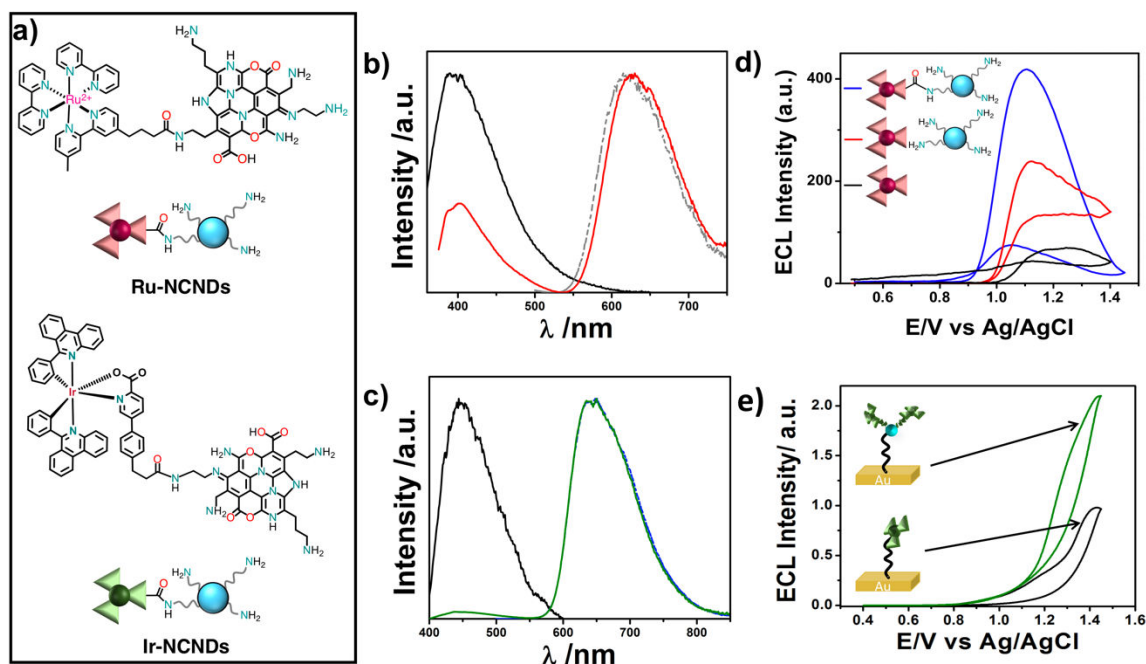


**Figure 7.** *a)* Covalently linked  $\text{Ru}(\text{bpy})_3^{2+}$ -NCND nanoconjugate on the top, and covalently linked Ir-COOH-NCND nanoconjugate on the bottom; *b)* Normalized emission spectra of Ru-NCNDs (red trace),  $\text{Ru}(\text{bpy})_3^{2+}$  (grey trace) and NCNDs (black trace) in Procell® solution ( $\lambda_{\text{exc}} = 340 \text{ nm}$ ); *c)* Normalized emission spectra of Ir-NCNDs (green trace), Ir-COOH (blue trace) and NCNDs (black trace) in Procell® solution ( $\lambda_{\text{exc}} = 380 \text{ nm}$ ); *d)* ECL intensity during a scan potential of  $10^{-4} \text{ M}$  PBS solution of  $\text{Ru}(\text{bpy})_3^{2+}$  (black trace), upon addition of  $0.1 \text{ mg/mL}$  of NCNDs (red trace) and of Ru-NCNDs (blue trace) with a  $10^{-4} \text{ M}$  concentration of Ru. Scan rate  $0.05 \text{ V s}^{-1}$ ; *e)* ECL Intensities recorded during a CV in PBS/ Triton X 100/ TPrA  $10 \text{ mM}$  of Ir-NCNDs (green trace) and Ir-COOH (black traces) after immobilization onto gold electrodes. Scan rate  $0.05 \text{ V s}^{-1}$ .

In the sixth chapter a new sensing approach based on Electrochemical Impedance Spectroscopy (EIS) and ECL for the detection of Troponin I (cTnI) is presented. The work aims to the use of an Ir(III) complex,  $[\text{Ir}(\text{pphent})_2(\text{Cepic})]$  to realize an **ECL biosensing** device for cTnI detection with enhanced properties. The innovation in this project consists in using a technique that, compared to the ones used for cardiac biomarkers detection, is higher sensitive by using a brighter iridium(III)-based metal complex, that can substitute the typical  $\text{Ru}(\text{bpy})_3^{2+}$ , permitting a detection of lower quantities of antigen in blood samples with a not expensive, fast and not harmful to the environment method.

The Ir-MAb conjugate is presented with their photophysical characterization, supported by confocal microscopy. The immunoassay configuration is shown in Figure 8a, and for each



concentration of cTnI electrochemical methods and confocal images can be useful to calculate the electrode surface coverage (Figure 8d-e). EIS is used as analytical technique in the range of concentration 1  $\mu\text{g/mL}$ -1  $\text{ng/mL}$  of cTnI. Changes in the EIS spectra can show the change in resistance and capacitance of the interface thus providing insight into the effect of surface modification (Figure 8b-c).

The LOD by applying this technique results 10  $\mu\text{g/mL}$  (Figure 8c) that can be additionally improved using ECL. Thanks to this technique the LOD reaches 0.42  $\mu\text{g/mL}$ , corresponding to  $1.76 \times 10^{-20}$  M ( $S/N=4$ ), resulting the lowest result until now reported for ECL based biosensors (Figure 8f-g).<sup>33-36</sup>

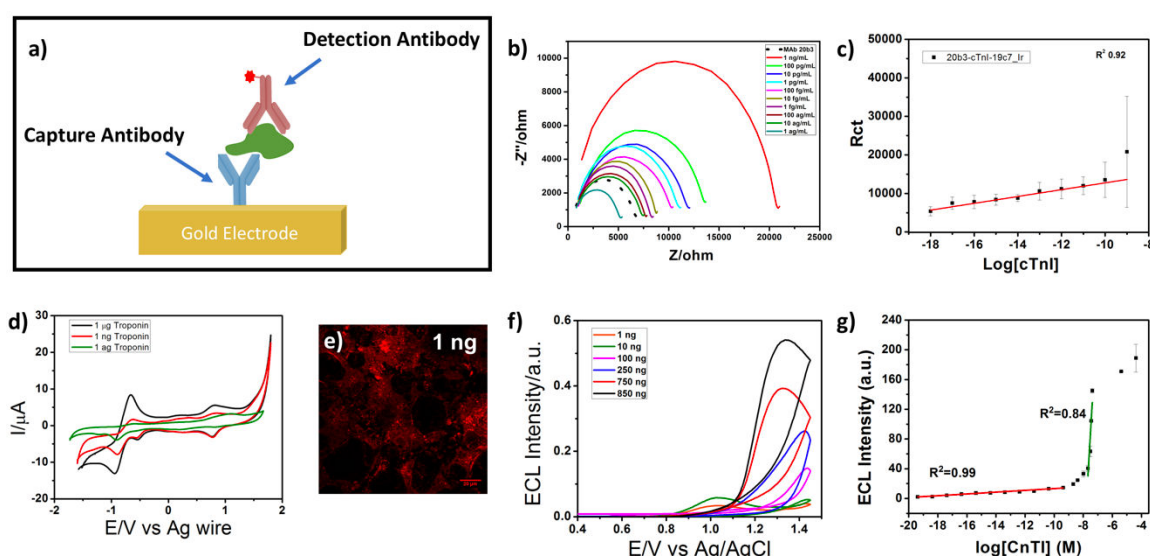


**Figure 8.** *a)* Representative scheme of the fabricated immunoassay for cTnI detection; *b)* Nyquist plots of immunoassay with the concentration of cTnI systematically varied from 1  $\mu\text{g/mL}$  to 1  $\text{ng/mL}$  in 1 mM DPBS ( $N=3$ ). The frequency range was between 0.01 and 100000 Hz, the ac amplitude was 25 mV amplitude and the dc potential set to the open circuit potential; *c)* Linear regression of  $R_{ct}$ ; *d)* Cyclic Voltammetry of the immunoassay at different concentration of cTnI: green trace 1  $\mu\text{g/mL}$ , red trace 1  $\text{ng/mL}$  and black trace 1  $\mu\text{g/mL}$ ; *e)* Confocal Images of the immunoassay with a concentrations of 1  $\text{ng/mL}$  of detection antibody. Scale bar 20  $\mu\text{m}$ ; *f)* Dependence of ECL intensity on the cTnI concentration (high concentration 1  $\text{ng}$ - 850  $\text{ng}$ ); *g)* Dependence of the ECL Intensity Area on  $\log[\text{cTnI}]$  (full range concentration) and linear regression of the two different zone of concentration. The error bars are comparable to, or smaller, than the size of the symbols.

This great result is coming from the improvement in the employed label, which results better than the standard  $\text{Ru}(\text{bpy})_3^{2+}$  in terms of efficiency. Also, the range studied with ECL

is 1 ag/mL-1 mg/mL of cTnI. Figure 8g shows the dependence of ECL intensity on the log[CnTI] over the entire range. From this plot  $K_D$  (dissociation constant) can be obtained and it is around  $10^{-8}$ M, fairly in agreement with the one in solution calculated for the same antibody ( $10^{-9}$  M)<sup>37</sup> and showing the great affinity of this antibody for CnTI.

On the way to conclude, we successfully studied new efficient systems ranging from metal complexes to nanoparticles for ECL applications. We explored the electrochemiluminescent properties of new Pt(II) and Ir(III) complexes as alternative of the existing  $\text{Ru}(\text{bpy})_3^{2+}$  label. The combination of labels and NCNDs bearing primary or tertiary groups on the surface as alternative co-reactant species to the toxic TPrA resulted in an interesting strategy to eliminate the toxic TPrA. In particular, NCNDs in covalently linked system with  $\text{Ru}(\text{bpy})_3^{2+}$  (Ru-NCNDs) is not only an innocent carrier for ECL active species, but act also as co-reactant in the ECL process, revealing itself an ECL self-enhancing platform. Finally, a real immunoassay for cardiac marker detection has been built with enhanced sensitivity and stability, which is of fundamental importance for biological and bio-medical detection applications. The same technology can then be applied to a variety of other analytes opening the venue to other assays.

## References

- (1) Bard, A. J. *Electrogenerated Chemiluminescence*; Marcel Dekker, Inc.: New York., 2004.
- (2) Miao, W. *Chem. Rev.* **2008**, *108* (7), 2506.
- (3) Hu, L.; Xu, G. *Chem. Soc. Rev.* **2010**, *39* (8), 3275.
- (4) Swanick, K. N.; Ladouceur, S.; Zysman-Colman, E.; Ding, Z. *Chem. Commun.* **2012**, *48*, 3179.
- (5) Barbante, G. J.; Doeven, E. H.; Francis, P. S.; Stringer, B. D.; Hogan, C. F.; Kheradmand, P. R.; Wilson, D. J. D.; Barnard, P. J. *Dalt. Trans.* **2015**, *44* (18), 8564.
- (6) Fernandez-Hernandez, J. M.; Longhi, E.; Cysewski, R.; Polo, F.; Josel, H.-P.; De Cola, L. *Anal. Chem.* **2016**, *88* (8), 4174.
- (7) Staffilani, M.; Höss, E.; Giesen, U.; Schneider, E.; Hartl, F.; Josel, H. P.; De Cola, L. *Inorg. Chem.* **2003**, *42* (24), 7789.

- (8) Miao, W.; Choi, J.-P.; Bard, A. J. *J. Am. Chem. Soc.* **2002**, *124* (48), 14478.
- (9) Liu, X.; Shi, L.; Niu, W.; Li, H.; Xu, G. *Angew. Chem. - Int. Ed.* **2007**, *46* (3), 421.
- (10) Santhanam, K.; Bard, A. J. *J. Am. Chem. Soc.* **1965**, *2243*, 139.
- (11) Richter, M. M. *Chem. Rev.* **2004**, *104* (6), 3003.
- (12) Sinn, S.; Biedermann, F.; Vishe, M.; Aliprandi, A. *ChemPhysChem* **2016**, *17*, 1829.
- (13) Aliprandi, A.; Mauro, M.; Cola, L. De. *Nat. Chem.* **2016**, *8* (January), 10.
- (14) Miskowski, V. M.; Houlding, V. H. *Inorg. Chem.* **1989**, *28* (8), 1529.
- (15) Lu, W.; Chan, M. C. W.; Zhu, N.; Che, C. M.; Li, C.; Hui, Z. *J. Am. Chem. Soc.* **2004**, *126* (24), 7639.
- (16) Ma, B.; Li, J.; Djurovich, P. I.; Yousufuddin, M.; Bau, R.; Thompson, M. E. *J. Am. Chem. Soc.* **2005**, *127* (1), 28.
- (17) Mauro, M.; Aliprandi, A.; Cebrián, C.; Wang, D.; Kübel, C.; De Cola, L. *Chem. Commun.* **2014**, *50* (55), 7269.
- (18) Chen, Z.; Wong, K. M.; Kwok, E. C.; Zhu, N.; Zu, Y.; Yam, V. W. *Inorg. Chem.* **2011**, *50*, 2125.
- (19) Li, C.; Wang, S.; Huang, Y.; Zheng, B.; Tian, Z.; Wen, Y.; Li, F. *Dalt. Trans.* **2013**, *42*, 4059.
- (20) Reid, E. F.; Cook, V. C.; Wilson, D. J. D.; Hogan, C. F. *Chem. A Eur. J.* **2013**, *19*, 15907.
- (21) Aliprandi, A.; Genovese, D.; Mauro, M.; De Cola, L. *Chem. Lett.* **2015**, *44* (9), 1152.
- (22) Long, Y.-M.; Bao, L.; Zhao, J.-Y.; Zhang, Z.-L.; Pang, D.-W. *Anal. Chem.* **2014**, *86* (15), 7224.
- (23) Xu, Z.; Yu, J.; Liu, G. *Sensors Actuators B Chem.* **2013**, *181*, 209.
- (24) Kang, J.; Yin, X. B.; Yang, X.; Wang, E. *Electrophoresis* **2005**, *26* (9), 1732.
- (25) Guo, Y.; Yang, J.; Wu, X.; Du, A. *J. Fluoresc.* **2005**, *15* (2), 131.
- (26) Babaei, A.; Mirzakhani, S.; Khalilzadeh, B. *J. Braz. Chem. Soc.* **2009**, *20* (10), 1862.
- (27) Guo, Z. H.; Dong, S. J. *Electroanalysis* **2005**, *17* (7), 607.
- (28) Li, F. *Talanta* **2003**, *59* (3), 627.
- (29) Yu, Y.; Zhou, M.; Cui, H. *J. Mater. Chem.* **2011**, *21* (34), 12622.
- (30) Zonarini, S.; Rampazzo, E.; Bonacchi, S.; Juris, R.; Marcaccio, M.; Montalti, M.; Paolucci, F.; Prodi, L. *J. Am. Chem. Soc.* **2009**, *131* (40), 14208.

- (31) Valenti, G.; Rampazzo, E.; Bonacchi, S.; Khajvand, T.; Juris, R.; Montalti, M.; Marcaccio, M.; Paolucci, F.; Prodi, L. *Chem. Commun.* **2012**, 48, 4187.
- (32) Ding, Z.; Quinn, B. M.; Haram, S. K.; Pell, L. E.; Korgel, B. A.; Bard, A. J. *Science* (80-. ). **2002**, 296 (5571), 1293.
- (33) Zhou, Y.; Zhuo, Y.; Liao, N.; Chai, Y.; Yuan, R. *Talanta* **2014**, 129, 219.
- (34) Qi, H.; Qiu, X.; Xie, D.; Ling, C.; Gao, Q.; Zhang, C. *Anal. Chem.* **2013**, 85, 3886.
- (35) Shen, W.; Tian, D.; Cui, H.; Yang, D.; Bian, Z. *Biosens. Bioelectron.* **2011**, 27 (1), 18.
- (36) Li, F.; Yu, Y.; Cui, H.; Yang, D.; Bian, Z. *Analyst* **2013**, 138 (6), 1844.
- (37) Conroy, P. J.; Okennedy, R. J.; Hearty, S. *Protein Eng. Des. Sel.* **2012**, 25 (6), 295.



# Acknowledgements

On the last notes of this thesis, I would like to spend my words of gratitude to a number of people who have been part of this incredible experience that I use to call “*Strasbourg Life*”.

Firstly, I would like to thank my supervisor Professor Luisa De Cola for giving me the opportunity to work in this project with all the freedom that a scientist needs to have. Thank you for all the interesting discussion about work and lifestyle, and for all the small hints and advices that you gave to me during these three years. I am really happy about the accomplished job.

I would also like to thank Professor Robert Forster with who I spent 4 thrilling months at Dublin College University in Ireland. Your creative soul mixed with your knowledges and expertise, your easy-going personality and your passion for research made my visiting period challenging and motivating. Thank you too for your humor about Italia, I am sure you love my country. Thanks as well to Dr. Elaine Spain and Dr. Kellie Adamson for their constant help during my stay. My work at DCU was much easier thanks to you two.

A big part of acknowledgements goes also to Professor Conor Hogan, from La Trobe University in Melbourne, with who I worked on different projects in Dublin and in Strasbourg during his sabbatical period in Europe. Thank you for your real daily help, for your kindness and your support, hoping that our future collaboration will be intense, positive and fruitful.

I would like to acknowledge all the members of the jury committee of my defense, Professor Paola Ceroni, Professor Neso Sojic and Dr. Antoine Bonnefont, for kindly accepting to read and judge this thesis. Thank you.

My sincere acknowledgements go also to Professor Francesco Paolucci and Professor Alexander Kuhn, two mentors for me since long time. Thank you because your advices and support are always for me reason to move on in this arduous path.

Dr. Giovanni Valenti and Dr. Stefania Rapino thank you two for the constant presence and friendship during these years. You are for me a model of honest devotion to work. I hope to keep always alive this connection born several years ago.

My gratitude goes to Prof. Maurizio Prato, who has been from far a good and wise advisor. I acknowledge him for the opportunity to expand my knowledges and for his enthusiasm that never turns off.

Francesca, my future Dr. Arcudi, your small body will never contain your powerful brain and your incredible energy in front of science. Thank you for the synergic work, for all the inspiring discussions about our job and our lives. You have been the perfect mate that every single person would love to have beside. The months you spent with me in Strasbourg will be unforgettable especially for the friendship you have sincerely created with me. There are not enough words to describe all this and you know that. Grazie, ce l'abbiamo fatta.

Some special thanks are for Dr. Matteo Mauro, the most brilliant colleague I have ever met here in Strasbourg. Thank you for all the advices and your friendship. You are like a brother for me. Surely, the most important thing you did was to allow me to meet Cristina, the sweetest human being on earth. Thank you too for everything. You have been home for me in many cases. Words are not enough neither in this case.

Becky, my soul mate, the craziest funniest lovely girl I had the chance to meet here. With you the world seems shrinking and shrinking and for us it will never be a problem the distance. You know all the reasons for which I thank you.

Ingrid, mi hermana. Eres la persona que me dio la primera razón para amar Estrasburgo. Has sido realmente importante para mi desde el principio y en mi corazón tienes un lugar que no será reemplazado por nadie. Has sido mi Familia y tu más que nadie sabe de sobra las razones.

J'ai pas les mots justes pour remercier Dr. Youssef pour tout ton support, ta gentillesse, ton aide, pour être toujours là pour moi, pour ton amitié sincère. Merci mon ami.

Dr. Richi, mon sourire constant, mon BOH préféré, merci beaucoup mon ami; aussi dans ce cas la je ne trouve pas beaucoup de mots pour te montrer tout les bonnes choses que tu m'as donné.

Alberto, lo unico que quiero decirte aqui es un profundo Gracias porque dejaste en mi corazón un pedacito de dulzura y humildad que te diferencian. Grazie Peque. Eres inolvidable.

I would love to express my gratitude for my sweet John Le Grand, mon ami Mike, mon pote Remi, la dolce Alessandra, la minion Matilde, the amazing Veronique and l'entusiasmante Camilla because you have been the best friends here I could have ever desired. Grazie.

Dr. Simone Silvestrini, thank you for your great support and amazing scientific discussion, but also for your friendship together with Federica. Grazie ragazzi.

Dr. Alessandro Aliprandi, thanks a lot for your kindness and help in the laboratory. Every conversation with you is a big stimulus for me.

Merci Claire d'abord pour ton amitié et après pour tout l'aide que tu m'as donné pendant ces trois ans. Un immense merci.

Thanks to all my colleagues of the past and of the present: Maurizio, Milica, Bertucci, Beatrice, Capaldo, Amparo, Damiano, Angeliq, Frank, Federica, Leana, Pierre, Stephan, Pengkun, Chien-Wei, Loic, Laetitia, Eko, Ines, Peppe Alonci, Yevhen, Valentina, Veronika, Dedy, Hiroki, Etienne, Christelle, Christof, Ligia, Vito, Tommaso, Luka.

Thanks from the bottom of my heart to my crew outside the work time: Pilar, Elena, Yuliya, Anna, Meiggie, Ramzi, Nadjib, Dimby, Andreina, Fabian, Micheal.

I would love to thank Dr. Monica Epifanio, my Sicilian mate in Dublin. Thank you amazing friend, you have pushed me to the best every single day of my irish stay and not only. Grazie di tutto.

Thanks to my Dance Company La Chéile in Dublin. Passing my irish time (and not only) with you was the most amazing thing I could have ever dreamt. To all of you an immense GRAZIE.

Thank you, Claudio, my smallest best friend. You are always there to support me and I know that you will never go away from my life.

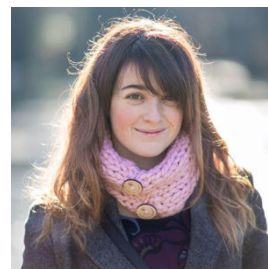
Thank you, Mattia, because during these stressful final months you have been always close to me giving me without any stop all the positive energies I needed. I know you will be always there from now on, as you have already shown me in the past 12 years.



As for every achievement of my life, my last words go to my Family, because without them I would not be here today. They are my support, my shoulders, my soul, my reason and wherever I will be they will be always with me.

## CURRICULUM VITAE

Carrara Serena



### PERSONAL DETAILS

**DATE OF BIRTH** 25/10/1989  
**GENDER** Female  
**NATIONALITY** Italian  
**ADDRESS** CDE- 46 Boulevard de la Victoire  
Logement 607  
67000 Strasbourg Cedex

**EMAIL** [serenella.carrara@gmail.com](mailto:serenella.carrara@gmail.com)  
[scarrara@unistra.fr](mailto:scarrara@unistra.fr)

**MOBILE** +33782434188  
+393405651022

### PROFILE

Highly-qualified and passionate scientist with four years experience in the area of electrochemistry and photophysics, in particular with application in biodiagnostics. Seeking a challenging role as researcher in the biosensing/biodiagnostic field where my skill set and experience will add significant value. Proven ability to supervise projects, deliver results to a tight deadline, and adhere to good laboratory practice. Effective as part of a team or solo.

### EDUCATION

**Dates** 03/02/2014-11/04/2017  
**Qualification** **PhD Candidate in Chemistry**, Supervision Prof. Luisa De Cola  
**Organization** Institut de Science et d'Ingénierie Supramoléculaires (ISIS) - Université de Strasbourg

**Dates** 17/10/2013  
**Qualification** **Master Degree (M.Sc) in Photochemistry and Molecular Materials 110/110 cum Laude** (with honour)  
**Principal Subject** Generation and tracking of two-dimensional motion by bipolar electrochemistry (Supervisors Prof. Alexander Kuhn, Prof. Francesco Paolucci)  
**Organization** Università Alma Mater Studiorum di Bologna

**Dates** 29/09/2011  
**Qualification** **Bachelor Degree (B.Sc) in Chemistry 110/110 cum Laude** (with honour)  
**Principal Subject** Structural characterization of the quaternary system H<sub>2</sub>O/CTAB/Butanol/Heptane by means conductimetry and Small Angle X-Ray Scattering (Supervisor Prof. Delia Chillura)

**Organization** Università degli Studi di Palermo

**Higher education** Liceo Classico Statale “Umberto I” Palermo, mark 100/100 cum laude (with honour)

#### CORE SKILLS & COMPETENCES

**Excellent skills in electrochemistry**, which includes potentiodynamic and potentiostatic methods, basic electrochemical impedance spectroscopy, electrochemiluminescence (ECL). Skills in bipolar electrochemistry and electropolymerisation. Good expertise in fabrication of OLED and characterization.

**Excellent knowledges in photophysics**, which includes UV-Vis electronic absorption, steady state and time-resolved fluorescence spectroscopy, confocal and fluorescence microscopy, fluorescence anisotropy.

**Good knowledges in assays/sensors development**, from fabrication to their employment.

**Basic knowledges in scattering techniques** (small angle and wide angle x-ray and neutron scattering, dynamic light scattering) **and in microscopy**, which includes scanning electron microscopy and transmission electron microscopy.

**Basic knowledges of organo-metallic synthesis.**

#### COMPUTER SKILLS & COMPETENCES

Good knowledge of Word, Excel, PowerPoint, SciFinder Scholar, ChemDraw, Origin. Good knowledge of computer assembly and problem solving. I completed the European Computer Licence. Skills Card N° IT – 1307238.

#### LANGUAGES & COMPETENCE

**Mother Tongue** Italian  
**Other Languages** English, Level C1\*, TOEFL (IbT) 95/120 (08/06/2013), Full professional proficiency  
French, Level C1\*, Full professional proficiency  
Spanish, Level B2\*, Independent user

\*Common European Framework of Reference for Languages

#### ADDITIONAL SKILLS

Driving Licence B  
Contemporary dancer in small amateur companies

#### PUBLICATIONS

1. **S. Carrara**<sup>#</sup>, F. Arcudi<sup>#</sup>, M. Prato & L. De Cola, “Amine-Rich Carbon NanoDots as platform for self-enhancing in electrochemiluminescence”, *Just Accepted in Angewandte Chemie International Edition*. DOI: 10.1002/anie.201611879.
2. P. Ai, M. Mauro, C. Gourlaouen, **S. Carrara**, L. De Cola, Y. Tobon, U. Giovanella,

C. Botta, A. A. Danopoulos, P. Braunstein, "Bonding, luminescence, metallophilicity in linear Au<sub>3</sub> and Au<sub>2</sub>Ag Chains stabilized by rigid diphosphanil NHC ligands", *Inorganic Chemistry* **2016**, 55, 8527-8542.

3. J. Roche, **S. Carrara**, J. Sanchez, J. Lannelongue, G. Loget, L. Bouffier, P. Fischer & A. Kuhn, "Wireless powering of e-swimmers", *Scientific Reports* **2014**, 4, Article number: 6705 doi:10.1038/srep06705.

*In preparation*

1. A. Ruiz-Carretero, Y. Antoini, E.A. Prasetyanto, A. Operamolla, **S. Carrara**, S. Sinn, E. Orgiu, G. Farinola, L. De Cola, "Synthesis, photophysical properties, packing mode and electronic mobility of oligothiophene-substituted Pt(II) complexes"
2. **S. Carrara**, A. Aliprandi, C.F. Hogan & L. De Cola, "Revealing Aggregation-Induced Electrochemiluminescence of Pt(II) complexes"
3. **S. Carrara**, K. Adamson, E. Spain, L. De Cola & R.J. Forster, "ECL immunoassay for detection of Troponin I with enhanced properties"

#equal author contribution

**COMMUNICATIONS & POSTERS**

1. *Oral Communication*: **S. Carrara**, F. Arcudi E. Longhi, M. Prato and L. De Cola, "Toward efficient nanostructured materials for ECL applications"; EuCheMS 2016 ,11-15/09/2016 Seville, Spain.
2. *Oral Communication*: **S. Carrara**, F. Arcudi E. Longhi, M. Prato and L. De Cola, "Toward efficient nanostructured materials for ECL applications"; ECL 2016 ,29-31/08/2016 Bordeaux, France.
3. *Poster*: F. Arcudi, **S. Carrara**, E. Longhi, M. Mauro, M. Prato and L. De Cola, "A facile route to carbon dots and their application in electrically driven devices"; ISMSC ,28/06-02/07/2015 Strasbourg, France.
4. *Poster*: **S. Carrara**, C-W. Hsu, N. Licciardello, E. Longhi, M. Mauro and L. De Cola, "Toward efficient nanostructured materials for ECL"; E-WISPOC 2015,1-6/02/2015 Bressanone, Italy.
5. *Poster*: **S. Carrara**, E. Longhi and L. De Cola, "Doped polymeric nanoparticles as new ECL system for bioapplications"; ECL 2014,7-10/09/2014 Bertinoro, Italy.



# Towards new efficient nanostructured hybrid materials for ECL applications

## Résumé

Cette thèse de doctorat vise à développer de nouveaux matériaux hybrides pour les applications ECL, allant des complexes métalliques aux nanoparticules. Dans le domaine de complexes métalliques, les propriétés électrochimiluminescentes de nouveaux complexes de Pt(II) et d'Ir(III) ont été explorés comme alternative au marqueur  $\text{Ru}(\text{bpy})_3^{2+}$  existant. Passant aux nanomatériaux, la combinaison d'étiquettes et de carbon nanodots portant des groupes primaires ou tertiaires à la surface comme espèces co-réactives alternatives a abouti à une stratégie intéressante pour éliminer la TPrA. En particulier, les carbon nanodots dans un système lié par liaison covallent avec  $\text{Ru}(\text{bpy})_3^{2+}$  sont non seulement un support innocent pour les espèces actives d'ECL, mais agissent également comme co-réactif dans le procédé ECL, se révélant être une plateforme auto-améliorante en ECL. Enfin, un véritable immuno-essai pour la détection des marqueurs cardiaques a été mis au point avec une sensibilité et une stabilité accrues, ce qui est d'une importance fondamentale pour les applications de détection biologique et biomédicale. La même technologie peut alors être appliquée à une variété d'autres analytes, ouvrant ainsi le site à d'autres dosages.

Mots-clés : électrochimiluminescence, complexes métalliques, carbon nanodots, co-réactif, immuno-essai

## Résumé en anglais

This doctoral dissertation aim to develop new hybrid materials for ECL applications, ranging from metal complexes to nanoparticles. In the field of metal complexes, the electrochemiluminescent properties of new Pt(II) and Ir(III) complexes were investigated as alternative of the existing  $\text{Ru}(\text{bpy})_3^{2+}$ . Passing to nanomaterials, the combination of labels and NCNDs bearing primary or tertiary groups on the surface as alternative co-reactant species resulted an interesting strategy to eliminate the toxic TPrA. In particular, NCNDs in covalently linked system with  $\text{Ru}(\text{bpy})_3^{2+}$  is not only an innocent carrier for ECL active species, but act also as co-reactant in the ECL process, revealing itself an ECL self-enhancing platform. Finally, a real immunoassay for cardiac marker detection has been built with enhanced sensitivity and stability, which is of fundamental importance for biological and bio-medical detection applications. The same technology can be applied to a variety of other analytes opening the venue to other assays.

Keywords : electrochemiluminescence, metal complexes, carbon nanodots, co-reactant, immunoassay

